VILNIUS UNIVERSITY

CENTER FOR PHYSICAL SCIENCES AND TECHNOLOGY

JULIUS VENGELIS

CHARACTERIZATION OF PHOTONIC CRYSTAL FIBER DISPERSION AND INVESTIGATION OF SUPERCONTINUUM GENERATION

Doctoral dissertation
Physical sciences, physics (02P)

Vilnius, 2018

The doctoral dissertation was prepared in Vilnius University from 2014 to 2018.

Scientific supervisor – assoc. prof. dr. Vygandas Jarutis (Vilnius University, physical sciences, Physics – 02P)

VILNIAUS UNIVERSITETAS
FIZINIŲ IR TECHNOLOGIJOS MOKSLŲ CENTRAS

JULIUS VENGELIS

FOTONINIŲ KRISTALŲ ŠVIESOLAIDŽIŲ DISPERSIJOS CHARAKTERIZAVIMAS IR SUPERKONTINUUMO GENERACIJOS TYRIMAS

Daktaro disertacija
Fiziniai mokslai, fizika (02P)

Vilnius, 2018

Disertacija rengta 2014 – 2018 metais Vilniaus universitete.

Mokslinis vadovas – doc. dr. Vygandas Jarutis (Vilniaus universitetas, fiziniai mokslai, fizika – 02P)

Table of Contents

Acknowledgements

There are many people who I am sincerely grateful for the wonderful experiences, shared knowledge and provided opportunities to work and grow as a scientist and as a personality during my doctoral studies in Laser Research Center of Vilnius University.

Firstly, I would like to thank my doctoral studies supervisor assoc. prof. dr. Vygandas Jarutis for his guidance, patience, criticism and overtime work during these years. All of this helped me to advance and seek my goals.

Secondly, I would like to thank prof. habil. dr. Valdas Sirutkaitis who was *de facto* my second supervisor and mentor. I am thankful to him for his lectures who raised my interest in laser physics and nonlinear optics, also, for the given opportunity to work in his group in Laser Research Center of Vilnius University and for encouragement to seek a career in academia.

I would also like to express my gratitude to other contributors and all personnel of Laser Research Center for support. I am especially thankful to dr. Rimantas Grigonis and assoc. prof. dr. Viktorija Tamulienė for involving me in joint research projects. In addition, I thank dr. Julianas Želudevičius from Center for Physical Sciences and Technology for technical support.

I also thank my friends Dovilė, Giedrė, Žydrūnas, Birutė and Darius for their optimistic remarks and for believing in me.

Finally, a special thanks goes to my student colleagues, especially to Agnė, Rosvaldas, Balys and Rusnė, who have become not only trusted colleagues but also dear friends outside work. Thank you all for being on this great journey with me!

<div align="right">

Julius Vengelis

Vilnius

2018

</div>

List of abbreviations

BBO – β-barium borate.

CCD – charge-coupled-device.

CW – continuous wave radiation.

D – optical fiber dispersion parameter.

FP – Fabry-Perot etalon.

FROG – frequency-resolved optical gating.

FSR – free spectral range.

FWHM – full width at half maximum.

GVD – group velocity dispersion.

GDD – group delay dispersion.

GVM – group velocity mismatch.

GNLSE – generalized nonlinear Schrödinger equation.

IR – infrared spectrum range.

KTP – potassium titanyl phosphate.

MZI – Mach-Zehnder interferometer.

NA – numerical aperture.

Nd:YAG – Nd^{3+}:$Y_3Al_5O_{12}$.

NIR – near infrared spectrum range.

PBG – photonic bandgap.

PCF – photonic crystal fiber.

PM – polarization-maintaining.

SEM – scanning electron microscope

SPM – self-phase modulation.

TOD – third order dispersion.

VIS – visible spectrum range.

XFROG – cross-correlation frequency-resolved optical gating.

XPM – cross-phase modulation.

Yb:KGW – Yb^{3+}:$KGd(WO_4)_2$.

ZDW – zero group velocity dispersion wavelength.

Introduction

Many of us would agree that optical fibers are one of the greatest technological innovations of the 20th century. Although the basic physics of light guiding was demonstrated in the 1840s by Daniel Colladon and Jacques Babinet and later described in John Tyndall's books about the nature of light [1, 2], main technological innovations of optical fiber technology emerged at the second half of the 20th century [3] when in 1970 scientists working at *Corning* demonstrated dramatic reduction of losses in optical fibers [4]. The wide use of optical fibers in telecommunications and many other areas including sensing, medicine, machining, etc. have become a part of our life in the digital age [5]. At the end of the 20th century, after decades of intensive research, the technology of conventional optical fibers has been perfected in many ways and most limitations of the existing technology have been reached, so scientists began to look for completely different methods of optical fiber design.

The idea to create a new type of optical fiber dates back to the invention of multidimensional (2D and 3D) photonic crystals in the 1980s [6, 7]. A photonic crystal can be defined as a structure patterned with a periodicity of dielectric constant which makes light behave in a similar way to electrons in crystal lattices [8]. Consequently, a photonic crystal fiber (PCF) can be described as a special optical fiber with a built-in periodic microstructure region along the fiber. One particularly important feature of electron and crystal lattice interaction is that under certain conditions the periodic potential created by the crystal may create a frequency band in which electron propagation with energies falling in this frequency band is prohibited [9]. In case of photonic crystals this frequency band is called photonic bandgap (PBG)[10]. The idea behind a photonic crystal fiber was to employ the PBG effect to confine light in the fiber: this would enable to manipulate properties of the medium (photonic crystal fiber) by changing structural parameters of the microstructured area.

It is not common knowledge that the first proposal of a special fiber employing 1D photonic crystal for light guiding was made by P. Yeh and colleagues in their papers in 1976 and 1978 – before the introduction of

photonic crystals [11, 12]. The authors proposed and analysed the possibility of creating optical fibers with multiannulus cladding of periodically changing refractive index between neighbouring rings and core which would have lower refractive index than the cladding. Such structure is essentially a 1D photonic crystal and was named Bragg fiber.

The idea of photonic crystal fiber made of a 2D photonic crystal with an air core was proposed by Phillip Russell in 1992 [13]. The first successfully fabricated photonic crystal fiber was reported in optical fiber conference in 1996 [14] and the subsequent paper by J. Knight, T. Birks, P. Russell and D. Atkin [15]. However, first PCF had a solid core at the center of microstructured region and light inside such PCF propagated due to modified total internal reflection [16]. The first PCF which had hollow core and employed the originally proposed photonic bandgap mechanism for confining light was reported in 1999 [17]. Interestingly, although proposed much earlier, the first successful fabrication of Bragg fibers was reported in 1999 and 2000 [18, 19].

The introduction of photonic crystal fibers has given a huge impact in many areas such as spectroscopy, microscopy, sensing, frequency metrology, optical coherence tomography, low coherence interferometry, nonlinear optics, etc. [20–25]. Many of these applications are related to PCF application as a medium for supercontinuum generation – a remarkable nonlinear optical phenomenon which was first demonstrated in bulk media in 1970 [26, 27] and achieved using PCF in 1999 [28, 29]. We can describe supercontinuum generation as a nonlinear optical phenomenon of extreme spectral broadening of light. Supercontinuum generation mechanism is very complicated since it is a result of many interacting nonlinear phenomena. The application of photonic crystal fiber as a medium for supercontinuum generation has been a milestone in nonlinear optics. Firstly, it enabled investigation of supercontinuum generation in nonlinear media with unique properties which could be adjusted by altering the structural parameters of PCF microstructured region. Freedom to design PCF properties opened the opportunity for researchers in the field to observe supercontinuum generation in PCF using a wide range of pump source

parameters which was impossible in bulk media, conventional fibers or liquids. Secondly, it allowed the use of pump sources with relatively small peak intensities which were compensated by large length of nonlinear medium (PCF). Consequently, supercontinuum generation in PCF has been observed using subnanosecond, nanosecond and even continuous-wave laser radiation [30–35] which opened new application opportunities and brought additional insight on the physics of supercontinuum generation. Experimental simplicity, opportunity to use nonlinear media with unique dispersive and waveguide properties and the possibility to use a wider range of pump sources renewed the interest in supercontinuum generation leading to a large range of applications of PCF based supercontinuum sources in the aforementioned fields.

A great amount of research concerning physics of supercontinuum generation in PCF has been performed in the last two decades. This has significantly expanded the understanding of the physics involved [21, 36–38] which was accompanied by the developed qualitatively accurate numerical simulation models for supercontinuum generation. Despite this, there are still numerous cases (certain experimental conditions) of supercontinuum generation that require deeper analysis.

One of such cases, which is discussed only in a few papers [39–48], is the use of chirped femtosecond pump pulses for supercontinuum generation in PCF. This could be beneficial as the ability to change certain pump radiation parameters of a single laser, such as chirp of pump pulse, would allow direct control of supercontinuum characteristics in real time.

Another special case which also is a subject of this doctoral dissertation is research regarding broadband supercontinuum generation in the entire visible range of optical spectrum using subnanosecond pump sources, usually Nd^{3+} based Q-switched microlasers. Due to the fact that it is difficult to manufacture PCFs with ZDW shifted below 600 nm using conventional PCF fabrication techniques, achieving supercontinuum spanning in the whole visible range in case of subnanosecond pump pulses is a complex task [49]. Broadband supercontinuum sources with subnanosecond pulse widths and spectrum spanning through the entire visible

range could be efficient seed radiation sources for subnanosecond optical parametric generators. Although various methods of subnanosecond supercontinuum spectrum extension to cover the whole visible range have been reported [34, 35, 50–59], they require complex experimental setups or rather sophisticated technological modifications of PCF, so the goal of creating a simple and practical visible supercontinuum source with subnanosecond pulse durations still remains.

Finally, there are issues regarding characterization of photonic crystal fibers, namely phase refractive index of solid-core PCF mode (which is essentially an effective refractive index of the microstructured region) and group velocity dispersion measurement. Conventional optical fiber dispersion measurement techniques [60–72] are in many ways unsuitable or simply too complicated to apply in case of photonic crystal fibers. As for the measurement of phase refractive index of PCF mode, to the best of our knowledge, no experimental methods exist. The only experimental method, proposed to measure this parameter in conventional telecommunications optical fibers [73], is unsuitable for photonic crystal fibers. These parameters play a key role in supercontinuum generation so it is very important to have experimental techniques to estimate them reliably.

The introduced scientific problems lead to the following objective of this thesis.

Objective of the thesis

Development of novel methods of photonic crystal fiber dispersion characterization and investigation of supercontinuum generation in case of chirped femtosecond pump pulses or subnanosecond duration pump pulses.

Main tasks of the thesis

- Investigate the possibility to use interplay between nonlinear and dispersive effects during supercontinuum generation in photonic crystal fiber as means to quantitatively characterize group velocity dispersion of the photonic crystal fiber itself.

- Develop experimental method to measure phase refractive index of photonic crystal fiber fundamental mode.

- Investigate supercontinuum generation in highly nonlinear polarization-maintaining photonic crystal fiber with two zero group velocity dispersion wavelengths in case of chirped femtosecond pump pulses using cross-correlation frequency-resolved optical gating technique as one of the investigation methods.

- Investigate supercontinuum generation in highly nonlinear polarization-maintaining photonic crystal fiber with two zero group velocity dispersion wavelengths in case of subnanosecond pump pulses using streak camera as one of the investigation methods.

Statements to defend

1. By analyzing cross-correlation frequency-resolved optical gating trace of a femtosecond supercontinuum generated in a photonic crystal fiber it is possible to estimate group velocity dispersion of photonic crystal fiber. An essential requirement is that supercontinuum generation regime when practically all spectrum components are generated at the same time must be realized.

2. In case of polarization-maintaining photonic crystal fiber the demonstrated novel experimental GVD measurement method is also capable of distinguishing GVD of orthogonal polarization modes, allowing to calculate difference of their group refractive indices and identify effective limits of PCF birefringence.

3. Phase refractive index of photonic crystal fiber mode can be estimated by analyzing phase shift of interfering adjacent continuous wave

13

laser longitudinal modes corresponding to shift from constructive to destructive interference.

4. In case of femtosecond supercontinuum generation in highly non-linear polarization-maintaining photonic crystal fiber with two zero group velocity dispersion wavelengths orthogonal polarization modes produce slightly different supercontinua.

5. Chirping femtosecond pump pulses which central wavelength is in anomalous GVD region of PCF, affects initial soliton formation stage. Subsequently, soliton fission and dispersive wave generation processes are also influenced.

6. By performing subnanosecond supercontinuum spectrogram measurements with streak camera it is possible to directly distinguish part of supercontinuum radiation that leaks away from photonic crystal fiber fundamental mode.

Scientific novelty

- It was shown that supercontinuum generation in photonic crystal fiber under certain conditions can be used to quantitatively characterize group velocity dispersion of photonic crystal fiber itself. Spectral range of proposed GVD measurement technique is limited by spectral extent of cross-correlation frequency-resolved optical gating trace which in principle can cover the entire supercontinuum bandwidth.

- It was shown that it is possible to estimate photonic crystal fiber mode phase refractive index by analyzing phase shift of interfering adjacent continuous wave laser longitudinal modes at the same interference order corresponding to shift from constructive to destructive interference. When polarized light is used, the technique can distinguish phase refractive index for orthogonal polarization modes of polarization-maintaining photonic crystal fiber.

- It was demonstrated experimentally and with numerical simulations that during femtosecond supercontinuum generation in highly nonlinear polarization-maintaining photonic crystal fiber with two zero group velocity dispersion wavelengths distinct supercontinua corresponding to orthogonal polarization modes are formed.

- A comparative study of supercontinuum generation using chirped femtosecond pump pulses or bandwidth-limited pulses at the same peak power was performed experimentally using XFROG method and numerically with full-vector simulation model. It was shown that pump chirp has influence on supercontinuum formation.

- Supercontinuum radiation that leaks away from photonic crystal fiber fundamental mode was observed directly during subnanosecond supercontinuum spectrogram measurements with streak camera.

Practical value

- A new experimental method for quantitative estimation of photonic crystal fiber group velocity dispersion was demonstrated.

- The demonstrated experimental method for group velocity dispersion estimation is fast, requires only short piece of fiber and is specifically suitable for photonic crystal fibers. To the best of our knowledge, there are no other experimental methods that can measure GVD of orthogonal PCF polarization modes simultaneously.

- To the best of our knowledge, the first experimental method for measuring phase refractive index of photonic crystal fiber mode was demonstrated.

- Experimental and numerical investigation of supercontinuum generation in highly nonlinear polarization-maintaining photonic crystal fiber with two zero group velocity dispersion wavelengths was performed. Possible reasons why pump pulse chirp influences supercontinuum formation were discussed.

- Subnanosecond supercontinuum extension over the whole visible spectrum range and beyond was demonstrated using first or second harmonic pump of Q-switched Nd:YAG microlaser without any sophisticated technological modifications of the PCF or complicated experimental setups.

Approbation

Scientific papers directly related to this thesis in periodical journals with an impact factor which are included in the Web of Science database

[A1] J. Vengelis, V. Jarutis, V. Sirutkaitis, Visible supercontinuum generation in photonic crystal fiber using various harmonics of subnanosecond Q-switched laser, Opt. Eng. **55** (9), 096107–1–9 (2016).

[A2] J. Vengelis, V. Jarutis, V. Sirutkaitis, Estimation of photonic crystal fiber dispersion by means of supercontinuum generation, Opt. Lett. **42** (19), 1844 – 1847 (2017).

[A3] J. Vengelis, V. Jarutis, V. Sirutkaitis, Extension of supercontinuum spectrum, generated in polarization-maintaining photonic crystal fiber, using chirped femtosecond pulses, Opt. Eng. **57** (1), 016102–1–10 (2018).

[A4] J. Vengelis, V. Jarutis, V. Sirutkaitis, Measurement of the phase refractive index of a photonic crystal fiber mode, Opt. Lett. **43** (11), 2571 – 2574 (2018).

Conference proceedings

[AP1] J. Vengelis, V. Jarutis and V. Sirutkaitis, Supercontinuum generation in polarization maintaining photonic crystal fiber by using various harmonics of sub-nanosecond Q-switched laser, Proc. SPIE **9894**, 98941C–1–11 (2016).

[AP2] J. Vengelis, V. Jarutis and V. Sirutkaitis, Extension of supercontinuum spectrum, generated in photonic crystal fiber, by using chirped femtosecond pulses, Proc. SPIE **10380**, 1038016–1–10 (2017).

Scientific papers not related to this thesis in periodical journals with an impact factor which are included in the Web of Science database

[B1] K. Stankevičiūtė, I. Pipinytė, I. Stasevičius, J. Vengelis, G. Valiulis, R. Grigonis, M. Vengris, M. Bardauskas, L. Giniūnas, O. Balachninaitė, R. C. Eckardt, V. Sirutkaitis, Femtosecond optical parametric oscillators synchronously pumped by Yb:KGW oscillator, Lith. J. Phys. **53** (1), 41 − 56 (2013).

[B2] J. Vengelis, I. Stasevičius, K. Stankevičiūtė, V. Jarutis, R. Grigonis, M. Vengris, V. Sirutkaitis, Characteristics of optical parametric oscillators synchronously pumped by second harmonic of femtosecond Yb:KGW laser, Opt. Comm. **338**, 277 − 287 (2015).

[B3] J. Vengelis, A. Tumas, I. Pipinytė, M. Kuliešaitė, V. Tamulienė, V. Jarutis, R. Grigonis, V. Sirutkaitis, Characteristics of optical parametric oscillator synchronously pumped by Yb:KGW laser and based on periodically poled potassium titanyl phosphate crystal, Opt. Comm. **410**, 774 − 781 (2018).

Conference proceedings

[BP1] K. Stankevičiūtė, I. Pipinytė, J. Vengelis, A. Marcinkevičiūtė, R. Šuminas, R. Grigonis, R. C. Eckardt, V. Sirutkaitis, Optical parametric oscillators synchronously pumped by fundamental and second harmonic radiation of femtosecond Yb:KGW laser, Proc. SPIE **8845**, 884519–1–6 (2013).

[BP2] K. Stankevičiūtė, S. Melnikas, S. Kičas, L. Trišauskas, J. Vengelis, R. Grigonis, M. Vengris and V. Sirutkaitis, Synchronously pumped femtosecond optical oscillator with broadband chirped mirrors, Proc. SPIE **9503**, 950312–1–9 (2015).

Conference presentations directly related to this thesis, presented by Julius Vengelis

[C1] J. Vengelis, V. Jarutis and V. Sirutkaitis, Supercontinuum generation in photonic crystal fiber by using multi-wavelength picosecond pulses, Northern optics and photonics 2015, June 2 – 4, Lappeenranta, Finland 2015.

[C2] J. Vengelis, V. Jarutis and V. Sirutkaitis, Supercontinuum generation in polarization maintaining photonic crystal fiber by using various harmonics of subnanosecond Q-switched laser, SPIE Photonics Europe, April 4 – 7, Brussels, Belgium 2016.

[C3] J. Vengelis, V. Jarutis and V. Sirutkaitis, Extension of supercontinuum spectrum, generated in photonic crystal fiber, by using chirped femtosecond pulses, SPIE Optics + Photonics 2017, August 6 – 10, San Diego, California, United States of America 2017.

[C4] J. Vengelis, V. Jarutis, V. Sirutkaitis, Measurement photonic crystal fiber dispersion by means of supercontinuum generation, 42nd Lithuanian National Physics Conference, October 4 – 6, Vilnius, Lithuania 2017.

[C5] J. Vengelis, V. Jarutis, V. Sirutkaitis, Experimental measurement of phase refractive index of PCF mode and its dispersion, EPS-QEOD Europhoton 2018, September 2 – 7, Barcelona, Spain 2018.

Conference presentations directly related to this thesis, with Julius Vengelis as co-author

[C6] M. Kuliešaitė, J. Vengelis, Investigation of supercontinuum generation in photonic crystal fiber using chirped femtosecond pulses, Open Readings 2017, March 14 – 17, Vilnius, Lithuania 2017.

[C7] M. Kuliešaitė, J. Vengelis, V. Jarutis, Measurement of photonic crystal fiber dispersion by means of supercontinuum generation and cross-correlation frequency-resolved optical gating, Open Readings 2018, March 20 – 23, Vilnius, Lithuania 2018.

[C8] V. Jarutis, J. Vengelis, V. Sirutkaitis , M. Franckevičius and V. Gulbinas, Photonic crystal fiber characterization using streak camera, Northern optics and photonics 2018, September 12 – 14, Lund, Sweden 2018.

Other conference presentations

[D1] A. Marcinkevičiūtė, R. Šuminas, J. Vengelis, K. Stankevičiūtė, V. Sirutkaitis, Construction of a synchronously pumped femtosecond optical parametric oscillator, Open Readings 2013, March 21 – 23, Vilnius, Lithuania 2013.

[D2] K. Stankevičiūtė, I. Pipinytė, J. Vengelis, A. Marcinkevičiūtė, R. Šuminas, R. Grigonis, R.C. Eckardt, V. Sirutkaitis, Optical parametric oscillators synchronously pumped by fundamental and second harmonic radiation of femtosecond Yb:KGW Laser, XX-th Lithuania - Belarus Seminar Lasers and Optical Nonlinearity, November 21 – 22, Vilnius, Lithuania 2013.

[D3] J. Vengelis, K. Stankevičiūtė, R. Šuminas, A. Marcinkevičiūtė, Construction and investigation of synchronously pumped folded cavity femtosecond optical parametric oscillator, Open Readings 2014, March 19 – 21, Vilnius, Lithuania 2014.

[D4] K. Bagočius, M. Sirutavičius, S. Butkus, J. Vengelis, I. Pipinytė, V. Jarutis, V. Sirutkaitis, Changes of the nonlinear absorption in crystals under irradiation with trains of high repetition rate femtosecond pulses, SPIE Laser Damage 2018, September 23 – 26, Boulder, Colorado, United States of America 2018.

Contributions

All experimental and numerical simulation work, except for experiments with streak camera (see chapter 5), that enabled the writing of this thesis was carried out in Laser Research Center at Vilnius University during 2014 – 2018 under the supervision of assoc. prof. dr. Vygandas Jarutis. Experiments with streak camera were performed in Ultrafast Spectroscopy Laboratory at Center for Physical Sciences and Technology in 2017.

The contribution and responsibilities of the author of this thesis are: design and construction of all experimental setups, performance of all experiments, except for streak camera measurements, processing of experimental data and some part of numerical simulation data. However, the author is also very grateful for the significant contribution of:

- **Assoc. prof. dr. Vygandas Jarutis** supervised doctoral studies, helped to develop ideas, consulted on data interpretation, presentation and publication. He also created numerical simulation model, XFROG analysis program and performed numerical simulations.

- **Prof. habil. dr. Valdas Sirutkaitis** initiated the presented research and helped to create conditions for experimental work. He also consulted on experimental design details.

- **Prof. dr. Mikas Vengris** helped to automate experimental setup for cross-correlation frequency-resolved optical gating measurements and provided valuable remarks related to certain experiments.

- **Prof. habil. dr. Vidmantas Gulbinas** created conditions for experiments with streak camera and consulted on experiment design and implementation details.

- **Dr. Marius Franckevičius** performed (together with author of this thesis) measurements with streak camera, consulted on experiment design and implementation details.

Structure of the thesis

The doctoral dissertation is organized as follows:

- Chapter 1 is a literature overview of photonic crystal fibers, current optical fiber group delay dispersion measurement techniques, supercontinuum generation in photonic crystal fibers and frequency-resolved optical gating technique and its application to supercontinuum generation investigation. This chapter is not included in the summary of the doctoral dissertation.

- Chapter 2 describes novel experimental method for estimation of photonic crystal fiber dispersion by means of supercontinuum generation. Experiment results for two different photonic crystal fibers are presented and discussed.

- Chapter 3 describes group refractive index of photonic crystal fiber fundamental mode measurements and a new technique for measuring phase refractive index of photonic crystal fiber fundamental mode. Experimental data is combined with data from chapter 2 to estimate photonic crystal fiber mode phase refractive index dispersion. Experiment results for two different photonic crystal fibers are presented and discussed.

- Chapter 4 is devoted to investigation of femtosecond supercontinuum generation in photonic crystal fiber – a comparative study of supercontinuum generation using chirped femtosecond pump pulses and bandwidth-limited pulses at the same peak power is performed experimentally using cross-correlation frequency-resolved optical gating and numerically with full-vector simulation model.

- Chapter 5 is devoted to investigation of supercontinuum generation in photonic crystal fiber using subnanosecond pump pulses from a Q-switched Nd:YAG microlaser: experimental data acquired from spectrum measurements and spectrograms from streak camera are analyzed together with numerical simulation data.

Chapter 1
Literature overview

1.1 Photonic crystal fibers

1.1.1 Towards photonic crystal fiber – a brief historical note

As most of us know, conventional optical fibers are made of higher refractive index core and lower refractive index cladding. Light in such fibers propagates due to total internal reflection – a phenomenon which use for light trapping was demonstrated already in the 19th century [1, 2]. Such conventional optical fibers have strict design limitations: limited choice of materials for fabrication (thermal properties of cladding and core glass have to be the same), strict modal cut-off wavelength, limited core diameter of fiber in order to achieve single-mode operation (which is necessary for telecommunication applications) and very narrow fiber dispersion variation limits [16].These limitations encouraged researchers to look for alternative light guiding methods in optical fibers.

The introduction of multidimensional (2D and 3D) photonic crystals in the 1980s [6, 7] gave birth to a new idea of light guiding in optical fibers. A photonic crystal can be defined as a structure patterned with a periodicity of dielectric constant which makes light behave in a similar way to electrons in crystal lattices [8]. A particularly important feature that attracted attention of researchers is that during electron and crystal lattice interaction under certain conditions the periodic potential created by the crystal lattice may create a frequency band in which electron propagation with energies falling in this frequency band is prohibited [9]. This was also predicted to be possible for photonic crystal and light interaction for which this frequency band was called photonic bandgap (PBG)[10]. The idea behind the photonic crystal fiber, proposed by Philip Russell in 1992 [13], was to employ the PBG effect to confine light inside the fiber by making a 2D photonic crystal (in the form of microscopic capillaries embedded in the fiber material) stretching along the optical fiber. From this idea the definition of photonic crystal fiber (also called microstruc-

tured fiber) followed – it is a special optical fiber with a built-in periodic microstructure region along the fiber.

Interestingly, the first PCF, reported by P. Russell and colleagues [14, 15], employed a different principle of light guiding based on modified total internal reflection phenomenon and had a solid core surrounded by microstructured region of air holes (Fig.1.1 b). It appeared that the air holes in the PCF that P. Russell's group was able to fabricate at that time were too small and the air-filling factor was not high enough to achieve photonic bandgap guidance [20]. The fabrication of originally proposed photonic crystal fiber with PBG mechanism for confining light was reported a few years later [17, 74]. This fiber had a hollow core surrounded by the microstructured region of air holes (Fig.1.1 d).
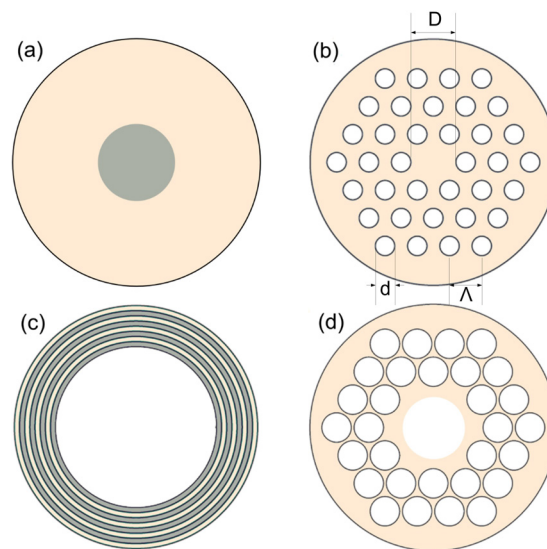
Figure 1.1: Cross-section examples of different types of optical fibers: (a) – conventional optical fiber; (b) – solid-core PCF; (c) – Bragg fiber; (d) – hollow-core PCF. Notation: Λ – pitch; d – diameter of microstructure; D – diameter of core.

Although rarely mentioned in literature, it is worth to note that the first proposal of a novel optical fiber employing 1D photonic crystal for light guiding was made by P. Yeh and colleagues in their papers in 1976 and 1978 – before the introduction of photonic crystals [11, 12]. The authors proposed and analysed the possibility of creating optical fibers with cladding made of rings with periodically alternating refractive index

between neighbouring rings (which was called Bragg grating) and core which would have lower refractive index than the cladding (Fig.1.1 c). Such structure is very similar to a 1D photonic crystal. It was named Bragg fiber. Although proposed much earlier, the first successful fabrication of Bragg fibers was reported only in 1999 by Y. Fink, etc. and in 2000 by F. Brechet and colleagues [18, 19]. The reason for Bragg fibers often being excluded as a separate type of fiber is that some researchers in the field claim that such fibers do not strictly support photonic bandgaps [75, 76].

1.1.2 Principles of light guiding in different types of photonic crystal fibers

Photonic crystal fibers are classified into two main types based on light guiding mechanism inside the fiber: **solid-core** (also called solid-core guiding) and **hollow-core** (also called photonic bandgap guiding) photonic crystal fibers. We will now discuss principles of light guiding and main properties of these PCFs in more detail.

Solid-core photonic crystal fibers, similarly to conventional optical fibers, employ modified total internal reflection to guide light. They have a solid core surrounded by a region of periodic microstructures, usually made of air capillaries (Fig.1.1 b) with the size scale of the order of micrometers. Light guiding in such PCFs is explained using effective refractive index model proposed in papers by J. Knight, N. Mortensen, K. Koshiba and their colleagues [77–79]. According to this model the refractive index of the core is greater than the effective refractive index of the cladding, therefore light is confined in the core because of modified total internal reflection. The term "modified" comes from the fact that cladding (which is defined as the area surrounding the solid core) refractive index is modified by the periodic microstructure system and strongly depends on the geometric parameters of microstructures and wavelength of light, whereas in conventional optical fibers the cladding refractive index is almost independent of wavelength [16]. The periodicity of microstructures in such PCFs is of paramount importance because it

ensures that only one waveguide is formed and allows to use the effective refractive index model to explain light guiding [77]. Using the effective refractive index model, solid-core PCF can be well parametrized using an effective V parameter:

$$V = \frac{2\pi}{\lambda} a_{\text{eff}} \sqrt{n_{\text{co}}^2 - n_{\text{fsm}}^2} = \sqrt{U^2 + W^2}, \tag{1.1}$$

where a_{eff} is effective mode diameter in the PCF, n_{co} – core refractive index, n_{fsm} – effective refractive index of the fundamental mode, U and W are called longitudal and transversal attenuation parameters respectively which are defined as:

$$U = \frac{2\pi}{\lambda} a_{\text{eff}} \sqrt{n_{\text{co}}^2 - n_{\text{eff}}^2}, \tag{1.2}$$

$$W = \frac{2\pi}{\lambda} a_{\text{eff}} \sqrt{n_{\text{eff}}^2 - n_{\text{fsm}}^2}. \tag{1.3}$$

Here n_{eff} is the effective refractive index of photonic crystal fiber. As we see, the notation is very similar to the V parameter definition used in conventional optical fiber analysis.

Hollow-core photonic crystal fibers, as the name suggests, have a hole in the core, which is larger than typical microstructure diameter in that PCF, surrounded by periodic microstructure region. The hole is usually an air capillary so it has lower refractive index than the microstructured region around it. Light confining mechanism in these PCFs is based on a different principle – photonic bandgap effect. It can be briefly explained in the following way. The periodic array of microstructures along the PCF forms a 2D bandgap which prevents light of certain frequencies (which depend on the geometrical parameter of microstructures) propagating through it. The introduction of larger hole in the center can be interpreted as a defect in the 2D photonic crystal which leads to light localizing at the defect zone (core) – a sort of waveguide forms inside the bandgap. When light is coupled in such PCF, it cannot propagate in the cladding zone due to photonic bandgap, so it is trapped in the core even though it has lower refractive index than the surrounding clad-

ding [17, 74, 80]. PBG mechanism for a certain light frequency works if the cladding has at least one bandgap for that frequency [81]. This is usually achieved when the central hole is larger than the surrounding microstructures.

Apart from solid-core and hollow-core PCFs, there are also **specific types of optical waveguides** which have hollow cores and some of them have microstructured regions around the core but light guiding is based on different physical mechanisms, therefore they cannot be called bandgap guiding photonic crystal fibers [82]. Several examples of various hollow-core waveguides are shown in Fig.1.2 and Fig.1.3. The first image in Fig.1.2 depicts a classical bandgap guiding hollow-core PCF, whereas photonic crystal fiber in Fig.1.2 (b) is called Kagome fiber. This PCF, first reported in 2002 [83], is characterized by a specific star-of-David pattern of glass webs in the cladding. Light in it is not confined by PBG effect but by Von Neuman-Vigner quasi-bound states in continuum of scattering lattice states [84]: the modes guided in such fiber exist without any significant interaction as it is mitigated by due to high degree of transverse-filed mismatch between the cladding and core modes[85]. Such PCFs are used for supercontinuum generation in gas-filled hollow-core PCFs [86–90] and guiding ultrabroadband radiation, as they have more than 20 times larger bandwidths compared to classical hollow-core PCFs (1000 Tz and more [85]). Another specific type of PCF is a nanoscale hollow-core PCF (Fig.1.2c) – the core can have less than 200 nm diameter. Light in such photonic crystal fiber is trapped due to discontinuity of the electromagnetic radiation field at the interface between the central hole and surrounding glass [92]. Fig.1.2(d) depicts Bragg fiber. As already mentioned, it consists of a 1D photonic structure (periodic concentric rings around the lower refractive index air hole in the core). With a correct selection of concentric ring material refractive index and their spacing this fiber possesses the ability of omniguidance – 1D photonic crystal can reflect light from all angles and of various polarizations [93–95]. It is important to remind that some researchers claim that Bragg fibers do not strictly employ PBG for light guiding [75, 76] so the question whether
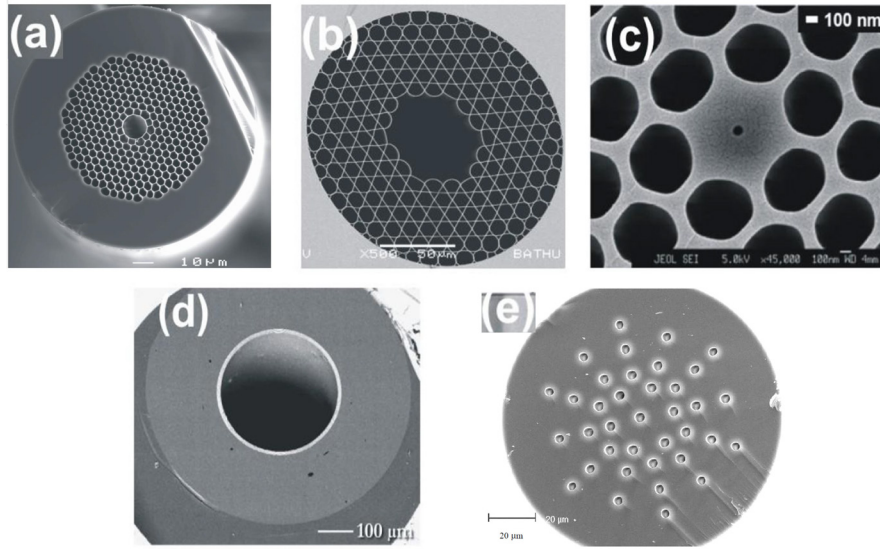
Figure 1.2: Examples of SEM pictures of hollow-core photonic crystal fibers: (a) – classical bandgap guiding hollow-core PCF (b) – Kagome PCF; (c) – nanoscale hollow-core PCF; (d) – Bragg fiber; (e) – Fresnel fiber. Images (a)-(d) are adapted from [82], (e) – from [91].

they can be accredited to hollow-core bandgap guiding PCFs is disputable. Another unique photonic crystal fiber (seen in Fig.1.2e), proposed by J. Canning, is the Fresnel fiber [96]. Light in such fiber can propagate because it scatters on surfaces of microholes and consequently interferes constructively. Therefore, a peak light intensity forms in the center of the Fresnel fiber [16, 96–98]. The name "Fresnel fiber" comes from the fact that concentric rings of microstructures form Fresnel zones which have various effective refractive indices. The concentric ring diameter is determined by the requirement to have a π or 2π phase change at each ring. Fresnel fibers have a unique ability to focus light at the far field without the need of any focusing optics at the end of fiber. The final and the latest PCF is the twisted coreless PCF (Fig.1.3). It was first reported in 2016 by G. Wong, R. Beravat, X. Xi, M. Frosz and P. Russell [100]. Since such PCF does not have any defect in the microstructured region, light is confined by a different and very complicated mechanism. In short this can be described the following way. Twisting PCF microstructures increases effective axial refractive index (which is proportional to the square of the
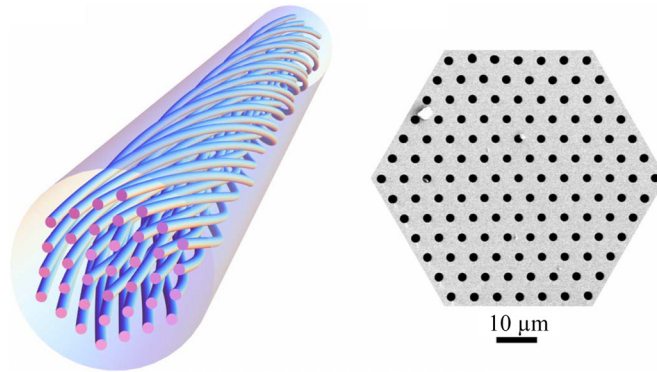
Figure 1.3: Principal view of twisted coreless PCF (left) and SEM image of its cross-section (right) by Beravat, etc. [99].

twisting radius and the twist rate) of coupled electric field lobes which are situated in the hollow microstructures forcing them to create a helical paths around the PCF axis. This in turn creates guiding conditions for light in such PCF [99–101].

1.1.3 Main properties and applications of photonic crystal fibers

The inherent ability to engineer structural parameters of microstructured region of photonic crystal fibers, such as diameter of microstructures (d), distance between them, called pitch, (Λ), size of core (D) and the whole microstructured region (Fig.1.1 b) has enabled realization of numerous unique features which have been inaccessible for conventional optical fibers. As already obvious from the previous subsection, different PCF microstructure geometries can determine different waveguiding properties and physics of light confinement. In this subsection other prominent properties of photonic crystal fibers and their applications will be discussed.

Ability to engineer PCF with unconventional group velocity dispersion. Group velocity dispersion (GVD) is the dependence of group velocity of light traveling in transparent medium from the wavelength

(frequency). It can be defined as:

$$GVD = \frac{\partial}{\partial \omega} \frac{1}{v_\mathrm{g}} = \frac{\partial^2 \beta}{\partial \omega^2},$$ (1.4)

where ω is frequency of light and β is the propagation constant :

$$\beta = k n_\mathrm{eff},$$ (1.5)

which is a product of PCF effective refractive index (n_eff) and wavenumber (k) in vacuum. Due to practical reasons, in fiber optics GVD is usually defined as a derivative with respect to wavelength and a parameter, called dispersion parameter (D), is used instead of GVD:

$$D = -\frac{2\pi c}{\lambda^2} \cdot GVD.$$ (1.6)

This expression takes into account both waveguide and material dispersion of PCF. D can in some cases approximately be defined as [102]:

$$D = D_\mathrm{w} + D_\mathrm{m} = -\frac{\lambda}{c} \frac{d^2 n_\mathrm{geom}}{d\lambda^2} + D_\mathrm{m},$$ (1.7)

where n_geom is refractive index component induced due to PCF geometry, D_w and D_m are respectively waveguide and material dispersion components of the PCF. In general, waveguide and material dispersion components cannot be separately estimated – only the overall D value is measured or simulated. It is important to note that in scientific literature about optical fibers D is simply called dispersion, but is should not be confused with material dispersion which is the dependence of refractive index from wavelength (frequency).

Variation of photonic crystal fiber's microstructure region geometric parameters offers high control of waveguide dispersion component. This can be shown analyzing PCF with various numerical approaches such as plane wave expansion method [103], multipole method [104] and the finite element method [105]. However, they involve rather time-consuming

computations. Alternatively, using the aforementioned effective refractive index model, K. Saitoh with colleagues have defined numerically based simple empirical relations between the effective V parameter (Eq.1.1) and PCF structural parameters [102] (Fig.1.4).
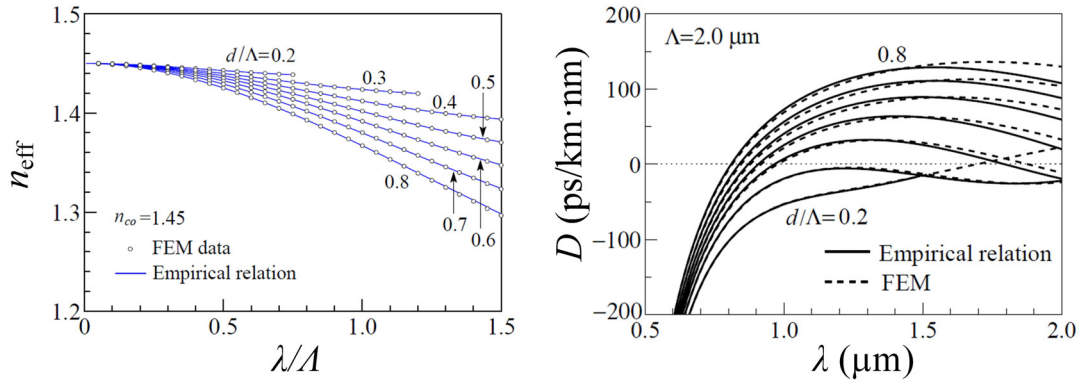

Figure 1.4: Examples of effective refractive index and dispersion dependence on geometrical parameters of PCF and wavelength of light by Saitoh, etc. [102].

In conventional single mode optical fibers the wavelength of zero group velocity dispersion (ZDW) is around 1.3 µm and can be shifted very little usually to longer wavelengths [106]. For PCFs the ZDW can be shifted far more radically. In case of solid-core PCFs, if the whole microstructure area is made very small, it is possible to shift ZDW of the fundamental guided mode to visible range of spectrum [107–110]. More than that, it is possible to flatten the dispersion profile [111–113]. Photonic crystal fibers with shifted ZDW are particularly useful for supercontinuum generation in the visible range [21], PCFs with ZDW in the visible range can also be used for dispersion compensation in telecommunication applications [16], whereas dispersion flattening opens new applications of PCFs for optical parametric amplification [114], generation of supercontinuum in the infrared (IR) [115], etc.

Another degree of freedom to tune dispersion in case of hollow-core PCFs comes from the idea that we can fill the hollow core of such PCFs with gas (usually inertial gas, like helium, argon or xenon) and by adjusting pressure of the gas change dispersion and nonlinearity of the PCF [86–90].

Endlessly single mode propagation. Another distinctive property specific to solid-core photonic crystal fibers is the opportunity to design PCF that can maintain single mode regime in an extremely large range of wavelengths as first reported by T. Birks and colleagues [116]. Such PCFs are called endlessly single mode. A simple explanation of this PCF feature is that by varying the fill factor (which is the ratio of the microhole diameter d and the pitch Λ) we can trap only the fundamental mode inside the PCF's core, whilst higher order modes can still leak away [117]. In more mathematical terms this means that the effective V number of the PCF can be kept below the single mode cut-off frequency, which for PCFs has been estimated to be V=2.5 and the respective filling factor is $d/\Lambda \approx <0.4$ [117]. Endlessly single mode PCFs with shifted dispersion can be used in various telecommunication-related applications.

Large mode area photonic crystal fibers. Endlessly single mode property can be used to design PCF with large mode areas and endlessly single mode behaviour [118]. Conventional optical fibers have a strict limit on the core size and the numerical aperture (NA), so in order to manufacture large mode area step index fiber, one needs control the difference between core and cladding refractive indices which is the limit for the mode field diameter in conventional fibers. Large mode area photonic crystal fibers can be fabricated by decreasing microstructure diameter, increasing pitch between the microstructures or, in case of hollow-core PCFs, increasing diameter of central hole. The size is practically limited by bending losses. In paper by Baggett and colleagues [119] it has been shown that although conventional fibers can have similar mode field diameter as hollow-core PCFs for a certain wavelength, hollow-core PCFs remain single mode for a large range of wavelengths which cannot be achieved in step index fibers. Typically, mode field diameter of large mode area PCFs can be several time greater than the corresponding conventional fiber mode field area. Large mode area PCFs can be used for high power beam guiding [120], fiber amplifiers and lasers [121].

High/low nonlinearity PCF. Another distinctive feature of photonic crystal fibers is the ability to engineer them with high or very low nonlin-

ear response. The nonlinearity coefficient for optical fibers is defined as
[122]:

$$\gamma = \frac{2\pi n_2}{\lambda a_{\text{eff}}}, \tag{1.8}$$

where n_2 is nonlinear refractive index. According to Eq.1.8, low nonlinearity can be achieved by increasing the effective mode diameter (a_{eff}) and decreasing nonlinear refractive index of the optical fiber material. The former is applied in low nonlinearity solid-core PCFs where larger diameter means lesser intensity of propagating light which leads to lesser PCF nonlinearity. However, hollow-core PCFs offer much smaller nonlinearity: it comes due to the fact that, as discussed before, light propagates in the central air hole and weakly overlaps with cladding glass. Very low nonlinear refractive index of air (smaller by roughly three orders of magnitude compared to silica) and the possibility to fabricate large mode areas yields ultralow PCF nonlinearities. For standard step index fiber the nonlinearity coefficient value is of the order of 2 $W^{-1}km^{-1}$, whereas ultralow nonlinearity hollow-core PCFs can have nonlinearity as low as 0.023 $W^{-1}km^{-1}$ [13]. This PCF feature is particularly useful for high peak power ultrashort pulse delivery over relatively long distances as with low nonlinearity PCFs nonlinear optical effects which would otherwise distort the pulses are avoided [123, 124].

Highly nonlinear PCFs are engineered the opposite way – by confining light in a very small diameter core (which can be of the order of 1 μm) in a solid-core photonic crystal fiber. Forcing light to propagate in such small effective area yields very high intensities which results in very high nonlinearity of the PCF. For example, highest reported nonlinearity of conventional fiber, fabricated by adding extra impurities to enhance γ, is around 20.4 $W^{-1}km^{-1}$ at 1550 nm[125], whereas solid-core highly nonlinear PCFs have nonlinearities exceeding 240 $W^{-1}km^{-1}$ at 850 nm [13]. This means that supercontinuum generation threshold using highly nonlinear PCF can be more than 2 orders of magnitude smaller compared to conventional optical fibers at the same experimental conditions [126]. In case of multicomponent core glass, nonlinearities can be much higher

[127, 128] with highest reported value exceeding 46000 $W^{-1}km^{-1}$ for chalcogenide glass solid-core PCF at 1.55 μm [129]. As already mentioned, combined with broad dispersion engineering limits, this is the key reason of wide application of PCFs for supercontinuum generation.

For hollow-core PCFs nonlinearity can be increased by filling the core with gas. This idea gave a huge impulse to research leading to vacuum-ultraviolet supercontinuum generation in such photonic crystal fibers as reported in several papers [86–89].

Birefringent photonic crystal fibers. Birefringence is a property of optically transparent non-isotropic medium when the refractive index of the medium depends on the polarization direction of light propagating through it. In fiber optics fibers with built-in strong birefringence are called polarization-maintaining (PM) fibers. If the polarization of light launched into the fiber is aligned with one of the principal polarization axes, this polarization state will be preserved even if the fiber is bent. In conventional PANDA (Fig.1.5 a) and Bow Tie (Fig.1.5 b) fibers high birefringence is induced by mechanical stress due to additional element in the fiber [130], whereas for conventional fibers with elliptical core (Fig.1.5 c) birefringence comes from the broken axial symmetry of the fiber structure [130, 131].

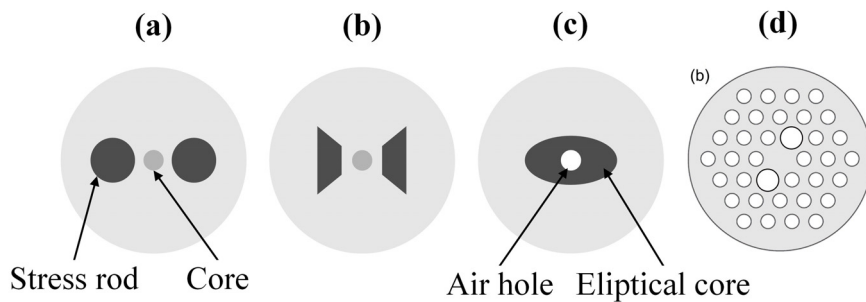**Figure 1.5:** Examples of cross-section of different types of birefringent fibers: (a) – PANDA fiber; (b) – Bow Tie fiber; (c) – elliptical core fiber; (d) – solid-core birefringent PCF.

Birefringence in both solid-core and hollow-core photonic crystal fibers can be obtained by engineering asymmetrical central defect or, in solid-core PCF, by adjusting size and shape of microstructures surrounding

silica core (such as in Fig.1.5 d). This causes non-axisymmetric distribution of effective refractive index [132–135]. Compared to conventional birefringent fibers, PCF birefringence can be one order of magnitude larger (of the order of 10^{-3}) [134]. Birefringence of PCF is defined as [16]:

$$B = \frac{\lambda(\beta_{\mathrm{x}} - \beta_{\mathrm{y}})}{2\pi} = \left| n_{\mathrm{effx}} - n_{\mathrm{effy}} \right|, \tag{1.9}$$

where β_{x}, β_{y} and n_{effx}, n_{effy} are propagation constants and effective refractive indices for orthogonal polarization modes respectively. An important feature coming from non-axisymmetric distribution of effective refractive index is insensitivity to temperature in a very broad range of temperatures [136]. This makes them very useful for sensing [137] and telecommunication applications (as polarization mode compensator [16]).

In conclusion to this section, we see that diversity of possible PCF microstructure configurations together with listed characteristic photonic crystal fiber features, which can be combined together in various ways, has great potential for many applications. The use of PCFs for supercontinuum generation is the most notable of them as it allows to use such fiber-based supercontinuum sources in many other areas: in wavelength-division multiplexed (WDM) light wave systems [138], optical coherence tomography (OCT) systems [23, 139], frequency metrology [22, 140], as wideband probe in femtosecond spectroscopy [141], etc.

1.2 Optical fiber group delay dispersion measurement techniques

1.2.1 Optical fiber dispersion

When light travels through transparent dielectric medium it experiences a certain group delay of the medium which comes from the fact that temporal response of the medium has finite duration [142]. Group delay

is a wavelength (frequency) dependent quantity which can be defined as:

$$T_\text{g} = \frac{\partial \varphi}{\partial \omega}, \tag{1.10}$$

where φ is spectral phase of the pulse. In fact, wavelength (frequency) dependence of group delay is called group delay dispersion (GDD):

$$GDD = \frac{\partial T_\text{g}}{\partial \omega} = \frac{\partial^2 \varphi}{\partial \omega^2}. \tag{1.11}$$

The GDD per unit length is the aforementioned group velocity dispersion (Eq.1.4) which for optical fibers is defined as specified in Eq.1.6. It is again important to note that in scientific literature about optical fibers D is often called dispersion parameter or simply dispersion, but it should not be confused with material dispersion which in the dependence on refractive index from wavelength (frequency).

In case of optical fibers, apart from material dispersion, there are also several other types of dispersion [66]. These are: waveguide dispersion (arising from wavelength-dependent waveguiding effects) and intermodal dispersion (arising in multimode fibers when propagation velocity of pulse is not the same for different modes due to optical path difference). As mentioned in the previous section, photonic crystal fibers can be engineered to have unique dispersive properties since changing geometrical parameters of microstructured region yields different waveguide dispersion. Unlike in conventional optical fibers, waveguide dispersion can be much greater than material dispersion.

Optical fiber dispersion has critical effect on light pulses traveling through the fiber. For example, transform limited pulses (they have the lowest possible pulse duration for a given spectrum bandwidth) will broaden in time when traveling through dispersive medium, while chirped pulses can be compressed or broadened in time depending on the sign of the chirp and sign of fiber dispersion. Dispersion of a PCF plays a central role in determining pulse propagation dynamics and supercontinuum spectrum formation [21, 36]. For these reasons it is of paramount

importance to be able to estimate dispersion accurately and reliably.

In the two following subsections numerical and mostly used experimental optical fiber and PCF dispersion measurement techniques are briefly reviewed and their feasibility for PCF dispersion measurement is discussed.

1.2.2 Numerical method for photonic crystal fiber dispersion estimation

The most popular photonic crystal fiber dispersion estimation method is numerical analysis of light propagation in the investigated PCF. A cross-section image, which is usually taken using scanning electron microscope (SEM), is analyzed to determine the structural parameters of microstructured region: diameter of microstructures (d), pitch (Λ), size of core (D) and the whole microstructured region. This is used to simulate a mesh of microstructures in the medium. Furthermore, a boundary condition that mode electric field on the boundary (the outermost microstructure) is zero is used for further simulations. Example of such analysis is shown in Fig.1.6.
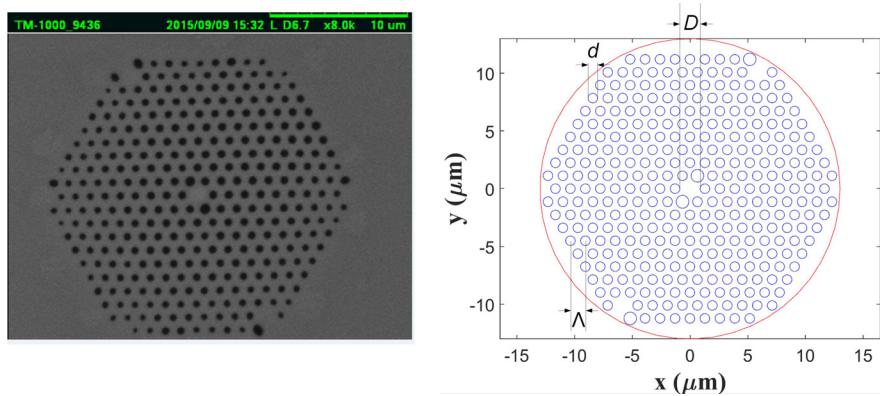

Figure 1.6: SEM image of cross-section of PM PCF used in our experiments (left) and numerically simulated mesh of the microstructured region (right).

The refractive index of PCF medium is calculated using Sellmeier equation:

$$n^2(\lambda) = 1 + \sum_{j=1}^{3} \frac{a_j}{1 - (b_j/\lambda)^2}, \qquad (1.12)$$

with coefficients for fused silica (the most popular PCF material) being $a_1 = 0.6961663$, $a_2 = 0.4079426$, $a_3 = 0.8974794$, $b_1 = 0.0684043$ μm, $b_2 = 0.1162414$ μm, $b_3 = 9.896161$ μm [143]. Then the modal refractive index is computed for each wavelength. Various numerical approaches have been used for dispersion profile calculation such as scalar method [109], semi-vectorial finite element difference method [144, 145] and fully-vectorial models [146–152]. Full-vectorial approach is more accurate for PCFs with large air filling factor (d/Λ>0.35) and it accounts for birefringence in case of PM PCF. Once the modal refractive index for various wavelengths is calculated, other parameters such as group velocity dispersion can be calculated as well and then used to simulate light propagation in PCF.

Numerical simulation seems to be a straightforward and relatively simple method for estimation of PCF dispersion. However, it has some problems which are associated with PCF cross-section analysis. First problem is that in reality sizes of PCF microstructures can vary. This might be due to several reasons such as deformation because of induced mechanical stresses when cleaving the fiber ends or during preparation for SEM measurement or actual slight microstructure size variations along the PCF. Example of microstructure size variation is shown in Fig.1.7 where microstructure diameters of SEM image of our PM PCF cross-section, depicted in Fig.1.6, have been analyzed. Apart from four largest
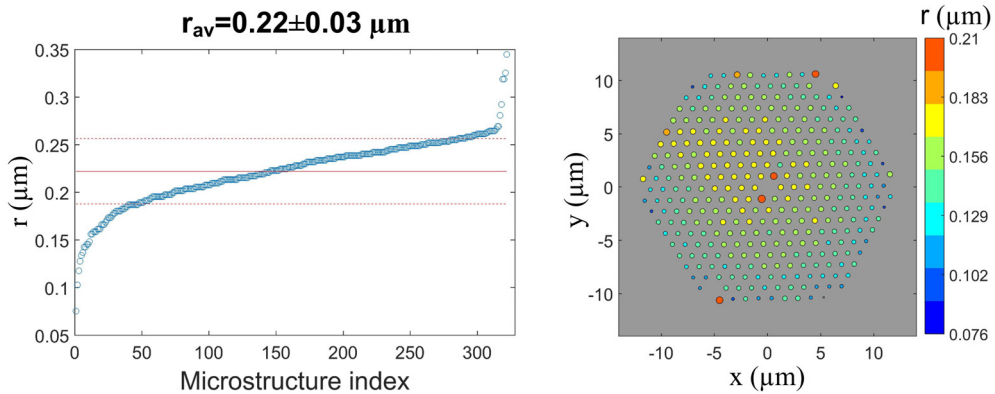

Figure 1.7: Radii of PCF microstructures (left) and spatial distribution of microstructures with different radii (right). Microstructure indexing is according to their size.

air holes (marked as red dots in Fig1.7) which have been fabricated on

purpose to induce PCF birefringence, other microstructures also vary in size. The variations do not have any pattern of distribution (except for the four largest holes placed specific locations) and it is also notable that even the four largest air holes vary in size (0.319 μm, 0.319 μm, 0.325 μm, 0,344 μm). As was stated in earlier section, PCF dispersion is very sensitive to geometrical parameters of microstructured region which includes size of microstructures. The problem is solved assuming that using average microstructure diameter value for the simulated mesh (Fig.1.6) should produce correct results. Despite this, the question of accuracy still remains.

Another problem is that during numerical simulations one can only use standard refractive index value of fused silica for PCF core material calculated from corresponding Sellmeier equation. In reality, it is not possible to know the actual value of refractive index of the PCF core material due to subtleties of PCF manufacturing (for example, the exact concentration of impurities are not known, also, slight changes of PCF core material optical properties might occur during PCF drawing process). As a result, the actual dispersion of the PCF fundamental mode may differ from the calculated.

1.2.3 Experimental methods for photonic crystal fiber group delay dispersion estimation

Pulse delay. In pulse delay (otherwise called time-of-flight) method difference in transit times of pulses generated by tunable wavelength laser source and propagating through a certain length optical fiber are measured using a photodiode. Thus, group delay of the fiber with respect to a reference wavelength pulse can be plotted and subsequently fitted with a certain order polynomial. From Eqs.1.10 and 1.11 it follows that the derivative of this polynomial curve (group delay) is group delay dispersion of the fiber [60–62, 66]. As mentioned before, GDD measured per unit length of fiber under test is called group velocity dispersion. Example of experimental setup for this measurement is depicted in Fig.1.8.
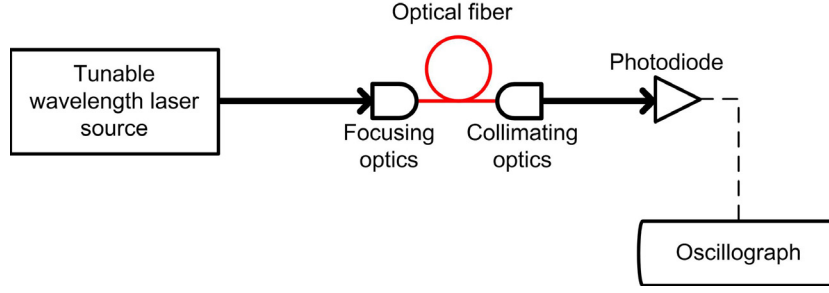
Figure 1.8: Example of experimental setup for GDD measurement setup using pulse delay technique.

Pulse delay method is advantageous for being straightforward and simple, but is limited to temporal resolution of photodiode which considering ultrafast photodiodes usually does not exceed several tens of picoseconds. Consequently, very long fiber lengths (hundreds of meters and more) are required to achieve a detectable difference in transit time. In case of photonic crystal fibers this is a significant problem due to relatively high cost and much greater optical losses in PCFs compared to conventional optical fibers.

Phase shift technique. In phase shift method light from a CW tunable laser or similar source is sinusoidally modulated. The modulation frequency (f), usually chosen as high as possible to achieve best temporal resolution, produces sidebands around the carrier frequency of the optical signal. When part of the signal travels through the optical fiber under test, it experiences a phase shift due to group delay of the fiber [64]:

$$\varphi(\lambda) = 2\pi f T_{\mathrm{g}}(\lambda) = 2\pi f \frac{L}{v_{\mathrm{g}}(\lambda)}, \tag{1.13}$$

where f is the modulation frequency, L is the fiber length and $T_{\mathrm{g}}(\lambda)$ is the wavelength-dependent group delay. The measured phase shifts with respect to the reference same wavelength signal are used to calculate group delay of the fiber and subsequently group delay dispersion:

$$GDD = \frac{\partial T_{\mathrm{g}}(\lambda)}{\partial \lambda} = \frac{1}{2\pi f} \frac{\partial \varphi(\lambda)}{\partial \lambda}. \tag{1.14}$$

Example of experimental setup of phase shift technique is shown in Fig.1.9.
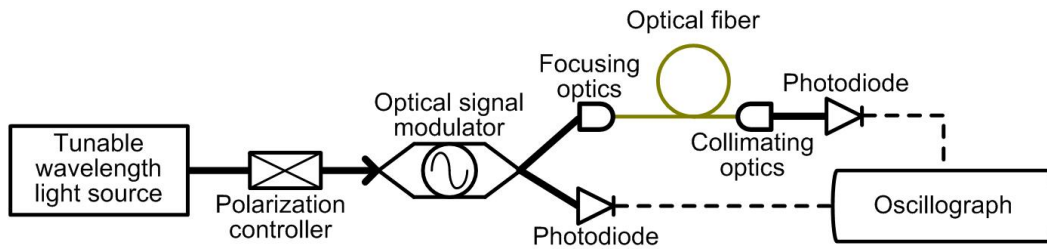

Figure 1.9: Example of experimental setup for GDD measurement using phase shift technique.

The accuracy of this method depends on how precisely one can measure phase shift and on sinusoidal modulation frequency [64, 66]. This method requires shorter fiber lengths (typical length is ten meters) compared to classical time delay method and has greater resolution (of the order of 1 ps) [64], but these parameters are still not good enough for photonic crystal fiber dispersion measurement and are limited to light source tunability capabilities.

A similar method reported by Christensen and colleagues [65] relies on measuring the **amplitude modulation** of the signal which depends on the square of the modulation frequency (f).

White-light interferometric techniques. Interferometric methods use interference of reference and the investigated beam (which has passed the optical fiber under test) coming from the same light source to estimate group delay dispersion [66–70]. Partially coherent sources such as halogen lamps or superluminescent diodes are used since short coherence time is enough to make precise measurements. Therefore, this is called white-light interferometry. In a typical white-light interferometry setup (Fig.1.10) light from broadband source is divided into two parts one for each arm of the interferometer (usually Mach-Zehnder or Michelson interferometer). One beam is directed to the optical fiber under test, while the other beam acts as a reference. A compensating plate is placed in the interferometer with the reflected beam which is used to match the dispersion that the other beam, transmitted through the beamsplitter, experiences. The output from both interferometer arms is recombined and interference fringes
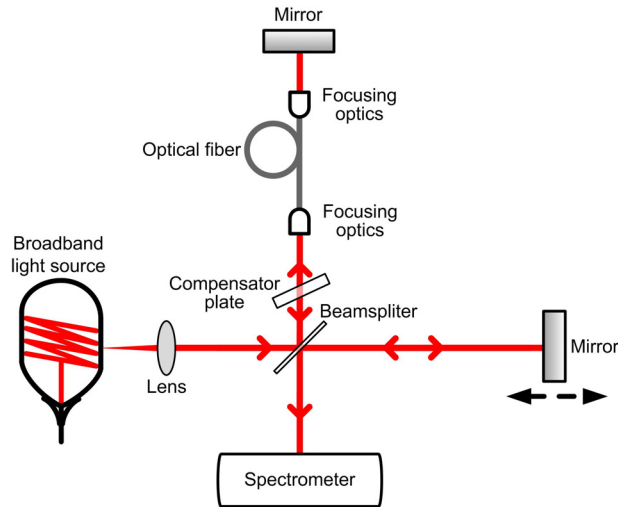
Figure 1.10: Example of experimental setup for GDD measurement using spectral interferometry.

form.

In temporal interferometry fringes for a certain wavelength are detected using a photodiode as the reference arm length is changed – signal is recorded in the time domain. Analysis of the interferogram allows to evaluate peak of the interferogram and, as different wavelength of the broadband light source is selected, the relative group delay of different wavelength components can be estimated directly [67]. Consequently group delay dispersion is a derivative of group delay.

In spectral interferometry fringes are recorded using spectrometer and spectral distribution of phase delay over the whole bandwidth of light spectrum is usually evaluated via Fourier transformation of the interferogram and curve fitting [71]. Group delay dispersion is estimated by differentiating the evaluated phase delay. Alternatively one can perform analysis of the stationary phase point (equalization wavelength) position dependence on the path length difference of interferometer arms [153].

Interferometric techniques have been widely applied to measure both solid-core and hollow-core photonic crystal fiber group delay dispersion [154–160]. White-light interferometric techniques have several advantages: ability to measure GDD of short PCF samples, relatively high group delay resolution (of the order of 100 fs [66]) compared to the

aforementioned measurement methods and wide spectral measurement range. However, there are also considerable flaws. Firstly, free-space interferometers are very sensitive to environmental changes such as variations of ambient temperature, mechanical vibrations, etc. which may affect measurement results. Secondly, accuracy of spectral interferometric measurements depends on wavelength resolution of the spectrometer so high resolution spectrometers are required. Finally, efficient coupling of low-coherence white light (such as a halogen lamp light) into the PCF core is much more difficult than coupling laser radiation especially when the radius of PCF core is very small (as is the case for highly nonlinear PCFs).

Spectral modulation technique. The three already discussed experimental GDD measurement techniques have been used for a long time and are viewed as standard when it comes to conventional optical fiber dispersion measurement. Spectral modulation technique proposed by G. Genty and colleagues in 2004 was developed specifically for photonic crystal fibers and uses the interplay between nonlinear and dispersive effects in the PCF to estimate its dispersion [72]. The principle is as follows. When an ultrashort laser pulse with sufficient energy and wavelength in the anomalous GVD range of the PCF enters the fiber, soliton formation occurs. The parameter describing formation process is called the soliton number (N):

$$N^2 = \frac{L_{\mathrm{D}}}{L_{\mathrm{NL}}} = \frac{\gamma P_{\mathrm{p}} \tau_0^2}{|GVD|}, \tag{1.15}$$

where $L_{\mathrm{D}} = \frac{\tau_0^2}{|GVD|}$ is dispersive length of the PCF, $L_{\mathrm{NL}} = \frac{1}{\gamma P_{\mathrm{p}}}$ is nonlinear length of the PCF, γ is the aforementioned optical fiber nonlinearity coefficient (Eq.1.8), P_{p} – peak power of the pulse, τ_0 – duration of the initial pulse. If N=1, fundamental soliton is formed which maintains its shape through propagation in the medium. However, if initial pulse parameters are such that $N = 1 \pm \xi$ with $\xi \in \left[-\frac{1}{2}, \frac{1}{2}\right]$, during pulse evolution into soliton a dispersive wave breaks from the pulse [161]. The key moment is that soliton and dispersive wave interfere and this interference produces spectral oscillations [162] (Fig.1.11). This is used to estimate dispersion of the medium (PCF).
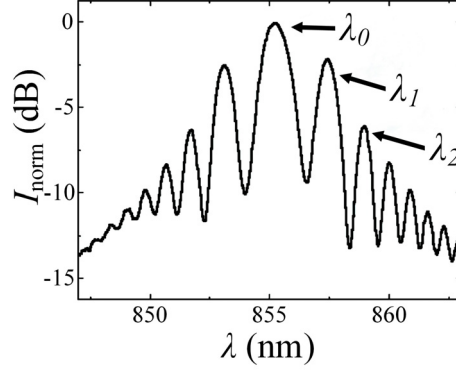
Figure 1.11: Example of spectral oscillations recorded at PCF output. Image adapted from [72].

Using the fact that phase difference between two adjacent oscillation peaks at wavelengths λ_1 and λ_2 is 2π, GDD of photonic crystal fiber can be estimated. If the PCF length satisfies condition $L > \pi\tau_0^2/|GVD|$, dispersion parameter at λ_0 can be approximated as [72]:

$$D(\lambda_0) = -\frac{2\pi c}{\lambda^2}GVD \approx \frac{2}{cL}\frac{10^6}{\left(\frac{\lambda_0}{\lambda_2}-1\right)^2 - \left(\frac{\lambda_0}{\lambda_1}-1\right)^2}[ps/(nm \cdot km)], \qquad (1.16)$$

where λ_0 is the initial pulse central wavelength. The PCF length condition in practice means that femtosecond pulses (of the order of 100 fs) and fiber length of tens of centimeters have to be used [72].

The measurement is performed in the following way. Ultrashort optical pulses from a tunable laser source (such as Ti:sapphire laser) are launched into photonic crystal fiber and the output spectrum from the PCF is recorded with spectrometer (Fig.1.12). The input power is increased gradually until oscillations are clearly visible. Then dispersion
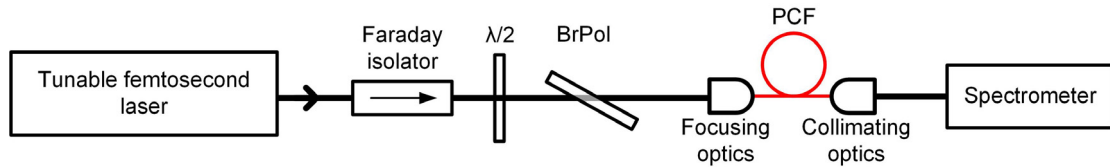

Figure 1.12: Example of GDD measurement setup using spectral modulation technique: $\lambda/2$ – half-wavelength waveplate; BrPol – Brewster type polarizer.

44

is calculated for the central wavelength using Eq.1.16. It is important to note that input power cannot be high as other nonlinear effects (such as Raman intra-pulse scattering) might distort the symmetry of the spectral oscillations causing difficulties when determining peak wavelengths of oscillations (Fig.1.11). The laser wavelength is tuned and procedure is repeated for different wavelengths – dispersion of PCF in a certain spectral range is estimated.

Spectral modulation method enables direct measurement of photonic crystal fiber group delay dispersion within practical PCF lengths. Despite the advantages, the technique is limited to anomalous dispersion range of the PCF – where soliton formation and subsequent spectral oscillations occur. In addition, the uncertainty of GDD measurement can be up to 10%.

Other GDD measurement methods include pulse synchronization technique [163], hybrid interferometric-pulse delay technique [164] and mode-field diameter techniques [66]. However, these are case-specific and rarely used, therefore, they will not be discussed in more detail.

In conclusion we can summarize that most currently popular experimental optical fiber group delay dispersion measurement techniques have significant limitations preventing them from being widely used for photonic crystal fiber GDD measurements. Spectral modulation technique seems to be best suited for photonic crystal fiber dispersion measurements but it also has notable drawbacks. Hence, we may conclude that there is still need for better GDD measurement methods when it comes to photonic crystal fibers.

1.3 Supercontinuum generation in photonic crystal fibers

1.3.1 Brief historical overview

Supercontinuum generation is a nonlinear optical phenomenon when initial narrow-band high intensity pulses propagating in nonlinear

medium undergo extreme spectral broadening which results in broadband spectrally continuous output. This is a very complex nonlinear optical phenomenon involving multiple interacting nonlinear processes.

First experiments observing nonlinear spectral broadening of laser radiation have been reported just several years after the creation of first laser [165]: in 1964 B. Stoicheff and W. Jones used radiation with broadened spectrum for Raman spectroscopy measurements [166]. Several other researchers reported broadening of laser light spectrum in liquids a few years later and identified the nonlinear nature of these effects [167–169].

In 1970 R. Alfano and S. Shapiro performed experiment focusing 5 mJ energy picosecond pulses from neodymium laser into borosilicate BK7 glass and achieved broadband white-light continuum spanning through the entire visible range of spectrum (400 nm –700 nm) [26]. This report is recognized as the first observation of supercontinuum generation since authors achieved more than 10 times greater spectral extent than reported in earlier papers. The same effect was also observed in other glasses [27, 170]. Interestingly, the phenomenon in the original paper by R. Alfano and S. Shapiro was called "parametric emission". Other researchers at that time used terms like superbroadening [170] or white-light continuum [171]. Term "supercontinuum" was first introduced in 1984 in reports by J. Manassah, R. Alfano and colleagues [172, 173]. After first demonstrations supercontinuum generation immediately became object of intense research. It was obvious that sources having broad spectral bandwidth, high brightness and good spatial coherence would be of great use in many fields [174]. Soon it became clear that supercontinuum generation in bulk media involved spatial an temporal effects. An excellent review of supercontinuum generation in bulk media is given in [175].

At the same year that first supercontinuum in bulk medium was demonstrated, scientists working at *Corning* demonstrated dramatic reduction of losses in optical fibers [4]. This immediately attracted interest for use of optical fibers not only for communications applications but also as nonlinear medium. Soon afterwards several nonlinear effects were demonstrated in optical fibers by a group led by R. H. Stolen at Bell

laboratories: Kerr effect, self-phase modulation, four-wave mixing, stimulated Raman scattering and stimulated Brillouin scattering [176–180]. The reason of interest in fiber supercontinuum sources was the potential simplicity, compactness and robustness of such systems.

First supercontinuum generation in optical fibers was reported by C. Lin and R. Stolen in 1976 when they used 10 ns dye laser pulses pumping in the normal GVD range of conventional silica fiber to generate supercontinuum [181]. Spectral broadening in this experiment was attributed to combination of self-phase modulation, cross-phase modulation, four-wave mixing effects and Raman scattering. Subsequent research by other groups involved supercontinuum generation studies with pump wavelengths near ZDW of conventional silica fibers (around 1310 nm) or near 1550 nm telecommunications window which is in the anomalous dispersion region [182–184]. It was discovered that spectral broadening in case of pumping in anomalous GDD region was particularly related to soliton dynamical phenomena [185–187]. The choice of pumping around 1550 nm at that time (1990s) was related to the desire of developing wavelength division multiplexing systems as reported in numerous papers[188–193]. These and related studies [194, 195] emphasized the key importance between wavelength of pump pulse and GDD of optical fiber. This was an additional motivation to develop fibers with unconventional dispersive properties.

First supercontinuum generation in photonic crystal fiber was reported by J. Ranka and colleagues at CLEO conference in 1999 [28] and subsequent paper in 2000 [29]. They used 100 fs pump pulses from Ti:sapphire laser to generate supercontinuum in solid-core PCF, spanning from 390 nm to 1600 nm. As explained by the authors, soliton formation, subsequent fission and other related phenomena (such as dispersive wave generation, four-wave mixing, soliton self-frequency shift, etc.) played a crucial role in supercontinuum formation process. This was later verified by many other reports of supercontinuum generation using femtosecond pulses [32, 196–200]. Among these experiments, it is important to mention report about supercontinuum generation in highly birefringent PCF by M.

Lehtonen and colleagues [201] where authors claimed that highly birefringent PCFs are more beneficial in supercontinuum generation due to lesser peak power requirements.

The application of photonic crystal fiber as a medium for supercontinuum generation has been a significant moment in nonlinear optics. Firstly, it enabled investigation of supercontinuum generation in nonlinear media with unique properties which could be adjusted by altering the structural parameters of PCF microstructured region. Freedom to design PCF properties opened the opportunity for researchers in the field to observe supercontinuum generation in PCF using a wide range of pump source parameters which was impossible in bulk media, conventional fibers or liquids. Secondly, it allowed the use of pump sources with relatively small peak intensities which were compensated by large length of nonlinear medium (PCF). In just a few years following first experiment, due to keen interest in the topic, supercontinuum generation in PCF was demonstrated under various pump conditions: picosecond pump pulses and subnanosecond (100 ps – 1 ns) pump pulses [33, 35, 202–205], nanosecond pulses [31, 32, 34] and even continuous-wave (CW) laser radiation [30, 206–208]. In case of longer pulses modulation instability was claimed to be the main process stimulating other nonlinear processes and subsequently spectral broadening as reported by A. Demircan and U. Bandelow [209]. Such rapid progress lead to deeper knowledge on the physics of supercontinuum generation. It became well-known that broadest supercontinuum would be achieved by choosing pump wavelength close to ZDW of the PCF. This and related insights were applied in various applications and evolved into commercial broadband sources such as supercontinuum sources based on mode-locked fiber oscillators delivering ultrabroadband radiation in ultraviolet, visible and infrared spectrum ranges.

Outside the aforementioned "standard conditions", research of supercontinuum generation in solid-core PCFs still continues with the aim to further expand supercontinuum bandwidth, gain more knowledge about nonlinear processes involved and introduce novel materials which

would be cheaper and better suited for the task. Several main directions of research can be outlined:

- Investigation of supercontinuum generation in non-silica glass based PCFs such as tellurite ($TeO_2 - Na_2O - ZnF_2$) , ZBLAN ($ZrF_4 - BaF_2 - LaF_3 - AlF_3 - NaF$) and chalcogenide glasses [129, 210–212].

- Investigation of supercontinuum generation in PCFs with specific dispersive or structural features such as two zero-dispersion wavelengths [213–215], PCF with multiple cores [216–218], dispersion flattened or all-normal dispersion PCFs [219–221], PCFs with sub-wavelength inclusions [55, 222, 223], etc.

- Investigation of supercontinuum generation in PCFs using special experimental conditions such as chirped pump pulses [39–48], dual-wavelength pumping [50–53], etc.

Another important direction of research is supercontinuum generation in gas-filled hollow-core photonic crystal fibers. Due to additional degree of freedom to adjust PCF dispersion by changing gas pressure and the introduction of Kagome type hollow-core PCFs (Fig.1.2 b), which have extremely broad guiding bandwidth [83, 85], lower damage threshold and a window of transparency up to the vacuum ultraviolet region, it became possible to shift ZDW of PCF event further to the short wavelength part of spectrum (up to UV range) and consequently achieve supercontinuum expansion to the vacuum ultraviolet range [86–90].

In the following three subsections a short introduction to main nonlinear phenomena involved in supercontinuum generation in solid-core PCFs will be given. Afterwards, a more detailed review will be given about supercontinuum generation using chirped femtosecond pulses and visible supercontinuum generation with subnanosecond pump pulses – two topics related to this doctoral dissertation.

1.3.2 Main nonlinear processes involved in supercontinuum generation in photonic crystal fibers

Nonlinear refractive index. When light propagates in a transparent dielectric medium it interacts with atoms that compose it and experiences loss and dispersion. As mentioned in earlier section, in case of optical waveguides the total dispersion experience is due to material and waveguide dispersion components (in the simplest case of single mode waveguide). For photonic crystal fibers the latter dispersion component has paramount importance. Due to characteristic feature of solid-core PCFs to strongly confine light in the core, the electric field strength of high peak intensity light pulses propagating through the PCF can become comparable to Coulomb electric field strength of the atoms in the medium. This triggers nonlinear optical response of the medium. Due to the nonlinear response, the refractive index becomes intensity dependent:

$$n = n_0 + n_2 I, \tag{1.17}$$

where I is peak intensity of pulse, n_0 is linear refractive index and n_2 is nonlinear refractive index of material:

$$n_2 = \frac{3\chi^{(3)}}{4n_0^2 c\varepsilon_0}, \tag{1.18}$$

here $\chi^{(3)}$ is third order nonlinear susceptibility of material, c – speed of light in vacuum and ε_0 – electric constant. This phenomenon is called Kerr effect. It is important to note that optical fibers are centrosymmetric media, therefore the second order nonlinear susceptibility for such media is zero. As mentioned in subsection 1.1.3, for optical fibers the nonlinearity is defined using optical fiber nonlinearity coefficient γ (Eq.1.8). From Eq.1.17 it follows that high intensity pulses change phase velocity of light propagating in matter $v_{\mathrm{f}} = \frac{c}{\mathrm{Re}[n(\omega, I]}$ and absorption coefficient $\kappa = \frac{\omega \mathrm{Im}[c(\omega, I)]}{c}$. Hence, the nonlinear response of medium in turn changes properties of light propagating through it. This is called self-interaction of

light.

We will now introduce equation used to describe ultrashort pulse propagation in photonic crystal fibers. One can define electric field of linearly polarized wave propagating in PCF along z axis as $E(r,t) = \frac{1}{2}\left\{E(x,y,z,t)\exp\left[-i\omega_0 t\right] + c.c.\right\}$. , then in the frequency domain, the Fourier transform of $E(x,y,z,t)$ is $\tilde{E}(x,y,z,\omega) = F(x,y,z,\omega)\overset{*}{A}(z,\omega-\omega_0)\exp\left[i\beta_0 z\right]$ where $\overset{*}{A}(z,\omega)$ is complex spectral envelope and ω_0 is center frequency of the pulse, β_0 is propagation constant and $F(x,y,\omega)$ is the transverse modal distribution. Having in mind that transverse modal distribution for a given frequency does not change during propagation, only spectral envelope can be considered in further analysis. The time domain envelope of the pulse is obtained from Fourier transform of complex spectral envelope:

$$A(z,t) = \frac{1}{2\pi}\int\limits_{-\infty}^{\infty}\overset{*}{A}(z,\omega-\omega_0)\exp\left[-i(\omega-\omega_0)t\right]d\omega \tag{1.19}$$

Using this result and changing the time frame notation to co-moving at group velocity of pulse ($T = t - v_{\mathrm{g}}z$), one can derive the time domain equation describing ultrashort pulse propagation in photonic crystal fibers which is called generalized nonlinear Schrödinger equation (GNLSE) [36]:

$$
\begin{aligned}
&\frac{\partial A}{\partial z} + \frac{\alpha}{2}A - \sum_{k\geq 2}\frac{i^{k+1}}{k!}\beta_k\frac{\partial^k A}{\partial T^k} = i\gamma\left(1 + i\tau_{\mathrm{sh}}\frac{\partial}{\partial T}\right)\times \\
&\times\left(A(z,T)\int_{-\infty}^{\infty}R(T')\left|A(z,T-T')\right|^2 dT'\right).
\end{aligned}
\tag{1.20}
$$

The left-hand side of GNLSE describes linear propagation effects: $\frac{\partial A}{\partial z}$ – pulse envelope propagation, $\frac{\alpha}{2}A$ – losses experienced during propagation, the third term describes dispersion effects with $\beta_k = \frac{\partial^k\beta}{\partial\omega^k}$ being dispersion coefficients which are obtained from the Taylor series expansion of the propagation constant around the center (carrier) frequency:

$$\beta(\omega) = \beta_0 + \left(\frac{\partial\beta}{\partial\omega}\right)(\omega-\omega_0) + \frac{1}{2}\left(\frac{\partial^2\beta}{\partial\omega^2}\right)(\omega-\omega_0)^2 + \frac{1}{6}\left(\frac{\partial^3\beta}{\partial\omega^3}\right)(\omega-\omega_0)^3 + ...$$

$$\tag{1.21}$$

The right-hand side of Eq.1.20 describes nonlinear effects during pulse propagation. γ is the aforementioned nonlinearity coefficient (Eq.1.8), $i\tau_{\text{sh}}\frac{\partial}{\partial T}$ term defines the pulse self-steepening effect and the right terms in the integral define self-phase modulation, four-wave mixing and Raman effect-related processes with $R(t)$ being Raman response function which is usually defined as [122, 224]:

$$R(t) = (1 - f_{\text{R}})\delta(T) + f_{\text{R}}h_{\text{R}}(T),$$ (1.22)

where the first term defines instantaneous electronic response and the second – delayed Raman response of the medium with Raman contribution factor (f_R) usually specified as 0.18 and h_{R} (Raman cross section) specified according to experimentally measured value [225]. $\delta(T)$ is Dirac delta function. We also need to note that in order to calculate the value of τ_{sh} one needs to compute the effective mode diameter in the photonic crystal fiber a_{eff} and the effective refractive index of PCF [21]. GNLSE can also include other effects such as polarization, noise, mode dependence on frequency, etc.

Numerical techniques used to solve GNLSE include split-step-Fourier method [122], Runge-Kutta techniques [226], direct integration of GNLSE [227], etc. Using GNLSE one can obtain results which are usually in good qualitative agreement with experiments. Now we will discuss in more detail other nonlinear phenomena involved in supercontinuum generation.

Self-phase and cross-phase modulation. Nonlinear phase modulation of a pulse caused by Kerr effect due to the pulse itself is called self-phase modulation (SPM). If for the moment we disregard dispersion of the fiber, then we can express phase of high intensity pulse propagating in it as $\phi(t, z) = \omega_0 t - kz$. According to Eq.1.17, Kerr effect induces a change in refractive index $\Delta n = n_2 I(t)$ which subsequently causes change of pulse phase:

$$\Delta\phi(t, z) = -\frac{\omega_0 z}{c}n_2 I(t),$$ (1.23)

where z is propagation distance. The variation of phase also results in

change of instantaneous frequency:

$$\Delta\omega = \frac{\partial\phi(t,z)}{\partial t} = -\frac{\omega_0 z}{c} n_2 \frac{dI(t)}{dt}.$$

(1.24)

From this equation it follows that refractive index temporal dependence on pulse intensity unavoidably causes broadening of pulse spectrum (generation of additional frequency components). In case of temporally symmetric unchirped pulse propagating in medium which nonlinear response time is much faster than duration of the pulse, spectrum broadening is symmetric and temporal envelope of the pulse is unchanged [36]. However, if initial pulse is chirped or propagates in medium where nonlinear response is slow compared to pulse duration (such as solutions of polar molecules which have orientational nonlinearity), the extent and shape of broadened spectrum will be considerably different [122].

A similar effect to self-phase modulation is cross-phase modulation (XPM) – phase modulation of a pulse caused by Kerr effect due to interaction with a co-propagating pulse. For two pulses with the same polarization the change of frequency can be defined as:

$$\begin{aligned}
\Delta\omega_1 &= -\frac{\omega_1 z}{c} n_2 \frac{d}{dt}\left(I_1(t) + 2I_2(t)\right), \\
\Delta\omega_2 &= -\frac{\omega_2 z}{c} n_2 \frac{d}{dt}\left(2I_1(t) + I_2(t)\right),
\end{aligned}$$

(1.25)

where I_1 and I_2 are peak intensities of pulses with ω_1 and ω_2 frequencies respectively. In case of orthogonal polarization pulses in isotropic media (such as optical fibers or glasses), factor "2" must be replaced with "2/3".

Self-phase and cross-phase modulation can cause complex spectral broadening especially if other nonlinear processes are involved which is the case for supercontinuum generation [228, 229]. In reality, dispersion of the medium cannot be ignored which means that there is complex interplay between self-phase modulation and dispersion. When central frequency of pulse is in normal dispersion region of the medium, self-phase modulation will lead to both spectral and temporal broadening of the pulse accompanied with pulse chirping [230]. In case of anomalous dispersion region, distinctly different phenomena occur.

Soliton generation and higher order solitons. When wavelength of pulse propagating in optical fiber is in anomalous dispersion range, for a certain peak power (called critical power) value the nonlinear positive chirp due to self-phase modulation can balance negative linear chirp due to anomalous group velocity dispersion of the fiber and solitons are formed. Solitons are solitary waves which propagate in the medium and can interact with other waves without changing their temporal and spectral shape. Since their first discovery in the 19th century as water waves in canals [231], solitons have been extensively studied and related effects have been identified in many areas of physics [232, 233], including fiber optics – in 1980 R. Mollenauer and colleagues reported first experimental observation of solitons in optical fibers [234]. In optics there are several types of solitons, but in case of supercontinuum generation the so called Schrödinger solitons are of importance. These type of solitons are analytical solutions of GNLSE without the Raman, shock and higher order dispersion terms. It can be shown that soliton solution of the initially injected pulses can be written in the form [36]:

$$A_{\mathrm{s}}(\tau) = N \sec h \left(\frac{\tau}{\tau_0} \right), \tag{1.26}$$

where τ is the pulse duration and N is the soliton number defined according to Eq.1.15. Here we need to point out that soliton number depends on both fiber (GVD, γ) and pulse (τ_0^2, P_{p}) parameters. As already mentioned when discussing spectral modulation technique (page 44), when N=1, a fundamental soliton is formed which is very stable. Higher integer N values correspond to higher order solitons. During propagation of higher order solitons their spectral and temporal shape changes periodically (example of numerically simulated solitons is shown in Fig.1.13 [36, 38].
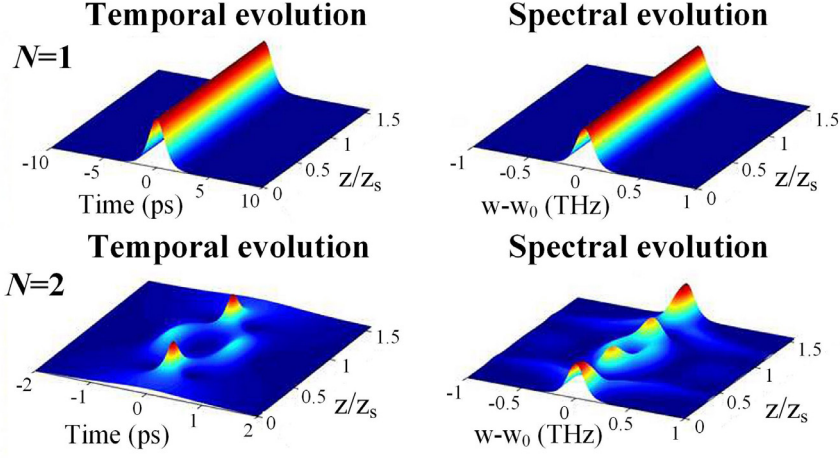
Figure 1.13: Example of numerically simulated fundamental and second order soliton evolution during propagation. Image adapted from [38].

The distance of periodic temporal and spectral shape reproduction is called soliton period and can be approximated as $z_s \approx \frac{\tau^2}{2|GVD|}$. This corresponds to a point where higher order soliton has maximum bandwidth [21]. In general, higher order soliton temporal and spectral evolution can be very complicated.

Soliton fission, self-frequency-shift and dispersive wave generation. In reality, it is very difficult to balance anomalous dispersion and self-modulation effects as there are other dispersive and nonlinear effects. For example, in case of high power femtosecond pulse propagation in optical fiber higher order dispersion and Raman scattering perturb soliton formation process [235]. This results in fission of the N-order soliton into N fundamental solitons [183] of different widths and peak powers [186]:

$$\tau_s = \frac{\tau_0}{2N+1-2k}, \ P_{ps} = \frac{(2N+1-2k)^2}{N^2}P_{p0}, \quad (1.27)$$

where τ_0 and P_{po} are duration and peak power of the higher order soliton respectively, k=1 to N' with N' being integer closest to N when it is not an integer number. The characteristic fission length is proportional to soliton number and fiber dispersive length $L_{fiss} \sim L_D/N$ [236]. Soliton fission effect is extremely important to supercontinuum generation as effects that trigger soliton breakup also affect the newly-emerged fundamental

solitons which in turn yields extensive spectrum broadening [126, 200].

Firstly, breaking of higher order soliton with wavelength close to zero group velocity dispersion wavelength of the PCF due to higher order dispersion can be perturbed and subsequently part of soliton energy will be radiated in the form of **dispersive wave** (sometimes called non-solitonic radiation or Cherenkov radiation) [161, 237–240]. As mentioned in subsection about spectral modulation (page 44), mathematically this can be understood as oscillation of soliton number $N = 1 \pm \xi$ and $\xi \in \left[-\frac{1}{2}, \frac{1}{2} \right]$ after which soliton number returns to integer value with part of energy being transferred to a dispersive wave – electromagnetic radiation which has low intensity and temporally broadens during propagation due to dispersion. The frequency of dispersive wave is determined by phase-matching condition [238, 239, 241]: for a soliton with w_{s} frequency propagating at group velocity v_{gs} a dispersive wave with frequency w_{DW} can be generated when [21]:

$$\beta(\omega_{\mathrm{s}}) - \frac{\omega_{\mathrm{s}}}{v_{\mathrm{gs}}} + (1 - f_{\mathrm{R}})\gamma P_{\mathrm{s}} = \beta(\omega_{\mathrm{DW}}) - \frac{\omega_{\mathrm{DW}}}{v_{\mathrm{gs}}}, \qquad (1.28)$$

where f_{R} is the aforementioned Raman contribution factor of the medium. From this equation it is obvious that higher order dispersion terms in propagation constant expression are necessary to achieve phase-matching for dispersive wave generation. Sometimes even fourth or fifth order terms are taken into account [241]. For fibers with a single ZDW dispersive wave generation is responsible for supercontinuum spectrum extension into shorter wavelengths (where third order dispersion is negative).

Second crucial nonlinear process perturbing soliton fission is **soliton self-frequency shift**. In scientific literature it is also called Raman intra-pulse scattering. As the latter name suggests, self-frequency shift of solitons occurs due to Raman scattering phenomenon which causes each soliton overlapping Raman gain to experience a continuous frequency shift to lower frequencies (longer wavelengths) when propagating in the fiber [122, 242]. It was shown by J. Gordon [242] that frequency shift Δw_{R} is proportional to fiber dispersion and soliton duration ($\Delta \omega_{\mathrm{R}} \sim \frac{|GVD|}{\tau_0^4}$).

For specific GDD profile self-frequency shift can be mitigated or even prevented as reported by A. Voronin and D. Skryabin with their colleagues [243, 244]. However, in most cases soliton self-frequency shift and dispersive wave generation are the central mechanisms of supercontinuum spectrum broadening.

A question might arise which of two effects leading soliton fission dominates. According to review by Dudley and colleagues [21] higher order dispersion and subsequent dispersive wave generation dominates if pump pulses are extremely short (20 fs), whereas Raman induced self-frequency shift dominates for initial pulse duration greater than 200 fs. When input pulse duration is between the specified limits, it is considered that both perturbations are of similar magnitude. It is also important to note that dynamics of supercontinuum generation in case of femtosecond pump pulses can be even more complex as solitons and dispersive waves can interact via cross-phase modulation if their group velocities are matched for a certain propagation distance which leads to additional spectrum broadening in both long-wavelength and short-wavelength edges of supercontinuum as reported in multiple papers [245–247]. This interaction is often called trapping of dispersive wave as self-frequency-shifting soliton might induce a continuous shift of dispersive wave into shorter wavelengths.

Four-wave mixing. We have discussed that soliton formation and related dynamical phenomena are key processes to supercontinuum formation when pump wavelength is in anomalous dispersion range of the PCF. When pump wavelength is in normal GVD range, soliton formation does not occur and spectrum expansion in related to the aforementioned self-phase modulation and a nonlinear process called four-wave mixing [21, 36]. It is a nonlinear phenomenon arising in optical media with third order nonlinear optical susceptibility when two waves with frequencies ω_1 and ω_2 interact and two additional frequency components $\omega_3 = \omega_1 - (\omega_2 - \omega_1))$ and $\omega_4 = \omega_2 + (\omega_2 - \omega_1))$ are generated as a result. In general, a degenerate case is possible when two initial waves have the same frequency. After first four-wave mixing stage new frequency

components, if their intensity is high enough, can become new pump waves for the next stage of four-wave mixing. The gain coefficient for amplification in fiber can be expressed as [36]:

$$g = \sqrt{\left[(\gamma P_{\mathrm{p}})^2 - \left(\frac{\Delta k}{2} \right)^2 \right]}, \qquad (1.29)$$

For single mode fiber phase mismatch term is defined as $\Delta k = 2\gamma P_{\mathrm{p}} + 2 \sum_m^{\infty} \left(\frac{\beta_{2m}}{(2m)!} \right) (\omega_m - \omega_0)^{2m}$, where β_{2m} are even order dispersion coefficients (Eq.1.21) [21]. From this equation it is obvious that maximum amplitude gain corresponding to zero phase mismatch is $g_{\max} = \gamma P_0 = 1/L_{\mathrm{NL}}$. In photonic crystal fibers four-wave mixing process can be very efficient as absence of spatial effects leads to greater efficiency of this phenomenon. An important fact to note is that when supercontinuum spectrum extends into anomalous GVD range, soliton related effects can occur as demonstrated in [21]. The closer to ZDW of the fiber the pump wavelength (in normal GVD range) is, the quicker and more efficiently phenomena related to soliton dynamics can occur. Moreover, it was shown that solitons and dispersive waves can also interact via four-wave mixing if phase-matching conditions are satisfied resulting in additional supercontinuum spectrum broadening [199, 246, 248, 249]. Nevertheless, for femtosecond pulses the characteristic four-wave mixing interaction length for various spectral components of supercontinuum cannot be long due to very short pulse durations meaning that four-wave mixing influence to supercontinuum generation is weaker than that of the aforementioned nonlinear processes.

Modulation instability. Now we will consider spectrum broadening processes when longer pump pulses are used. Numerical studies by several groups claim that, during supercontinuum generation in case of longer (picosecond, nanosecond) pulses and even CW radiation, the envelope of long pump pulse is rapidly modulated and this can induce pulse fission into soliton-like subpulses followed by self-frequency shift and dispersive wave generation [208, 250, 251]. However, initial pulse

fission is caused by different nonlinear processes than in femtosecond pump pulse case. First process is called modulation instability. As pointed out in paper by Stolen and colleagues [225], it can be interpreted as time domain equivalent of four-wave mixing process when initial waves are absent – the process is seeded by noise. Modulation instability caused frequency sidebands which in time-domain correspond to rapid modulation of pump pulse temporal envelope grow during pulse propagation in fiber and eventually the pulse can even break up into a sequence of soliton-like subpulses [122, 209]. The characteristic period of modulation instability oscillations is much shorter than fission length of pump pulse, so the duration of the subpulses (or modulations on the pulse envelope if fission does not occur) is significantly shorter than pump pulse duration. It can be expressed as [122]:

$$T_{\mathrm{MI}} = \sqrt{\frac{2\pi^2 \, |GVD|}{\gamma P_{\mathrm{p}}}}. \tag{1.30}$$

This is typically tens or hundreds of femtoseconds [21]. Efficient spectrum broadening occurs when pump wavelength is close to ZDW of the PCF: group velocity mismatch of generated additional spectrum components is smaller closer to ZDW, so temporal interaction length is longer. An important feature of the resulting spectrum broadening is noise-based origin which means that there is very little phase stability from shot to shot [38].

Raman scattering. Another important process in supercontinuum generation is stimulated Raman scattering. In general, Raman scattering is a phenomenon when the incident photon with frequency w_1 is absorbed in the medium and a lower frequency photon w_2 is emitted due to interaction with intrinsic vibrations of the medium called phonons. The difference of frequencies $\omega_{\mathrm{s}} = \omega_1 - \omega_2$ is called Stokes shift. When the intensity of incident light is very high (the case of focused laser radiation) the generated lower frequency wave is subsequently amplified (using the energy of the initial higher frequency wave) and this is called stimulated Raman scattering [122]. Under certain conditions stimulated Raman anti-

Stokes scattering can occur simultaneously. During this process wave with higher frequency than pump ($\omega_3 = \omega_1 + \omega_s$) can be generated and amplified. This is a considerably less efficient nonlinear process and requires fulfillment of phase-matching condition ($\Delta\beta = 2\beta_1 - \beta_2 - \beta_3 = 0$). Another type of stimulated Raman scattering important in this discussion is cascaded stimulated Raman scattering. This process can be explained as follows. When the efficiency of stimulated Raman scattering is very high, the amplification of Stokes-shifted wave is eventually saturated and initial pump wave is depleted. At this moment the Stokes-shifted wave becomes new pump and a new wave with double Stokes shift is generated. The process can repeat itself many times as long as the amplification of newly generated n-times-Stokes-shifted wave can be saturated.

When long pump pulses with wavelength in the anomalous GVD range are used for supercontinuum generation, stimulated Raman scattering is manifested as amplification of noise at lower frequency (Stokes) sideband of the pump pulse. For silica fibers the Raman gain dependence on the Stokes-shifted frequency offset with respect to pump wave frequency is depicted in Fig.1.14. The amplified sideband can cause
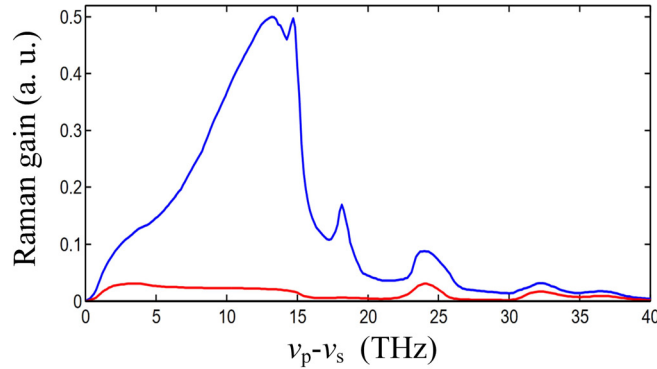

Figure 1.14: Raman gain dependence on the Stokes-shifted frequency (ν_s) offset with respect to pump wave frequency (ν_p) for silica at λ=1 μm. Blue line marks the case when pump and Stokes-shifted wave polarizations are the same, red line – when they are orthogonal. Image adapted from [122].

generation of more lower frequency sidebands through cascaded Raman scattering [252]. This adds more rapid modulation to the pump pulse temporal envelope. There are several other features to be mentioned.

Raman gain coefficient is considerably (several times) smaller than that of four-wave mixing, so Raman scattering is observed when four-wave mixing efficiency is reduced due to temporal walk-off or increased phase mismatch. This usually occurs in normal dispersion range of the fiber, so Raman scattering is the main broadening process in normal GVD region [21]. Furthermore, due to the fact that Raman Stokes gain is much stronger than anti-Stokes gain, spectrum modulation is asymmetric – long-wavelength components experience significantly greater influence of this effect. Finally, soliton-like subpulses after fission may undergo the aforementioned dispersive wave generation and self-frequency shift phenomena. If their duration is not short enough, these soliton-like subpulses under certain conditions can interact with each other and exchange energy which in turn enhances self-frequency shift of the higher energy subpulses [253].

1.3.3 Supercontinuum generation using chirped femtosecond pulses

As seen from the previous subsection, supercontinuum generation is severely affected both by photonic crystal fiber and pump pulse parameters. In this subsection a short review of research about supercontinuum generation using chirped femtosecond pulses will be presented. Chirp of an optical pulse is the time dependence of its instantaneous frequency. Chirp can be quantified as a rate of change of pulse instantaneous frequency (Hz/s) or as amount of GDD (s^2) required to dispersively compress the chirped pulse to a bandwidth-limited pulse – this quantification will be used in this doctoral dissertation. Positive pulse chirp means that instantaneous frequency increases with time, negative – decreases in time. Unlike research regarding pump pulse duration, energy or wavelength effect to supercontinuum generation, influence of pump pulse chirp has been investigated in just a few reports. In first report by K. Corwin and colleagues [45] the effect of chirp to supercontinuum generation was investigated through numerical simulations by

imposing quadratic phase chirp but keeping pulse spectral bandwidth constant and comparing results at the same pulse energy which meant that chirp increased pulse duration and decreased peak power of the pulse. Pump wavelength was at anomalous GVD range, close to the ZDW. It was concluded that maximum supercontinuum spectral bandwidth was achieved with unchirped pump pulses as they had highest peak power and shortest duration. In paper by X. Fu and colleagues [42] numerical simulation results where compared at the same peak power and spectral bandwidth. They indicated that chirping of pump pulses yields broader supercontinuum spectrum than in case of unchirped pulses. Numerical simulations performed by Z. Zhu, etc. [44] considered the influence of both positive and negative chirp at constant pump pulse duration (chirp increased pump pulse bandwidth). The main results were that positive chirp increases supercontinuum spectrum bandwidth and there exists an optimum value of positive chirp corresponding to formation of only one fundamental soliton. This was also reported in numerical studies by Tianprateep, etc. [46]. Experimental study by A. Fuerbach with colleagues [41], where positively chirped pulses were used to pump PCF in the anomalous dispersion range, also displayed similar results and agreed well with their numerical simulations. The research emphasized pump pulse chirp influence to initial stage of supercontinuum formation when due to anomalous GVD the chirped pump pulse is firstly compressed before fission and other soliton related effect can occur. H. Zhang, etc. [40] in their report theoretically analyzed the case of PCF with two closely spaced (by 152 nm) ZDWs and clarified that sufficient positive pump chirp causes supercontinuum spectrum extension to normal dispersion region of the PCF via four-wave mixing and self-phase modulation processes. This was supported by results of theoretical work by X. Hu and colleagues [43] who compared chirp influence in case of femtosecond and picosecond pump pulse durations and concluded that in case of longer pulses chirp influence to supercontinuum spectrum bandwidth is weak.

Different results were observed experimentally and in numerical simulations by R. Driben and colleagues [39]: they claimed that in case of

low peak powers (2 kW - 10 kW) initial positive or negative pump chirping yields similar supercontinuum spectrum bandwidths, while at higher peak powers negative chirp results in greater spectrum extension due to enhanced soliton self-frequency shift resulting in stronger interaction between fundamental solitons.

Aside from research performed for pump pulses with wavelength in anomalous GVD range, two papers by Y. Li, etc. [47] and Ch. Cheng with colleagues [48] reported theoretical investigation of pump pulse chirp influence to supercontinuum generation in all-normal dispersion PCF with intention to investigate its influence to spectral flatness of supercontinuum. It was shown that in such case pump pulse chirp sign makes little difference to supercontinuum spectrum extension, but greater absolute chirp value enhances self-phase modulation resulting in greater spectrum extension.

In conclusion, we see that almost all current research regarding investigation of pump pulse chirp influence to supercontinuum generation in photonic crystal fibers is theoretical. Furthermore, some results reported by different groups are inconsistent. It is clear that deeper analysis with more experimental background is necessary to understand influence of pump pulse chirp to supercontinuum generation in PCFs. We can also note that essentially all of the overviewed reports analyze chirp influence in PCF with a single ZDW. Since the amount and sign of chirp applied to pump pulses can be controlled, this can be used to achieve control of supercontinuum spectrum in real time which, combined with the possibility to get broader supercontinuum, would be advantageous in certain applications of PCF based supercontinuum sources.

1.3.4 Visible supercontinuum generation using subnanosecond pulses

In this subsection we will discuss the case of supercontinuum generation in solid-core PCFs extending through the entire visible range of spectrum by using subnanosecond pump pulses. Compact and low-

cost subnanosecond laser systems based on Q-switched Nd^{3+} microlasers have become popular pump sources for supercontinuum generation when nanosecond and subnanosecond (100 ps – 1 ns) supercontinuum is necessary. Broadband supercontinuum sources with subnanosecond pulse widths and spectrum extending through the entire visible range could be used as efficient seed radiation sources for subnanosecond optical parametric generators.

As discussed in previous subsection, supercontinuum generation in long pump pulse case occurs mainly due to modulation instability (four-wave mixing) and Raman scattering initiated pump pulse rapid modulation which, when pump wavelength is in anomalous GVD range, results in appearance of soliton-like subpulses which in turn can undergo self-frequency shift to longer wavelengths and at the same time excite dispersive waves which extend supercontinuum to shorter wavelengths. Another discussed feature is that soliton-like subpulses and dispersive waves can interact via cross-phase modulation if their group velocities are matched for a certain propagation distance which can produce extra broadening into shorter wavelengths [245–247]. Yet, the short-wavelength edge of supercontinuum spectrum using subnanosecond pulses is usually limited to roughly 500 nm [58].

With reference to the discussed unique properties of photonic crystal fibers and characteristic features of nonlinear phenomena involved in supercontinuum generation, it might seem that in order to extend supercontinuum generation further into blue and UV part of spectrum, one can simply shift ZDW of the solid-core PCF to even shorter wavelengths. This can in principle be done by increasing the microstructure diameter and pitch ratio (d/Λ) and at the same time decreasing Λ [107, 254]. Unfortunately, PCFs with ZDW at such short wavelengths are usually multimode and have increased losses (weaker light confinement in the core) which can be avoided only by increasing the size of microstructured region (number of air hole rings) [255]. More than that, such PCFs also have extremely small cores which size approaches the wavelength of light – coupling beam into the core is very complicated. These problems make photonic

crystal fibers with ZDW below 600 nm difficult to fabricate using conventional techniques and for this reason such PCFs are very uncommon. Several possible solutions to this problem have been reported.

Firstly, one can modify the PCF waveguide dispersion so that group refractive indices could be matched for long-wavelength and short-wavelength spectral components in a broader spectral range: soliton and dispersive wave interaction via cross-phase modulation in such case would also extend in a broader range resulting in greater supercontinuum spectrum extension. Waveguide dispersion modification for extension of supercontinuum spectrum can be done by carefully adjusting geometrical parameters of the PCF microstructured region as reported by Stone and colleagues [59]. Another interesting possibility reported by Zhang and colleagues [55] is insertion of nanosized air holes in the core of PCF which was shown to modify group index of the PCF and yielded supercontinuum spectrum extension from 400 nm to 2500 nm. Although this method seems straightforward, it requires carefully controlled and sophisticated modifications during PCF fabrication.

Second possibility is to use several photonic crystal fibers with different sequentially decreasing ZDWs as reported by Travers, etc. [49, 54]. This is often called cascaded supercontinuum generation as each PCF employed has ZDW optimized for a certain stage of supercontinuum generation. For example, first PCF usually has ZDW close to the pump wavelength so that modulation of initial pulse into soliton-like subpulses would be as effective as possible, while the following PCFs have ZDW shifted to shorter wavelengths to enhance the aforementioned interaction between soliton-like subpulses and dispersive waves. The benefit of such setup is the opportunity to pick PCFs with best possible parameters for each stage, however, multiple coupling stages mean that there are additional losses, the experimental setup is not compact and several different PCFs are required. An improvement to this method has been demonstrated by Kudlinski and colleagues [58] who used a special photonic crystal fiber with continuously decreasing ZDW. This allows progressive optimization of each stage of supercontinuum generation but the fabric-

ation of such PCF is very complicated: careful adjustment of the PCF drawing process is needed so that diameter of the PCF would decrease while keeping a constant air filling factor (d/Λ).

Another solution, which is also a progression from using several PCFs with different ZDWs, is the use of shorter pump wavelengths and tapered photonic crystal fibers: special PCFs with a smaller diameter section within. It is important to note that tapered PCFs are analogical to conventional tapered optical fibers which were first discussed in 1970 [256] and later used for supercontinuum generation as well [257, 258]. In the tapered part of PCF, geometrical parameters of microstructured region are considerably smaller yielding ZDW at shorter-wavelengths, so when PCF is pumped with shorter wavelength laser source the discussed nonlinear processes during supercontinuum yield shift to shorter wavelengths, hence, broader spectrum can be obtained as suggested in several papers [34, 49, 56, 259]. Although this has proven to be a working solution, it nonetheless requires carefully controlled modification of the PCF.

Finally, dual-wavelength pumping can be used to obtain broader supercontinuum spectrum spanning in the whole visible range as reported by Champert, etc. [50] and Čiburys with colleagues [53]. Two different wavelengths are usually fundamental and second harmonic of the pump laser. The broadening of supercontinuum spectrum still depends on the characteristics of PCF, but the use of dual-wavelength pumping enhances interaction of nonlinear phenomena leading to greater spectrum extension [51]. Despite this, the use of two wavelengths means more complex experimental setup: extra stage for second harmonic generation, accurate synchronization of two pump pulses and coupling optics optimized for both wavelengths are required.

In conclusion, it is clear that current methods for achieving subnanosecond supercontinuum extending through the entire visible range of spectrum require either complex experimental setups or sophisticated technological modifications of PCF. Essentially all experiments were performed with PCFs having a single ZDW. Therefore, it is safe to say that the goal of creating a simple and practical visible supercontinuum source

with subnanosecond pulse durations is still relevant.

1.4 Frequency-resolved optical gating and its application to supercontinuum generation investigation

From the preceding discussion about nonlinear mechanisms involved in supercontinuum generation it is obvious that complex nonlinear interactions beyond this phenomenon induce not only extreme expansion of pulse's spectrum, but also drastic changes in its temporal characteristics. Hence, apart from measuring spectrum (spectral domain information) of supercontinuum, it is also important to obtain information in the time domain. Needless to say, this is a very difficult task for ultrashort pulses. In the following subsections we will briefly discuss principles of a widely used ultrashort pulse characterization technique – frequency-resolved optical gating (FROG) – and review its possible application to supercontinuum generation investigation.

1.4.1 Principles of FROG

Frequency-resolved optical gating (FROG) technique is a method for full characterization of optical pulses. It was invented by R. Trebino and D. Kane in 1991 [260] and presented in their publications in 1993 [261–263]. We can define the electric field of laser pulse in the time domain as [264]:

$$E(t) = \mathrm{Re}\left\{\sqrt{I(t)}\exp[i\omega_0 t - i\phi(t)]\right\}, \tag{1.31}$$

then in the frequency domain it is expressed as:

$$\widetilde{E}(\omega) = \mathrm{Re}\sqrt{\{S(\omega - \omega_0)}\exp[-i\varphi(\omega - \omega_0)], \tag{1.32}$$

where $I(t)$ and $\phi(t)$ are the intensity and temporal phase of the pulse, whereas $S(\omega - \omega_0)$ and $\varphi(\omega - \omega_0)$ are the spectrum and spectral phase of the

pulse. The term "full" means that FROG enables retrieval of full electric field characteristics (intensity, duration and temporal phase of the pulse) or equivalently spectrum characteristics (spectrum and spectral phase of the pulse) [264].

FROG involves gating the pulse with a time-delay replica of itself in an instantaneous nonlinear medium and spectrally resolving the signal afterwards. "Instantaneous nonlinear medium" means that nonlinear response of the medium is much faster than duration of the interacting pulses. We can say that the unknown optical pulse is gated by itself, hence comes the term "gate" in acronym "FROG". The measured FROG signal is essentially a spectrogram – a joint representation of time-dependent spectrum or in other words a set of spectra at all temporal slices of the pulse. It can be defined as [264]:

$$I_{\text{FROG}}(\omega, \tau) = \left| \int_{-\infty}^{\infty} E_{\text{sig}}(t, \tau) \exp[-i\omega t] dt \right|^2,\qquad(1.33)$$

where $E_{\text{sig}}(t, \tau$ is the FROG signal electric field. The fundamental problem to solve in order to retrieve the phase of optical pulse from the spectrogram is that common spectrogram inversion methods require knowledge of the gate function [265]. Since in this case the gate function is the unknown pulse itself, usual algorithms cannot be implemented.

The solution proposed by R. Trebino and colleagues is to rewrite the expression spectrogram as a two-dimensional phase retrieval problem [262]. If we assume that $E_{\text{sig}}(t, \tau)$ is the Fourier transform with respect to delay (τ) of a function $\widetilde{E}_{\text{sig}}(t, \Omega)$ such that $\widetilde{E}_{\text{sig}}(t, \Omega = 0) = E(t)$ then the spectrogram can be rewritten as [262]:

$$I_{\text{FROG}}(\omega, \tau) = \left| \int_{-\infty}^{\infty} \int_{-\infty}^{\infty} \widetilde{E}_{\text{sig}}(t, \Omega) \exp[-i\omega t - i\Omega\tau] dt d\Omega \right|^2.\qquad(1.34)$$

This is the squared 2D Fourier transform of $\widetilde{E}_{\text{sig}}(t, \Omega)$. Now it is clear that in order to find the phase of optical pulse one needs to find the phase of Fourier transform of the quantity $\widetilde{E}_{\text{sig}}(t, \Omega)$ which is a 2D phase retrieval problem. The key moment is that, unlike 1D phase retrieval problem

(measuring $E(t)$ from $S(\omega)$) which has infinitely many solutions (the measured spectrum can correspond to infinitely many pulse shapes), a 2D phase retrieval problem has essentially one solution – we can determine $E(t)$ unambiguously [261, 262, 264, 265].

Several FROG pulse retrieval algorithms exist [261, 262, 266–269], they can all be used simultaneously to achieve the most accurate results, however, we will discuss in detail only the most reliable and universal one – generalized projections algorithm [268]. The power of this iterative method rises from the fact that it is one of the few algorithms that can be proven to converge when certain conditions are met [265]. In order to find $E(t)$ ($E_{\text{sig}}(t, \tau)$) one needs to satisfy two conditions. First condition is imposed by the measurement data – the measured spectrogram (called FROG trace) is the squared magnitude of the one-dimensional Fourier transform of $E_{\text{sig}}(t, \tau)$ defined by Eq.1.33 [265]. The second condition is that the signal field must satisfy a certain mathematical form defined by the particular nonlinear optical process used during the measurement. Various FROG versions, which will be outlined later, have different signal electrical field forms [265]:

$$E_{sig}(t, \tau) = \begin{cases} E(t)|E(t - \tau)|^2 & \text{PG \quad FROG} \\ E(t)^2 E^*(t - \tau) & \text{SD \quad FROG} \\ E(t)E(t - \tau) & \text{SHG \quad FROG} \\ E(t)|E(t - \tau)|^2 & \text{TG \quad FROG} \end{cases} \quad (1.35)$$

where PG FROG – polarization-gate FROG, SD FROG – self-diffraction FROG, SHG FROG – second harmonic generation FROG, TG FROG – transient-grating FROG.

The algorithm is initiated by guessing the initial signal field (usually noise) form and then determined by making "projections" onto one constraint and then moving to the closest point in another constraint. The process is continued until the point of convergence (the correct solution) is reached. Convergence of the solution is guaranteed if the constraint sets are convex – all line segments at the connection of the two con-

straints are entirely within the set [265]. When the constraint sets are not convex, a generalized projection must be defined which in most cases enables convergence. It can be shown that replacing the magnitude of $\widetilde{E}_{\text{sig}}^{(k)}(\omega_i, \tau_j)$ with the square root of the measured FROG trace gives the smallest change in the signal field that corresponds to the measured trace [264, 265]. Therefore, this basic replacement is a generalized projection for all FROG versions. In mathematical form this can be defined as follows. When the initial guess of $E(t)$ is made, the first correction of it is made according to nonlinear-optical constraint: the k+1 iteration of $E_{\text{sig}}^{'}(t, \tau)$ must be chosen such that function distance between iterations, expressed as:

$$Z = \sum_{i,j=1}^{N} \left| E_{\text{sig}}^{(k)}(t_i, \tau_j) - E_{\text{sig}}^{(k+1)}(t_i, \tau_j) \right|^2, \qquad (1.36)$$

would be minimal. The minimization is performed by computing the direction of steepest descent of Z – calculating the derivative of Z with respect to $E^{(k+1)}(t_i)$ [265]. Once this procedure is performed, the Fourier transform of $E_{\text{sig}}^{'}(t, \tau)$ is performed and the data constraint is applied: the magnitude of $\widetilde{E}_{\text{sig}}^{(k)}(\omega_i, \tau_j)$ is replaced with the square root of the measured FROG trace. Afterwards, inverse Fourier transform is performed and from the resulting signal field we can compute $E(t)$. Then the process is repeated. Schematic of FROG algorithm is depicted in Fig.1.15.
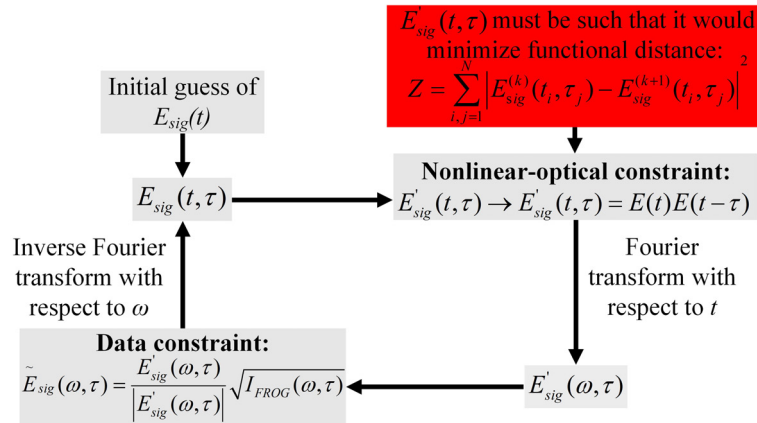

Figure 1.15: Schematic of FROG algorithm. The mathematical form of nonlinear-optical constraint in this case is for SHG FROG.

The accuracy of FROG analysis is evaluated by computing the FROG error which is the root-mean-square (rms) difference between the measured trace $I_{\text{FROG}}(\omega_i, \tau_i)$ and the computed trace $I_{\text{FROG}}^{(k)}(\omega_i, \tau_i)$. It can be expressed as [265]:

$$G = \sqrt{\frac{1}{N^2} \sum_{i,j=1}^{N} \left| I_{\text{FROG}}(\omega_i, \tau_i) - \zeta I_{\text{FROG}}^{(k)}(\omega_i, \tau_i) \right|^2}, \qquad (1.37)$$

where ζ is a real number that minimizes G (renormalization constant). Needless to say, the discussed principles of FROG are very basic and actual computational algorithms are much more sophisticated.

Main types of FROG. As was already mentioned, the nonlinear-optical constraint in FROG pulse retrieval algorithms has different forms for different experimental realizations of FROG. We will now quickly outline them.

A popular FROG geometry is second harmonic generation frequency-resolved optical gating (SHG FROG). Basically, SHG FROG is simply a spectrally resolved autocorrelation [267, 270]. It is one of the most popular FROG experimental realizations as it is the most sensitive (due to the employment of $\chi^{(2)}$ nonlinearity) and accurate. The disadvantages of SHG FROG are unintuitive trace, need of phase-matching to achieve second harmonic generation and ambiguity in the direction of time.

Another FROG version is polarization-gate frequency-resolved optical gating (PG FROG) [262, 263, 271, 272]. In this setup the pulse is split into two pulses one of which ("probe") is directed through a pair of crossed polarizers while the other ("gate") propagates through a half-wave plate which is set to yield 45° linear polarization with respect to the probe pulse polarization. In medium with third order nonlinear susceptibility the gate pulse induces birefringence due to Kerr effect so medium starts to act as a wave plate until the gate pulse is present. As a consequence, the probe pulse which overlaps with the gate pulse in the medium experiences a slight rotation of polarization and some light is transmitted through the second polarizer. Its spectrum is then measured as a function of gate

pulse delay. Unlike SHG FROG, PG FROG traces are relatively intuitive, have no ambiguities and are intrinsically phase-matched which is relevant in case of broadband pulses. The disadvantages of PG FROG are significantly lower sensitivity (due to the use of third order nonlinear effect) and requirement of high quality polarizers (extinction ration at least 10^{-5}) which also limit sensitivity of the measurement and are unavailable in deep UV spectral region [264].

Self-diffraction frequency-resolved optical gating (SD FROG) [273, 274] also employs Kerr effect: when two beams overlap in a medium with third order nonlinear optical susceptibility, as a result of interference between them and Kerr effect, a refractive index diffraction grating is induced which in turn makes both beams diffract. One of the diffracted beams can be spectrally resolved as a function of delay which gives the SD FROG trace. Merits of SD FROG are greater sensitivity to even-order temporal phase distortions than PG FROG, absence of ambiguities and most importantly no need of polarizers. The latter advantage enables measurement of ultrashort pulses in the deep UV where high quality polarizers are not available [265]. However, self-diffraction requires thin nonlinear medium (less than 200 μm thickness) and small beam overlap angles. In addition, it is a wavelength dependent phenomenon: when measuring ultrashort pulses with large bandwidths, distortions can occur. Furthermore, relatively high pulse energies are required.

A more progressive FROG type is the transient-grating frequency-resolved optical gating (TG FROG) [264, 265, 275]. It employs a three beam geometry: the investigated pulse is split into three pulses. Just as in SD FROG, two beams overlap in a medium with third order nonlinear optical susceptibility inducing the refractive index diffraction grating. In TG FROG the third beam is also overlapped in the medium with induced diffraction grating and as a result it is diffracted – a fourth (signal) beam is produced. The signal beam is then spectrally resolved as a function of delay of one of the other beams. If one of the two beams inducing refractive index diffraction grating is variably delayed, then mathematical form of TG FROG trace is the same as SD FROG trace, but if the time

delay is changed for the third beam, TG FROG trace mathematical form is identical to PG FROG trace [265]. This type of FROG has several advantages. Unlike PG FROG, it requires no polarizers, therefore, it can be used for deep UV pulse measurements. Distinct from SD FROG thick nonlinear medium and wider angles can be used significantly reducing scattered light background: TG FROG is considerably more sensitive than the aforementioned FROG techniques which use third-order nonlinear media and has no ambiguities. The only drawback is that good spatial and temporal overlap of the three beams is required [265].

Apart from the discussed traditional types of FROG, numerous other refined FROG versions were also demonstrated: surface third harmonic generation FROG (STHG FROG) [276], nonlinear-optical waveguide based FROG [277], interferometric FROG (IFROG) [278], cross-correlation FROG (XFROG) [279] and more. It is also worth mentioning another FROG-based technique – grating eliminated no-nonsense observation of ultrafast incident laser light E-fields (GRENOUILLE) which is a simplified version of FROG [280]. Huge variety of FROG versions make it a very versatile, operable from UV to mid-IR in single shot or multi-shot mode, accurate, simple and rigorous technique for characterizing ultrashort laser pulses [281, 282]. A particularly important feature of FROG is that one of its versions (XFROG) can be used to characterize even the most complex pulses – supercontinuum radiation.

1.4.2 Cross-correlation FROG and its application to supercontinuum generation investigation

Cross-correlation FROG (XFROG), first presented by S. Linden with colleagues in 1998 [279], uses a known reference pulse to characterize the investigated pulse. Principal experimental setup for XFROG measurements employing sum-frequency generation is shown in Fig.1.16. Sum-frequency generation XFROG is in principle spectrally resolved cross-correlation. It is also important to note that other geometries such as difference-frequency generation XFROG [283] and polarization-gate
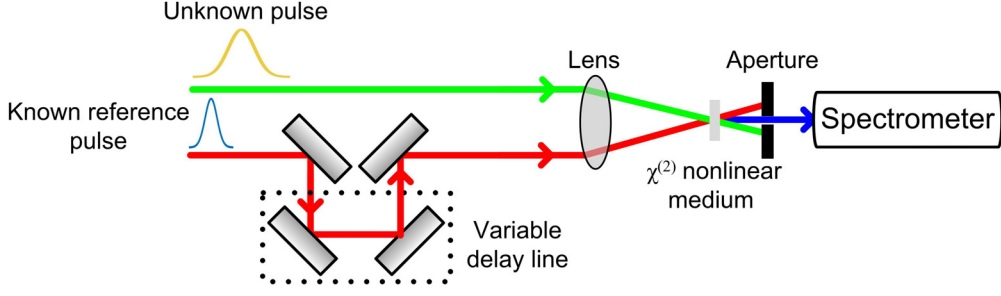
Figure 1.16: Example of experimental sum-frequency generation XFROG setup.

XFROG [284] have also been demonstrated. We can define XFROG trace as [279]:

$$I_{\text{XFROG}}(\omega, \tau) = \left| \int_{-\infty}^{\infty} E_{\text{cross}}(t, \tau) \exp[-i\omega t] dt \right|^2, \qquad (1.38)$$

where E_{cross} is the XFROG signal electric field which in case of sum-frequency XFROG is:

$$E_{\text{cross}}(t, \tau) = E_{\text{test}}(t) E_{\text{ref}}(t - \tau), \qquad (1.39)$$

with $E_{\text{test}}(t)$ being electric field of the unknown pulse and $E_{\text{ref}}(t - \tau)$ — electric field of reference pulse. Schematic of XFROG algorithm is depicted in Fig.1.17. It is very similar to FROG schematic (Fig.1.15), except for the fact that a constant well-known reference pulse electric field is always used in the signal field expression.
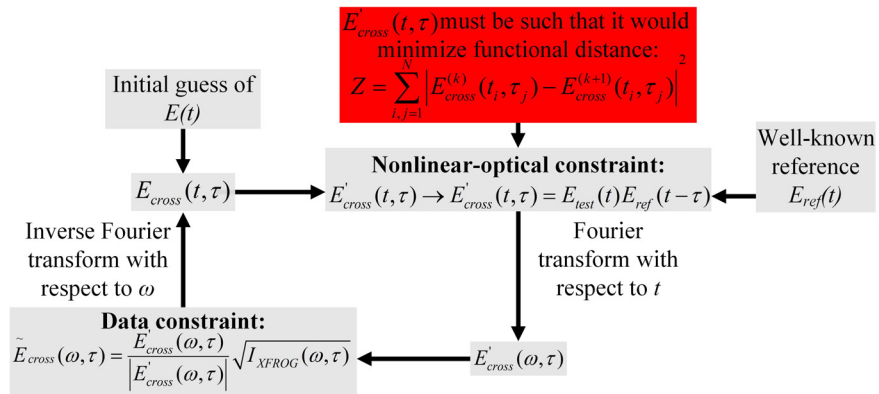

Figure 1.17: Schematic of XFROG algorithm.

XFROG has several advantages over conventional FROG techniques. Firstly, strong reference pulse amplifies the weak test pulse which allows

to characterize extremely weak pulses [285] making XFROG much more sensitive than SHG FROG. Furthermore, XFROG does not require spectral overlap of measured and reference pulses, is much more intuitive than SHG FROG and, unlike SHG FROG, does not have time ambiguity. Finally, difference-frequency generation XFROG can be used to avoid problems related to measurement of UV pulses. The outlined XFROG properties enable to use it for investigation of complex pulses including supercontinuum pulses [264].

First supercontinuum XFROG measurement was reported by L. Xu and colleagues in 2001 [286]. Using a conventional optical fiber and 600 fs pulses from chirped pulse Er-fiber amplifier they generated supercontinuum in 880 nm – 2400 nm spectral range and managed to perform sum-frequency generation XFROG measurements. The issue of achieving extremely broad bandwidth was overcome by applying angle dithering technique proposed by P. O'Shea and colleagues[287]: by rapidly rotating the nonlinear crystal within a certain angular range one can achieve integrated phase-matching for the whole spectral range of supercontinuum over the signal integration time. The measured spectrum is an averaged value of many single-shot spectra each at different crystal rotation angles which correspond to phase-matching for distinct spectral components of supercontinuum. Later publication by J. Dudley, etc. [288] points out that analyzing XFROG traces of supercontinuum generated in PCF using femtosecond pulses from Ti:sapphire laser helps intuitively reveal dispersive wave and Raman soliton components, whereas X. Gu with colleagues [289] hypothesized that the observed fine spectral structure of supercontinuum may reflect single-shot spectra which cannot be directly observed due to "washing out" when averaging many spectra. Subsequent report by Q. Cao, etc. [290] stresses that XFROG analysis reveals fine temporal structure of supercontinuum which is in good agreement with numerical simulations that are based on the established theory of supercontinuum generation in PCF. In another paper by A. Efimov with colleagues [291] XFROG analysis confirmed that additional spectral broadening during supercontinuum generation is observed due to soliton

and dispersive wave interaction. Similar conclusions were made in paper by B. Tsermaa and colleagues [292]. In all mentioned reports after the first publication, femtosecond pulses from Ti:sapphire laser were used for supercontinuum generation in photonic crystal fiber and angle dithering method was applied to achieve sufficient phase-matching bandwidth. It is worth mentioning that XFROG was also employed for investigation of supercontinuum generation in conventional tapered optical fibers [293, 294]. Finally, first experimental method for single-shot polarization-gate XFROG was demonstrated recently by T. Wong and colleagues [295]. They adapted the pulse front tilt approach in the reference arm of the setup which enabled PG XFROG measurements in single shot mode. In addition, PG XFROG geometry has no phase-matching related problems which removed the need to use angle dithering.

Chapter 2

Novel method for estimation of photonic crystal fiber dispersion by means of super-continuum generation

Material related to this chapter is published in A2 and presented in C4 and C7.

As discussed in previous chapter, group velocity dispersion (GVD) is a crucial parameter to know when investigating supercontinuum generation in photonic crystal fibers since it essentially determines nonlinear interactions during supercontinuum spectrum formation [21]. Although there are several methods to determine this parameter for optical fibers [60–62, 64, 65, 67–70, 72], in case of photonic crystal fibers their drawbacks prevent them from being widely used for PCF dispersion measurements.

In this chapter a novel group velocity dispersion measurement technique for photonic crystal fibers based on interplay between nonlinear and dispersive effects during supercontinuum generation in the PCF will be presented. After outlining principles of this measurement method and describing experimental setup, results for two different photonic crystal fibers will be presented and discussed.

2.1 Principles of the technique

Having in mind the importance of group velocity dispersion to supercontinuum generation, a question might arise if we can obtain any quantitative information about GVD of photonic crystal fiber from supercontinuum radiation generated in it. At first it seems that numerous nonlinear phenomena and their complex interaction during supercontinuum formation prevents extraction of any quantitative information about GVD of the nonlinear medium (PCF). However, there is one characteristic feature of supercontinuum generation to be considered.

As noted in literature review, in case of femtosecond pump pulses with pump wavelength in anomalous GVD range of the PCF, supercon-

tinuum evolution in photonic crystal fiber can be divided into several stages: initial pump pulse compression into higher order soliton, soliton fission, dispersive wave generation and simultaneous self-frequency shift of fundamental solitons [21, 36, 38, 296]. To demonstrate this, we simulated supercontinuum evolution along a highly nonlinear PCF using generalized nonlinear Schrödinger equation (GNLSE) by including effects of higher-order dispersion and stimulated Raman scattering. Fig.2.1 depicts numerical simulation results of supercontinuum evolution in our polarization-maintaining (PM) PCF for fast polarization mode. The term "fast" means that group refractive index for this mode is lower than for orthogonal one. This corresponds to greater group velocity of fast polarization mode. Full description of our numerical simulation model and
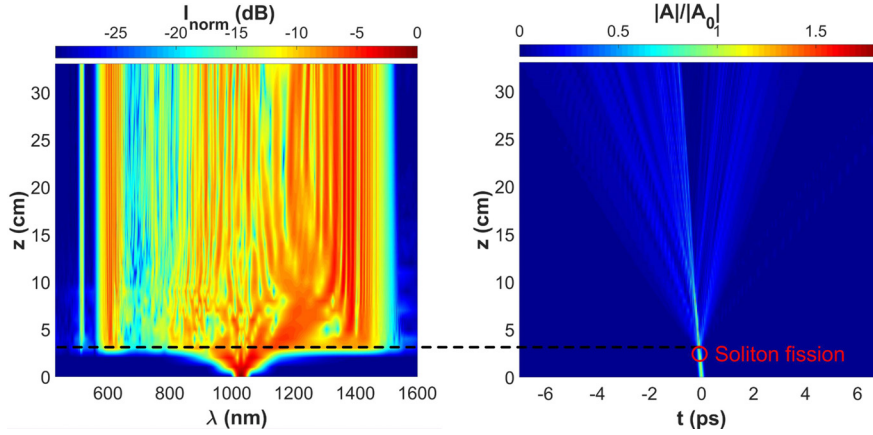
Figure 2.1: Simulated supercontinuum spectrum (left) and pulse (right) evolution during propagation in our PM PCF for fast polarization mode: λ_p=1030 nm, E_p=0.5 nJ, τ(at FWHM)=110 fs, ZDW1(fast mode)=838 nm, ZDW2(fast mode)=1059 nm. Dashed black line indicates propagation distance at which essentially all supercontinuum spectrum components are generated.

more comments of the results will be given in chapter 4 of this thesis. Currently, only the characteristic point of soliton fission is important for our discussion. Results in Fig.2.1 reflect the well-known fact that soliton fission point corresponds to extremely fast supercontinuum spectrum expansion [21]. There are several key moments that we need to point out:

- Soliton fission occurs after very short propagation length in PCF.

Fission length can be approximated as [236]:

$$L_{\text{fiss}} \approx \frac{L_{\text{D}}}{N} = \sqrt{\frac{L_{\text{D}}}{L_{\text{NL}}}} = \tau_0 \sqrt{\frac{\gamma P_{\text{p}}}{|GVD|}}, \tag{2.1}$$

where N is soliton number, $L_{\text{D}} = \frac{\tau_0^2}{|GVD|}$ is dispersive length of the PCF, $L_{\text{NL}} = \frac{1}{\gamma P_{\text{p}}}$ is nonlinear length of the PCF, γ is the aforementioned optical fiber nonlinearity coefficient (Eq.1.8), P_{p} – peak power of the pulse, τ_0 – duration of the initial pulse. In our numerical simulation results soliton fission occurs after roughly 2.5 cm of propagation, but at greater pump powers (tens of nanojoules which is a more realistic case than 0.5 nJ) this distance can be just a few milimeters.

• At fission point spectrum extension is so rapid that practically all spectral components (except a narrow range around pump wavelength) of the supercontinuum are created at the same time. The discrepancy related to spectral components around pump is negligible as soliton fission length is very short compared to the whole propagation length.

• After soliton fission there is essentially no further spectrum extension. Of course, this is true only when pump pulse energy is low (of the order of nanojoules): in such case peak intensity of the ejected fundamental solitons and generated dispersive waves is relatively low which prevents their interaction and further spectrum broadening [21, 36].

It is evident that under certain pump conditions (femtosecond pump pulses, pump wavelength in the anomalous GVD range of the PCF, pump pulse energies sufficient to generate supercontinuum but not too high) we can realize supercontinuum propagation regime when practically all spectrum components are generated at the same time and after this point propagation of supercontinuum is determined essentially by the dispersion characteristics of the PCF. We also observed this in our experiment: PCFs used in experiments "light up" with bright white light just after

5 mm of propagation in one PCF and 9 mm of propagation in the other PCF.

Now suppose we use cross-correlation frequency-resolved optical gating (XFROG) technique to obtain temporal and spectral distribution of supercontinuum after propagating certain distance in PCF. If we use sum-frequency generation XFROG, the measured wavelength at certain delay and corresponding supercontinuum spectral component are related as follows:

$$\frac{1}{\lambda_{SC}} = \frac{1}{\lambda_{sum}} - \frac{1}{\lambda_{ref}},\tag{2.2}$$

where λ_{sum} is sum-frequency wavelength, λ_{SC} – supercontinuum wavelength and λ_{ref} – known reference wavelength. A set of all spectra at all reference pulse delay values is called XFROG trace. This trace can be approximated by a polynomial:

$$T(\lambda) = \sum_{m=0}^{m} a_m \left(\frac{\lambda - \lambda_c}{\sigma}\right)^m,\tag{2.3}$$

here λ_c is the average wavelength, a_m – polynomial coefficients and σ^2 – variation of wavelengths. The fitted polynomial represents temporal delay of each wavelength with respect to reference pulse wavelength which can be related to group refractive index difference between reference and the measured spectral component:

$$T(\lambda) = \frac{L}{v_g(\lambda)} - \frac{L}{v_g(\lambda_{ref})} = \frac{L}{c}n_g(\lambda) - \frac{L}{c}n_g(\lambda_{ref}) = \frac{L}{c}\Delta n_g(\lambda),\tag{2.4}$$

where L is the aforementioned propagation distance (PCF length), $v_g(\lambda)$ and $v_g(\lambda_{ref})$ are group velocities of measured and reference pulses, $n_g(\lambda)$ and $n_g(\lambda_{ref})$ are group refractive indices of measured and reference pulses, $\Delta n_g(\lambda)$ is difference of group refractive indices between reference and the measured wavelengths. An important point is that group refractive index difference is related to temporal delay as:

$$\Delta n_g(\lambda) = \frac{cT(\lambda)}{L}.\tag{2.5}$$

Using Eq.2.4 we can express group refractive index for each spectral component of supercontinuum:

$$n_{\mathrm{g}}(\lambda) = n_{\mathrm{g}}(\lambda_{\mathrm{ref}}) + \frac{cT(\lambda)}{L} = n_{\mathrm{g}}(\lambda_{\mathrm{ref}}) + \Delta n_{\mathrm{g}}(\lambda). \tag{2.6}$$

Uncertainty limits of Δn_{g} at 95 % confidence level can be estimated as:

$$\delta(\Delta n_{\mathrm{g}}) = 2\frac{c}{L}\sqrt{\left(T\frac{\delta(L)}{L}\right)^2 + (\delta(T))^2}, \tag{2.7}$$

where $\delta(L)$ is uncertainty of PCF length (0.5 mm in our measurements) and $\delta(T)$ is reference pulse duration.

From literature review we recall that dispersion parameter for optical fibers is expressed as:

$$D = -\frac{2\pi c}{\lambda} \cdot GVD = -\frac{\lambda}{c}\frac{d^2 n}{d\lambda^2}, \tag{2.8}$$

where n is the phase refractive index of PCF which is related to group refractive index:

$$n_{\mathrm{g}} = n - \lambda\frac{dn}{d\lambda}. \tag{2.9}$$

Using this expression in Eq.2.4 and Eq.2.5, we obtain that $\frac{d^2 n}{d\lambda^2} = -\frac{c}{\lambda L}\frac{dT(\lambda)}{d\lambda}$, hence relation between dispersion parameter and measured XFROG trace can be expressed as:

$$D = \frac{1}{L}\frac{dT(\lambda)}{d\lambda}. \tag{2.10}$$

The uncertainty limits of dispersion measurement at 95 % confidence level can be estimated as:

$$\delta(D) = 2\sqrt{\left(D\frac{\delta(L)}{L}\right)^2 + \left(\frac{\delta\left(T'_\lambda\right)}{L}\right)^2}, \tag{2.11}$$

where $\delta(L)$ is uncertainty of PCF length and $\delta\left(T'_\lambda\right) = \delta\left(\frac{dT(\lambda)}{d\lambda}\right)$ is the uncertainty of derivative of temporal delay with respect to wavelength.

81

In general, calculation of function derivative uncertainty is a complicated task: we calculated $\delta\left(T_\lambda'\right)$ using method reported in paper by R. Cordero and P. Roth [297].

Expression in Eq.2.10 relates dispersion parameter of fiber and experiment data which means that, assuming the aforementioned pump conditions are met, we can estimate GVD of PCF using supercontinuum generation and information provided by its XFROG trace.

2.2 Experimental setup

Experimental setup for the measurement is shown in Fig.2.2. Laser
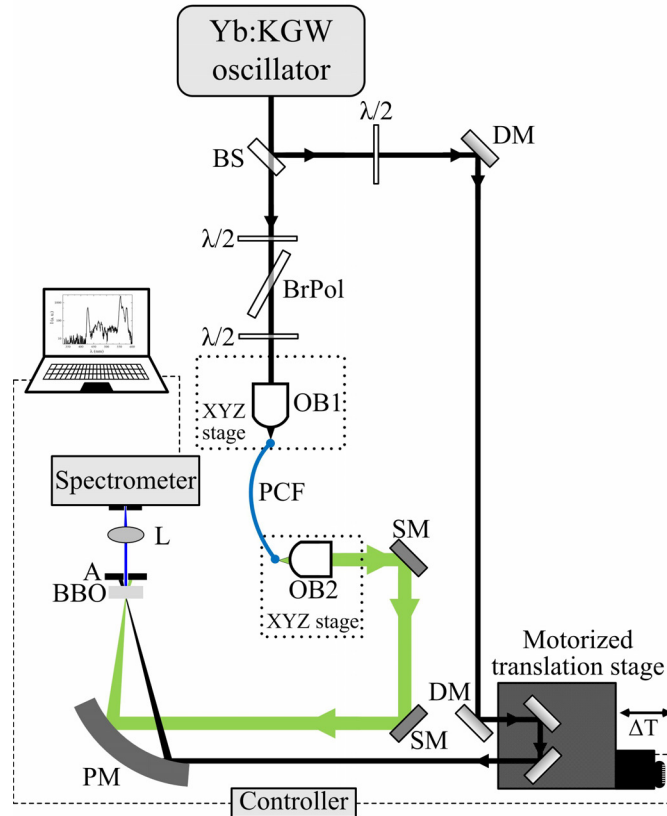
Figure 2.2: Experimental setup of supercontinuum generation and XFROG measurement apparatus: BS – beam splitter, $\lambda/2$ – half-wave plate, BrPol – Brewster type polarizer, OB1 and OB2 – $40\times$ microscope objective, SM – silver coated mirror, DM – dielectric highly reflective at 1030 nm mirror, PM – f=50.8 mm parabolic mirror, BBO – β-barium borate crystal, A – iris diaphragm, L – f=60 mm lens.

radiation from mode-locked Yb:KGW oscillator (*Flint, Light Conversion Ltd.*), generating λ_c=1030 nm E_p=72 nJ τ=110 fs pulses with 76 MHz repetition rate, was split into two beams by a 1:3 energy ratio beamsplitter. One (lower energy) beam was used as pump for supercontinuum generation, whereas the other (higher energy) beam was used as a reference pulse for XFROG measurement.

Such pump wavelength (1030 nm) was chosen for SC generation experiment since it is in the anomalous dispersion region of the PCF and close to one of the zero GVD wavelengths. It is widely known that pump wavelength in the anomalous dispersion region, but close to ZDW of the PCF yields efficient and broadband SC generation [21, 36, 38, 296]. More than that, in this case the PCF is PM and SC spectrum extends through both ZDWs of the PCF which means that SC generation mechanism is even more complicated due to the fact the GVD sign changes twice in the region of SC spectrum formation and there are two orthogonal polarization modes which each participate in SC generation. This interesting case might give some additional insight about SC generation mechanism.
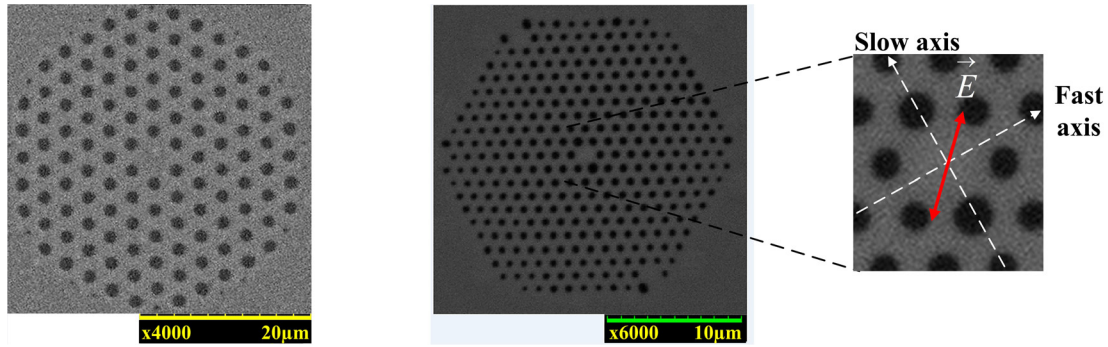

Figure 2.3: SEM images showing central part cross-section of highly nonlinear PCFs used in experiments: left – non-birefringent PCF, middle – PM PCF, right – enlarged core area image with marked principal axes of polarization of PM PCF and the actual pump polarization direction.

For supercontinuum generation (GVD measurements) we used two different PCFs:

- 33 cm long highly nonlinear ($\gamma = 11(Wkm)^{-1}$ at 1060 nm) photonic crystal fiber from *NKT Photonics A/S*, which for distinction from the

other PCF will be referred to as non-birefringent. The ZDW of the PCF specified by the manufacturer was at 1040±10 nm. and had core diameter of 4.8±0.2 μm. SEM image of this PCF cross-section is depicted in Fig.2.3 (left).

- 33 cm long polarization-maintaining highly nonlinear ($\gamma = 97(Wkm)^{-1}$ at 780 nm) photonic crystal fiber manufactured by *NKT Photonics A/S*. The ZDWs of the PCF specified by the manufacturer were at 800±15 nm and 1085±15 nm. Scanning electron microscope image of this PCF cross-section and enlarged core area image are shown in Fig.2.3 (middle and right). The PCF had core diameter of 1.8±0.3 μm and average pitch of 1.19±0.3 μm. Two larger holes next to the core are designed to induce birefringence and their orientation indicates slow and fast principal axes of polarization (Fig.2.3 right). Their diameter was d_{large}=0.7987 μm, whereas diameter of smaller holes d_{small}=0.5751 μm. Coupling efficiency into this PCF was improved by performing a simple modification to the PCF bare end tips. We spliced a conventional 105 μm core diameter silica fiber (*Nufern* MM-S105/125) to both ends of our PCF using a commercially available fiber fusion splicer. Optical microscope images of modified PCF end are shown in Fig. 2.4. The welding process caused collapse of microstructures at the end of PCF. After welding, both PCF ends were cleaved at some distance from the microstructure collapsing point. This distance depends on focusing conditions: in case of 1.8 μm core diameter it was ≈200 μm – less than the length of collapsed region in the PCF itself (this is why in Fig. 2.4 (a) no welded silica fiber is visible). This modification slightly changes focusing conditions allowing more light to be coupled into the PCF. It is also obvious that such simple modification seals PCF bare ends depriving any dust or humidity from getting into its microstructures.
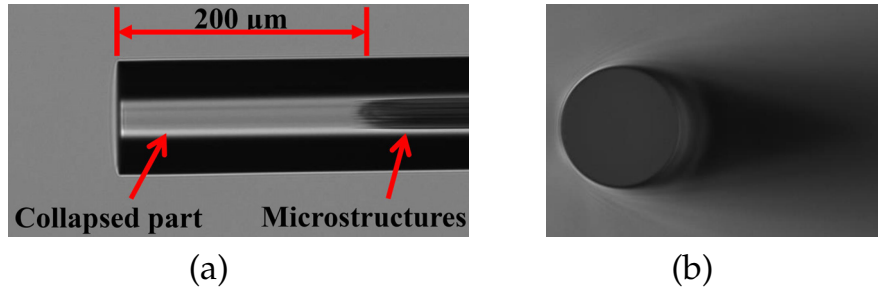
Figure 2.4: Optical microscope images of modified PCF end: (a) – side view, (b) – front view.

The input coupling end of PCF was mounted on *Thorlabs Nanomax 300D* 3-axis translation stage (marked as XYZ stage) and a low group velocity dispersion (GVD) glass 40× microscope objective was used to focus pump radiation into the PCF. When PM PCF was used, it was oriented in such a way that pump polarization would be in the intermediate position (45° angle) between fast and slow principal axes of polarization of the PCF (Fig. 2.3 right).

For sum-frequency generation we used a 300 μm thick β-barium borate crystal (BBO) cut at θ=30° and ϕ=0° for type II phase matching (e-oe): $1/\lambda_{SF} = 1/\lambda_{SC} + 1/\lambda_{1030}$. Very thin crystal and type II phase matching were chosen in order to achieve very large sum-frequency phase matching bandwidth. Supercontinuum and reference (higher energy pump) beams were focused to the BBO crystal by a 50 mm focal distance aluminium parabolic mirror. The angle between supercontinuum and reference beam was ≈15.5°. Using a fine tuning delay line we changed time delay of the reference pulse with respect to the supercontinuum pulse and recorded spectra of the corresponding sum-frequency spectrum (XFROG signal) produced during interaction between supercontinuum and pump pulses in the BBO crystal. This process was automated for faster data acquisition. Time resolution of the spectrogram was determined by the duration of reference pulse, whereas the spectral resolution was determined by the spectrometer (*Qmini, "RGB Photonics"*) and was 1.3 nm. Any unconverted pump or supercontinuum radiation transmitted through the BBO crystal was spatially filtered using an iris diaphragm.

2.3 Results and discussion

Polarization-maintaining PCF. Spectra of supercontinuum generated in PM PCF are displayed in Fig.2.5. The spectrum width of generated supercontinuum exceeded the sensitivity range of a single spectrometer, so two separate spectrometers (*Qmini, RGB Photonics* and *AvaSpec-NIR256-2.5, Avantes*) were used for registration.
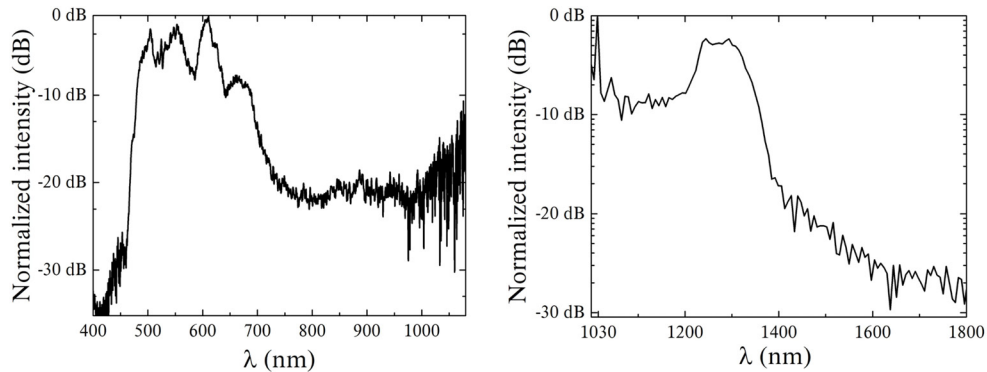

Figure 2.5: Spectra of supercontinuum generated in PM PCF using maximum available energy (9.41 nJ) pump pulses. Pulse energy was measured after focusing microscope objective.

It is also important to note that for both spectrometers corresponding spectral sensitivity correction functions were applied to all recorded SC spectra. Supercontinuum spectrum extends from roughly 450 nm to 1450 nm. As seen from Fig. 2.5, the intensity of distinct spectral components differs by several orders of magnitude which in fact complicates estimation of exact supercontinuum spectrum limits. In this chapter we focus on GVD estimation leaving detailed comments on supercontinuum generation physics to chapter 4 of this doctoral dissertation.

The XFROG trace of this supercontinuum is depicted in Fig.2.6 (left). The registered sum-frequency spectrum extends from 355 nm to 595 nm. This corresponds to supercontinuum spectrum from 541 nm to 1408 nm. Zero delay point was chosen at the point of maximum intensity of 515 nm wavelength – the second harmonic of pump wavelength. The actual point of zero delay is not important in our case since only the relative positions of temporal components are important for the analysis.
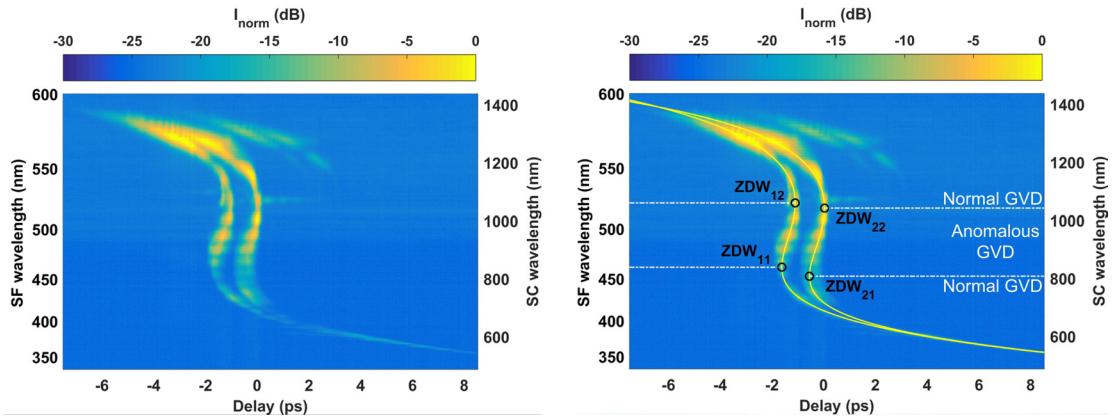
Figure 2.6: Left – measured XFROG trace of supercontinuum generated in our PCF. Left y axis depicts measured sum-frequency wavelengths, right y axis – calculated corresponding supercontinuum wavelengths. Right – XFROG trace with fitted polynomial curves (solid yellow lines). Circles in the trace represent estimated ZDWs and dashed-dotted lines separate regions of different GVD sign.

As seen from Fig.2.5 and Fig.2.6 (left) the long-wavelength limit of XFROG trace is practically determined by the long-wavelength limit of the supercontinuum: spectral components at the very edge of supercontinuum lack sufficient intensity to interact with reference beam via sum-frequency generation. Unfortunately, short-wavelength limit of the registered XFROG trace is determined by the spectral sensitivity limit of our spectrometer (350 nm). The intensity of various spectral components of XFROG trace differs by up to 3 orders of magnitude which is a reflection of the aforementioned fact that intensities of distinct supercontinuum spectral components also differ by several orders of magnitude. It is important to note that BBO crystal angle for sum-frequency generation was chosen to yield maximum spectral bandwidth of the XFROG trace. Apart from the original purpose of XFROG measurement (characterization of supercontinuum pulse, which will be discussed in chapter 4), XFROG trace reveals lots of additional information about the nonlinear medium (PCF).

Firstly, from Fig.2.6 (left) it is obvious that there are actually two distinct XFROG traces. They are associated with two orthogonal polarization modes of PCF: refractive index of birefringent PCF for each mode is

different, thus light corresponding to distinct polarization modes travels at different group velocity which is visible in the XFROG trace. To check this, we reduced energy of pump pulses coming into the PCF to minimum in order to obtain linear pump pulse propagation regime. Using an additional $\lambda/2$ phase plate for pump wavelength which was placed after the PCF we rotated polarization of output radiation so that only one polarization mode would satisfy sum-frequency phase matching condition in BBO crystal and measured XFROG traces in these two different cases. Results, depicted in Fig.2.7, clearly show that at orthogonal $\lambda/2$ phase plate orientations different parts of the trace have significantly greater intensity. This proves that XFROG trace depicts two orthogonal polarization modes.
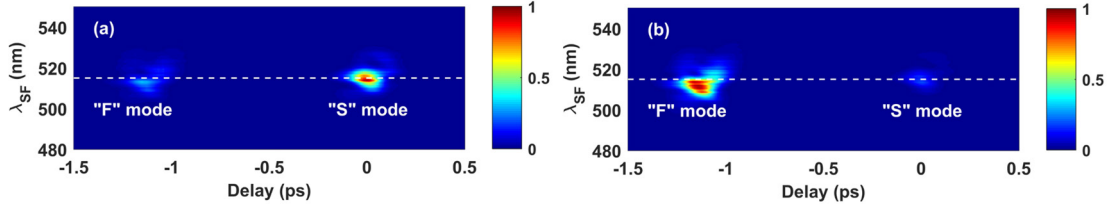

Figure 2.7: XFROG traces of minimum energy pump radiation coming out of the PCF for two orthogonal $\lambda/2$ phase plate orientations.

Secondly, by fitting polynomial curve on the XFROG trace (Fig.2.6 right) we can estimate GVD of the PCF. We need to note that in fiber optics GVD is expressed as dispersion parameter D which is related to GVD via Eq.2.8, so we will use D parameter. In our case (PM PCF) the analysis of XFROG trace allows to estimate dispersion for each orthogonal polarization mode and the difference of group refractive indices for each mode. A fifth order polynomial was used to fit each XFROG trace of polarization modes by picking the delay corresponding to the highest intensity value of the trace for every wavelength (solid yellow lines in Fig.2.6 right). The fitted polynomials represent relative delay of each supercontinuum spectral component to reference pulse wavelength (1030 nm). Dispersion parameter (D) and difference of group refractive indices is estimated according to Eq.2.10 and Eq.2.5 respectively. Results are depicted in Fig.2.8. Uncertainty of D and Δn_g at 95% confidence level is calculated according to Eq.2.11 and Eq.2.7 respectively.
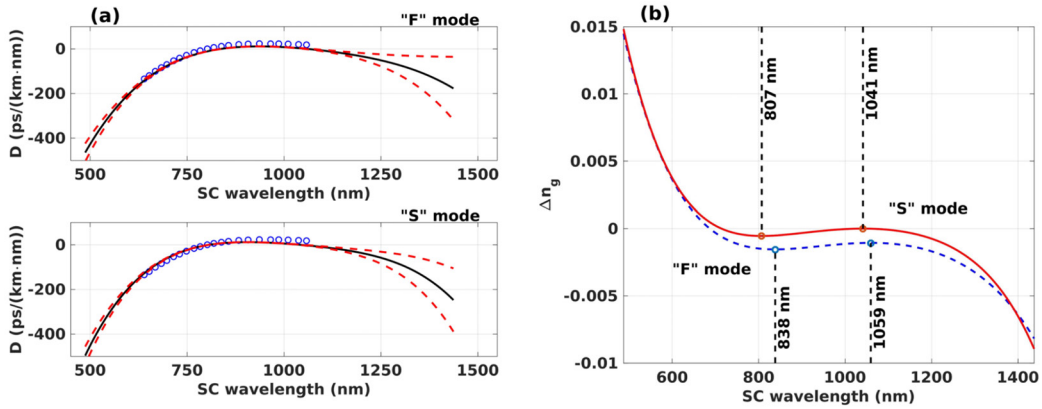
Figure 2.8: (a) Calculated dispersion parameter (solid line). Circles in figure depict dispersion data provided by the manufacturer. Dashed lines indicate uncertainty interval at confidence level of 95%. (b) Δn_{g} of orthogonal PCF modes with respect to group refractive index of slow mode at 1030 nm. "S mode" and "F mode" indicate D and Δn_{g} values for slow and fast axis respectively.

We can see that GVD and refractive indices between orthogonal polarization modes differ very little. For example, the maximum group refractive index difference between orthogonal modes is roughly 0.002. This is a typical value for birefringent PCFs [134]. Absolute uncertainty of birefringence measurement is roughly $< 2 \cdot 10^{-4}$, so we can claim that our method can distinguish very small differences of these parameters. Dispersion data provided by the manufacturer (circles in the left at Fig. 2.8 a) are in very good agreement with our measurement results proving that our assumption about suitability of supercontinuum as means to estimate GVD is correct. Tiny discrepancies for wavelengths around pump wavelength are due to the fact that spectral components very close to pump wavelength are generated before the characteristic extremely rapid spectrum expansion stage (Fig.2.1). However, we need to point that the manufacturer's data do not account for different polarization modes, so we cannot compare distinct dispersion values directly. We can also notice see that dispersion measurement uncertainty increases more rapidly at long-wavelength end. We believe this is due to thicker and greater intensity of XFROG trace at long-wavelength side which means that during polynomial curve fitting it was more difficult to pick highest

intensity point from the XFROG trace. Needless to say, the spectral limits of measurement are defined by the spectral extent of the XFROG trace.

Another important characteristic that we can directly estimate from XFROG trace (Fig.2.6) or correspondingly from Fig.2.8) are the zero GVD wavelengths. The ZDWs are indicated by the bending points in the XFROG trace (circles with ZDW inscription in Fig.2.6 right). For slow mode the ZDWs are at 807±2 nm and 1041±7 nm, whereas for fast mode they are at 838±2 nm and 1059±9 nm. The accuracy of ZDW values is determined by the uncertainty of dispersion δD at corresponding wavelengths. The fact that ZDWs are different for orthogonal polarization modes implies that supercontinuum formation dynamics and bandwidths for orthogonal polarizations are slightly different [201].

Finally, XFROG trace reveals characteristic behaviour of polarization modes and effective limits of PCF birefringence. As seen from Fig.2.6, orthogonal polarization modes are separated in time by more than 1 ps throughout the whole anomalous dispersion region. When GVD changes from anomalous (D>0) to normal (D<0), temporal distance of XFROG traces for orthogonal polarizations starts to decrease until the traces merge. We can interpret these merging points as effective limits of PCF birefringence. From Fig.2.6 or Fig.2.8 we can estimate that our PCF is birefringent for ≈590 nm – 1390 nm wavelengths. We believe that gradual merging of XFROG traces, meaning that there is no refractive index difference for orthogonal polarization modes (see Fig.2.6), can be explained by considering waveguide properties of the PCF. In long-wavelength normal GVD region the spatial mode size of long-wavelength supercontinuum spectral components exceeds the core diameter of PCF, so the longer the wavelength – the greater the size of the spatial mode and the less birefringent the PCF is. In short-wavelength normal dispersion region the spatial mode size of short-wavelength supercontinuum spectral components is less than the core diameter of the PCF, so the shorter the wavelength is – the smaller is the spatial mode size, the less it is influenced by the waveguide dispersion of PCF microstructures and the greater is the core material dispersion contribution to the overall dispersion. Since PCF core

material (fused silica) is not birefringent, XFROG traces of orthogonal polarization modes merge.

Measurements were repeated with XFROG traces of supercontinuum generated at several lower pump pulse energy values. Main results are shown in Fig.2.9, Fig.2.10 and Fig.2.11.
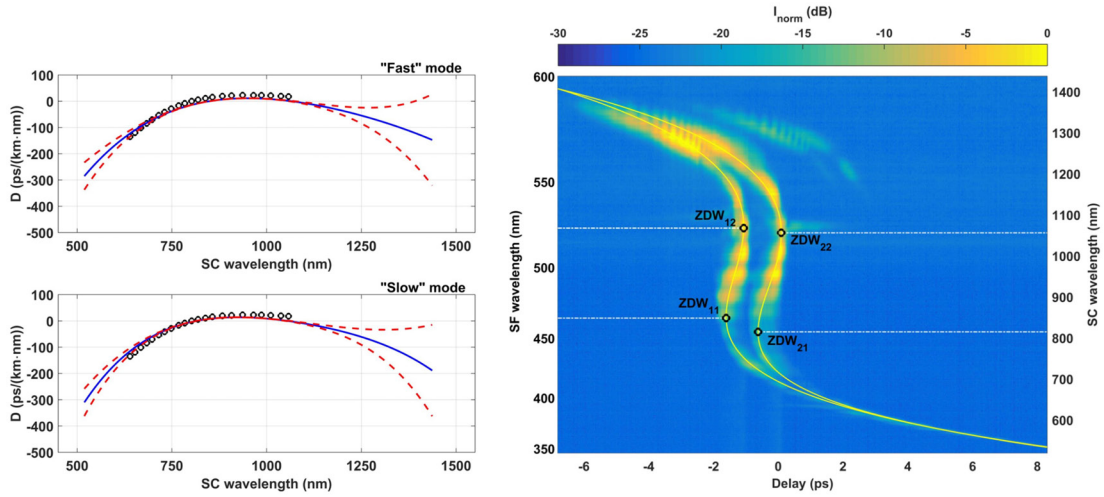

Figure 2.9: Measurement results when E_p=5.92 nJ. Estimated ZDWs for slow mode are 814 nm and 1056 nm, for fast mode – 848 nm and 1067 nm.
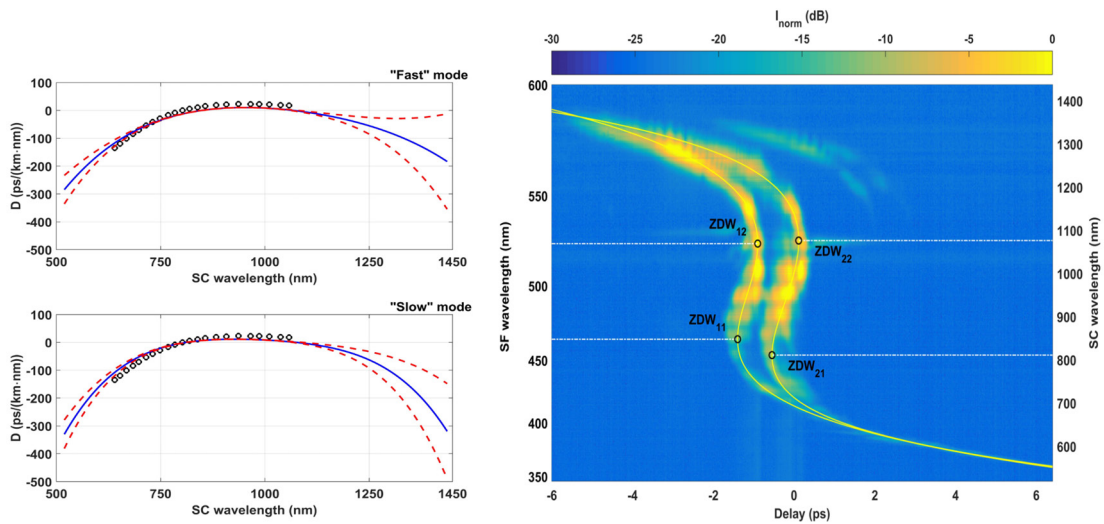

Figure 2.10: Measurement results when E_p=3.95 nJ. Estimated ZDWs for slow mode are 811 nm and 1076 nm, for fast mode – 848 nm and 1069 nm.
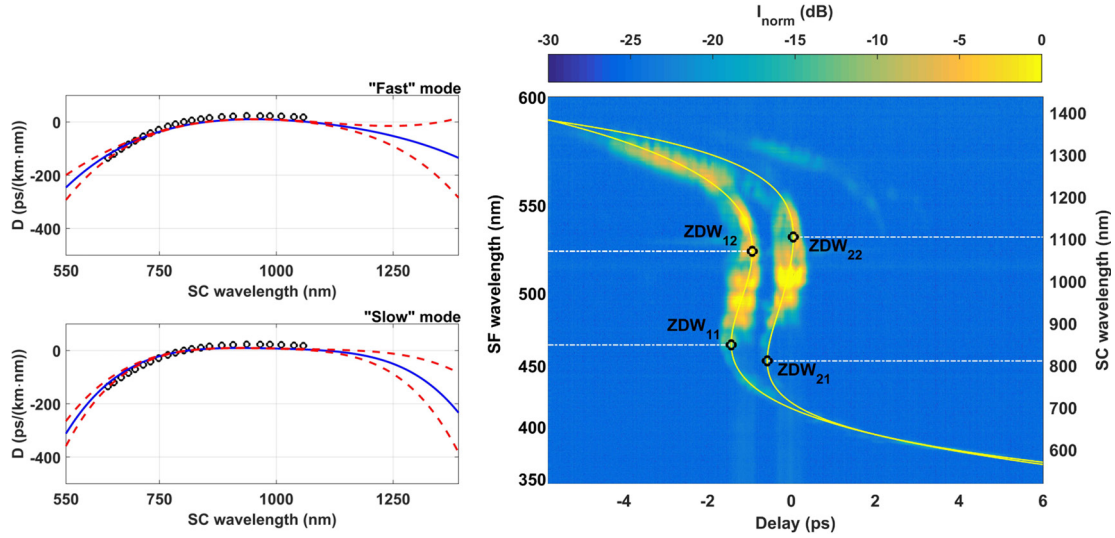
Figure 2.11: Measurement results when E_p=1.97 nJ. Estimated ZDWs for slow mode are 811 nm and 1104 nm, for fast mode – 849 nm and 1070 nm.

Measurements with supercontinuum generated at lower pump pulse energies revealed that polynomial fitting procedure is increasingly more complicated due to narrower spectral extent of XFROG trace (and supercontinuum) and increasing relative intensity of noise. Therefore, we believe that measurement in case of maximum supercontinuum pump pulse energy is the most reliable. Estimated ZDW values (specified in captions of Fig.2.9, Fig.2.10 and Fig.2.11) are very similar in almost all cases except for second ZDW for fast polarization mode which has slightly broader variation limits: we believe this is the consequence of increasingly more complicated polynomial fitting procedure at lower pump pulse energies.

Dispersion parameter calculation results are summarized in Fig.2.12. It is clear that results for both polarization modes in case of different supercontinuum pump pulse energies are very similar. This indicates that our assumption about extremely rapid supercontinuum spectrum expansion is still valid at lower pump pulse energies, thus correct measurement results can be obtained. Slight discrepancies are visible only at both ends of dispersion curve. This is related with the aforementioned difficulties fitting polynomial curve on the XFROG trace in case of lower supercon-

tinuum pump pulse energies. Slight discrepancies with manufacturer's data are visible around pump wavelength for all supercontinuum pump energy cases – this is due to the aforementioned fact that spectral components very close to pump wavelength are generated before the characteristic extremely rapid spectrum expansion stage (Fig.2.1). On the other hand, it is again important to remember that manufacturer's data do not account for different polarization modes, we cannot compare distinct dispersion values directly. However, we can see good quantitative agreement and that our method enables GVD estimation in significantly broader spectral range.
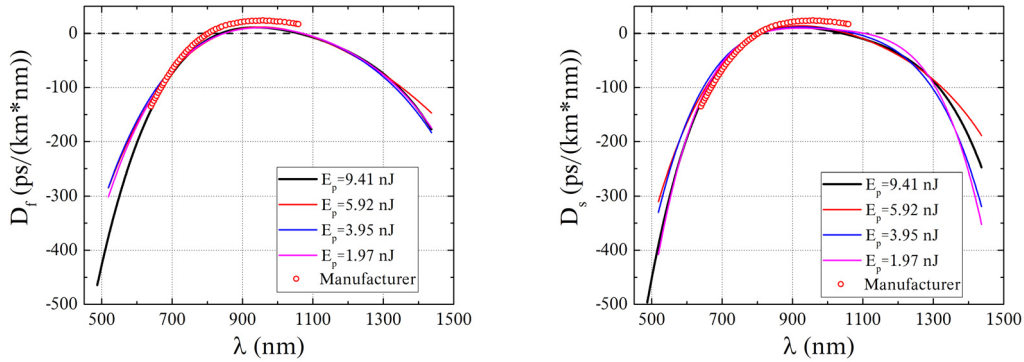

Figure 2.12: Dispersion parameter for fast (left) and slow (right) polarization modes calculated from XFROG traces of supercontinuum generated at different pump pulse energies. Red circles represent manufacturer's data.

Non-birefringent PCF with one ZDW. Now we will analyze measurement results obtained with other (non-birefringent) photonic crystal fiber with ZDW at 1040 ± 10 nm (specified by the manufacturer). In the first section of this chapter we pointed out that in order to achieve accurate GVD measurement, pump wavelength has to be in the anomalous GVD range which results in simultaneous generation of practically all supercontinuum spectrum components. The case we will discuss now is different as central wavelength of the femtosecond pump pulses (1030 nm) is close to ZDW of the PCF but is in normal GVD range of the PCF (D<0). As already discussed in literature review chapter of this thesis, in such case self-phase modulation of the pulse is mainly responsible for initial

93

spectrum broadening and when spectral components of supercontinuum extend to anomalous GVD range, soliton related dynamics can occur. The closer to ZDW the pump wavelength (in normal GVD range) is, the quicker and more efficiently phenomena related to soliton dynamics can occur as demonstrated in [21]. In what follows we will see how this affects GVD measurement.

Spectra of generated supercontinuum are displayed in Fig.2.13. As with the previous PCF, spectrum width of generated SC exceeded the sensitivity range of a single spectrometer, so two separate spectrometers (*Qmini, "RGB Photonics"* and *AvaSpec-NIR256-2.5, Avantes*) were used for registration and for both spectrometers corresponding spectral sensitivity correction functions were applied to all recorded SC spectra. Supercontinuum spectrum extends from roughly 700 nm to 1500 nm. Similarly to the previous case, intensity of distinct supercontinuum spectral components differed by several orders of magnitude which complicates estimation of exact supercontinuum spectrum limits. It is obvious that supercontinuum spectrum is different from spectrum generated with the previous PCF which is due to different GVD of the PCF and partly due to lower nonlinearity (($\gamma = 11(Wkm)^{-1}$ at 1060 nm).
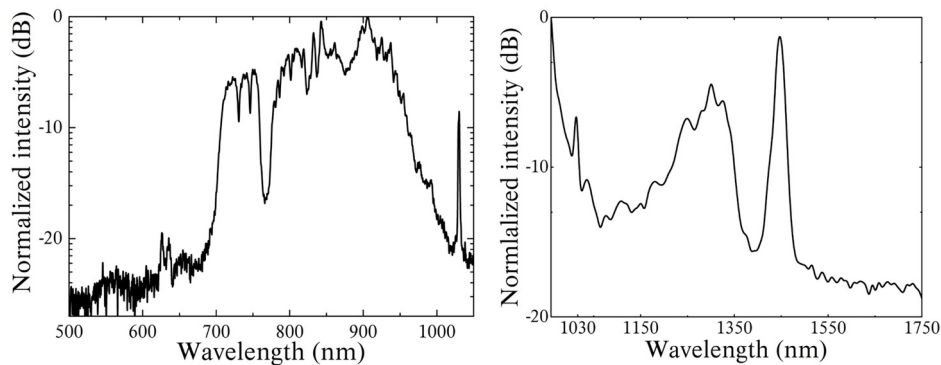

Figure 2.13: Spectra of supercontinuum generated in non-birefringent PCF using maximum available energy (9.41 nJ) pump pulses. Pulse energy was measured after focusing microscope objective.

The XFROG trace of this supercontinuum at maximum pump energy is depicted in Fig.2.14 (left). The registered sum-frequency spectrum extends from 420 nm to 610 nm. This corresponds to supercontinuum

spectrum from 710 nm to 1500 nm. The long-wavelength limit of XFROG trace is limited by the spectral extent of supercontinuum, while the short-wavelength limit is slightly shorter: spectral components at the very edge of supercontinuum lack sufficient intensity to interact with reference beam via sum-frequency generation. Zero delay point was chosen at the point of maximum intensity of 515 nm wavelength – the second harmonic of pump wavelength. As in the previous analysis, the actual point of zero delay is not important in our case since only the relative positions of temporal components are important for the analysis.
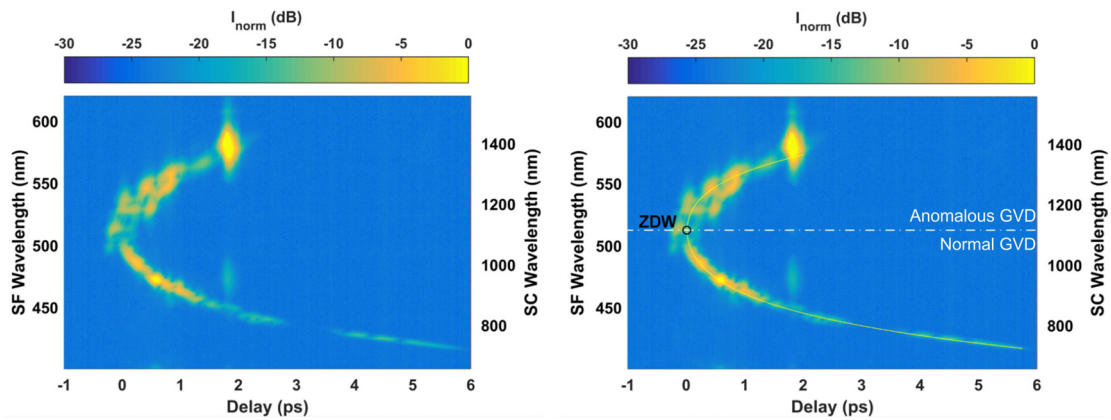

Figure 2.14: Left – measured XFROG trace of the supercontinuum generated in the other PCF at maximum pump energy (9.41 nJ). Right axis depicts calculated supercontinuum wavelengths. Right – XFROG trace with fitted polynomial curve (solid yellow line). Circle in the trace represent estimated ZDW and dashed-dotted line separates regions of different GVD sign.

GVD estimation procedure in this case is practically the same except that a fourth order polynomial was used to fit XFROG trace by picking the delay corresponding to the highest intensity value of the trace for every wavelength (solid yellow line in Fig.2.14 right). The fitted polynomial represents relative delay of each supercontinuum spectral component to reference pulse wavelength (1030 nm). Calculated GVD (in the form of dispersion parameter D) is depicted in Fig.2.15. Results show that this PCF has a single ZDW at 1114±10 nm. Greater uncertainty of polynomial fitting in the long wavelength range is related to greater temporal extent of the XFROG trace which results in greater polynomial fitting uncertainty (how accurately the highest intensity point is picked at each delay).
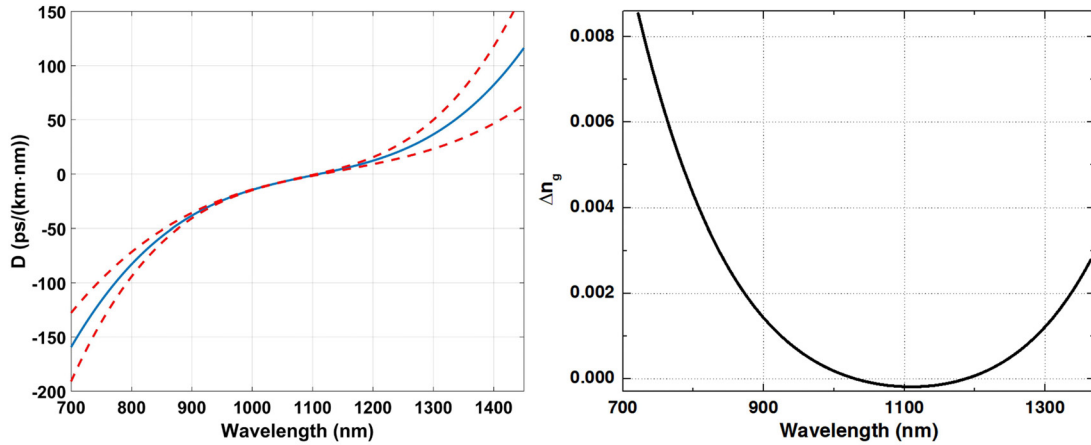
Figure 2.15: Left – calculated dispersion parameter (solid line). Dashed red lines indicate uncertainty interval at confidence level of 95%. Right – Δn_{g} with respect to group refractive index at 1030 nm.

Further on, measurements were repeated with XFROG traces of supercontinuum generated at several lower pump pulse energy values. The results are summarized in Fig.2.16 where dispersion parameters are compared among themselves and with manufacturer's data. We can see that GVD measurement results are reasonably similar at different supercontinuum pump pulse energies, but at short-wavelength and long-wavelength ends there are discrepancies. They are due to the aforementioned fact that polynomial curve fitting in case of lower pump pulse energies is more difficult (has higher uncertainty) because of relatively greater intensity of noise in XFROG trace.

Manufacturer's data at short-wavelength end is in best agreement with measurement results obtained at maximum pump pulse energy. However, in the vicinity of pump wavelength and long-wavelength end, there are discrepancies. As mentioned before, discrepancy between measurement and manufacturer's data around pump wavelength is related to the fact that spectral components very close to pump wavelength are generated before the characteristic extremely rapid spectrum expansion stage (Fig.2.1). Since discrepancy is small, we can claim that when pump wavelength is close to ZDW of the PCF, but in normal GVD range, spectrum quickly extends to anomalous GVD range and assumption of extremely

rapid spectrum broadening is still valid. Larger discrepancy between measurement and manufacturer's data in the long-wavelength region can be explained considering soliton self-frequency shift phenomenon [122, 242]. Unlike our PM PCF which has a relatively narrow anomalous GVD spectral range, the second (non-birefringent) PCF has anomalous GVD range extending outside spectral limits of both our measurements and manufacturer's data. As noted in [21, 36], under sufficient pump pulse energy this enables efficient soliton self-frequency shift towards longer wavelengths after the point of extremely rapid supercontinuum spectrum expansion – spectrum evolution in long-wavelength region is slightly different in long-wavelength edge than depicted in Fig.2.1 (top). In other words this means that our assumption of simultaneous generation of practically all supercontinuum spectrum components at the point of rapid supercontinuum spectrum expansion is not strictly valid which in turn results in lesser accuracy of GVD measurement.
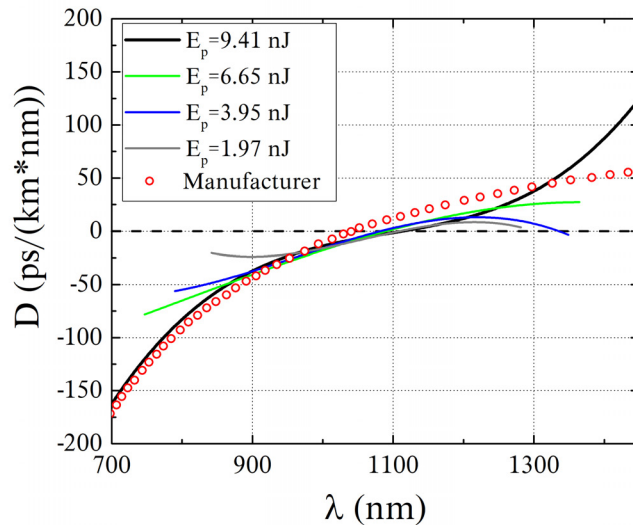

Figure 2.16: Calculated dispersion parameter from XFROG traces of supercontinuum generated at different pump pulse energies. Red circles represent manufacturer's data.

2.4 Conclusions

In conclusion, we demonstrated a novel experimental technique for measuring GVD of PCFs based on cross-correlation frequency-resolved optical gating (XFROG) trace analysis of a femtosecond supercontinuum generated in a photonic crystal fiber.

We discussed that this method is feasible due to characteristic feature of femtosecond supercontinuum generation in PCFs when at certain conditions essentially all supercontinuum spectrum components are generated simultaneously at the same time after very short propagation distance (Fig.2.1). The main conditions to achieve this are related to pump pulse wavelength and energy. The most rapid supercontinuum spectrum extension occurs when pump wavelength is in anomalous GVD range of the PCF [21, 36]. However, our experiments with the second (non-birefringent) PCF indicated that when pump wavelength is very close to ZDW, but in normal GVD range, fairly accurate GVD measurement is also possible: this implies that in this case supercontinuum spectrum extension at certain point after propagating in PCF is also very rapid. Pump pulse energy has to be sufficient to generate supercontinuum after very short propagation distance, but not too high to prevent nonlinear phenomena that could cause additional spectrum broadening after point of extremely rapid spectrum expansion. In our measurements this energy is of the order of several nanojoules.

Experimental results also showed that for PM PCF our experimental technique is capable of distinguishing GVD of orthogonal polarization modes, allowing to calculate difference of their group refractive indices (Δn_{g}) with relatively high accuracy (absolute uncertainty $< 2 \cdot 10^{-4}$) and observe complex behaviour of these polarization modes which in turn allows to identify effective limits of PCF birefringence. To the best of our knowledge, there are no other experimental methods that can measure GVD of orthogonal PCF polarization modes simultaneously.

We can also note that our method allows quantitative estimation of PCF GVD in a very broad spectral range: we were able to measure GVD

from roughly 540 nm to 1400 nm for PM PCF and from 710 nm to 1500 nm for other (non-birefringent) PCF. Measurement range is limited by spectral extent of cross-correlation frequency-resolved optical gating trace which in principle can cover the entire supercontinuum bandwidth. Beyond these limits the uncertainty of the measurement becomes unacceptably high. With reference to the fact that it works with short PCFs, is fast and not sensitive to environmental conditions, we can claim that this measurement technique is promising compared to other experimental photonic crystal fiber GVD measurement methods [60–62, 64–72].

Chapter 3

Measurement of photonic crystal fiber mode phase refractive index dispersion

Material related to this chapter is published in A4 and presented in C5.

In the previous chapter we presented a new GVD measurement technique and stressed how this parameter is important for pulse propagation in optical fiber and supercontinuum generation. On the other hand, complete information about optical fiber's mode dispersion is provided by phase refractive index $n(\lambda)$ which in case of solid-core photonic crystal fibers is actually an effective refractive index of the microstructured region [77]. If one could determine phase refractive index dispersion (dependence of n from λ) of fiber mode, other related parameters such as group refractive index dispersion, GVD, etc. could be easily calculated from it – dispersion properties of the optical fiber mode would be completely characterized. Phase refractive index is related with group refractive index n_{g} via Eq.2.9. One may formally solve this differential equation with respect to n. The result is:

$$n(\lambda) = \frac{\lambda}{\lambda_0} n(\lambda_0) - \frac{\lambda - \lambda_0}{\lambda_0} n_{\mathrm{g}}(\lambda_0) - \lambda \int_{\lambda_0}^{\lambda} \frac{\Delta n_{\mathrm{g}}(\lambda')}{\lambda'^2} d\lambda' . \qquad (3.1)$$

where λ_0 is a certain reference wavelength. First term of Eq.3.1 is related to phase refractive index $n(\lambda_0)$ at certain wavelength (λ_0), second term – to group refractive index $n_{\mathrm{g}}(\lambda_0)$, third term – to group refractive index dispersion (GVD). From this it is clear that phase refractive index has complete information about dispersion of optical fiber mode.

Currently, to the best of our knowledge, no experimental methods for PCF phase refractive index measurement exist. One method based on observing two sets of fringes in Michelson interferometer corresponding to interference between reference arm light and Fresnel reflection from the front and back surfaces of fiber has been proposed for phase refractive index estimation for conventional telecommunications optical fibers [73].

However, the experimental implementation of this method is complicated as it requires very careful identification which fringes correspond to interference between reference arm light and Fresnel reflections from the front and back surfaces of the fiber and also requires some art of fitting of the experimental results. Moreover, in case of PCF the amount of back-reflected light is not sufficient for measurement.

In this chapter we will present group refractive index measurement results and a novel method for measuring phase refractive index of PCF fundamental mode. Using GVD data acquired previously, we then estimate phase refractive index dispersion of PCF fundamental mode.

3.1 Measurement of group refractive index of photonic crystal fiber

3.1.1 Experimental setup

To measure group refractive index of photonic crystal fiber fundamental mode we used experimental setup shown in Fig.3.1. The whole setup is essentially an intensity autocorrelator. Laser radiation from mode-locked Yb:KGW oscillator (*Flint, Light Conversion Ltd.*), generating λ_c=1030 nm E_p=72 nJ τ=110 fs pulses with 76 MHz repetition rate, was split into two pulses by a 1:1 energy ratio beamsplitter. One pulse was directed to PCF which both ends were mounted on *Thorlabs Nanomax 300D* 3-axis translation stages (marked as XYZ stage) and a low group velocity dispersion (GVD) glass $40\times$ microscope objectives were used to focus pump radiation into the PCF and subsequently collimate outgoing beam. Further on, the beam is directed to 50 mm focal distance aluminium parabolic mirror. It focuses beam coming from PCF together with the second beam into a 3 mm thick BBO crystal cut at θ=22.5° and ϕ=90° for type I phase matching where non-collinear sum-frequency generation occurs. As in conventional intensity autocorrelator, highest intensity of generated sum-frequency radiation is achieved when optical path lengths for both
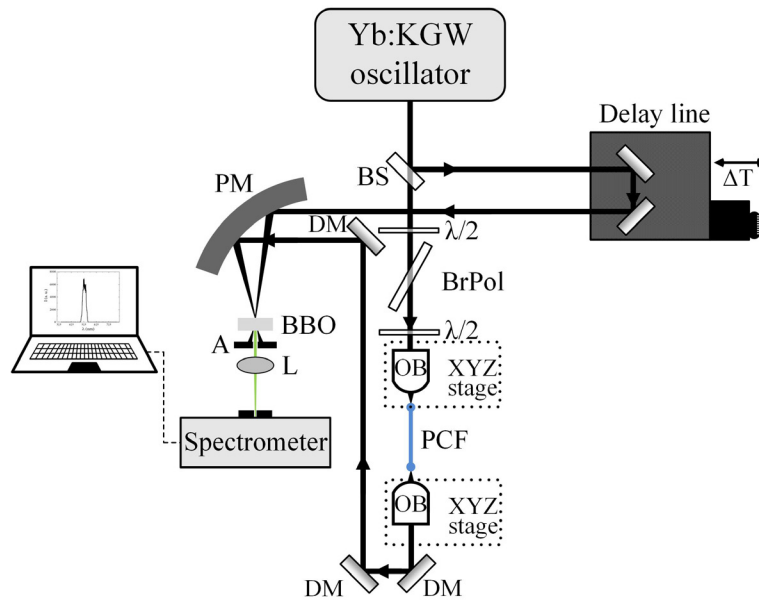
Figure 3.1: Experimental setup for measuring group refractive index of PCF mode: BS – beam splitter, $\lambda/2$ – half-wave plate, BrPol – Brewster type polarizer, OB – 40× microscope objective, SM – silver coated mirror, DM – dielectric highly reflective at 1030 nm mirror, PM – parabolic mirror, BBO – β-barium borate crystal, A – iris diaphragm, L – f=60 mm lens.

pulses are equal. Delay line position corresponding to highest intensity of sum-frequency radiation can be estimated by visual, observation of sum-frequency beam intensity on a screen but for greater precision we used spectrometer (*Qmini, "RGB Photonics"*) to measure spectrum and intensity of sum-frequency pulses.

Group refractive index was measured for the same PCFs that we used for GVD measurement in chapter 2 (page 83)just shorter – both were 13.6 cm long. There are two important facts to note about the PCF. Firstly, PCF needs to be inserted straight, so that we could assume that optical path change in this arm is only due to different group refractive index of PCF compared to that of air. Secondly, intensity of pulses coming into the PCF must be kept very low to prevent supercontinuum generation which would significantly distort the temporal profile of the pulse. For this reason an optical attenuator consisting of half-wave waveplate and Brewster-type polarizer was used to reduce energy of pulses coming into PCF. The threshold energy of supercontinuum generation (measured with

a power meter) was determined by observing the spectrum of pulses coming out of the PCF.

3.1.2 Principle of measurement, results and discussion

The measurement procedure is as follows. Firstly, sum-frequency generation is achieved without photonic crystal fiber and microscope objectives. As mentioned, highest intensity of sum-frequency is achieved when optical paths of both arms are equal:

$$L_{\text{opt1}} = L_{\text{opt2}} = n_{\text{air}}L_0, \tag{3.2}$$

where L_{opt1} is optical path length of first arm (without PCF and microscope objectives), L_{opt2} is optical path length of second arm (it can be changed via delay line), L_0 is physical length of first arm without PCF and microscope objectives (which in this case is equal to second arm length) and n_{air} is the refractive index of air.

Secondly, group refractive index of the microscope objectives used in experiments is estimated. It is important to note that microscope objectives are a combination of several different material lenses with possible air spaces between them so the measured value is actually an effective group refractive index of the system. By inserting only the two microscope objectives into one arm of the autocorrelator, we change optical path length of the first arm, so for sum-frequency generation to occur, optical path length of the second arm needs to be adjusted by a certain length ($\Delta L^{(1)}$) to equalize optical paths of both arms. We can express this in the following system of equations:

$$\begin{cases} L_{\text{opt1}} = n_{\text{air}}(L_0 - 2L_{\text{ob}} - L^{'}) + n_{\text{air}}L^{'} + 2n_{\text{ob}}L_{\text{ob}}, \\ L_{\text{opt2}} = n_{\text{air}}(L_0 + \Delta L^{(1)}), \\ L_{\text{opt1}} = L_{\text{opt2}}, \end{cases} \tag{3.3}$$

where L_{ob} is the physical length of a single microscope objective, $L^{'}$ – distance between inserted microscope objectives and n_{ob} is the group

refractive index of microscope objective. From Eq.3.3 we get expression for n_{ob}:

$$n_{ob} = \frac{n_{air}\Delta L^{(1)} + 2n_{air}L_{ob}}{2L_{ob}}. \tag{3.4}$$

The measurement uncertainty at 95% confidence level can be estimated as:

$$\delta(n_{ob}) = 2\sqrt{\left(\delta(\Delta L^{(1)})\frac{\partial n_{ob}}{\partial \Delta L^{(1)}}\right)^2 + \left(\delta(L_{ob})\frac{\partial n_{ob}}{\partial L_{ob}}\right)^2}, \tag{3.5}$$

with $\delta(\Delta L^{(1)})$ being the uncertainty of $\Delta L^{(1)}$ measurement and δL_{ob} – uncertainty of microscope objective length measurement. During the experiment we determined that $\Delta L^{(1)}$=22.05 mm. Length of microscope objective was L_{ob}=45 mm and refractive index of air was assumed to be n_{air}=1. Using Eq.3.4 we calculated that group refractive index of microscope objective at 1030 nm wavelength is n_{ob}=**1.245** $\pm$**0.006**.

Finally, the investigated PCF is inserted into the setup (as shown in Fig3.1). Consequently, optical path length of the second arm needs to be adjusted by a certain length ($\Delta L^{(2)}$) to equalize optical paths of both arms:

$$\begin{cases} L_{opt1} = n_{air}(L_0 - 2L_{ob} - 2L'' - L_f) + 2n_{air}L'' + 2n_{ob}L_{ob} + n_{gf}L_f, \\ L_{opt2} = n_{air}(L_0 + \Delta L^{(2)}), \\ L_{opt1} = L_{opt2}, \end{cases} \tag{3.6}$$

where L'' is the distance between microscope objective and PCF, L_f – length of PCF and n_{gf} – group refractive index of PCF fundamental mode. From this system of equations n_{gf} is:

$$n_{gf} = \frac{n_{air}\Delta L^{(2)} + n_{air}L_f - 2L_{ob}(n_{ob} - n_{air})}{L_f}, \tag{3.7}$$

and the uncertainty at 95% confidence level can be calculated from:

$$\delta(n_{gf}) = 2\left(\left(\delta(\Delta L^{(2)})\frac{\partial n_{gf}}{\partial \Delta L^{(2)}}\right)^2 + \left(\delta(L_f)\frac{\partial n_{gf}}{\partial L_f}\right)^2 + \right.$$
$$\left. + \left(\delta(L_{ob})\frac{\partial n_{gf}}{\partial L_{ob}}\right)^2 + \left(\delta(n_{ob})\frac{\partial n_{gf}}{\partial n_{ob}}\right)^2\right)^{\frac{1}{2}}. \tag{3.8}$$

Here $\delta(\Delta L^{(2)})$ is uncertainty of $\Delta L^{(2)}$ measurement, δL_f – uncertainty of PCF length measurement and $\delta(n_{ob}$ is uncertainty of microscope objective group refractive index measurement. From experiment we determined that for our non-birefringent PCF $\Delta L^{(2)}$=101.62 mm and the corresponding photonic crystal fiber group refractive index for the fundamental mode at 1030 nm wavelength is n_{gf}=**1.585±0.008**.

Measurement of PM PCF group refractive index is slightly more complicated: the BBO crystal used for sum-frequency generation is azimuthally rotated by 45° so that we could observe sum-frequency for both polarization modes simultaneously. Then $\Delta L^{(2)}$ values were measured: $\Delta L^{(2)}(fast)$=105.324 mm and $\Delta L^{(2)}(slow)$=105.63 mm. Corresponding group refractive indices at 1030 nm wavelength: $n_{gf}(fast)$ =**1.6123±0.0048** and $n_{gf}(slow)$=**1.6146±0.0048**. The difference between group refractive indices of orthogonal polarization modes is 0.0023 which is in very good agreement with value extracted from XFROG trace (0.002).

An important detail is that group refractive index of PCF mode is specified for the central wavelength of femtosecond pulses we used in the experiment. This is due to the fact that the measured $\Delta L^{(2)}$ value corresponds to highest sum-frequency radiation intensity which is the case when central parts of both temporally matched pulses interact. By definition, central wavelength corresponds to central part of pulse.

Group refractive index measurement for other wavelengths using our setup requires tunable wavelength laser source such as optical parametric generator. Alternatively, we can use data of group refractive index difference with respect to n_g of 1030 nm wavelength obtained in previous chapter (Fig.2.8 (b) and Fig2.15 right). Calculated group refractive index dispersion of fundamental mode for both investigated PCFs is depicted in Fig.3.2.
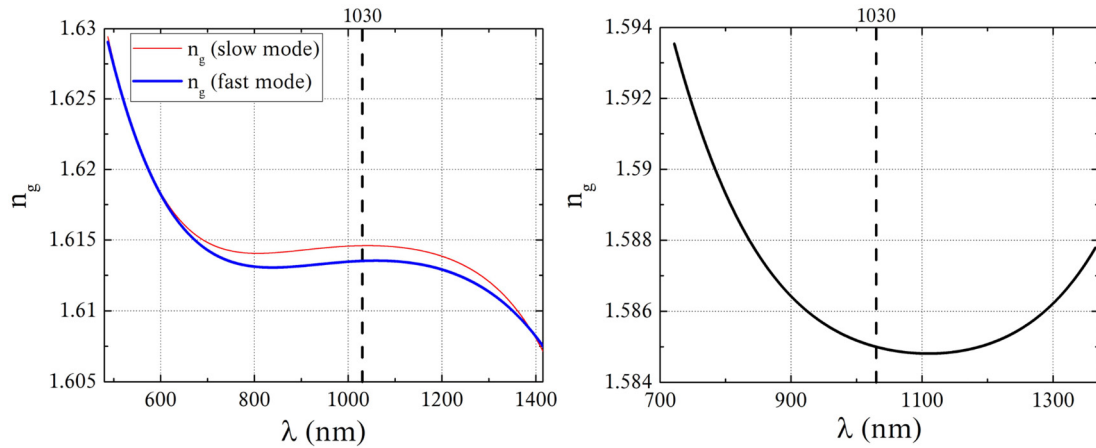
Figure 3.2: Calculated group refractive index dispersion of investigated PCFs: left – n_g of both polarization modes of the PM PCF; right – n_g of the non-birefringent PCF.

3.2 Measurement of phase refractive index of photonic crystal fiber mode

3.2.1 Experimental setup

Now we will discuss phase refractive index measurement. In case of photonic crystal fibers simultaneous measurement of mode phase refractive index (which for solid-core PCFs is actually effective refractive index) is a very complicated task. The main problem is that light needs to be well coupled into the PCF for the mode to be actually formed otherwise we would measure effective refractive index of something that is even not well defined due to the light from the cladding of the PCF. One problem resulting from this limitation is the need of coupling optics which refractive index must be taken into account. Classical interferometric setups used to measure refractive indices, such as Michelson interferometer, cannot be employed because in case of PCF mode phase refractive index measurement we cannot continuously change PCF length which is necessary to change optical path difference between interferometer arms.

The idea for measuring phase refractive index of PCF mode is as fol-

lows. We propose to use Mach-Zehnder interferometer (MZI), Fabry-Perot (FP) etalon, continuous wave (CW) laser and simultaneously observe the phase shift of interfering adjacent longitudinal modes of CW laser in MZI corresponding to shift from constructive to destructive interference. Experimental setup for measurement is depicted in Fig.3.3. The laser source
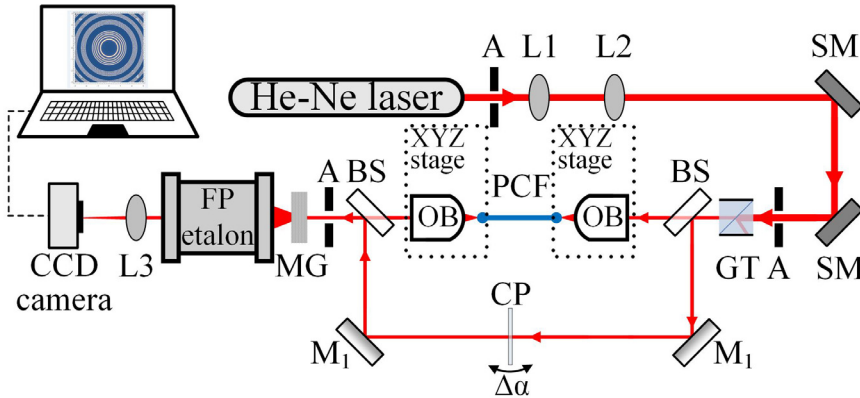

Figure 3.3: Experimental setup for phase refractive index of PCF measurement: A – iris diaphragm, L1, L2 – lenses, SM – silver coater mirror, GT – Glan-Taylor polarizer, BS – non-polarizing beamsplitter, M$_1$ – broadband dielectric mirror highly reflective (>99%) at 450 nm – 700 nm spectral range, OB – 40× microscope objective, PCF – photonic crystal fiber, MG – matted glass plate, FP etalon – Fabry-Perot etalon, L3 – f=500 mm imaging lens.

used was a CW red (λ=632.816 nm) He-Ne laser (*HNL100R-EC, Thorlabs*) which had 10 mW average output power. He-Ne laser cavity length was 485.39 mm (specified by the manufacturer) which corresponded to longitudinal mode spacing of 320 MHz (0.427 pm). For a given CW laser source an appropriate Fabry-Perot etalon should be used to resolve adjacent longitudinal laser modes and its free spectral range (FSR) needs to be larger than laser intermodal distance. FSR is a range of wavelengths which can be measured without overlap of higher order interference mode, it can be defined as:

$$\lambda_{\text{FSR}} = \frac{\lambda^2}{2b}, \tag{3.9}$$

where b is the base of Fabry-Perot etalon.

Laser radiation was guided to a Mach-Zehnder interferometer. In one arm of MZI we placed the investigated PCF with coupling optics and in the other arm – a compensator glass plate.

Phase refractive index was measured for the same PCFs that we used for GVD and group refractive index measurement. Since phase refractive index of PM PCF is slightly different for orthogonal polarization modes, we need to use polarized light. To polarize radiation coming from He-Ne laser, we used a Glan-Taylor polarizer which was placed before Mach-Zehnder interferometer. Polarization direction of laser radiation was matched with one of PCF principle axes of polarization in the following way. We temporarily placed a second crossed Glan-Taylor polarizer after the PCF and then rotated both Glan-Taylor polarizers (keeping them crossed) and observed light intensity after the crossed polarizer: when laser light polarization matches one of PCF principle axes of polarization, no light is visible after the crossed polarizer. After this was done, orthogonal polarization direction for the second experiment was set by simply rotating Glan-Taylor polarizer perpendicularly. In case of non-birefringent PCF there is no need to use polarizers.

To distinguish interference of different longitudinal modes of He-Ne laser, light coming out of Mach-Zehnder interferometer was directed to Fabry-Perot etalon (interferometer). The base of Fabry-Perot interferometer was chosen relatively long (40 mm) to achieve sufficient free spectral range (5 pm) and good resolvable power ($1.28 \cdot 10^6$). A matted glass plate was placed in front of Fabry-Perot etalon to scatter light which in turn provided relatively homogeneous light distribution. The interference rings coming from Fabry-Perot interferometer were imaged with a 500 mm focal length lens onto CCD camera. A compensating glass plate was made of fused silica (n_{cp}=1.457 for He-Ne laser wavelength) and was 2 mm thick. It was mounted on a high precision rotation stage which served as means for fine thickness adjustment. When it is initially set to be perpendicular to incident beam propagation direction, difference of beam traveling path through compensating glass plate (ΔL_{cp}) can be calculated as:

$$\Delta L_{\text{cp}} = \frac{d}{\cos\left[\arcsin\left(\frac{\sin(\Delta\alpha)}{n_{\text{cp}}}\right)\right]} - d, \qquad (3.10)$$

where d is thickness of compensator plate and $\Delta\alpha$ is change of compensating plate rotation angle. The uncertainty of ΔL_{cp} at 95% confidence level can be defined as:

$$\delta(\Delta L_{\text{cp}}) = 2\sqrt{\left(\delta(d)\frac{\partial L_{\text{cp}}}{\partial d}\right)^2 + \left(\delta(\Delta\alpha)\frac{\partial L_{\text{cp}}}{\partial \Delta\alpha}\right)^2}, \tag{3.11}$$

where $\delta(d)$ is uncertainty of compensating glass plate thickness measurement and $\delta(\Delta\alpha)$ is uncertainty of its rotation angle.

3.2.2 Principle, results and discussion

Due to presence of several longitudinal modes in He-Ne laser radiation, interference rings observed after Fabry-Perot interferometer have fine structure: each sub-ring corresponds to different longitudinal mode. Thus, distinct sub-rings have different interference conditions. The phase increment for two adjacent longitudinal modes (λ_1 and λ_2) in the first arm of MZI with respect to reference arm can be written as:

$$\varphi_1 = \left[(n_{\text{ob}} - 1)L_{\text{ob}} + (n_{\text{PCF}}-)L_{\text{PCF}} + (n_{\text{cp}} - 1)L_{\text{cp1}}\right]\frac{2\pi}{\lambda_1}, \tag{3.12}$$

$$\varphi_2 = \left[(n_{\text{ob}} - 1)L_{\text{ob}} + (n_{\text{PCF}}-)L_{\text{PCF}} + (n_{\text{cp}} - 1)L_{\text{cp2}}\right]\frac{2\pi}{\lambda_2}, \tag{3.13}$$

where n_{ob} is phase refractive index of microscope objective, n_{PCF} – phase refractive index of PCF mode, n_{cp} – phase refractive index of compensating plate, L_{ob}, L_{PCF} – length of microscope objective and photonic crystal fiber respectively, L_{cp1}, L_{cp2} – length of beam traveling path through the compensating glass plate. By adjusting beam traveling path through the compensating glass plate one may obtain the situation when one of the interference rings corresponding to particular wavelength λ_1 disappears, so $\varphi(\lambda_1, L_{cp1}) = \pi + 2\pi m$. Meanwhile the adjacent interference rings corresponding to wavelengths $\lambda_2 = \lambda_1 \pm \Delta\lambda$ in general remain clearly visible as $\varphi(\lambda_2, L_{\text{cp1}}) \neq \varphi(\lambda_1, L_{\text{cp1}})$. Here $\Delta\lambda = \frac{\lambda^2 \Delta\nu}{c}$, $\Delta\nu = c/(2L_{\text{laser}})$ is the CW laser resonator mode spacing. In a similar manner by adjusting beam traveling path through the compensating glass plate further one may extinguish

interference ring of the λ_2 wavelength, so $\varphi(\lambda_2, L_{cp2}) = \pi + 2\pi m$. It is important to realize that integer number m in these situations (interference order) remains unchanged as long as $\varphi(\lambda_2, L_{cp}) - \varphi(\lambda_1, L_{cp}) < 2\pi$ or

$$\frac{\Delta\lambda}{\lambda^2}[(n_{PCF} - 1)L_{PCF} + (n_{ob} - 1)L_{ob} - (n_{cp} - 1)L_{cp}] < 1. \tag{3.14}$$

By taking into account that $\Delta\lambda/\lambda_{1,2} \leqslant 1$ ($\sim 10^{-6}$), we may safely ignore dispersion of all optical elements as long as we consider only laser modes. In this way we obtain

$$\varphi_1(\lambda_1, L_{cp1}) = \pi + 2\pi m, \tag{3.15}$$

$$\varphi_2(\lambda_2, L_{cp2}) = \pi + 2\pi m, \tag{3.16}$$

By subtracting Eq.3.16 from Eq.3.15 we get:

$$[(n_{ob} - 1)L_{ob} + (n_{PCF}-)L_{PCF}]\frac{\lambda_2 - \lambda_1}{\lambda_2\lambda_1} + (n_{cp} - 1)\left(\frac{L_{cp1}}{\lambda_1} - \frac{L_{cp2}}{\lambda_2}\right) = 0. \tag{3.17}$$

Due to the aforementioned extremely small longitudinal mode difference ($\lambda_2 - \lambda_1 = \Delta\lambda = 0.427$ pm), we can also assume that $\lambda_1 \approx \lambda_2 = \lambda = 632.816$ nm, thus $\frac{\lambda_2 - \lambda_1}{\lambda_2\lambda_1} \approx \frac{\Delta\lambda}{\lambda^2}$. In addition, we can substitute $L_{cp2} = L_{cp1} + \Delta L_{cp} \rightarrow$ $\left(\frac{L_{cp1}}{\lambda_1} - \frac{L_{cp2}}{\lambda_2}\right) = L_{cp}\frac{\Delta\lambda}{\lambda^2} + \frac{\Delta L_{cp}}{\lambda}$ which leads to the following expression:

$$[(n_{ob} - 1)L_{ob} + (n_{PCF} - 1)L_{PCF}]\frac{\Delta\lambda}{\lambda^2} = -(n_{cp} - 1)\left[L_{cp}\frac{\Delta\lambda}{\lambda^2} + \frac{\Delta L_{cp}}{\lambda}\right]. \tag{3.18}$$

If the term $(n_{ob} - 1)L_{ob}$ is not known in advance, there are a couple options to eliminate it. First of all, we may try to monitor all interference rings of Fabry-Perot etalon corresponding to different laser wavelengths to obtain a set of equations $\varphi(\lambda_l, L_{cpl}) = \pi + 2\pi m, l = 1, \ldots, N$. When the number of rings $N \geqslant 3$, then we can determine n_{PCF}. However, this method requires FP etalon with high spectral resolving power and ultra-high precision phase tuning device. Alternatively, we can repeat measurements by monitoring only adjacent interference rings but using different length

(L_{PCF2}) fiber. We can then write the following system of equations:

$$\begin{cases} [(n_{\text{ob}} - 1)L_{\text{ob}} + (n_{\text{PCF}} - 1)L_{\text{PCF1}}] \frac{\Delta\lambda}{\lambda} = -(n_{\text{cp}} - 1) \left[L_{\text{cp}} \frac{\Delta\lambda}{\lambda} + \Delta L_{\text{cp1}} \right], \\ [(n_{\text{ob}} - 1)L_{\text{ob}} + (n_{\text{PCF}} - 1)L_{\text{PCF2}}] \frac{\Delta\lambda}{\lambda} = -(n_{\text{cp}} - 1) \left[L_{\text{cp}} \frac{\Delta\lambda}{\lambda} + \Delta L_{\text{cp2}} \right], \end{cases} \quad (3.19)$$

where ΔL_{cp1} and ΔL_{cp2} are differences of beam traveling path through compensating glass plate for respective PCF lengths. By subtracting lower equation from the upper we arrive to the expression of phase refractive index of PCF mode:

$$n_{\text{PCF}} = 1 + \frac{(n_{\text{cp}} - 1)(\Delta L_{\text{cp2}} - \Delta L_{\text{cp1}})}{L_{\text{PCF1}} - L_{\text{PCF2}}} \frac{\lambda}{\Delta\lambda}. \quad (3.20)$$

The uncertainty of phase refractive index measurement at 95% confidence level can be defined as:

$$\delta(n_{\text{PCF}}) = 2 \left(\left(\delta(\Delta L_{\text{cp1}}) \frac{\partial n_{\text{PCF}}}{\partial \Delta L_{\text{cp1}}} \right)^2 + \left(\delta(\Delta L_{\text{cp2}}) \frac{\partial n_{\text{PCF}}}{\partial \Delta L_{\text{cp2}}} \right)^2 + \right.$$
$$\left. + \left(\delta(\Delta\lambda) \frac{\partial n_{\text{PCF}}}{\partial \Delta\lambda} \right)^2 + \left(\delta(L_{\text{PCF1}}) \frac{\partial n_{\text{PCF}}}{\partial L_{\text{PCF1}}} \right)^2 + \left(\delta(L_{\text{PCF2}}) \frac{\partial n_{\text{PCF}}}{\partial L_{\text{PCF2}}} \right)^2 \right)^{\frac{1}{2}}. \quad (3.21)$$

Here $\delta(\Delta L_{\text{cp1}})$ and $\delta(\Delta L_{\text{cp2}})$ are uncertainties of ΔL_{cp} measurement for respective PCF lengths, $\delta(\Delta\lambda)$ – uncertainty of intermodal distance between longitudinal modes which, as specified by the manufacturer, is $2 \cdot 10^{-17}$ m and $\delta(\Delta L_{\text{PCF1}})$, $\delta(\Delta L_{\text{PCF2}})$ are uncertainties of ΔL_{PCF} measurement.

As already mentioned, in case of PM PCF separate ΔL_{cp} measurements have to be performed for each orthogonal light polarization direction to obtain phase refractive index values for slow and fast polarization modes.

Example of recorded interference rings (their partial images) corresponding to phase shift between constructive and destructive interference of adjacent longitudinal laser modes is depicted in Fig.3.4 (a, b). From experimental images we can clearly see changes in interference rings corresponding to adjacent longitudinal laser modes intensity. Experimental observations are in very good agreement compared to numerically simulated simplified (it includes only three strongest intensity longitudinal
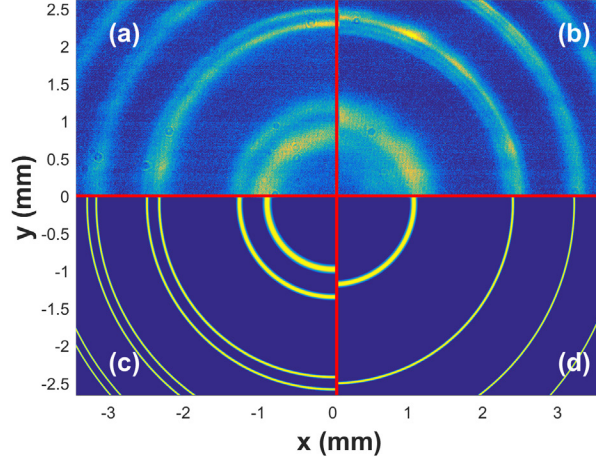
Figure 3.4: Example of experimentally recorded interference images and corresponding numerical simulation results: (a) and (b) – recorded interference ring partial images corresponding to phase shift between constructive and destructive interference of adjacent longitudinal laser modes; (c) and (d) – numerically simulated simplified partial view of interference rings for the corresponding phase shift of the same adjacent longitudinal laser modes.

modes to make interpretation simpler) partial view of interference rings shown in aggregated view in Fig.3.4 (c, d). The main difference between experiment and numerical simulations is notably lower contrast of experimental images, which is due to slightly inhomogeneous distribution of light coming into Fabry-Perot etalon and stray light.

We performed measurements with 14.5 cm and 37.1 cm long polarization-maintaining PCFs and also with 12.1 cm and 44.8 cm long non-birefringent PCFs. Estimated phase refractive index for PM PCF polarization modes are: $n_{\text{PCF}}(fast)$=**1.4393**±**0.0007** and $n_{\text{PCF}}(slow)$=**1.4376**±**0.0007**. For non-birefringent PCF the estimated phase refractive index of fundamental mode is n_{PCF}=**1.4244**±**0.0007**. It is worth to note that for group refractive indices the inequality is opposite, i.e. $n_{\text{g}}(slow) > n_{\text{g}}(fast)$.

We also performed numerical simulations of PCF fundamental mode phase refractive index. To numerically estimate phase refractive index we employ full-vector model and numerically solve the following equation for electric field $\vec{E}_t = (E_x, E_y)$ and mode refractive indices $n_m = \sqrt{\varepsilon_m}$:

$$\Delta_t \vec{E}_t + k^2 \varepsilon \, \vec{E}_t + \vec{\nabla}_t(\vec{\nabla}_t ln(\varepsilon) \cdot \vec{E}_t) = k^2 \varepsilon_m \vec{E}_t, \tag{3.22}$$

112

where $\varepsilon = \varepsilon(x, y)$ is the dielectric permittivity of the PCF and $k = 2\pi/\lambda$ is wavenumber. Numerically simulated phase refractive index values are: n_{fast}=1.4397 and n_{slow}=1.4396 for PM PCF and n=1.44 for non-birefringent PCF at 632.8 nm. Numerically simulated phase refractive index values are in good agreement with experimentally measured ones.

If a suitable CW tunable wavelength laser source is used, the demonstrated principles can be used to measure PCF mode phase refractive index for various wavelengths (limited by laser source wavelength tunability) – phase refractive index of PCF mode dispersion can be estimated. On the other hand, with reference to Eq.3.1, we can use GVD data from our previous measurements (chapter 2) and measured group refractive index data to estimate phase refractive index of PCF mode dispersion. Results are depicted in Fig.3.5. It is essential to note that displayed results were calculated from experimentally obtained data. The results show that in
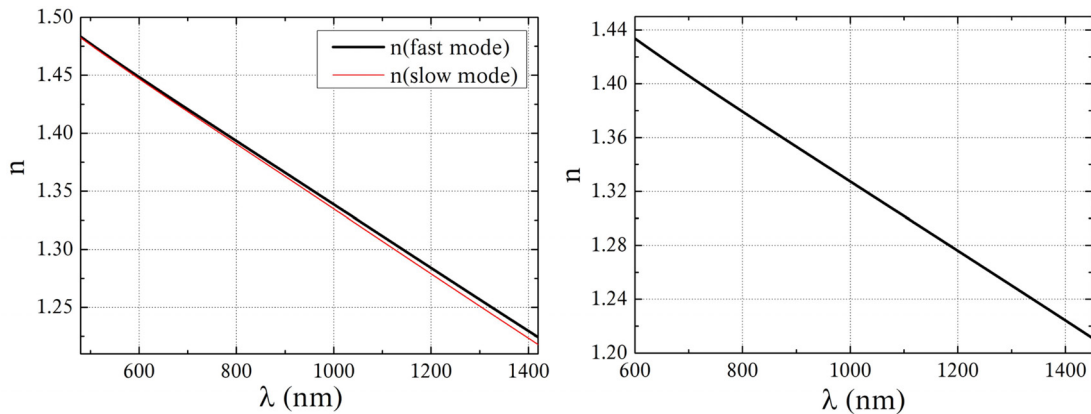

Figure 3.5: Calculated phase refractive index dispersion of investigated PCFs: left – for PM PCF; right – for non-birefringent PCF.

both PCFs phase refractive index decreases with wavelength. This is due to the fact mode field diameter in both PCFs increases with wavelength and exceeds the core diameter which means for longer wavelengths air microstructures surrounding the core have greater influence to the fiber's waveguiding properties, hence, the phase refractive index (which, as mentioned, for solid-core PCFs is actually effective refractive index [77]) decreases.

3.3 Conclusions

In conclusion, we have demonstrated, to the best of our knowledge, the first experimental technique for measuring phase refractive index of photonic crystal fiber mode. It is based on observing phase shift of interfering adjacent longitudinal modes of CW laser and measuring the change of compensating plate rotation angle ($\Delta\alpha$) which had to be applied to observe a single shift from constructive to destructive interference.

We discussed that for correct measurement, phase shift within the same interference order needs to be observed – condition defined by Eq.3.14 must be satisfied. We showed that with sufficiently fine control of beam path length through compensating glass plate in case of PM PCF this technique can distinguish phase refractive indices of orthogonal polarization modes. In principle, the presented technique can be applied to measure refractive index of any optical element.

We also experimentally measured group refractive index of fundamental mode for the investigated PCFs and, using GVD measurement data from previous chapter, calculated group refractive index dispersion (Fig.3.2).

Finally, using GVD measurement data and measured group refractive index data, we calculated phase refractive index dispersion of PCF mode (Fig.3.5). Such approach which uses only experimental data is a good alternative to experimental phase refractive index dispersion measurement (employing the presented technique) with a tunable wavelength laser source.

Straightforward experimental implementation and relatively high accuracy make the demonstrated technique a promising alternative to theoretical PCF mode phase refractive index estimation.

Chapter 4

Investigation of supercontinuum generation in polarization-maintaining photonic crystal fiber in case of chirped femtosecond pulses

Material related to this chapter is published in A3 and AP2, presented in C3 and C6.

As discussed in literature review chapter of this thesis, supercontinuum generation strongly depends on both photonic crystal fiber and pump pulse parameters. Although a lot of research about the influence of various pump pulse parameters on supercontinuum characteristics has been done [21], the use of chirped femtosecond pulses as a pump for supercontinuum generation has been investigated in just a few papers and almost all research is theoretical [39–48]. Since the amount and sign of chirp applied to pump pulses can be controlled by using certain optical elements (such as a pair of diffraction gratings or dispersive prisms), this can be used to achieve control of supercontinuum spectrum in real time which can be advantageous in certain applications.

In this chapter we present investigation of supercontinuum generation in highly nonlinear polarization-maintaining photonic crystal fiber with two ZDWs using chirped femtosecond pulses. For analysis we employ numerical simulation model and XFROG technique: the temporal characteristic of supercontinuum pulse provided by XFROG analysis gives much more insight than can be gained by observing only changes in supercontinuum spectrum. Firstly, we briefly describe our numerical simulation model that we used during investigation. Secondly, we discuss important features of XFROG analysis and discuss physics of supercontinuum generation in our polarization maintaining PCF with two ZDWs when pump pulses are bandwidth-limited. The outlined principles of supercontinuum formation are a good reference point during subsequent analysis. Finally, experimental setup and results of supercontinuum gen-

eration investigation in case of chirped pump pulses are presented and discussed.

4.1 Numerical simulation model

For numerical simulation we assume, as the most popular approach, that only fundamental orthogonal polarization PCF modes interact with each other. The measured GVD data of our PCF is used for numerical simulations. In such case the generation of supercontinuum in polarization maintaining PCF is simulated by the set of generalized nonlinear Schrödinger equations for "slow" and "fast" fundamental modes only. Where it is appropriate, we use subscripts S and F for "slow" and "fast" modes correspondingly. The equations of nonlinear interaction take the following form:

$$\frac{\partial S_S}{\partial z} = -i(\beta_S - \hat{\beta}_0)S_S - i\gamma_S \int_{-\infty}^{\infty} dt' e^{-i\Omega t'} A_S(t') I_e(t') \,, \qquad (4.1)$$

$$\frac{\partial S_F}{\partial z} = -i(\beta_F - \hat{\beta}_0)S_F - i\gamma_F \int_{-\infty}^{\infty} dt' e^{-i\Omega t'} A_F(t') I_e(t') \,, \qquad (4.2)$$

where A_j is the electric field strength amplitude, S_j – spectral amplitude related to A_j by the Fourier transform, β_j – wavenumber and γ_j is the coefficient of nonlinear interaction of the mode j defined as:

$$\gamma_j = \frac{\chi^{(3)}\beta_j}{2n_j^2} \,, \quad \text{j=S,F} \,. \qquad (4.3)$$

Modes are coupled through the effective intensity:

$$I_{\text{eff}}(t) = (1 - f_R)I(t) + f_R \int_0^{\infty} g_R(\tau)I(t - \tau)d\tau \,, \qquad (4.4)$$

$$I(t) = |A_S(t)|^2 + |A_F(t)|^2 \,. \qquad (4.5)$$

The reference wavenumber $\hat{\beta}_0$ in principle can be associated either with slow or fast mode, but in our case it is slightly more convenient to define

it as follows:

$$\hat{\beta}_0 = \frac{1}{2}\left(\beta_S(\omega_0) + \beta_F(\omega_0)\right) + \frac{1}{2}\left(\left(\frac{d\beta_S}{d\omega}\right)_{\omega_0} + \left(\frac{d\beta_F}{d\omega}\right)_{\omega_0}\right)\Omega\,, \quad \Omega = \omega - \omega_0\,. \quad (4.6)$$

GNLSE takes into account Kerr nonlinearity and stimulated Raman scattering which is described by the response function which we define as:

$$g_R(\tau) = \frac{\tau_1^2 + \tau_2^2}{\tau_1^2 \tau_2^2}\sin(t/\tau_1)e^{-t/\tau_2}\,, \quad (4.7)$$

where we use typical values $f_R = 0.18$, $\tau_1 = 12.2$ fs, $\tau_2 = 32$ fs [21]. In this numerical simulation model chirp of pump pulse is accounted for through initial conditions when amplitude of the pulse is defined:

$$A_j(t) = A_0 \exp\left[-\frac{t^2}{t_0^2}(1 + i\Gamma)\right]\,, \quad \text{j=S,F}. \quad (4.8)$$

here Γ is the chirp parameter. Γ=0 corresponds to the case of bandwidth-limited pulse.

4.2 Supercontinuum generation in case of bandwidth-limited femtosecond pump pulses

In chapter 2 we demonstrated that XFROG trace of supercontinuum generated in photonic crystal fiber can yield lots of additional information about the fiber itself. In this section we perform analysis of supercontinuum XFROG traces generated in PM PCF to obtain temporal characteristic and use it to describe physics of supercontinuum generation in our PM PCF with two ZDWs.

4.2.1 Reference pulse FROG analysis

XFROG analysis requires a well-known reference pulse electric field information. As noted in chapter 2, the reference pulse was a higher

energy copy of the same pulse used for supercontinuum generation. Reference pulse electric field information was obtained by performing FROG measurement of pump pulses. Experimental setup for this measurement is very similar to XFROG measurement (Fig.2.2) only there is no PCF, coupling optics (microscope objectives) and a different BBO crystal is used (3 mm thick BBO crystal cut at θ=22.5° and ϕ=90° for type I phase matching). For FROG analysis we used "FROG" software (version 3.2.4, *Femtosoft*). Main results of reference pulse FROG analysis are shown in Fig.4.1 and Fig.4.2.
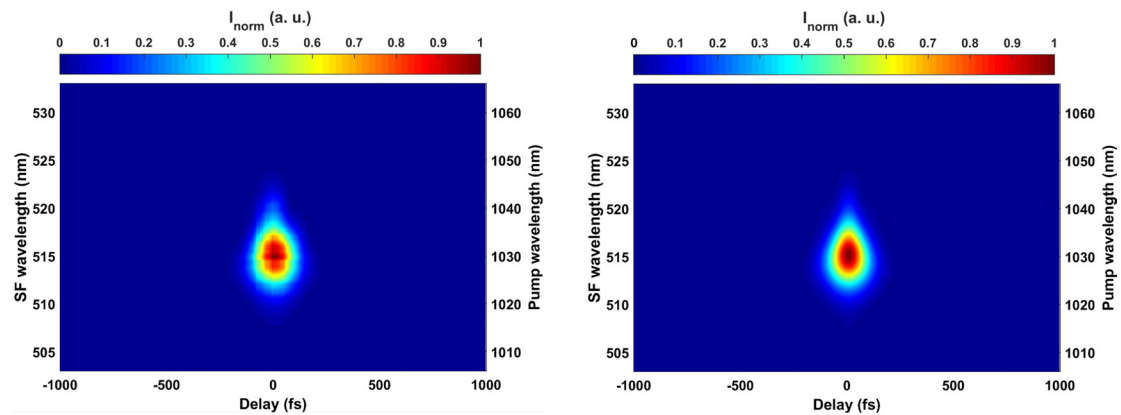
Figure 4.1: Measured (left) and retrieved (right) FROG traces of reference pulse. Left axis in each picture depicts measured sum-frequency wavelengths, right axis – calculated corresponding reference pulse wavelength.
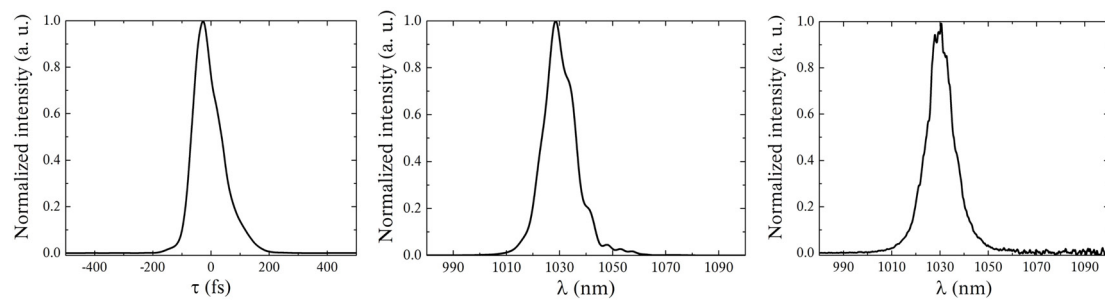

Figure 4.2: Retrieved electric field intensity as a function of time (left) and wavelength (middle); right – independently measured spectrum of the reference pulse.

We can clearly see that measured and retrieved FROG traces are in excellent agreement. Pulse duration (at FWHM) estimated from FROG

analysis is 110.12 fs essentially matches pump pulse duration (110 fs at FWHM) measured with a commercial scanning autocorrelator (*Geco, Light Conversion Ltd.*). The same can be said comparing retrieved spectrum with independently measured reference pulse spectrum (Fig.4.2 right), therefore we can claim in confidence that reference pulse FROG analysis data are reliable.

4.2.2 Additional considerations regarding supercontinuum XFROG analysis

Before going into XFROG analysis of supercontinuum generated in PCF in case of bandwidth-limited pump pulses there are several issues regarding XFROG traces that need to be resolved in order to obtain reliable results.

Firstly, GDD of microscope objective used to focus pump beam into PCF (Fig.2.2) has to be determined and compensated since it also adds some positive chirp to pump pulse. GDD of other optical components that pump pulse passes is assumed to be negligible compared to that of microscope objective. We estimated GDD of microscope objective performing a simple experiment which setup is depicted in Fig.4.3.
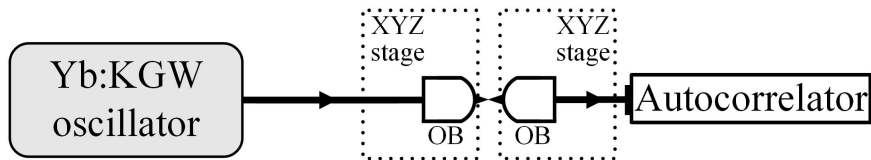

Figure 4.3: Experimental setup for determining pulse chirp gained when passing microscope objective.

We measured duration of pulses used to as pump in supercontinuum generation when they passed two identical microscope objectives which were used for light coupling/decoupling into PCF. Results indicated that 110 fs duration (at FWHM) pulses were stretched to 120 fs after passing both microscope objectives. Using pulse dispersive spreading

formula

$$\tau = \tau_0 \sqrt{1 + \left(\frac{L_{\mathrm{ob}}}{L_{\mathrm{obD}}}\right)^2},$$ (4.9)

where τ_0 is initial pulse duration, L_{ob} is the length of microscope objective glass and L_{obD} is the dispersive length for microscope objective glass defined as:

$$L_{\mathrm{obD}} = \frac{\tau_0^2}{4 \ln 2 \, |GVD|},$$ (4.10)

we calculated that after passing only one microscope objective the pulse stretches to 112.6 fs. This corresponds to $\approx$954 fs^2 chirp added by the microscope objective.

The extra GDD added by microscope objective was compensated using a pair of SF11 glass dispersive prisms which were placed before the focusing microscope objective (in setup depicted in Fig.2.2). The prisms were set to Brewster angle of incidence for pump wavelength (λ_{p} =1030 nm) to minimize reflection losses: maximum available pump pulse energy when using dispersive prism pair was 8.61 nJ. The beam was directed to pass the prisms twice to compensate for spatial chirp which occurs after passing through the prism pair. Amount of GDD after double pass through a pair of dispersive prisms depends on the prism material dispersion component (positive) and the angular dispersion component (negative) [298] and can be defined as:

$$GDD = GDD_{\mathrm{m}} + GDD_{\mathrm{a}} = \frac{\lambda^3 L}{2\pi c^2} \frac{d^2 n}{d\lambda^2} - \frac{4 l_{\mathrm{p}} \lambda^3}{\pi c^2} \left(\frac{dn}{d\lambda}\right)^2,$$ (4.11)

where L is overall optical beam path length in the prisms, l_{p} is the distance between the prisms and n is the refractive index of prism glass. In our case GDD compensating values of L and l_{p} were 11.46 mm and 160.6 mm respectively.

Second issue is related to large spectral extent supercontinuum XFROG trace and its complexity. Maximum grid size (the field of delay and frequency values that satisfy the Fourier transform relationship) of "FROG" software (version 3.2.4, *Femtosoft*) was too small for supercon-

tinuum XFROG trace which resulted in truncation of the trace during analysis. Therefore, a new XFROG analysis program (as *Matlab* code) using iterative Fourier transform algorithm with generalized projections was written which uses dynamic frequency sampling intervals allowing to avoid trace truncation.

Finally, apart from applying spectrometer sensitivity correction functions, intensities of measured XFROG traces have to be additionally corrected accounting for the different phase-matching efficiency of sum-frequency generation for distinct spectral components of supercontinuum [287, 289]. We have performed such intensity correction accounting for different phase matching efficiency due to phase mismatch: our current geometry yielded perfect phase matching for 790 nm wavelength, so correction was made with respect to this wavelength. Accuracy of the correction was checked by comparing independently measured and retrieved from XFROG analysis supercontinuum spectra (Fig.4.4). We can clearly
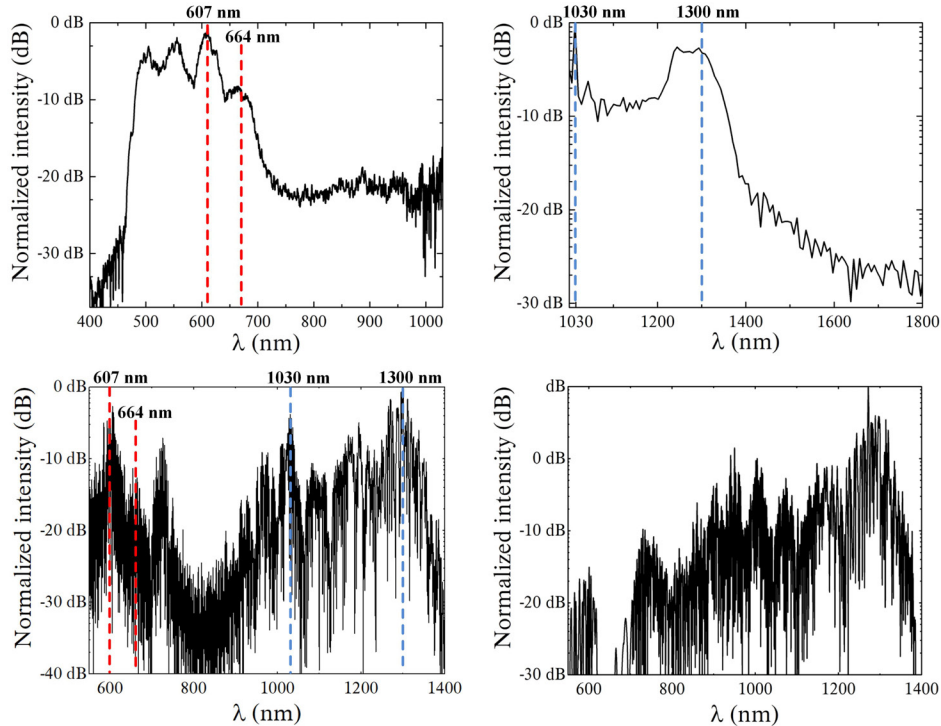

Figure 4.4: Top row: independently measured supercontinuum spectra. Bottom left: retrieved supercontinuum spectrum when phase matching efficiency correction was applied to XFROG trace; bottom right: retrieved supercontinuum spectrum when correction was not applied. Dashed red and blue lines mark characteristic features of spectra to alleviate comparison.

see that applying phase matching efficiency correction yields reasonable qualitative agreement between independently measured and retrieved supercontinuum spectra. It is considerably better than in case when phase matching efficiency correction was not applied. The accuracy of correction is limited since we used plane wave approximation sum-frequency efficiency formula and in ideal case correction would also have to account for second order nonlinear optical susceptibility dispersion. More importantly, the comparison is delicate as independent spectrum measurement had to be performed with two different spectrometers which had distinct dynamic ranges and the retrieved supercontinuum spectrum actually depicts single-shot spectrum while independently measured spectra depict averaged over 76000 shots (1 ms integration time of the spectrometer) spectrum. This might be one of the reasons why retrieved supercontinuum spectrum exhibits fine structure which is not visible in independently measured spectra [264, 289, 292].

4.2.3 Results and discussion

After resolving issues outlined in the previous subsection we can now move to results and their discussion. Fig.4.5 shows XFROG analysis results of supercontinuum generated in PCF in case of bandwidth-limited maximum energy (8.61 nJ) pump pulses. Zero delay point in XFROG trace and retrieved temporal intensity was chosen at the point of maximum intensity of 515 nm wavelength, but the actual point of zero delay is not important for the analysis because only relative positions of temporal components matter. We can highlight several features of the depicted results:

- The measured and retrieved XFROG traces are in very good agreement which is an indication of convergence of the retrieved electric field. Yet, the retrieved XFROG trace has a pattern of small slightly varying size dots. This has been observed in other reports as well [289, 294]. We believe that this is an artefact from XFROG algorithm which appears during Fourier transform of extremely broad spectral
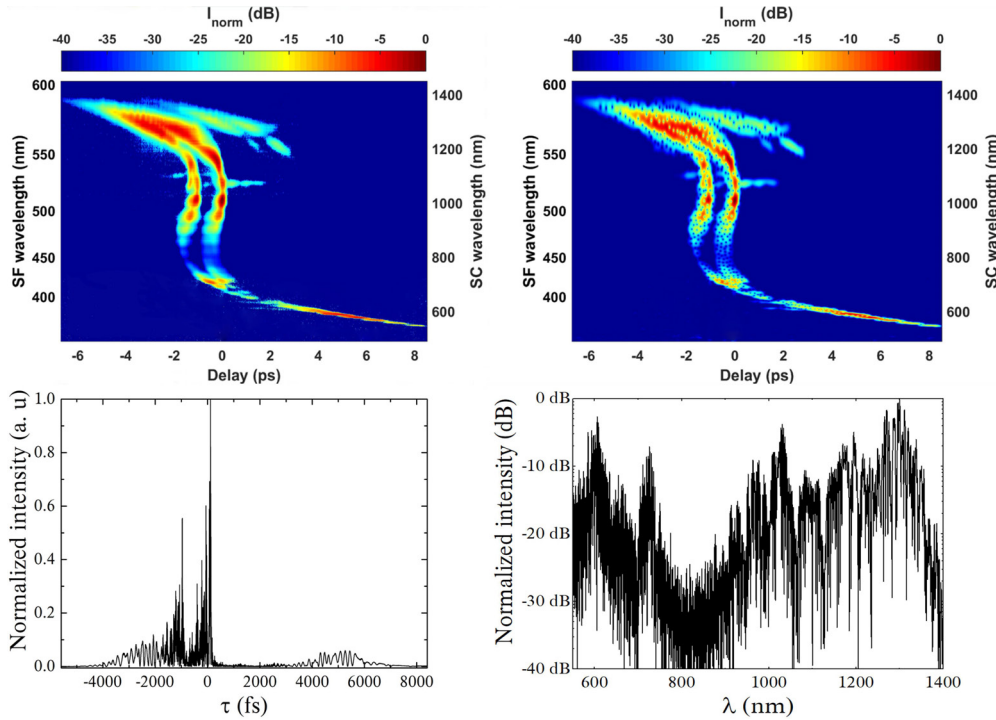
Figure 4.5: XFROG analysis results in case of maximum energy pump pulses: measured (top left) and retrieved (top right) XFROG traces; retrieved temporal (bottom left) and spectral intensity (bottom right). Left axis in top figures depicts measured sum-frequency wavelengths, right axis – calculated corresponding supercontinuum wavelengths.

bandwidth of the analyzed trace. This would explain why such effect is not visible in reference pulse FROG trace.

- Retrieved supercontinuum spectrum has roughly the same shape as the independently measured one (see Fig.4.4 top), but exhibits fine-scale structure. One possible explanation of this is that the retrieved supercontinuum spectrum depicts is single-shot while the independently measured spectra are actually averaged over 76000 shots. Slight variations of supercontinuum pulse from shot to shot may wash out fine structure in the averaged spectrum as suggested in [289]. Another possible reason may be the aforementioned XFROG algorithm artefact due to Fourier transform of ultrabroadband spectrum.

- We can clearly see that orthogonal polarization modes produce slightly different supercontinuum spectrum. Although XFROG ana-

lysis algorithm retrieves aggregated spectrum, it is directly visible in the XFROG trace.

- Temporal structure of supercontinuum has two relatively narrow high amplitude features which have fine-scale structure and many lower amplitude broader features. With reference to chapter 1 of this thesis we can claim that two sharp peaks correspond to orthogonal polarization solitons and low amplitude features are dispersive waves. Most importantly, we can see from XFROG trace that dispersive waves correspond to short-wavelength and long-wavelength spectrum components. This is directly related to GVD of the PCF (Fig2.12).

Additional information about supercontinuum is provided by numerical simulation results. The first and the most interesting result, which concurs which XFROG measurement results, is that orthogonal polarization modes produce slightly different supercontinua (Fig.4.6(b)), which is the consequence of different PCF GVD for the orthogonal modes. It is also obvious that the calculated aggregated spectrum is somewhat different from experimental ones (Fig.4.6(a)). It is possible in principle to match characteristic peaks observed experimentally (denoted with numbers 1-5) with corresponding peaks either of slow or fast mode. Indeed, the peaks 3-5 can be associated with both orthogonal polarization modes while peaks 1 and 2 should be attributed to the fast mode only. The ≈ 100 nm difference in the long-wavelength wing of the SC spectrum seen comparing Fig.4.6(a) and (b) is due to the fact that our numerical simulation model does not accurately account losses in the PCF. Therefore, theoretical SC spectrum is wider compared to experimental one even though lower pump pulse energies were used in simulation. Unfortunately, we could not reliably estimate the spectral distribution of losses in our PCF.
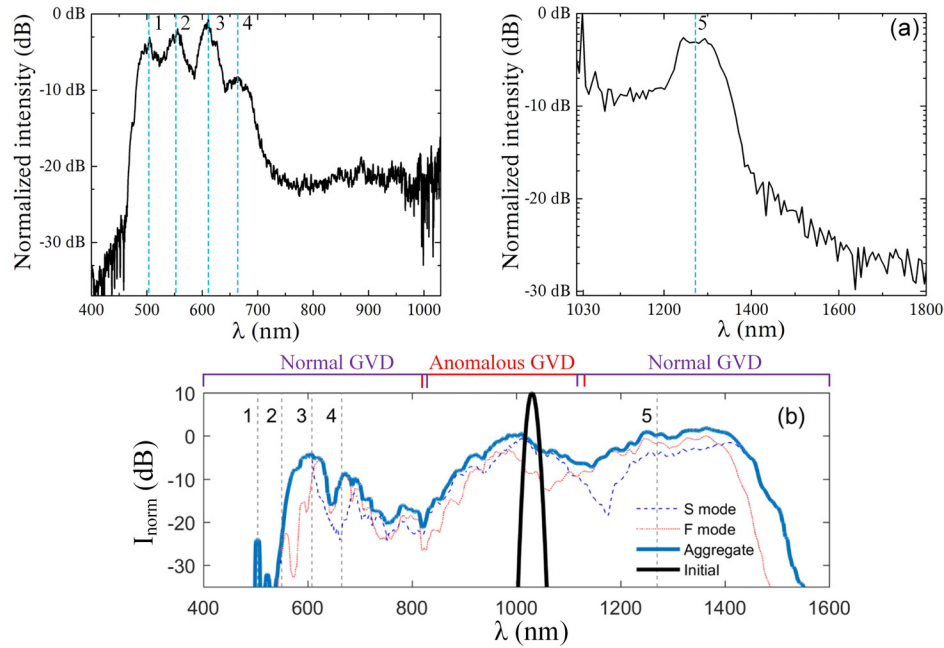
Figure 4.6: Supercontinua generated in PCF in case of bandwidth-limited pump pulses: (a) – spectra obtained experimentally which were measured with different spectrometers; (b)– numerically simulated spectra with initial parameters $\tau_S = \tau_F = 110$ fs at FWHM, $E_S = E_F = 0.5$ nJ, L=33 cm.

More important information can be gained from simulated supercontinuum temporal intensity evolution (Fig.4.7). It is obvious that temporal structure for orthogonal supercontinua is also slightly different which is a result of different PCF GVD. Evolution of initial pulse for both
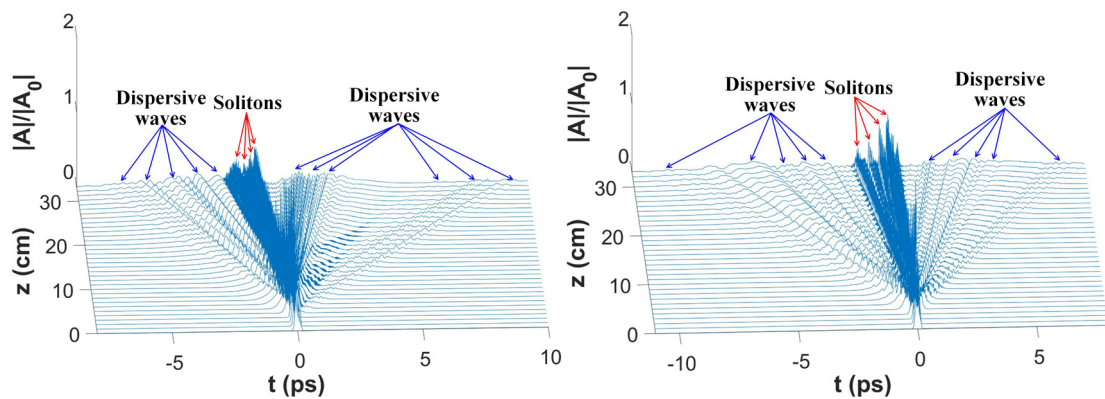

Figure 4.7: Evolution of supercontinuum temporal intensity during propagation in our PCF: left – fast polarization mode, right – slow polarization mode.

polarization modes is very similar. At first few centimeters of propagation

due to anomalous GVD of the PCF a soliton is formed. This is followed by fission into fundamental solitons (relatively high amplitude narrow peaks) accompanied by emission of dispersive waves (low amplitude broad features). Numerical simulation shows that absolute majority of dispersive waves are generated at point of soliton fission which corresponds to point of extremely rapid supercontinuum spectrum extension as is visible from Fig.2.1 (left). One can also see that in numerical simulations fission occurs after roughly 3 cm of propagation, however, we observed experimentally (measuring distance of propagation after which the PCF "lights up") that this fission point which corresponds to extremely rapid spectrum extension (see Fig.2.1) occurs after 5 mm of propagation. This discrepancy is most likely due to different (lower) pump pulse energy used in numerical simulations. Further on, due to GVD of the PCF temporal distance between solitons and dispersive waves increases. This is also accompanied by spread dispersive waves in time. We can notice that fundamental solitons appearing after fission are ahead of time with respect to initial pump pulse. With reference to group refractive index profile of our PCF (Fig.3.2 left), this indicates that their wavelength is longer than pump pulse wavelength: we can explain this by soliton self-frequency shift which occurs towards longer wavelengths. However, in this case soliton self-frequency shift is weak: pump wavelength is close to one of the ZDWs of the PCF so the shift is very small because it can only occur in anomalous GVD range [21, 242]. Furthermore, it is clearly visible that dispersive waves are radiated in both directions of time. From XFROG analysis results (Fig.4.5) we can relate trailing (with respect to solitons) dispersive waves with short wavelength supercontinuum spectral components while leading dispersive waves correspond to long-wavelength spectral components. The further is the spectral component from zero time point (initial pump pulse temporal position), the greater is the wavelength difference between pump and the spectral component. Such results reflect the fact that our PCF has two ZDWs and supercontinuum spectrum is extended not only in anomalous GVD region (related to soliton generation)

but also into both normal GVD regions where dispersive wave generation manifests itself. During final stage of temporal evolution there are no noticeable effects in supercontinuum temporal evolution which is also reflected in numerically simulated supercontinuum spectrum evolution (fig.2.1 left) in a sense that it clearly shows that essentially no additional supercontinuum spectral components are generated after point of soliton fission: only small scale redistribution of spectral intensity is observed at distinct wavelengths.

Numerical simulation results of pulse evolution support our claim that temporal structure of supercontinuum obtained from XFROG analysis (Fig.4.6 bottom left) depicts solitons and dispersive waves of two orthogonal polarization modes. Discrepancies that are visible while comparing experiment and numerical simulation results might be due to several reasons: 1) XFROG analysis shows overall temporal structure of supercontinuum while numerical simulation provides information about distinct polarization mode pulse evolution so they cannot be compared directly; 2) XFROG trace short-wavelength part is limited by spectrometer spectral sensitivity range, so analysis results reveals limited information of supercontinuum pulse temporal structure; 3) we could not estimate PCF losses reliably, thus there might be discrepancies. Nevertheless, numerical simulation results provide a good qualitative representation of supercontinuum temporal evolution.

For additional insight, we performed XFROG analysis of traces obtained using several lower pump pulse energies and measured supercontinuum spectrum dependence on pump pulse energy in case of bandwidth-limited pump pulses. Fig.4.8 shows XFROG analysis results at several different pump pulse energies. Compared to XFROG analysis results in the case of maximum available pump pulse energy there are several things to note. Firstly, all retrieved XFROG traces are in very good agreement with the corresponding measured one. Furthermore, they all have a pattern of small slightly varying size dots. This supports our previous claim that this is probably an artefact from XFROG algorithm. Second important feature is that lesser extension of retrieved spectral intensity,
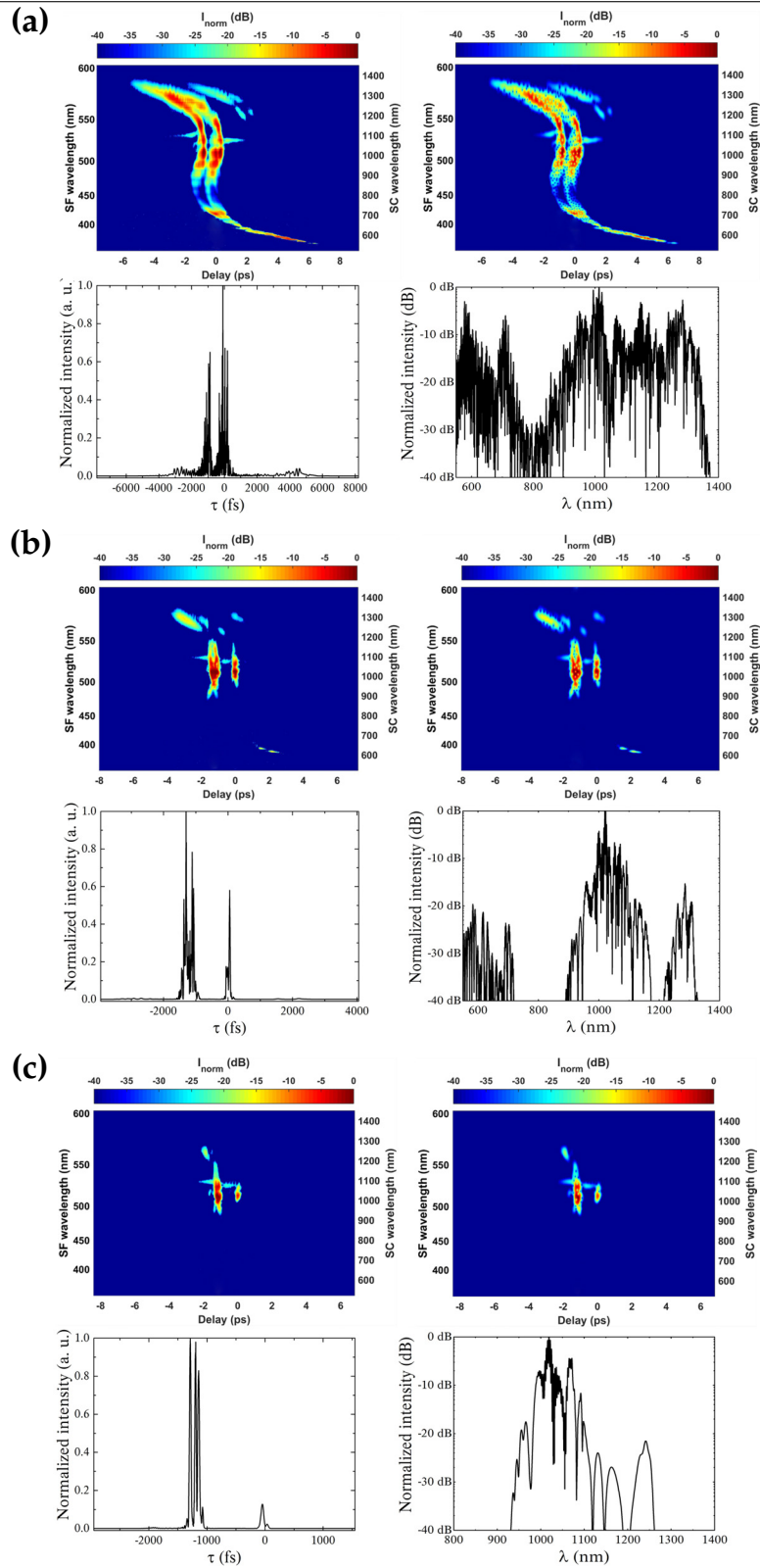
Figure 4.8: XFROG analysis results in case of lower energy pump pulses: (a) – 3.94 nJ, (b) – 0.5 nJ, (c) – 0.13 nJ energy pump pulses. Top left figure of each block depicts measured XFROG trace; top right – retrieved XFROG trace; bottom left – retrieved temporal intensity; bottom right – retrieved spectral intensity.

observed at lowest pump energies, corresponds to weaker dispersive waves. When pump pulse energy is 0.13 nJ (Fig.4.9 c), almost entire supercontinuum spectrum is in anomalous GVD region and its extension is related to soliton fission [21]: we can see several peaks in retrieved temporal intensity. A very low amplitude dispersive wave is still visible around -2000 fs temporal position which corresponds to long-wavelength spectral components at normal GVD region.

Fig.4.9 shows independently measured supercontinuum spectrum dependence on pump pulse energy. With reference to XFROG analysis
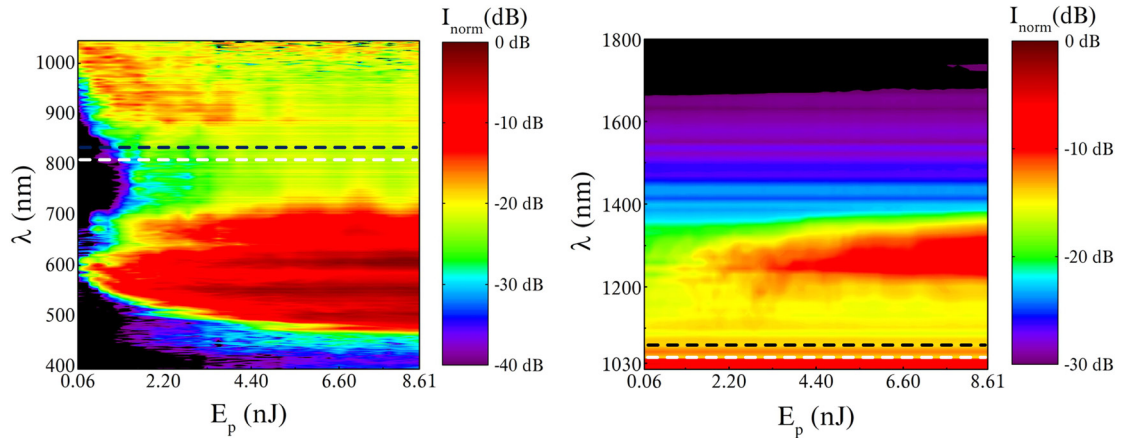

Figure 4.9: Supercontinuum dependence on bandwidth-limited pump pulse energy: (a) registered using VIS/NIR range spectrometer and (b) registered using IR spectrometer. Dashed white lines depict ZDWs for slow polarization mode while black dashed lines – ZDWs for fast polarization mode.

data (Fig.4.5 and Fig.4.8) and numerical simulation results (Fig.2.1, Fig.4.6 and Fig.4.7) we can describe physics behind evolution of supercontinuum spectrum in our highly nonlinear PM PCF with two ZDWs when increasing pump power. At lowest pump energies (0.06–0.1 nJ) spectrum broadens around the pump wavelength due to self-phase modulation and towards the IR due to soliton self-frequency shift phenomena and dispersive wave generation. As mentioned, pump wavelength is relatively close to second ZDW of the PCF, so soliton self-frequency shift is very limited since it can only occur in anomalous GVD range where solitons are formed. Spectrum extension beyond anomalous GVD range into the IR due to dispersive wave generation is weak as pump pulse energy at

this stage is low. For higher pump pulse energies (0.1–2.5 nJ) spectrum broadening is stronger due to increased role of dispersive wave generation and stronger soliton fission-related effects in supercontinuum formation: higher pump pulse energy means higher order of initially formed soliton (see Eq.1.15), moreover, characteristic soliton fission length decreases with increasing pump power ($\sim 1/\sqrt{P_0}$)[21, 296]. Enhancement of dispersive wave generation when pump pulse energy is increased is related to the fact that dispersive wave phase matching condition includes peak power of soliton (Eq.1.28): when more and higher peak power fundamental solitons are formed at fission point, more different frequency dispersive waves can be generated which in turn results in additional spectrum broadening. We can see spectral components generated in the visible part of spectrum around 694 nm and in IR part of supercontinuum spectrum a peak around 1300 nm wavelength. We think the peak forms mainly due to four wave-mixing process: we calculated that group velocities for wavelengths at $1279.4_{(slow)} + 694_{(fast)} = 899.8_{(slow)} + 899.8_{(slow)}$ interaction are equal and their coherence length is $L_c = 2.82$ cm. Such relatively long L_c results in efficient four-wave mixing producing a peak around 1300 nm. Notice that not all interacting wavelengths are of the same polarization mode. This proves our assumption that orthogonal polarization mode interact during supercontinuum formation. For even higher pump energies (2.5–8.61 nJ) enhanced self-phase modulation, dispersive wave radiation together with the aforementioned nonlinear processes cause additional extension of supercontinuum bandwidth. We can also notice additional peaks emerging in the visible range. These can be attributed to enhanced dispersive wave radiation as suggested in [146, 147]. At this energy range the increase of spectrum bandwidth is small and mainly in the short wavelength limit of supercontinuum. This can be explained with reference to group refractive index dispersion (Fig.3.2 left) and remembering dispersive wave phase matching condition (Eq.1.28) which includes peak power of soliton and group velocites of soliton and dispersive wave. The greater is the peak power of soliton, the higher is the frequency of dispersive

wave, however, group refractive index difference between wavelengths in anomalous dispersion range and those further in the VIS and IR range grows with increasing/decreasing wavelengths (see Fig.3.2) which imposes phase-matching limitations [21, 36, 296]. Another supercontinuum bandwidth limitation comes from quickly growing PCF losses for very short (<400 nm) wavelengths and distinct increased loss peaks in long wavelength region (>1600 nm). Finally, it is essential to remind that due to birefringence of our PCF supercontinuum generation is even more complicated as orthogonal polarization modes form distinct supercontinua which interact during formation resulting in a slightly different overall supercontinuum spectra (which we experimentally measure).

4.3 Supercontinuum generation in case of chirped femtosecond pump pulses

4.3.1 Experimental setup

For investigation of supercontinuum generation using chirped pump pulses we used two different experimental setups depicted in Fig4.10. In first experimental setup (Fig.4.10 a) we used a pair of SF11 glass dispersive prisms to chirp pump pulses, measured supercontinuum spectrum and compared it with supercontinuum spectrum achieved with bandwidth-limited pump pulses at the same peak power. Supercontinuum spectra need to be compared at the same peak power level, since the strength of nonlinear phenomena in general depends on peak intensity of laser radiation (peak power/area) – in this case the area in which pump radiation is focused is the same in all cases, so peak power of pump radiation is the key parameter. Duration of pump pulse also has effect on super-continuum spectrum formation, however, in this case (comparison at the same peak power level) the initial chirped pump pulse has the same spectral bandwidth as unchirped pump pulse, which, we believe, creates the most similar initial conditions for supercontinuum spectrum formation
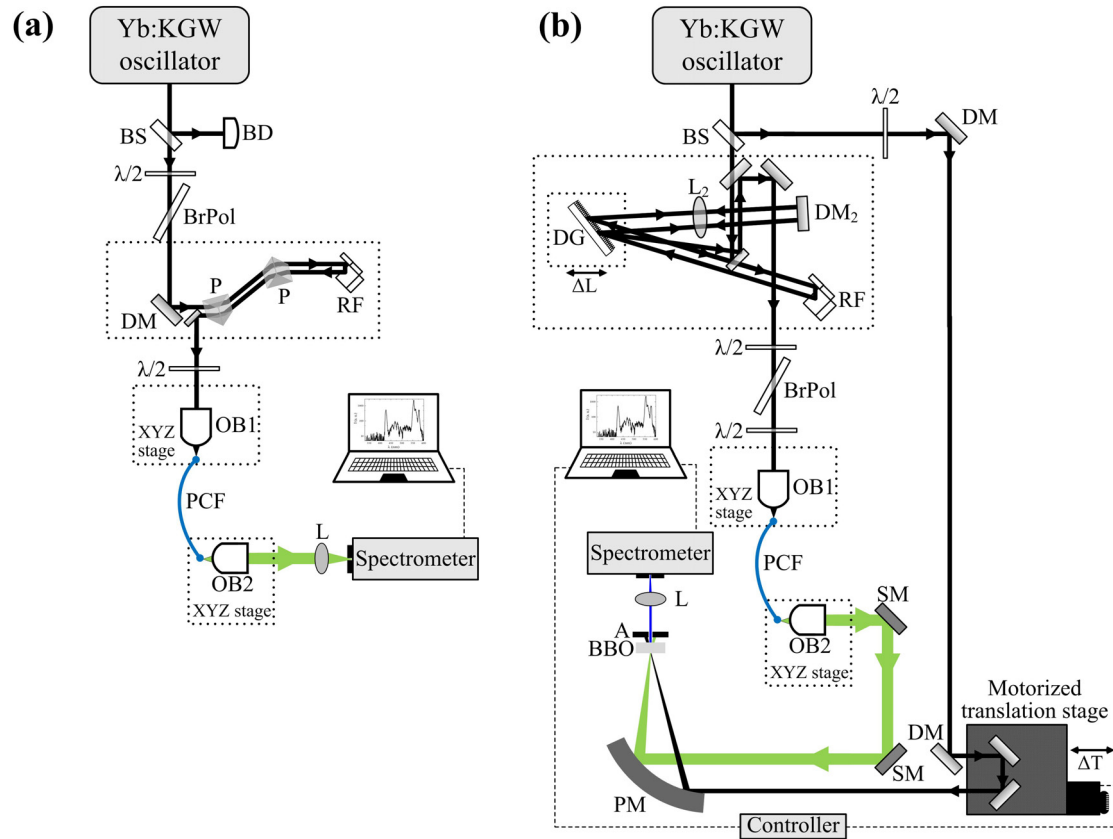
131

Figure 4.10: Experimental setups for supercontinuum generation investigation using chirped femtosecond pump pulses: (a) – spectrum measurement setup using dispersive prism pair for chirping pump pulses; (b) - XFROG measurement setup using single diffraction grating compressor/stretcher for chirping pump pulses. Additional notation: BD – beam dump; P – dispersive prism; RF – retro-reflector; DG – diffraction grating; L_2 – f=150 mm lens; DM_2 – highly reflective dielectric mirror for 1030 nm wavelength at 0° angle of incidence.

leaving pump pulse chirp as the main difference. Therefore, comparison at the same peak power level should be the most accurate way to analyze any pump pulse chirp influence on supercontinuum formation in PCF.

We remind that chirp is quantified as amount of GDD required to dispersively compress the chirped pulse to a bandwidth-limited pulse. The amount and chirp after passing through the dispersive prism pair twice can be calculated from Eq.4.11, but since pump radiation (λ_P=1030 nm) is invisible to human eye, it would be very complicated to accurately de-

termine L and l_p. Therefore, to ensure accuracy, every time the distance between the prisms was changed and/or the optical beam path in any of the prisms was changed, we measured chirped pulse duration (before the focusing microscope objective) with a commercial scanning autocorrelator (*Geco, Light Conversion Ltd.*) and calculated corresponding values of chirp (Fig.4.11 left).
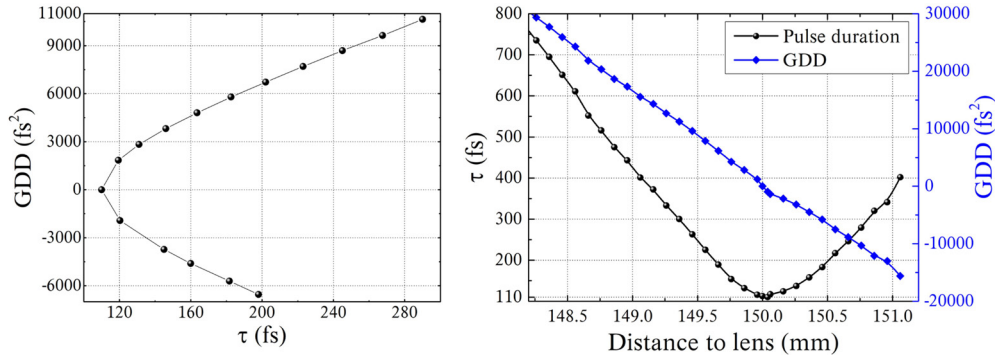

Figure 4.11: Left – measured chirped pulse durations and corresponding chirp values when using a pair of dispersive prisms; right – measured chirped pulse duration and corresponding chirp value dependence from distance between lens (L_2) and diffraction grating.

Experimental setup employing a pair of dispersive prisms for chirping pump pulses is beneficial for low losses of dispersion prisms (when prisms are set to Brewster angle for pump wavelength). One the other hand, such setup requires realignment each time we change distance between dispersive prisms. More than that, the amount of chirp that the passing pulse can gain is limited: maximum positive GDD that may be achieved with this method for a given prism material is limited to minimum distance between the prisms and maximum optical path length of beam in the prisms (in our case maximum practically achievable was GDD=+10664 fs^2), whereas maximum amount of negative GDD is limited to opposite of the named factors (in our case maximum practically achievable negative GGD was -6544 fs^2).

In the second experimental setup (Fig.4.10 b) we used a single diffraction grating stretcher/compressor setup for chirping pump pulses and performed XFROG measurements which results were later compared to XFROG analysis data in case of bandwidth-limited pump pulses at the

same peak power. Two main advantages when using diffraction grating-based setup are the opportunity to induce much greater chirp and no need for realignment of the system when we change distance between diffraction grating and lens L_2 – change pulse chirp (Fig.4.11 right).

We used aluminium diffraction grating with d=1200 mm^{-1} grating constant. It is also important to note that our diffraction grating was blazed (echelette grating) to yield maximum efficiency at first diffraction order: we employed Littrow configuration ($\Theta_{Littrow}$=38.17° for λ=1030 nm at given d) which yielded maximum diffraction efficiency at the first order. Unfortunately, due to relatively poor reflectivity of aluminium grating and the use of lens with no anti-reflection coatings, energy of pulses after passing the system was only 25.5% of initial energy value which corresponds to 2.2 nJ maximum chirped pump pulse energy. Nevertheless, we used this fact to our advantage. As already pointed out in previous section, XFROG trace measured at maximum pump pulse energy (Fig.4.5) is slightly truncated in the short-wavelength side due to limited spectral range of our spectrometer and for this reason XFROG analysis yields limited data about temporal structure of supercontinuum pulse in the short-wavelength region. Therefore, performing measurements at lower pump energies avoids this problem. In addition PM PCF was oriented such that pump polarization would be aligned with fast principal axis of polarization of the PCF. In this way supercontinuum generation was essentially determined by fast polarization mode of pump pulse which in turn simplified analysis of results.

4.3.2 Main results and discussion

Dispersive prism setup results. Chirped pump supercontinuum spectra at various chirp levels when a pair of dispersive prisms was used and corresponding bandwidth-limited pump supercontinuum spectra are displayed in Fig.4.12. As always, spectrometer spectral sensitivity correction functions were applied to corresponding measured spectra and experimental conditions for spectrum registration (integration time,
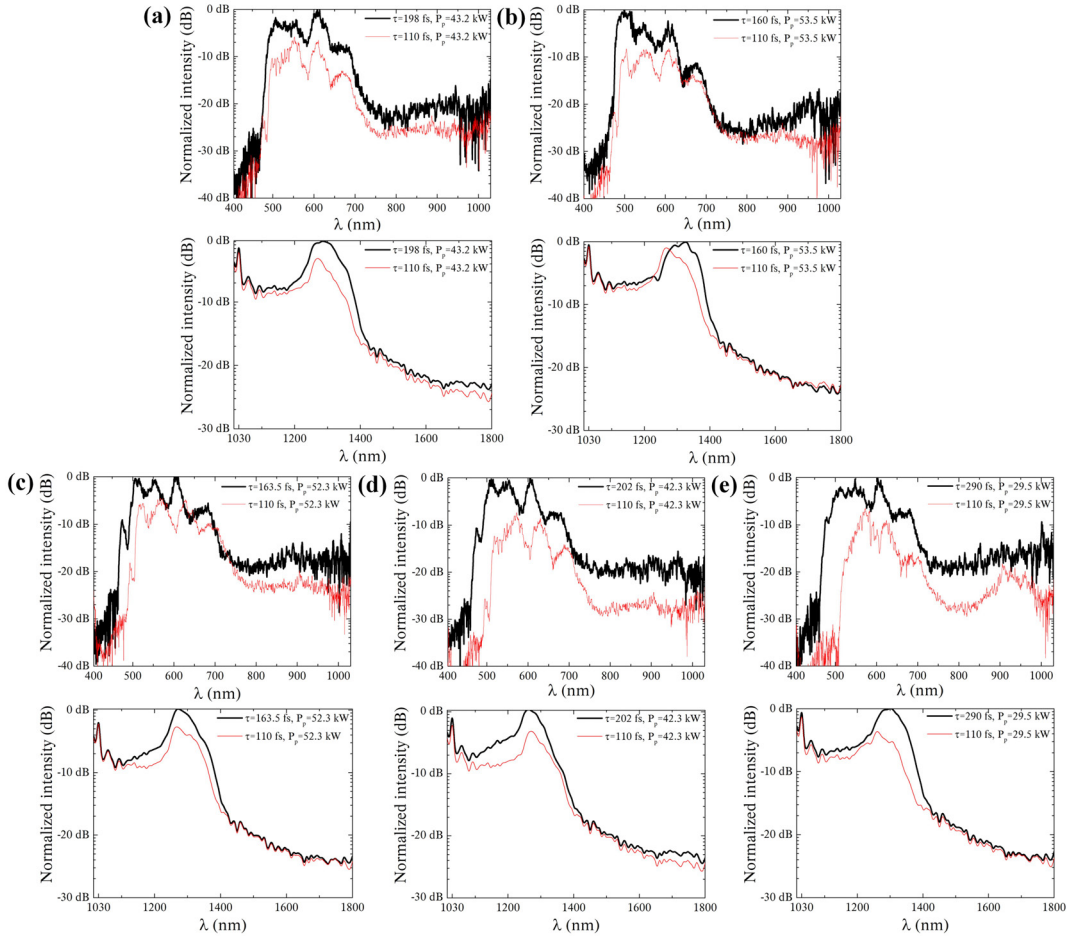
Figure 4.12: Spectra of supercontinuum generated in PCF using chirped maximum energy pump pulses (thick black line) and bandwidth-limited pump pulses at the same peak power (thin red line): (a) – GDD=-6544 fs^2, (b) – GDD=-4609 fs^2, (c) – GDD=4802 fs^2, (d) – GDD=6715 fs^2, (e) – GDD=10640 fs^2.

position of spectrometer coupling optics) were kept constant. Due to complicated nature of supercontinuum, it is difficult to pick a single quantity to analyze chirp influence to supercontinuum formation. Therefore, we chose direct comparison of spectra.

It is obvious that supercontinuum spectra in case of chirped pump pulses are somewhat different than the ones obtained using bandwidth-limited femtosecond pump pulses at the same peak power. Careful comparison reveals several important spectral features:

- Supercontinuum spectrum bandwidth in case of positively chirped pump pulses is noticeably broader than the corresponding bandwidth-

135

limited pump supercontinuum spectrum at the same peak power. Broadening increases with increasing value of chirp: overall broadening (visible and IR sides) ranges from several nanometers at small chirp values to nearly 100 nm for GDD=10640 fs^2.

- Spectrum in case of negatively chirped pump pulses is only slightly broader than the corresponding bandwidth-limited pump supercontinuum spectrum at the same peak power.

- The shape of supercontinuum spectrum in both cases is in principle the same, but the characteristic peaks of supercontinuum spectrum are slightly shifted both in the VIS and IR parts of the spectrum. The shift is considerably greater in case of positive chirp.

Measured spectra clearly indicate that pump pulse chirp has influence on supercontinuum spectrum formation. However, comparison of supercontinuum spectra alone is not enough to explain the outlined features.

Diffraction grating setup results. For this reason, XFROG measurement results (second experimental setup), shown in Fig.4.13) and Fig.4.14), were analyzed to obtain information about supercontinuum temporal intensity. All features and considerations highlighted during supercontinuum XFROG analysis in case of bandwidth-limited pump pulses are also valid here. As mentioned, it is difficult to pick a single quantity to analyze chirp influence to supercontinuum formation, so we chose direct comparison of XFROG analysis results.

As expected, from XFROG analysis we see that spectral features outlined above are valid in this case as well. One only needs to remember that in this case, due to reasons explained in experiment setup subsection, maximum pump pulse energy was several times lower (2.2 nJ instead of 8.61 nJ) that in dispersive prism pair setup. As a result spectrum extension is lesser. The main feature that XFROG analysis results illustrate is that chirping pump pulse slightly changes not only supercontinuum spectrum but also affects its temporal intensity. We can claim that supercontinuum
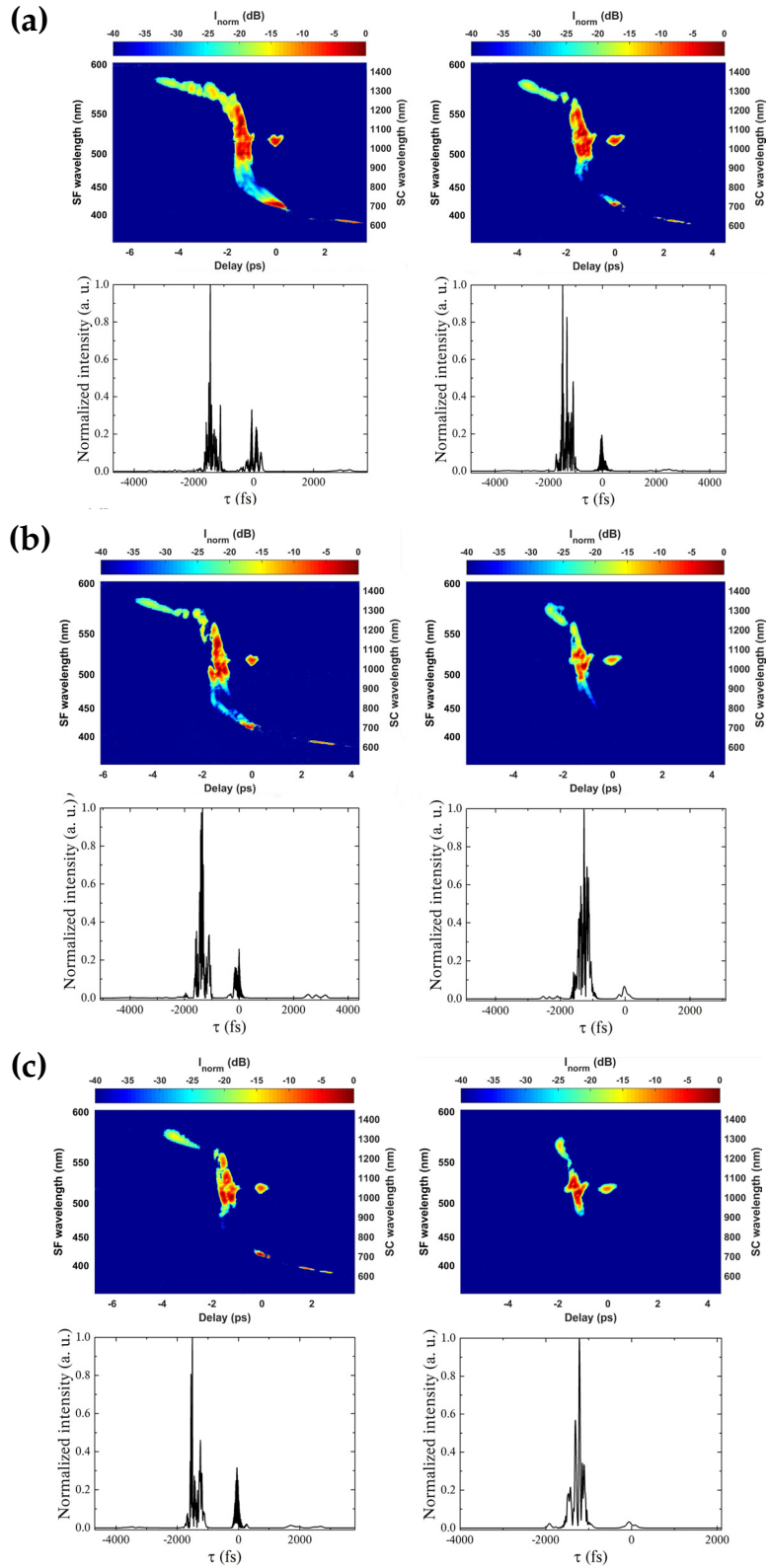
Figure 4.13: XFROG analysis results of supercontinuum in case of positively chirped pump (left) and bandwidth-limited pump (right) at the same peak power: upper row – measured XFROG trace; lower row – retrieved temporal intensity. (a) GDD=6150 fs^2; (b) GDD=12670 fs^2, (c) GDD=18650 fs^2.
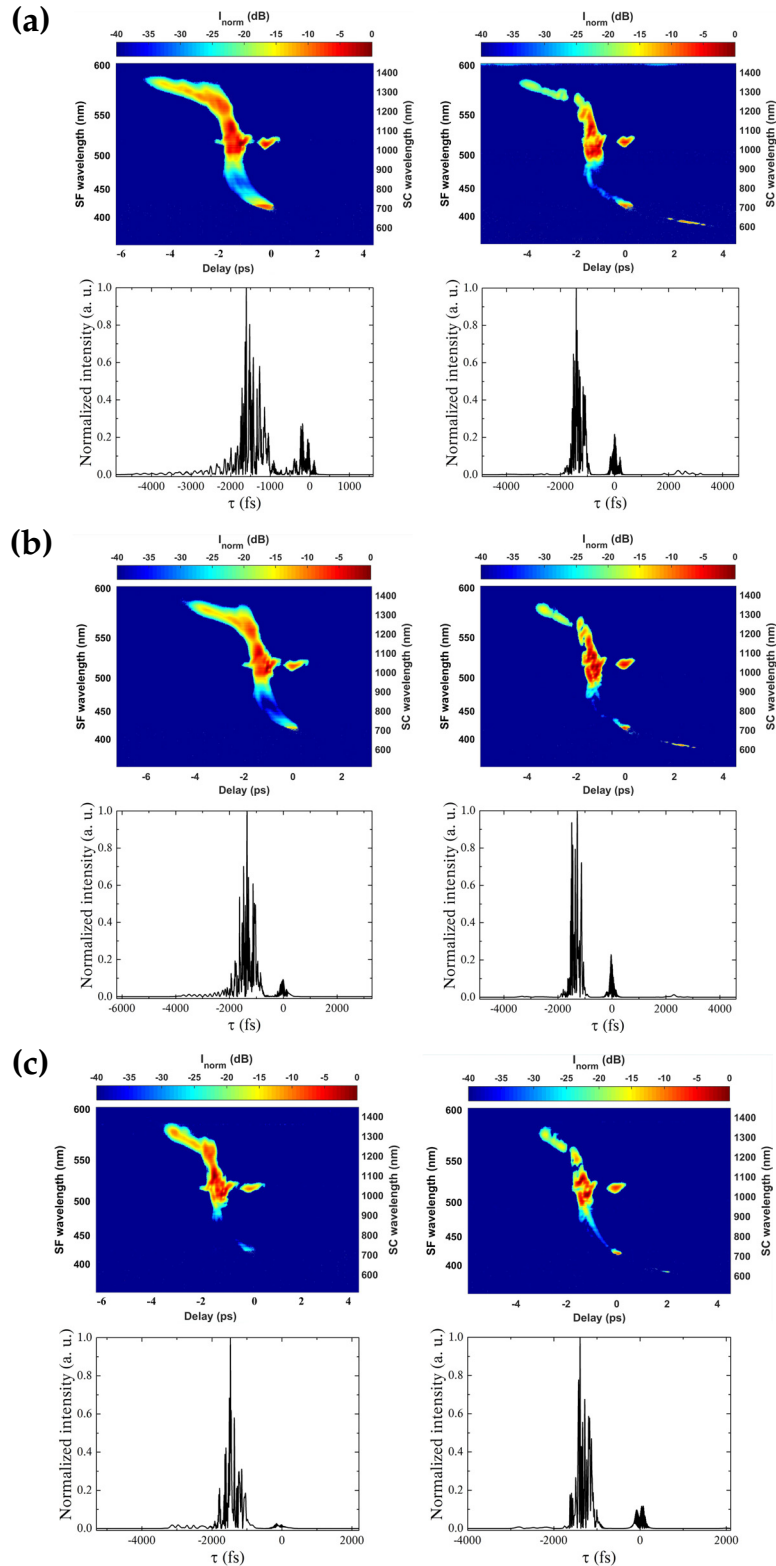
Figure 4.14: XFROG analysis results of supercontinuum in case of negatively chirped pump (left) and bandwidth-limited pump (right) at the same peak power: upper row – measured XFROG trace; lower row – retrieved temporal intensity. (a) GDD=-4500 fs^2; (b) GDD=-7510 fs^2, (c) GDD=-10323 fs^2.

temporal intensity in case of chirped pump is slightly different than in case of bandwidth-limited pump at the same peak power: this can be said both about soliton part of temporal intensity and dispersive waves.

The low intensity peak in each temporal intensity graph corresponds to slow polarization mode radiation – in XFROG trace it is visible as signal around 515 nm at zero delay. Although, as mentioned in experimental setup subsection, PM PCF was oriented such that pump polarization would be aligned with fast principal axis of polarization of the PCF, there is still radiation of orthogonal polarization mode. This indicates that some part of pump radiation is depolarized most likely in microscope objective during sharp focusing into the PCF.

To understand pump pulse chirp influence to supercontinuum formation we need to remember previously discussed stages of supercontinuum formation. We think that chirping pump pulse mostly affects soliton formation which in turn influences subsequent fission and dispersive wave generation which are key processes during femtosecond supercontinuum formation when pump wavelength is in anomalous GVD region of the PCF [21, 32, 36]. Since central wavelength of pump pulses is in the anomalous dispersion region of the PCF (Fig.2.12), soliton formation occurs due to balanced self-phase modulation and anomalous GVD effect on the pump pulse when it is propagating in the PCF. If the initial pump pulse is chirped, soliton formation process is altered.

In case of positive chirp, decrease of instantaneous frequency from leading front of the pulse to trailing front of the pulse (negative chirping) due to anomalous GVD of the PCF has to balance positive chirp of pump pulse and self-phase modulation induced increase of instantaneous frequency from leading front to trailing front of the pulse (positive chirping) before soliton formation and subsequent fission can occur. Compared to bandwidth-limited pulse case this means that pump pulse needs to travel longer distance in the PCF for the stage of soliton fission to occur. The greater the positive chirp, the longer distance pulse needs to travel. This was observed during our experiment: we could roughly estimate that distance of propagation after which the PCF "lights up" (this

corresponds to soliton fission distance) is longer when pump pulses are chirped compared to bandwidth-limited pump case at the same peak power. For greater positive chirp values the difference was somewhat longer. For example, in diffraction grating setup when pump chirp was 6150 fs^2, the propagation distance before "light up" for chirped pulses was roughly 9 mm longer than for bandwidth-limited pulses at the same peak power, whereas for 9612 fs^2 chirp case the difference was 12 mm. As a consequence of pump chirp, soliton fission process and dispersive wave emission processes are also affected, resulting in greater energy transfer to normal dispersion region and broader supercontinuum spectrum as suggested in some reports [39, 40]. Slightly shifted peaks (Fig.4.12) are probably a result of this as well. It is also important to remember that results depicted in Fig.4.12 are actually spectra of both polarization mode supercontinua which further complicates analysis.

In case of negative chirp, self-phase modulation induced positive chirping has to balance negative chirp of the initial pulse and negative chirping due to anomalous dispersion of the PCF – initial negative chirp acts against the nonlinear effect. This means that, compared to positive chirp case, pump pulse needs to travel even longer distance for soliton formation, subsequent fission and dispersive wave generation to occur. Aforementioned experimental observations confirmed this.

To check these assumptions we numerically simulated supercontinuum evolution in case of positively and negatively chirped pump pulses. Numerically simulated temporal and spectral intensity evolution in case of chirped pump pulses for fast PCF polarization mode is shown in Fig.4.15. Simulation results are compared with bandwidth-limited pulse case (Fig.4.8 left and Fig.2.1 left). Numerical simulation results confirm several assumptions:

- Pulse propagation distance before soliton fission is longer than in case of bandwidth-limited pump pulse: fast polarization mode supercontinuum temporal intensity simulations indicate that in case of bandwidth-limited pump pulse fission starts after approximately
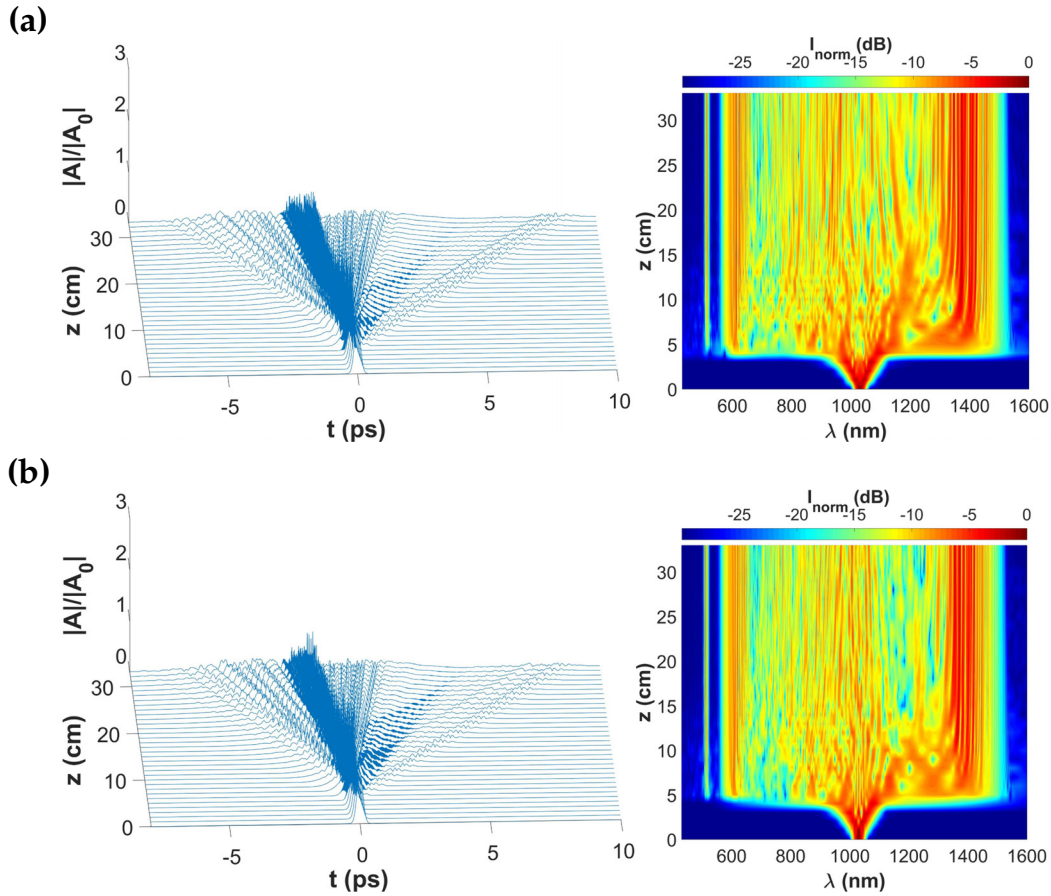
(a)

(b)

Figure 4.15: Supercontinuum fast polarization mode evolution during propagation in our PCF when pump pulses are chirped: (a) 6000 fs^2, (b) -6000 fs^2. Pulse duration and energy are adjusted accordingly. Left – temporal intensity evolution, right – spectral intensity evolution.

3 cm of propagation in PCF, while for positively chirped pump pulse the distance is roughly 4 cm.

- Pulse propagation distance before soliton fission is longer for negatively chirped pulse than for positively chirped pulse: in case of negatively chirped pump pulse fission starts after approximately 5 cm of propagation in PCF.

- Soliton fission process and dispersive wave generation processes are somewhat different compared with bandwidth-limited pulse case: we can notice differences between dispersive wave amplitudes and their temporal spread. For positive and negative chirp signs the difference is very small. However, due to complex nature of super-

continuum generation phenomenon even very small differences can yield noticeable changes in supercontinuum spectrum.

On the other hand, numerical simulation of spectrum evolution displays lesser chirped pump supercontinuum spectrum extension than is experimentally measured. This is clearly visible in Fig.4.16 where numerically simulated chirped pump pulse supercontinuum spectra are compared with bandwidth-limited spectrum at the same peak power.
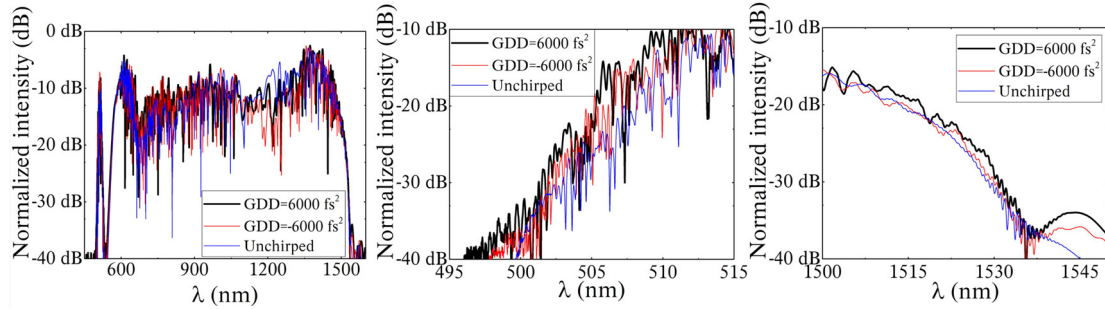

Figure 4.16: Left – simulated supercontinuum spectra for fast polarization mode in case of bandwidth-limited pump pulses, positively (6000 fs^2) and negatively (-6000 fs^2) chirped pump pulses; middle – broadening of simulated spectra at short-wavelength edge; right – broadening of simulated spectra at long-wavelength edge.

Such quantitative discrepancy might be due to unknown PCF losses at the edges of supercontinuum spectrum which resulted in different pump pulse energy used in numerical simulations. Nevertheless, qualitatively results indicate that chirped pump supercontinuum spectrum is broader than corresponding bandwidth-limited pump supercontinuum and that spectrum extension is greater in positively chirped pump case.

We will now briefly discuss several ways how pump pulse chirp might affect soliton fission and dispersive wave generation. One is related to the fact that pump chirp influences soliton self-frequency shift as shown in [299]: greater positive chirp causes greater soliton self-frequency shift, which also influences dispersive wave generation resulting in greater extension of supercontinuum spectrum. Since self-frequency shift is not strong in this case (pump wavelength is relatively close to one of the ZDWs of our PCF) this would explain why additional spectrum extension compared to bandwidth-limited pump case is relatively small.

Another reason might related to pulse self-steepening effect. Using a simplified model (GNLSE without Raman scattering and dispersion terms) we can describe pulse propagation as:

$$\frac{\partial S}{\partial z} = -i\frac{\chi^{(3)}}{2n_M^2}\frac{\omega}{c}n_{\mathrm{M}}\int_{-\infty}^{\infty}|A|^2 A\exp[-i\Omega t]dt, \qquad (4.12)$$

where A is the electric field complex amplitude, S – spectral amplitude related to A by Fourier transform and n_{M} – mode refractive index. In this case the initial pulse is assumed to have Gaussian shape:

$$A_0(t) = \frac{a}{\sqrt{s}}\exp\left[-\frac{1}{s}\frac{t^2}{\tau_0^2}\right], \qquad (4.13)$$

where τ_0 is initial pulse duration, $s = 1 + i\frac{2G}{\tau_0^2}$ and G is the chirp parameter. Adding notations: $\gamma = \frac{\chi^{(3)}}{2n_{\mathrm{M}}c}$, $\omega = \omega_0 + \Omega$ and $A = a\exp[i\varphi]$, one can write exact solution for complex amplitude A of the pulse in the following form:

$$a = \frac{a_0}{\sqrt[4]{(1+\alpha^2)}}\exp\left[-\frac{1}{1+\alpha^2}\frac{(t - 3\gamma a^2 z)^2}{\tau_0^2}\right], \qquad (4.14)$$

here $\alpha = \frac{2G}{\tau_0^2}$ is the dimensionless chirp parameter and phase in the complex amplitude expression is:

$$\varphi(t, z) = \frac{\alpha}{1+\alpha^2}\frac{(t - \gamma a^2 z)}{\tau_0^2} - \frac{1}{2}\arctan\alpha - \omega_0\gamma a^2 z. \qquad (4.15)$$

The solution describes pulse self-steepening effect when it propagates in nonlinear medium. When initial chirp is zero, the trailing slope of the pulse is steepening during propagation which corresponds to the short-wavelength spectrum range (Fig.4.17 left). Therefore SC broadening is stronger in short-wavelength range, compared to long-wavelength range. In addition, the solution reveals that slope steepening yields different expansion of SC spectrum in case of different chirp sign (see Fig.4.17 right). The change of instantaneous frequency due to self-steepening can be described as:

$$\Delta\omega = \frac{d\varphi}{dt} = \frac{\alpha}{1+\alpha^2}\frac{2(t-\gamma a^2 z)}{\tau_0^2}\left(1 - \gamma z\frac{\partial a^2}{\partial t}\right) - \omega_0\gamma z\frac{\partial a^2}{\partial t}. \tag{4.16}$$

It has two terms one of which depends on initial chirp and another does not (it always yields frequency change to higher frequencies). When initial chirp is positive, both terms have the same sign and describe stronger expansion of SC spectrum which in our case takes place on trailing slope of the pulse corresponding to short-wavelength edge extension. On the other hand, for negative initial chirp the chirp-dependent term has opposite sign, so the sum of the two terms yields smaller expansion of SC spectrum.
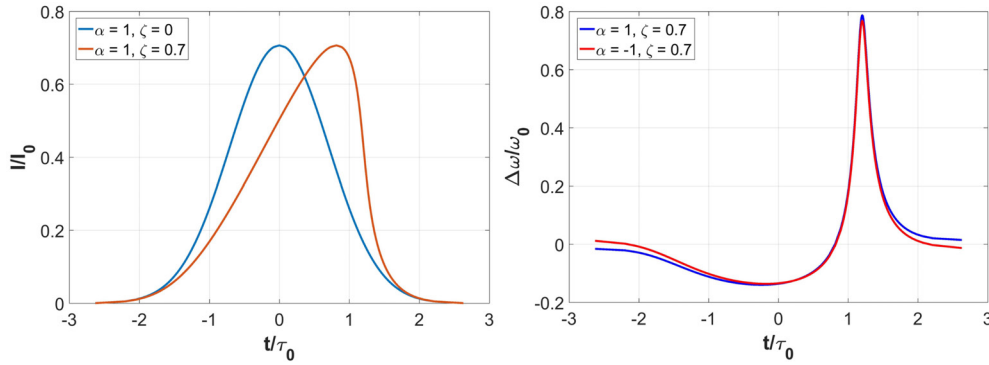

Figure 4.17: Left – principal illustration of pulse self-steepening effect, blue line indicates initial pulse, red line – pulse after propagation in nonlinear medium. Right – qualitative example of pulse self-steepening induced spectrum broadening when α=1 (blue line) and α=-1 (red line). ζ denotes normalized (to self-steepening distance) propagation distance.

In reality dispersion has a huge influence to pulse propagation in PCF and SC spectrum formation: it can counteract, balance or enhance pulse self-steepening effect [300] so we cannot directly apply the explanation above to describe our results. Despite this, such simple model qualitatively reflects the observed features of supercontinuum spectrum and its evolution.

4.4 Conclusions

In conclusion, we presented experimental and numerical simulation investigation results of supercontinuum generation in highly nonlinear PM photonic crystal fiber with two ZDWs using chirped pump pulses.

In case of bandwidth limited pump pulses at maximum available energy (8.61 nJ) we experimentally demonstrated supercontinuum generation in 450 nm – 1450 nm spectral range (Fig.4.6 a). XFROG measurement analysis revealed that dispersive wave generation is responsible for supercontinuum spectrum extension in both short-wavelength and long-wavelength sides (Fig.4.5 and Fig.4.8) where PCF GVD is normal. Although retrieved XFROG traces show good convergence, in all cases we observed fine-scale structure of retrieved supercontinuum spectra and small slightly varying size dotted pattern in retrieved XFROG traces which we think are artefacts from XFROG algorithm which appears during Fourier transform of extremely broad spectral bandwidth radiation. Despite this, retrieved supercontinuum spectra display reasonably good qualitative agreement with independently measured ones.

Numerical simulation results supported our claim that temporal structure of supercontinuum depicts solitons and dispersive waves. Most importantly, simulations revealed that orthogonal polarization modes produce slightly different supercontinua (Fig.4.6 b). This is reflected in both spectral and temporal evolution. Furthermore, the most accurate simulation results are produced when we take into account orthogonal polarization mode interaction during supercontinuum formation. This is supported by a particular feature of experimentally measured supercontinuum spectrum: we determined that spectral peak around 1300 nm form due to four-wave mixing process which involves spectral components of orthogonal polarization modes.

Experimental investigation of pump pulse chirp influence on supercontinuum spectrum formation results showed that chirped pump supercontinuum has somewhat broader spectrum compared to bandwidth-limited pump case at the same peak power (Fig4.12). Spectrum broadening increases with increasing positive chirp. Moreover, it is significantly greater for positive chirp compared to the case of negative chirp. As expected, XFROG analysis results showed that changes in spectrum broadening are also reflected in temporal characteristic of supercontinuum (Fig.4.13). Numerical simulation results, despite showing lesser spectral extent, sup-

145

ported our assumptions that chirp manifests itself at initial stage of supercontinuum spectrum formation which in turn influences soliton fission and dispersive wave generation processes. We can conclude that pump pulse chirping has relatively small influence on supercontinuum formation.

Chapter 5

Investigation of supercontinuum generation in polarization-maintaining photonic crystal fiber using subnanosecond pulses

Material related to this chapter is published in A1 and AP1, presented in C1, C2 and C8.

In the preceding chapter investigation of supercontinuum generation using femtosecond pump pulses was presented and discussed. It was obvious that when pump wavelength is in the anomalous GVD region of the PCF, supercontinuum spectrum broadening is dominated by self-phase modulation and soliton-related effects. However, as already mentioned in literature review, supercontinuum generation has been demonstrated using much longer (picosecond, nanosecond) pulses and even CW laser radiation [21, 30–35] and spectrum broadening in these cases is dominated by different nonlinear phenomena. A particularly important for practical applications case is broadband supercontinuum generation in the entire visible range of optical spectrum using subnanosecond pump sources such as Nd^{3+} based Q-switched microlasers. Such broadband supercontinuum sources with subnanosecond pulse widths and spectrum spanning through the entire visible range could be efficient seed radiation sources for subnanosecond optical parametric generators. Despite various reported methods to extend subnanosecond supercontinuum through the entire visible range [34, 35, 50–59], which require complex experimental setups or rather sophisticated technological modifications of PCF, therefore, there is still need for simple and practical visible supercontinuum source with subnanosecond pulse durations.

In this chapter we present investigation of supercontinuum generation using subnanosecond pump pulses from a Q-switched Nd:YAG microlaser. We show that using highly nonlinear polarization-maintaining photonic crystal fiber with two ZDWs one can obtain broadband supercontinuum spanning in the whole visible range. For analysis of physical mechanisms behind supercontinuum generation using subnanosecond

pulses we employ spectrum measurements and streak camera as well as numerical simulation model introduced in previous chapter.

5.1 Experimental setup

Experimental setups for measurements using subnanosecond pump pulses are depicted in Fig.5.1.
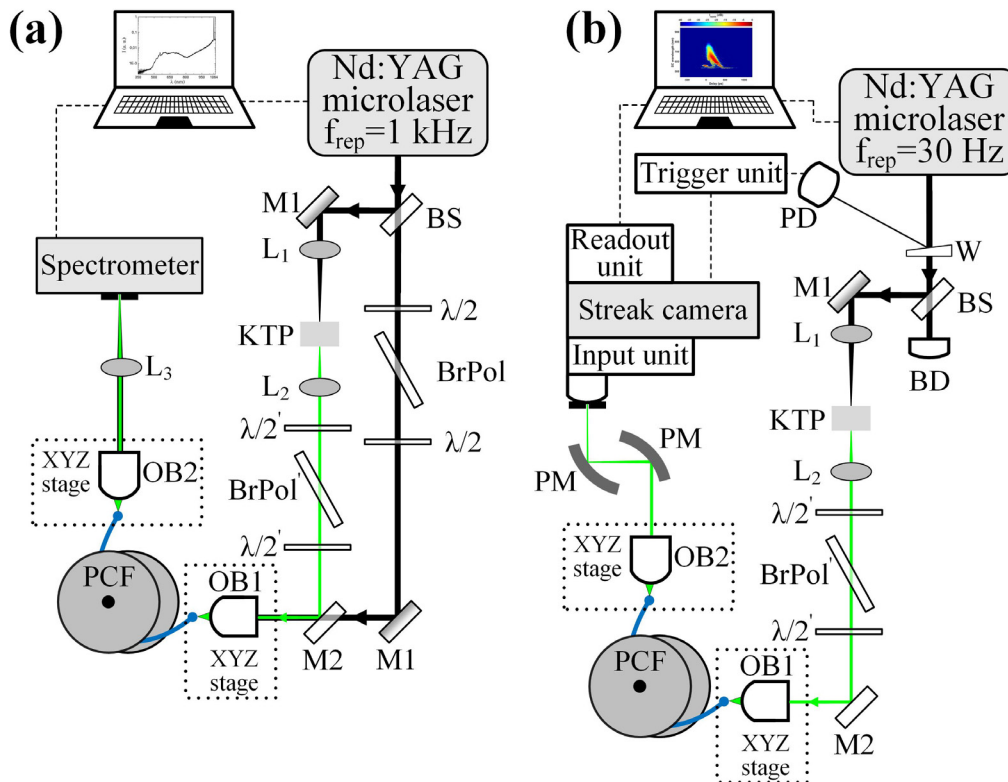

Figure 5.1: Experimental setups for supercontinuum generation investigation using subnanosecond pump pulses: (a) – setup for spectrum measurements; (b) – steak camera measurement setup. Additional notation: W – wedge; PD – photodiode; M1 – highly reflective dielectric mirror for 1064 nm wavelength at 45°; M2 – highly reflective dielectric mirror for 532 nm and highly transmitting for 1064 nm wavelength at 45°; L_1, L_2, L_3 – lenses; $\lambda/2$, $\lambda/2'$ – half-wave plate for 1064 nm and 532 nm respectively, BrPol, BrPol' – Brewster type polarizer for 1064 nm and 532 nm respectively, KTP – potassium titanyl phosphate crystal.

In the first setup (a) laser radiation from Q-switched Nd:YAG microlaser (*STA-07, Standa Ltd.*), generating λ_P=1064 nm E_P=50 µJ τ=300 ps pulses with 1 kHz repetition rate, was split into two beams by a 1:1 energy ratio

beamsplitter. One beam was used directly as pump for supercontinuum generation, whereas the other was used to generate second harmonic (532 nm) in 12 mm thick potassium titanyl phosphate (KTP) crystal cut at θ=90° and ϕ=23.5° for type II phase matching and coated with anti-reflection coatings for 1064 nm and 532 nm wavelengths. Second harmonic was then separately used as pump for supercontinuum generation. In both branches first half-wave plate and Brewster type polarizer were used as optical attenuator, while the second half-wave plate was used to rotate polarization direction. For supercontinuum generation we used the same highly nonlinear PM PCF with two ZDWs that we characterized and used for femtosecond supercontinuum generation, however, in this case a 15 m long PCF was used: long fiber length compensates for significantly lower peak power of pump pulses (compared to femtosecond case in previous chapter), so efficient spectrum broadening can occur.

An important thing regarding PCF that has to be taken into consideration is the maximum pulse energy that can be used for supercontinuum generation. We found that in this case it is limited by laser induced damage threshold (LIDT) of PCF's material. We measured LIDT using R on 1 method: starting from very low values pulse energy was continuously increased step by step using a combination of half-wave plate and a polarizer until damage was reached. The PCF damage was detected as a drop of output power. The average LIDT energy in case of first harmonic pulses(λ_p=1064 nm) was 4.5 μJ, whereas for second harmonic pulses (λ_p=532 nm) it was 3.5 μJ.

First experimental setup (a) was used for supercontinuum generation investigation by measuring spectra of light coming out of the PCF. The second setup (b) was used for direct supercontinuum spectrogram measurement with streak camera (*Hamamatsu C5680*). The setup can be described as follows. A small part of laser radiation was reflected from fused quartz wedge and used as trigger (converted into electric trigger signal in a photodiode) for streak camera: it controlled the timing of the streak sweep. Arrival of the trigger signal has to be adjusted so that a streak sweep is initiated when the light being measured arrives at the

149

streak camera. For this purpose, a trigger unit, which controls how long the trigger signal which initiates the streak sweep is delayed, was used. For our measurements a single fast sweep unit was used (*Hamamatsu M5676*): only one sweep was performed during each frame and 15000 frames were taken for each measurement. This imposed limitation to our pump laser repetition rate – it had to be lowered to 30 Hz. Consequently, pump pulse duration changed to 170 ps. The readout section of streak camera is a digital data acquisition and control system which reads and analyzes streak images produced on the phosphor screen. Temporal resolution of streak camera was 10 ps. Unfortunately, spectral sensitivity of streak camera photocathode extended in roughly 200 nm – 900 nm spectral range (Fig.5.2), so correct spectrogram measurements could be performed only with supercontinuum generated using second harmonic pump. In addition, an HC13 grade filter (Fig.5.2 right) had to be used to protect streak camera from saturation.
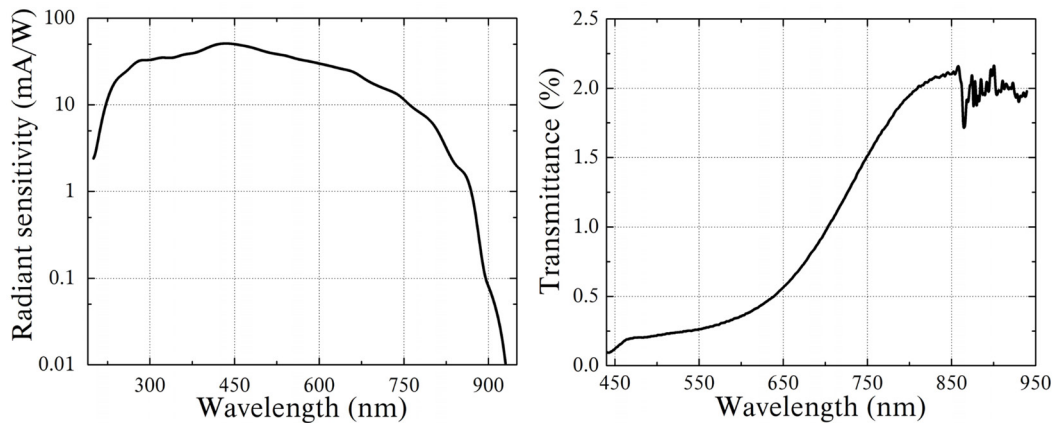

Figure 5.2: Left – radiant sensitivity of streak camera photocathode, right – transmittance of HC13 grade filter used in streak camera.

5.2 Results and discussion

Supercontinuum in case of 532 nm pump. For supercontinuum generation in case of second harmonic pump (λ_p=532 nm) we used maximum pump pulse energy of 2 µJ – roughly 57% of the measured LIDT pulse energy for this PCF. This corresponds to maximum peak power of

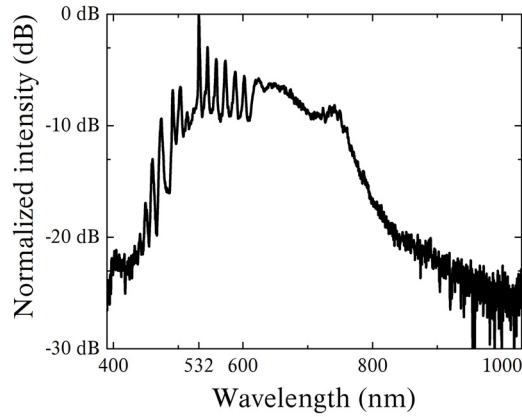6.67 kW. Generated supercontinuum spectrum is depicted in Fig.5.3. It

Figure 5.3: Spectrum of supercontinuum generated in our PCF at maximum available pump pulse energy (2 μJ) when λ_p=532 nm, τ=300 ps.

extended from roughly 400 nm to 900 nm and had clearly distinct Raman Stokes and anti-Stokes peaks up to 5th order (determined by frequency offset between peak and pump wavelength peak) indicating that Raman scattering of pump wavelength played an important role in supercontinuum formation: high cascaded Raman scattering order indicates high efficiency of the process. The relatively smooth spectrum for wavelengths longer than 600 nm continues up to roughly 750 nm when spectrum intensity starts to decrease significantly. We think that four-wave mixing is the main process responsible for spectrum broadening to longer wavelengths which is the case when pump pulse duration exceeds several picoseconds [21, 36, 122, 241].

More insight into supercontinuum generation is gained from its dependence on pump pulse energy and polarization (Fig.5.4). Supercontinuum dependence on pump pulse energy can be explained as follows. Initially (0.05 μJ – 0.14 μJ), distinct Stokes spectral components are generated due to cascaded Raman scattering of pump wave. Additional increase of pump pulse energy (0.14 μJ – 0.8 μJ) leads to generation of smooth spectrum in the long-wavelength side of supercontinuum as four-wave mixing starts to play the main role in expanding the spectrum. Notice that several additional Raman Stokes components emerge in relatively smooth supercontinuum spectrum part. This is probably a result of
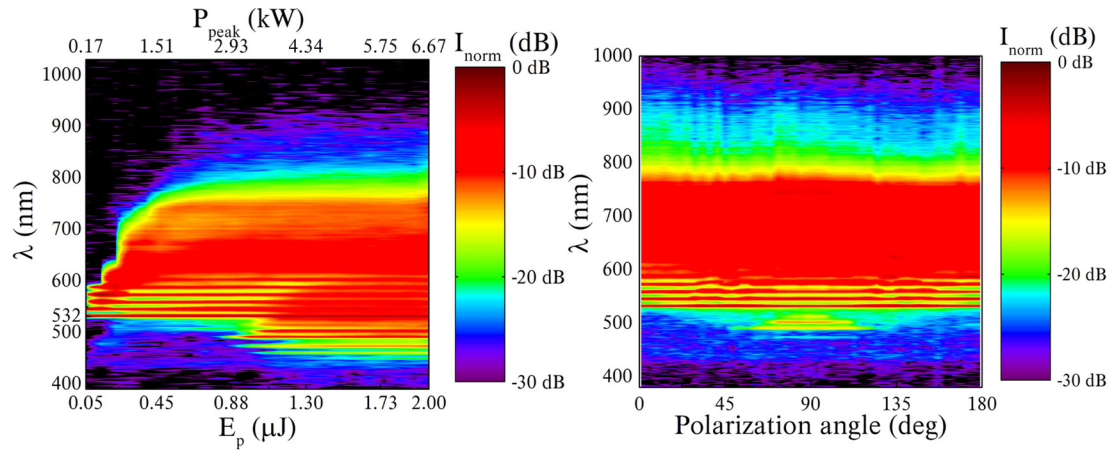
Figure 5.4: Supercontinuum spectrum dependence on pump pulse energy (left) and polarization (right). Polarization angle is noted as double angle of half-waveplate rotation with respect to one of principal polarization axis of the PCF.

coupling between Raman and four-wave mixing gain which can lead to enhancement of Raman gain to levels comparable to four-wave mixing gain as suggested in [21, 301, 302]. Finally (0.8 μJ – 2μJ), brightness of supercontinuum long-wavelength components increases even more due to increased gain of four-wave mixing process (see Eq.1.29) and generation of additional anti-Stokes peaks is observed – all of which lead to supercontinuum expansion down to 400 nm. Spectrum extension is limited by group velocity mismatch (GVM) between pump wavelength and other supercontinuum spectrum components (Fig.5.5 right) and lower PCF nonlinearity for long-wavelengths which both result in decreasing four-wave mixing gain.

Up to this point birefringence of our PCF was not taken into account when discussing supercontinuum spectrum formation. As in femtosecond pump case, it is an important factor which complicates analysis: when pump is polarized at an angle with respect to PCF principal axis of polarization, two distinct supercontinua corresponding to orthogonal polarization modes are generated and they can interact with pump pulse or each other through cross-phase modulation [122]. Although group refractive indices for orthogonal polarization modes are very similar, the nonlinear
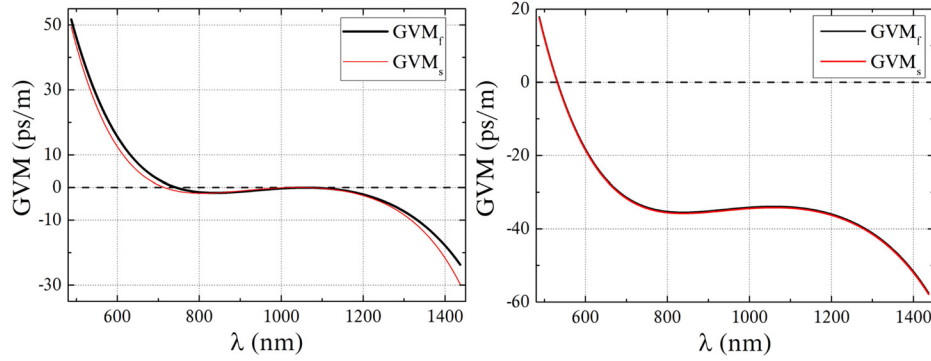
Figure 5.5: Calculated group velocity mismatch in PCF used in our experiments: left – with respect to λ=1064 nm, right – with respect to λ=532 nm.

nature of supercontinuum generation makes even extremely small differences important. Changing pump pulse polarization angle with respect to PCF principal axis of polarization (Fig.5.4 right) reveals some details about the role of PCF polarization modes. We can see that in second harmonic pump case it has notable effect on anti-Stokes peaks: they are cancelled when pump is polarized along one PCF principal axis of polarization and are strongest when pump is polarized along the orthogonal PCF principal axis of polarization. Raman anti-Stokes scattering dependence on pump pulse polarization is related to the fact that it requires phase-matching condition to be satisfied ($\Delta k = 2k_p - k_s - k_a = 0$) [122]. Since wave vectors of interacting waves depend on polarization, at certain polarization angles generation of anti-Stokes components in supercontinuum spectrum can be enhanced or suppressed.

Measurements with streak camera. In case of second harmonic pump we had the opportunity to perform direct supercontinuum spectrogram measurements with streak camera. Measurement limitations forced us to lower pump laser repetition rate to 30 Hz which in turn changed pump pulse duration to 170 ps and maximum available peak power to 16.2 kW. Despite some changes in experimental conditions, physics of spectrum broadening is in principle the same so, the discussed results and streak camera measurement results can be compared qualitatively.

Fig.5.6 depicts measured supercontinuum spectrograms at various pump energy levels. Analysis reveals peculiar results. Initially (0.05 µJ)
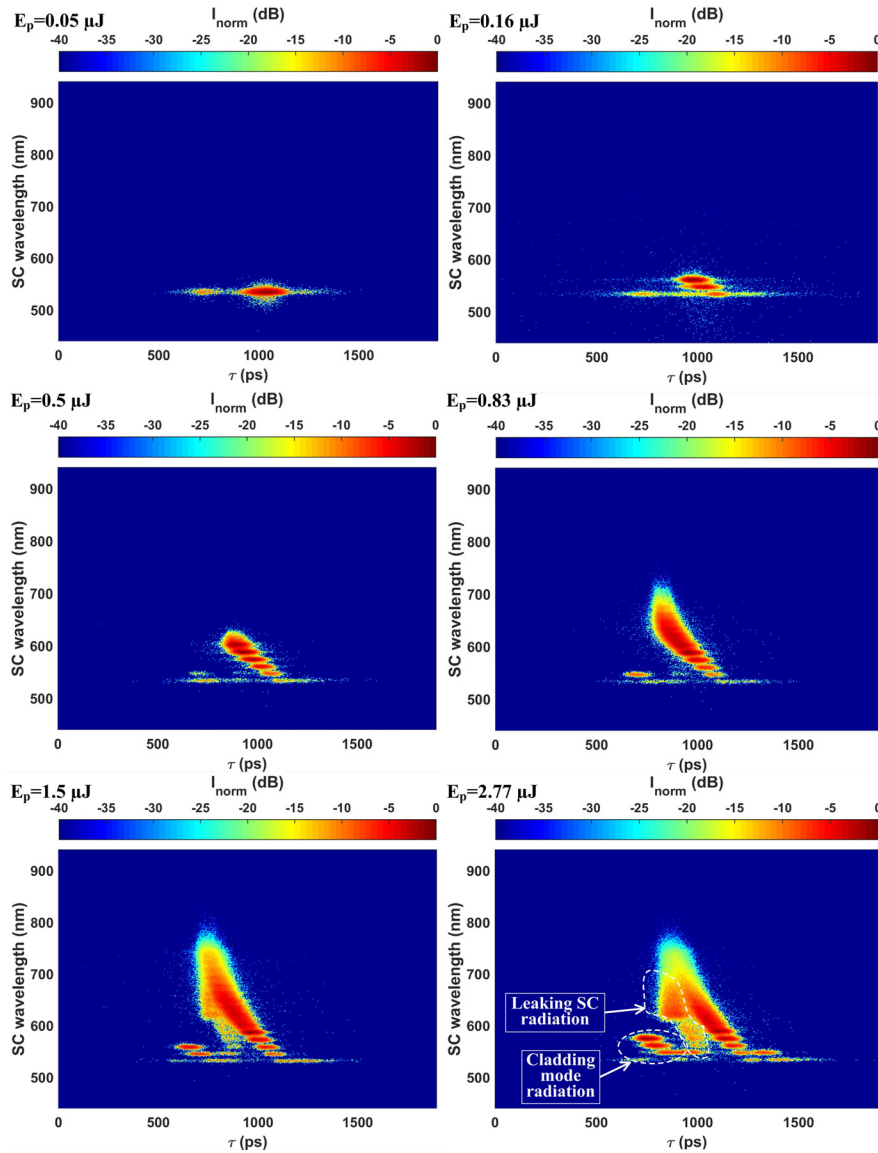
Figure 5.6: Measured spectrograms of supercontinuum at various pump pulse energies. Zero time point is arbitrary since only relative temporal positions of spectral components are important.

spectrum is broadened around the pump due to four-wave mixing and self-phase modulation. Surprisingly, in time domain the pulse is spread up to 900 ps: the peak which width (FWHM) corresponds to initial pump pulse is surrounded by a notable pedestal (Fig.5.7 left). With reference to GVD data (Fig.2.12), it is obvious that PCF dispersion cannot be the cause of such large pulse spreading in time. We think it is due to the fact that a notable portion of laser radiation is propagating not in the
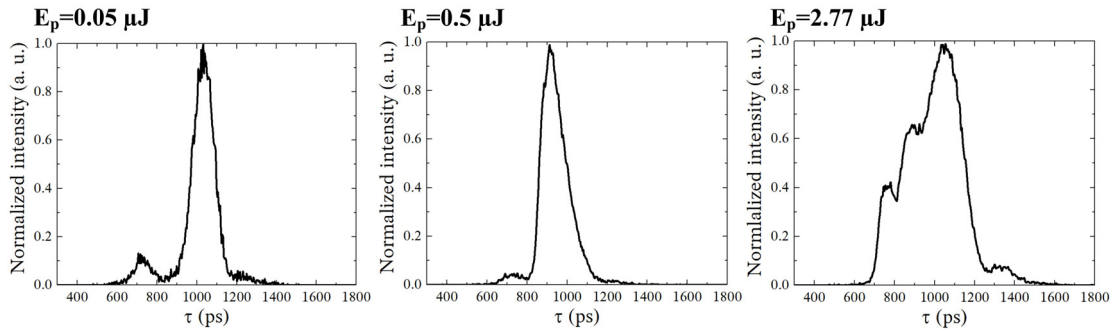
Figure 5.7: Measured supercontinuum pulse temporal intensity at various pump energies.

fundamental PCF spatial mode: the leading (with respect to fundamental mode radiation) part of this radiation propagates through the microstructured cladding part of the PCF, therefore effective refractive index for it is smaller than that of the fundamental PCF mode, while the trailing part of the radiation probably propagates in the cladding part outside the microstructured region where refractive index is higher than that of the fundamental PCF mode. We can also see that a small peak forms roughly at 320 ps distance ahead of the pump pulse. This is probably a spatial mode forming in the microstructured cladding part of the PCF (we will refer to it as cladding mode). Due to lower effective refractive index it propagates with greater group velocity than fundamental mode in the core of the PCF. Using estimated group refractive index values for fundamental mode (core mode) of PCF (Fig.3.2 left) we can calculate group refractive index for the cladding mode: n_g(at 532 nm)=1.6174. Since n_g for fundamental orthogonal polarization modes (core modes) at 532 nm differs only by 0.0001, we can assume that this is also true for the cladding mode. In general, higher order spatial modes can form in any waveguide, but propagation losses for them are usually significantly higher than that of fundamental mode [303]. According to numerical analysis, higher order modes in the core of our PCF should not exist for wavelengths above 500 nm. Results suggest that our PCF has considerable confinement losses: small portions of radiation from fundamental mode (core mode) are constantly leaking to the cladding. We think that some

155

part of this leaking radiation couples into cladding mode in turn enabling its formation. Fig.5.8 depicts numerically calculated profiles of possible cladding modes which have refractive indices yielding results closest to the measured temporal delay.
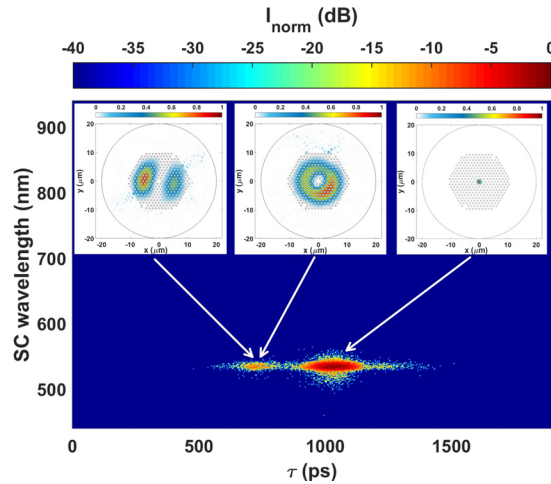

Figure 5.8: Measured spectrogram of supercontinuum at minimum pump pulse energy and spatial profiles of fundamental mode (right) and two possible cladding modes (left and center) which have refractive indices yielding results closest to the measured temporal delay.

When pump pulse energy is increased (0.16 μJ - 0.5 μJ), distinct Raman Stokes peaks appear in the spectrum due to cascaded Raman scattering. For even higher energies (0.83 μJ - 2.77 μJ), a relatively smooth supercontinuum spectrum part extending into longer wavelengths appears indicating that four-wave mixing dominates spectrum extension into long-wavelength region. Notice that long-wavelength spectrum components are shifted in time ahead of pump wavelength – this is due to lower group refractive index of PCF (Fig.3.2 left). However, part of generated supercontinuum radiation (referred to as leaking SC radiation in Fig.5.6) is shifted too far ahead in time (we determined this by calculating temporal walk-off with respect to pump wavelength) which implies that this radiation due to PCF propagation losses leaks away from the fundamental mode and propagates in the PCF cladding where effective refractive index is lower. Another important thing to notice is that leading temporal feature corresponding to the aforementioned cladding mode exhibits spectral broadening at higher pump pulse energies (see Fig.5.6).

156

This can be explained considering the fact that for higher pump energies more energy is leaked to cladding mode: when threshold for stimulated Raman scattering is reached, it occurs for cladding mode radiation as well.

Further on, we measured supercontinuum spectrograms at various pump polarization angles with respect to one of principal polarization axis of the PCF (Fig.5.9). Results of this measurement show that when pump
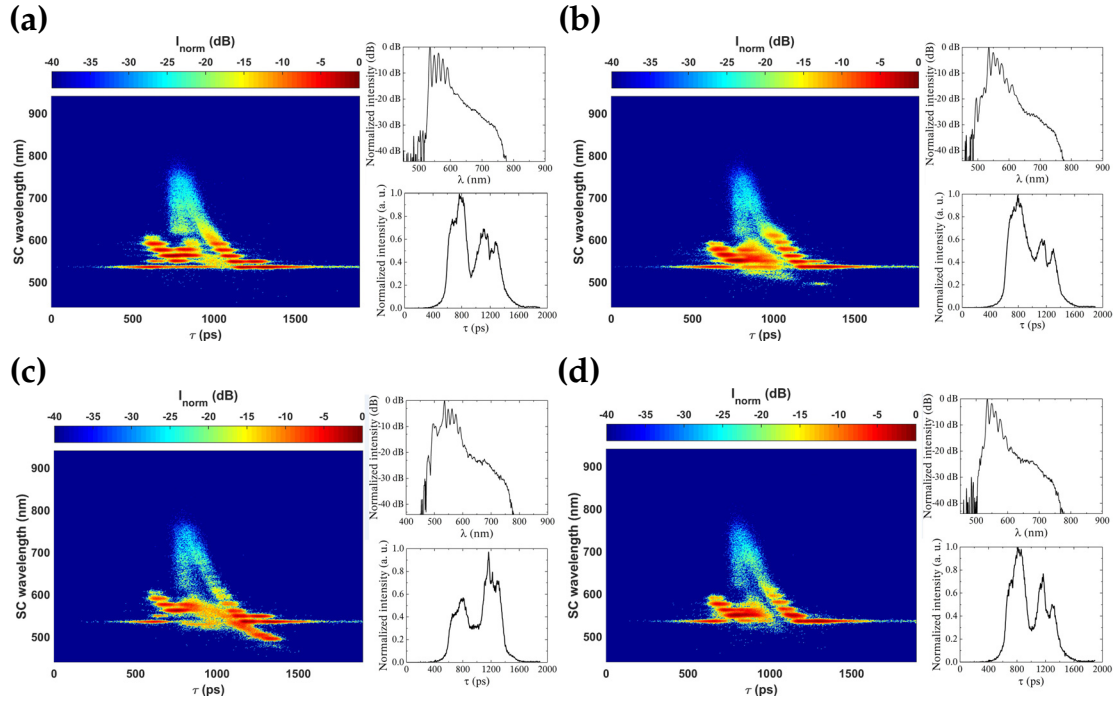
Figure 5.9: Spectrograms and corresponding spectral and temporal intensity of supercontinuum at various pump polarization angles with respect to one of principal polarization axis of the PCF: (a) – 0 deg, (b) – 45 deg, (c) – 90 deg, (d) – 135 deg. Zero time point is arbitrary since only relative temporal positions of spectral components are important

polarization is aligned with one of principal polarization axis of the PCF (Fig.5.9 c), Raman anti-Stokes peaks appear. This concurs with previous supercontinuum spectrum dependence on polarization measurements (Fig.5.4 right). As expected, leaking supercontinuum radiation and cladding mode radiation are visible in all cases. One may notice that spectrum extension in case of streak camera measurements is somewhat different from previous spectrum measurements (Fig.5.3). This is partly due to slightly different experimental conditions (peak power, pulse duration)

but another reason might be decreasing HC13 grade filter transmittance for wavelengths below 500 nm (Fig.5.2).

Numerical simulation results. As mentioned in literature overview, pulse temporal profile during supercontinuum generation in case of subnanosecond pulses should be modulated due to phenomenon called modulation instability which as suggested in [225] can be interpreted as time domain equivalent of four-wave mixing. In this case the characteristic period of modulations, calculated according to Eq.1.30, should be approximately 25 fs. As mentioned before, temporal resolution of streak camera in our case was 10 ps, so it is clear that fine temporal structure of supercontinuum temporal intensity could not be distinguished. For this reason, numerical simulation of supercontinuum evolution when propagating in PCF was performed using the same numerical simulation model described in chapter 4 of this thesis. Unfortunately, numerical simulation in this case is very time consuming: spectral range of simulated supercontinuum is very broad compared to initial pump pulse spectral width (5 pm), integration step is very small due to large PCF dispersion variations through the whole spectral range (depending on the PCF dispersion it is from 2 μm to several tens of micrometers) and, in order to maintain the necessary accuracy, very small spectral resolution has to be used – 10 points per 5 pm. Numerical simulation for propagation through 1 cm long PCF due to 2^{20} time-domain and frequency-domain grid points can take more than 1 hour, so we limited simulations to 150 cm PCF length. Pump pulse polarization was set to be in the intermediate position (45° angle) with respect to principal axes of polarization of the PCF and pump pulse energy was set to be equal for both modes (1.38 μJ). Although quantitative comparison with the experiment is not possible, this was sufficient to demonstrate key features of supercontinuum generation in our PCF and compare the results qualitatively.

Numerically simulated evolution of supercontinuum spectrum is shown in Fig.5.10. Results reveal that at first 30 cm of propagation it is hard to notice any spectrum expansion: self-phase modulation induces some spectrum broadening, but it is very small. Notable small scale
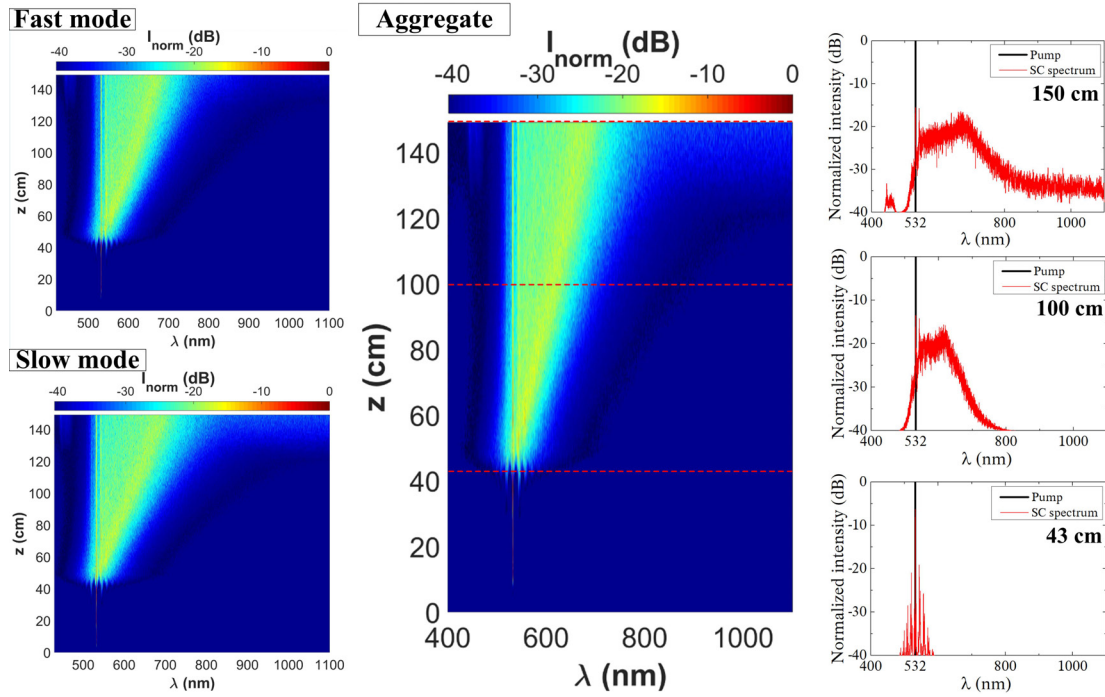
Figure 5.10: Numerically simulated evolution of supercontinuum spectrum (λ_p=532 nm, τ=170 ps): left- fast and slow mode evolution, center – aggregate supercontinuum spectrum evolution, right – aggregate supercontinuum spectra after various propagation distances.

spectrum expansion starts after roughly 30 cm of propagation in the PCF and after approximately 45 cm a sudden broadening occurs – spectrum bandwidth becomes sufficiently large for four-wave mixing to dominate spectrum broadening process which leads to rapid increase of spectrum bandwidth. Unlike femtosecond pump pulse case analyzed in previous chapter, spectrum continues to gradually expand after rapid broadening point. Another important observation is absence of distinct peaks due to cascaded Raman scattering. This is due to the fact that initially Raman gain is smaller than that of four-wave mixing so low intensity Raman peaks are absorbed in continuous spectrum generated due to four-wave mixing processes [21, 122]. After extensive spectrum broadening four-wave mixing gain is reduced and becomes comparable to Raman gain: at this point distinct Raman peaks begin to emerge on a continuous spectrum pedestal as observed in Fig.5.3. From our numerical simulations we can

claim that after 150 cm of propagation this point is not reached yet and four-wave-mixing dominates supercontinuum spectrum formation.

From Fig.5.10 it is also visible that orthogonal polarization modes yield very similar supercontinuum spectra: only in long-wavelength spectral region (above 700 nm) slow polarization mode supercontinuum in slightly broader. Such results were expected as they reflect the fact that group refractive indices for orthogonal polarization modes of the PCF are very similar in short wavelength region (below 650 nm), thus generated supercontinuum spectra are very similar as well.

More data to explain occurrence of rapid spectrum expansion after 45 cm of propagation can be gained from supercontinuum temporal intensity evolution simulation results shown in Fig.5.11. As expected, ortho-
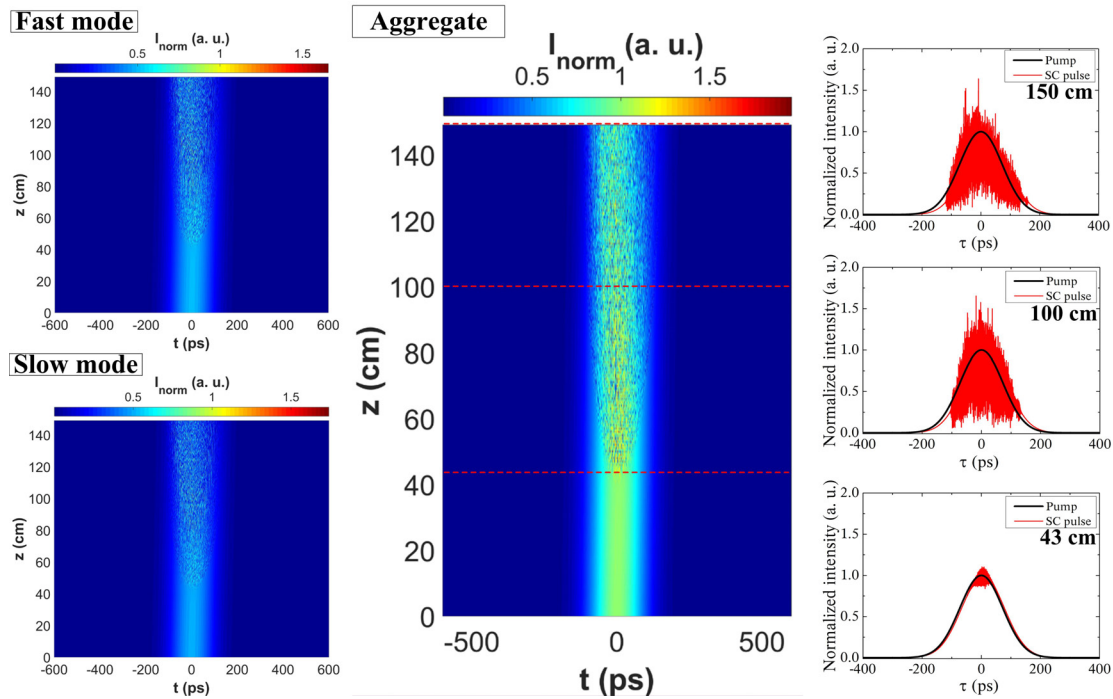
Figure 5.11: Numerically simulated evolution of supercontinuum temporal intensity (λ_p=532 nm, τ=170 ps): left- fast and slow mode evolution, center – aggregate supercontinuum temporal intensity evolution, right – aggregate supercontinuum temporal intensities after various propagation distances.

gonal polarization mode supercontinuum temporal intensities are very similar. The key point of temporal intensity evolution is appearance of fine temporal structure which matches point of rapid spectrum expansion.

Nonlinear process behind this is the aforementioned modulation instability phenomenon [21, 122, 209]. Estimated average oscillation period of these modulations in central part of pulse is approximately 35 fs which is in reasonable agreement with theoretically calculated period for pump wavelength. From temporal intensity evolution we also need to stress that after 150 cm of propagation in the PCF pulse temporal profile is spread to roughly 204 ps (estimated at FWHM with respect to modulated pulse amplitude). This is a result of temporal walk-off of various supercontinuum spectral components due to their different group velocities. More importantly, compared to temporal profiles obtained from streak camera measurements (Fig.5.7), supercontinuum temporal intensity is much narrower and does not display any features further away from the pump pulse which confirms our suggestion that a notable portion of supercontinuum radiation is propagating not in the fundamental PCF spatial mode – this effect could not be accounted in numerical simulation model and therefore is not visible.

Supercontinuum in case of 1064 nm pump. For supercontinuum generation in case of first harmonic pump we used maximum pump pulse energy of 2.75 μJ – roughly 61% of the measured LIDT pulse energy for this PCF. This corresponds to maximum peak power of 9.17 kW. Generated supercontinuum spectra are depicted in Fig.5.12. As in femtosecond supercontinuum case, the spectrum width exceeded sensitivity range of a single spectrometer, so two separate spectrometers were used for registration. Supercontinuum spectrum in case of first harmonic pump, extended through the entire visible range and beyond – from roughly 400 nm to 1300 nm. It is obvious that supercontinuum spectrum in case of subnanosecond pump durations is different from femtosecond pump case (Fig.4.6): it has no sharp peaks in spectral region with wavelengths less than pump wavelength (Fig.5.12 left), while for longer than pump wavelengths there are several distinguishable peaks (Fig.5.12 right). As in second harmonic pump case, such results are related to PCF dispersive properties and the fact that main nonlinear processes responsible for supercontinuum formation when pump pulse duration exceeds several
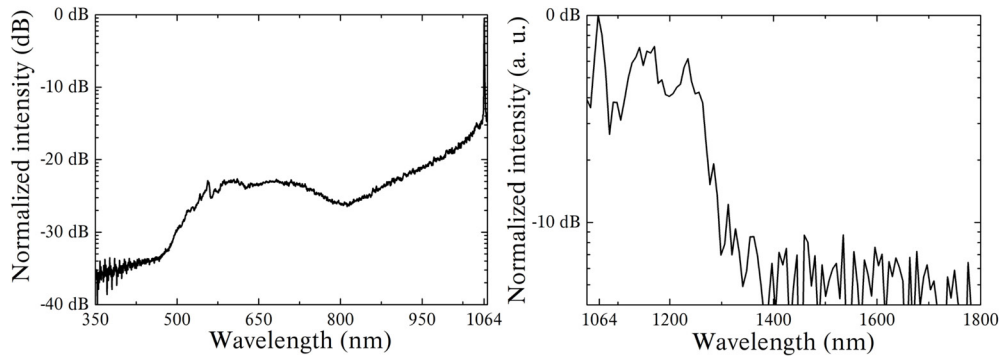
161

Figure 5.12: Spectra of supercontinuum generated in PM PCF using maximum available energy (2.75 µJ) pump pulses. Pulse energy was measured after focusing microscope objective.

picoseconds are four-wave mixing and stimulated Raman scattering effects [21, 36, 122, 241]. Since group refractive index is very similar for all wavelengths between 750 nm and 1250 nm (Fig.3.2), group velocity mismatch for interacting waves with respect to pump wavelength is very small compared to pump pulse duration (Fig.5.5 left) so generated spectrum components can co-propagate and interact in long distances which results in efficient and relatively smooth spectrum broadening due to four-wave mixing processes. The peaks at approximately 1116 nm, 1173 nm and 1237 nm correspond to multiples of frequency offset of -13.2 THz with respect to pump wavelength which matches maximum Raman gain frequency offset in fused silica (Fig.1.14), so these are Raman Stokes peaks generated on continuum pedestal.

The influence of the two key nonlinear processes is further clarified by analyzing supercontinuum spectrum dependence on pump pulse energy (Fig.5.13). At lowest pump pulse (0.4 µJ – 0.6 µJ) energies the low intensity Raman Stokes peaks at the aforementioned wavelengths appear followed by generation of continuous spectrum to shorter than pump wavelengths due to four-wave mixing. At higher energies (0.6 µJ – 2 µJ), distinct peaks in the visible range of spectrum start to emerge. Firstly, a peak at 619 nm appears and when pump energy is slightly increased a second peak appears at 636 nm: their frequency separation (roughly 13.2 THz) confirms that this happens due to stimulated Raman scattering.
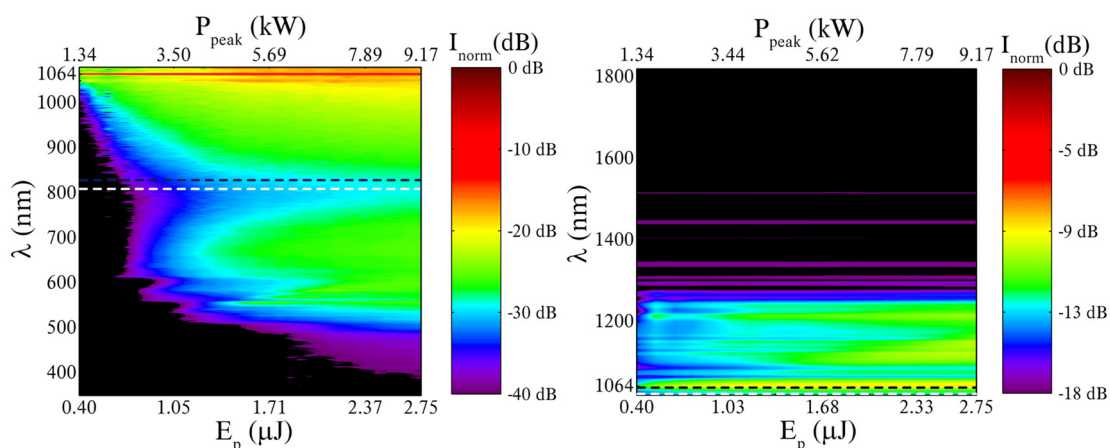
162

Figure 5.13: Supercontinuum dependence on pump pulse energy: left –
registered using VIS/NIR range spectrometer, right – using IR spectrometer.
Dashed white lines depict ZDWs for slow polarization mode while black dashed
lines – ZDWs for fast polarization mode.

When pump energy is increased slightly more, a continuous spectrum
shifting into longer wavelengths forms due to combined effect of four-
wave mixing, Raman processes and cross-phase modulation between
generated spectral components. The same situation occurs for the second
emerging peak at 562 nm which is followed by Stokes-shifted peak at
576 nm and formation of continuous spectrum. The third peak at 540 nm
is the source of Raman Stokes (553.1 nm and 566.9 nm) and anti-Stokes
(527 nm and 515.6 nm) spectrum components appearing at slightly higher
pump energies. Eventually (at approximately 2 µJ energy), all the peaks in
the visible spectral region are merged into a continuum. The situation is
similar in the IR part of supercontinuum where continuum forms around
Raman Stokes peaks. At highest pump energies (2 µJ – 2.75 µJ) spectrum
broadens into shorter wavelengths down to 400 nm, however, the intensity
of shortest wavelength components is more than an order of magnitude
lower than those closer to pump wavelength. As already noted, the reason
for this intensity limitation is large GVM between short-wavelength spec-
tral components and pump wavelength (Fig.5.5 left).

Numerical simulation results. Supercontinuum spectrum evolu-
tion when propagating in PCF is depicted in Fig.5.14. The aforementioned

163

considerations about extremely time-consuming numerical simulation are valid in this case as well: due to even broader supercontinuum spectrum bandwidth in this case it took more three hours to simulate propagation through 1 cm of PCF, so we limited numerical simulation to 50 cm. As in second harmonic case, pump pulse polarization was set to be in the intermediate position (45° angle) with respect to principal axes of polarization of the PCF and pump pulse energy was set to be equal for both modes (1.5 µJ). Supercontinuum spectrum evolution shows that at first
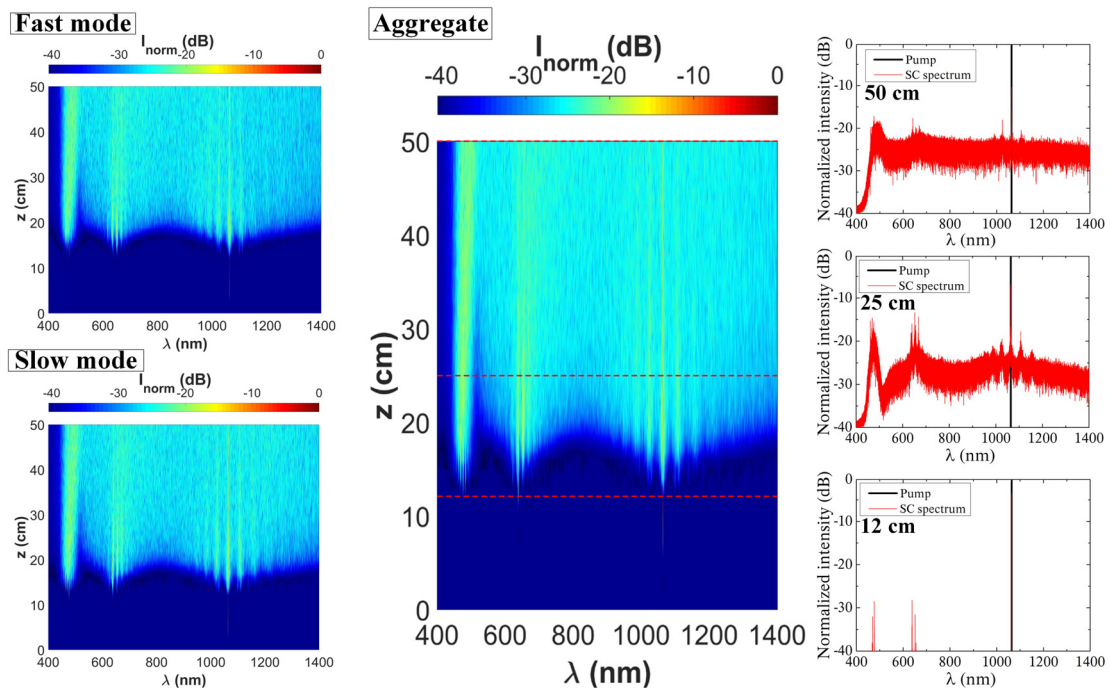
Figure 5.14: Numerically simulated evolution of supercontinuum spectrum (λ_p=1064 nm, τ=300 ps): left- fast and slow mode evolution, center – aggregate supercontinuum spectrum evolution, right – aggregate supercontinuum spectra after various propagation distances.

12 cm of propagation spectrum expansion is hardly noticeable: pump spectrum is slightly broadened due to self-phase modulation. Notable expansion begins after approximately 12 cm of propagation: distinct peaks appear in the visible range of spectrum. Subsequently, symmetrical sidebands emerge around pump and the generated peaks which during further propagation in the PCF gradually merge into continuous spectrum. The symmetrical positions of these sidebands suggest they are

related to four-wave mixing processes which together with self-phase and cross-phase modulation between generated spectrum components form supercontinuum. As in second harmonic pump case, distinct peaks due to cascaded Raman scattering are not visible: we can say that four-wave mixing processes dominate supercontinuum spectrum formation during first 50 cm of propagation in PCF. It is also notable that high intensity peak around 476 nm visible in numerical simulations is not observed in experimentally measured spectra (Fig.5.12). We think this is due to the fact that refractive index dispersion and GVD of our PCF were estimated in spectral region above 500 nm and data for shorter wavelengths (necessary in numerical simulations) were obtained by extrapolating measurement results. Another possible reason for discrepancies is the aforementioned fact that we could not estimate PCF losses reliably.

Temporal intensity evolution, shown in Fig.5.15, displays the same results as in second harmonic case: appearance of fine temporal structure of the pulse due to modulation instability matches point of notable super-continuum spectrum expansion. Estimated average period of oscillations in central part of pulse is approximately 20 fs. Notice that peak intensities of these oscillations are up to 7 times greater than the original pump pulse, while in second harmonic case the intensities were greater up to 1.6 times. The most probable explanation of such difference is related to GVD of the PCF. Although first harmonic pump wavelength (1064 nm) is in normal GVD region, it is actually very close to ZDWs (of both polarization modes) of the PCF. Therefore, supercontinuum spectrum extends into anomalous GVD range at very early stages of formation when temporal oscillations are only beginning to form. It is known that in anomalous GVD region temporal modulations that form are soliton-like subpulses which can have significantly greater amplitudes [21, 36, 122].

Supercontinuum spectrum and temporal intensity evolution for orthogonal polarization modes is essentially the same. Only careful comparison of spectra reveals that distinct peaks emerging at initial stage of propagation are at slightly different wavelengths (several nanometer difference), however, subsequent stage of continuous spectrum formation
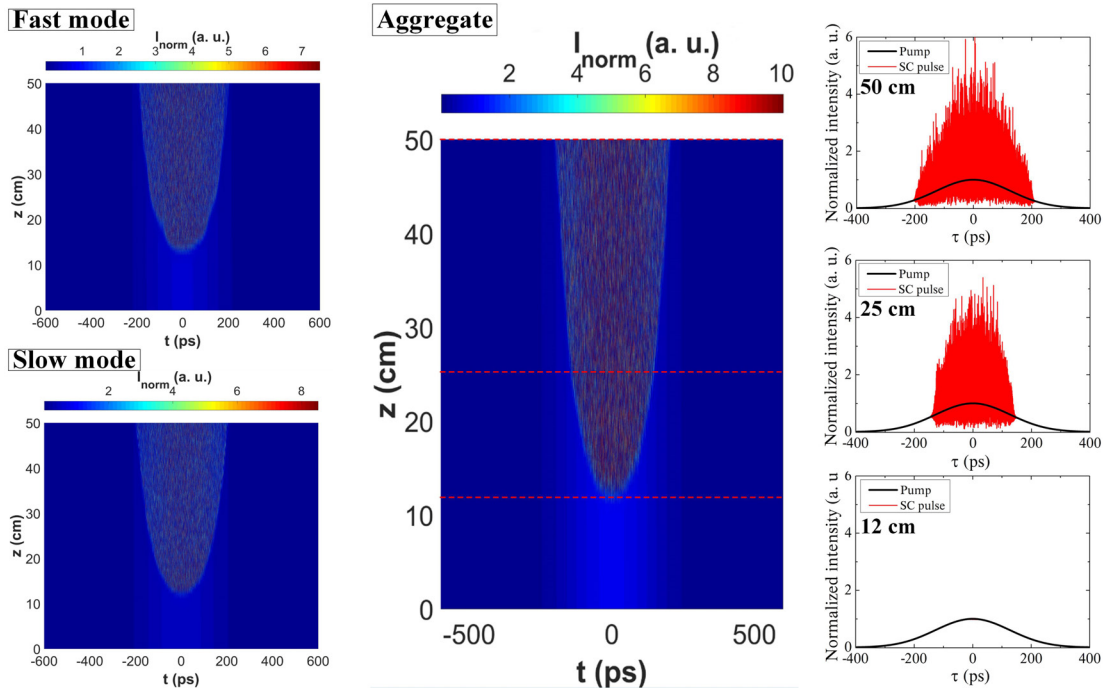
Figure 5.15: Numerically simulated evolution of supercontinuum temporal intensity ($\lambda_\mathbf{p}$=1064 nm, τ=300 ps): left- fast and slow mode evolution, center – aggregate supercontinuum temporal intensity evolution, right – aggregate supercontinuum temporal intensities after various propagation distances.

makes any differences indistinguishable. The same can be said about temporal intensity evolution: temporal positions of soliton-like subpulses are slightly (tens of femtoseconds) different. Such differences are due to different dispersive characteristics of PCF for orthogonal polarization modes.

5.3 Conclusions

In conclusion, we presented experimental and numerical simulation investigation results of supercontinuum, generated in highly nonlinear PM PCF with two ZDWs, using single-wavelength pumping setups with first or second harmonics of a subnanosecond Nd:YAG microlaser. Supercontinuum extended from 400 nm to 1300 nm in case of λ_p=1064 nm and from 400 nm to 900 nm in case of λ_p=532 nm. Spectrum extension in

both cases is mainly limited to group velocity mismatch between pump wavelength and generated supercontinuum spectrum components. Results confirmed that main nonlinear phenomena responsible for supercontinuum generation in subnanosecond pump pulse case are different than in femtosecond pump case: here four-wave mixing and processes related to Raman scattering play a central role in spectrum expansion.

During time-resolved supercontinuum observation with streak camera we could directly observe that a notable portion of supercontinuum radiation propagates not in the fundamental PCF spatial mode: some portion is constantly leaking to the cladding and another part of it can propagate in a cladding mode. We think that existence of the cladding mode is possible due to coupling of some part of constantly leaking radiation to this cladding mode. Using estimated group refractive index values for fundamental mode of PCF (Fig.3.2 left) we can calculate group refractive index of the cladding mode: n_g(at 532 nm)=1.6174.

Numerical simulation results confirmed that in both cases temporal shape of supercontinuum pulse has fine structure (oscillations with period of the order of several tens of femtoseconds) appearing due to modulation instability phenomenon. In addition, simulated evolution of supercontinua generated by orthogonal polarization modes displayed rather symbolic differences determined by slightly different dispersive characteristics of the PCF.

Finally, we need to note that spectrum extension over the whole visible spectrum range and beyond in PCF with two ZDWs was demonstrated without any sophisticated technological modifications of the PCF or complicated experimental setups. Such subnanosecond supercontinuum source is highly desirable in certain applications such as seeding subnanosecond optical parametric generators as conventional commercially available supercontinuum sources are not suitable for this task.

Main results and conclusions

1. A novel experimental technique for measuring GVD of PCFs based on cross-correlation frequency resolved optical gating (XFROG) trace analysis of a femtosecond supercontinuum generated in a photonic crystal fiber was demonstrated. Experiment results for two different PCFs showed that fairly accurate GVD measurement is possible when pump wavelength for supercontinuum generation is in anomalous GVD range or close to ZDW of the PCF in normal GVD range. This indicates that with such choice of pump wavelength, essentially all spectrum components of femtosecond supercontinuum are generated simultaneously at the same time after very short propagation distance in PCF making the proposed group velocity dispersion measurement method feasible.

2. GVD measurements were performed in 540 nm – 1400 nm spectral range for birefringent PCF and in 710 nm – 1450 nm spectral range for the second (non-birefringent) PCF. From results it is evident that measurement range is determined by spectral extent of XFROG trace which in principle can cover the entire supercontinuum bandwidth. In case of PM PCF, the novel technique also proved to be capable of distinguishing GVD of orthogonal polarization modes, which allowed to determine difference of their group refractive indices and determine effective limits of PCF birefringence. Unlike other experimental fiber GVD measurement techniques, our technique can measure GVD of orthogonal PCF polarization modes simultaneously.

3. An experimental method for measuring phase refractive index of PCF mode based on analyzing phase shift of interfering adjacent longitudinal continuous wave laser modes corresponding to shift from constructive to destructive interference was demonstrated. Correct measurement is performed only when analyzed shifts are within the same interference order (Eq.3.14). Measured phase refractive index for He-Ne laser wavelength for both PCFs is in very good agreement with theoretically calculated values.

4. Experimental and numerical investigation of femtosecond supercontinuum generation in highly nonlinear PM PCF with two ZDWs was performed and revealed that orthogonal polarization modes produce distinct slightly different supercontinua.

5. Experimental investigation of supercontinuum generation in highly nonlinear PM PCF with two ZDWs using chirped femtosecond pump pulses with wavelength in anomalous GVD range of PCF showed that chirped pump supercontinuum has somewhat broader spectrum compared to bandwidth limited pump case at the same peak power. This together with XFROG analysis results indicates that pump pulse chirp influences not only initial stage of soliton formation but also subsequent soliton fission and dispersive wave generation phenomena. Numerical simulations produced qualitatively similar results supporting our assumptions about influence of pump pulse chirp on supercontinuum formation.

6. Experimental and numerical investigation of supercontinuum generation in highly nonlinear PM PCF with two ZDWs using first or second harmonic of a subnanosecond Nd:YAG microlaser was performed and spectrum extension over the whole visible spectrum range and beyond was demonstrated without any sophisticated technological modifications of the PCF or complicated experimental setups. During supercontinuum investigation with streak camera we could directly observe that a portion of supercontinuum radiation propagates not in the fundamental PCF spatial mode: such radiation is separated in time due to different experienced effective refractive index of photonic crystal fiber, thus can be directly detected.

Bibliography

[1] J. Tyndall, *Notes of a course of nine lectures of light* (Longmans, Green and CO., 1870).

[2] J. Tyndall, *Six lectures on light* (D. Appleton and Company, 1873).

[3] R. J. Bates, *Optical switching and networking handbook* (McGraw-Hill, 2001).

[4] F. P. Kapron, D. B. Keck, R. D. Maurer, Radiation losses in glass optical waveguides, Appl. Phys. Lett. **17**(10), 423–425 (1970).

[5] C. K. Jonathan, Photonic crystal fibres, Nature **424**, 847 (2003).

[6] E. Yablonovitch, Inhibited spontaneous emission in solid-state physics and electronics, Phys. Rev. Lett. **58**(20), 2059–2062 (1987).

[7] S. John, Strong localization of photons in certain disordered dielectric superlattices, Phys. Rev. Lett. **58**(23), 2486–2489 (1987).

[8] J. D. Joannopoulos, P. R. Villneneuve, S. Fan, Photonic crystals: putting a new twist on light, Nature **386**, 143–149 (1997).

[9] Pal, B., etc. all, *Frontiers in guided wave optics and optoelectronics* (2010).

[10] K. M. Ho, C. T. Chan, C. M. Soukoulis, Existence of a photonic gap in periodic dielectric structures, Phys. Rev. Lett. **65**(25), 3152–3155 (1990).

[11] P. Yeh, A. Yariv, Bragg reflection waveguides, Opt. Commun. **19**(3), 427–430 (1976).

[12] P. Yeh, A. Yariv, E. Marom, Theory of Bragg fiber, J. Opt. Soc. Am. **68**(9), 1196–1201 (1978).

[13] P. S. Russell, Photonic-Crystal Fibers, J. Lightwave Technol. **24**(12), 4729–4749 (2006).

[14] J. C. Knight, T. A. Birks, P. S. J. Russell, D. M. Atkin, Pure silica single-mode fiber with hexagonal photonic crystal cladding, in *Optical Fiber Communication Conference 1996* (San Jose, 1996), 339–342.

[15] J. C. Knight, T. A. Birks, P. S. J. Russell, D. M. Atkin, All-silica single-mode optical fiber with photonic crystal cladding, Opt. Lett. **21**(19), 1547–1549 (1996).

[16] R. Buczynski, Photonic crystal fibers, Acta Phys. Pol. A **106**(2), 141–167 (2004).

[17] R. F. Cregan, B. J. Mangan, J. C. Knight, T. A. Birks, P. S. J. Russell, P. Roberts, D. C. Allan, Single-mode photonic band gap guidance of light in air, Science **285**, 1537–1539 (1999).

[18] Y. Fink, D. J. Ripin, S. Fan, C. Chen, J. D. Joannopoulos, E. L. Thomas, Guiding optical light in air using an all-dielectric structure, J. Lightwave Technol. **17**(11), 2039–2041 (1999).

[19] F. Brechet, P. Roy, J. MArcou, D. Pagnoux, Singlemode propagation into depressed- core-index photonic bandgap fibre designed for zero-dispersion propagation at short wavelengths, Electron. Lett. **36**(6), 514–515 (2000).

[20] F. Poli, A. Cucinotta, S. Selleri, *Photonic crystal fibers. Properties and applications* (Springer, 2007).

[21] J. M. Dudley, G. Genty, S. Coen, Supercontinuum generation in photonic crystal fiber, Rev. Mod. Phys **78**(4), 1135–1184 (2006).

[22] I. Babushkin, A. Tajalli, H. Sayinc, U. Morgner, G. Steinmayer, A. Demircan, Simple route toward efficient frequency conversion for generation of fully coherent supercontinua in the mid-IR and UV range, Light Sci. Appl. **6**, 1–8 (2017).

[23] L. Froehly, J. Meteau, Supercontinuum sources in optical coherence tomography: a state of the art and the application to scan-free time domain correlation techniques and depth dependant dispersion compensation, Opt. Fiber Technol. **18**, 411–419 (2012).

[24] B. Heise, S. E. Schausberger, S. Häuser, B. Plank, D. Salaberger, E. Leiss-Holzinger, D. Stifter, Full-field optical coherence microscopy with a sub-nanosecond supercontinuum light source for material research, Opt. Fiber Technol. **18**, 403–410 (2012).

[25] J. Clowes, Next generation light sources for biomedical applications, Optik & Photonik **3**(1), 36–38 (2008).

[26] R. R. Alfano, S. Shapiro, Emission in the region 4000 to 7000 Å via four-photon coupling in glass, Phys. Rev. Lett. **24**(11), 584–587 (1970).

[27] R. R. Alfano, S. L. Shapiro, Observation of self-phase modulation

and small-scale filaments in crystals and glasses, Phys. Rev. Lett. **24**(11), 592–594 (1970).

[28] J. K. Ranka, R. S. Windeler, A. J. Stentz, Visible continuum generation in air-silica microstructure optical fibers with anomalous dispersion at 800 nm, in *Conference on Lasers and Electo-Optics (CLEO) 1999* (Baltimore, 1999), 25.

[29] J. K. Ranka, R. S. Windeler, A. J. Stentz, Visible continuum generation in air-silica microstructure optical fibers with anomalous dispersion at 800 nm, Opt. Lett. **25**(1), 25 (2000).

[30] J. C. Travers, A. B. Rulkov, B. A. Cumberland, S. V. Popov, J. R. Taylor, Visible supercontinuum generation in photonic crystal fibers with a 400 W continuous wave fiber laser, Opt. Express **16**(19), 14435–14447 (2008).

[31] W. J. Wadsworth, N. Joly, J. C. Knight, T. A. Birks, F. Biancalana, P. S. J. Russell, Supercontinuum and four-wave mixing with Q-switched pulses in endlessly single-mode photonic crystal fibres, Opt. Express **12**(2), 299 (2004).

[32] J. M. Dudley, L. Provino, N. Grossard, H. Maillotte, R. S. Windeler, B. J. Eggleton, S. Coen, Supercontinuum generation in airâĂŞsilica microstructured fibers with nanosecond and femtosecond pulse pumping, J. Opt. Soc. Am. B **19**(4), 765 (2002).

[33] S. Coen, A. Hing Lun Chau, R. Leonhardt, J. D. Harvey, J. C. Knight, W. J. Wadsworth, P. S. J. Russell, Supercontinuum generation by stimulated Raman scattering and parametric four-wave mixing in photonic crystal fibers, J. Opt. Soc. Am. B **19**(4), 753–764 (2002).

[34] S. G. Leon-Saval, T. A. Birks, W. J. Wadsworth, P. S. J. Russell, M. W. Mason, Supercontinuum generation in submicron fibre waveguides, Opt. Express **12**(13), 2864–2869 (2004).

[35] C. Xiong, A. Witkowska, T. A. Birks, W. J. Wadsworth, Enhanced visible continuum generation from a microchip 1064 nm laser, Opt. Express **14**(13), 6188–6193 (2006).

[36] J. Dudley, R. Taylor, *Supercontinuum generation in optical fibers* (Cam-

bridge University press, 2010).

[37] X. Zhu, X. Zhang, J. Peng, X. , J. Li, Photonic crystal fibers for supercontinuum generation, Front. Optoelectron. China **4**(4), 415–419 (2012).

[38] J. M. Dudley, G. Genty, Supercontinuum light, Physics Today **66**, 29–34 (2013).

[39] R. Driben, N. Zhavoronkov, Supercontinuum spectrum control in microstructure fibers by initial chirp management, Opt. Express **18**(16), 16733–16738 (2010).

[40] H. Zhang, S. Yu, J. Zhang, W. Gu, Effect of frequency chirp on supercontinuum generation in photonic crystal fibers with two zero-dispersion wavelengths, Opt. Express **15**(3), 1147–1154 (2007).

[41] A. Fuerbach, C. Miese, W. Koehler, M. Geissler, Supercontinuum generation with a chirped-pulse oscillator, Opt. Express **17**(7), 5905–5911 (2009).

[42] X. Fu, L. Qian, S. Wen, D. Fan, Nonlinear chirped pulse propagation and supercontinuum generation in microstructured optical fibre, J. Opt. A Pure Appl. Opt. **6**, 1012–1016 (2004).

[43] X. Hu, Y. Wang, W. Zhao, Z. Yang, W. Zhang, C. Li, H. Wang, Nonlinear chirped-pulse propagation and supercontinuum generation in photonic crystal fibers, Appl. Opt. **49**(26), 4984–4989 (2010).

[44] Z. Zhu, T. G. Brown, Effect of frequency chirping on supercontinuum generation in photonic crystal fibers, Opt. Express **12**(4), 689–694 (2004).

[45] K. L. Corwin, N. R. Newbury, J. M. Dudley, S. Coen, S. A. Diddams, K. Weber, R. S. Windeler, Fundamental noise limitations to supercontinuum generation in microstructure fiber, Phys. Rev. Lett. **90**(11), 113904–1–4 (2003).

[46] M. Tianprateep, J. Tada, F. Kannari, Influence of polarization and pulse shape of femtosecond initial laser pulses on spectral broadening in microstructure fibers, Opt. Rev. **12**(3), 179–189 (2005).

[47] Y. Li, J. Hou, Z. Jiang, Chirped-pulse propagation and spectral

compression in all-normal dispersion photonic crystal fibers, Proc. SPIE **8419**, 84190K–1–6 (2012).

[48] C. Cheng, Y. Wang, Q. Lv, Effect of initial chirp on supercontinuum generation in dispersion decreasing fibers, Proc. SPIE **8331**, 83310O–1–8 (2016).

[49] J. C. Travers, Blue extension of optical fibre supercontinuum generation, J. Opt. **12**(11), 1–19 (2010).

[50] P. A. Champert, V. Couderc, P. Leproux, S. Février, V. Tombelaine, L. Labonté, P. Roy, C. Froehly, P. Nerin, White-light supercontinuum generation in normally dispersive optical fiber using original multi-wavelength pumping system, Opt. Express **12**(19), 4366–4371 (2004).

[51] E. Räikkönen, G. Genty, O. Kimmelma, M. Kaivola, K. P. Hansen, S. C. Buchter, Supercontinuum generation by nanosecond dual-wavelength pumping in microstructured optical fibers, Opt. Express **14**(17), 7914–7923 (2006).

[52] V. Couderc, P. Leproux, V. Tombelaine, L. Grossard, A. Barthélémy, Raman cascade suppression by using wide band parametric conversion in large normal dispersion regime, Opt. Express **13**(21), 8584–8590 (2005).

[53] A. Čiburys, R. Gadonas, D. Jokšas, Continuum generation in photonic crystal fibres by multi-wavelength amplified sub-nanosecond light pulses, Lith. J. Phys. **50**(1), 83–88 (2010).

[54] J. Travers, S. V. Popov, J. Taylor, Extended blue supercontinuum generation in cascaded holey fibers, Opt. Lett. **30**(23), 3132–3134 (2005).

[55] X. Zhang, X. Zhu, R. Xing, X. Yang, F. Jiang, H. Li, J. Peng, N. Dai, J. Li, Microstructure core photonic crystal fiber for blue extension of supercontinuum generation, Opt. Commun. **298-299**, 191–195 (2013).

[56] C. M. B. Cordeiro, W. J. Wadsworth, T. a. Birks, P. S. J. Russell, Engineering the dispersion of tapered fibers for supercontinuum generation with a 1064 nm pump laser, Opt. Lett. **30**(15), 1980–1982

(2005).

[57] S. P. Stark, A. Podlipensky, N. Y. Joly, P. S. J. Russell, Ultraviolet-enhanced supercontinuum generation in tapered photonic crystal fiber, J. Opt. Soc. Am. B **27**(3), 592–598 (2010).

[58] A. Kudlinski, a. K. George, J. C. Knight, J. Travers, A. Rulkov, S. V. Popov, J. Taylor, Zero-dispersion wavelength decreasing photonic crystal fibers for ultraviolet-extended supercontinuum generation, Opt. Express **14**(12), 5715–5722 (2006).

[59] J. M. Stone, J. C. Knight, Visibly white light generation in uniform photonic crystal fiber using a microchip laser, Opt. Express **16**(4), 2670–2675 (2008).

[60] L. G. Cohen, C. Lin, Pulse delay measurements in the zero material dispersion wavelength region for optical fibers, Appl. Opt. **16**(12), 3136–3139 (1977).

[61] L. Cohen, C. Lin, A universal fiber-optic (UFO) measurement system based on a near-IR fiber Raman laser, IEEE J. Quantum Electron. **14**(11), 855–859 (1978).

[62] B. Luther-Davies, D. Payne, W. Gambling, Evaluation of material dispersion in low loss phosphosilicate core optical fibres, Opt. Commun. **13**(1), 84–88 (1975).

[63] V. Pagé, L. R. Chen, Measuring chromatic dispersion of optical fiber using time-of-flight and a tunable multi-wavelength semiconductor fiber laser, Opt. Commun. **265**, 161–170 (2006).

[64] B. Costa, D. Mazzoni, M. Puleo, E. Vezzoni, Phase shift technique for the measurement of chromatic dispersion in optical fibers using LED's, IEEE J. Quantum Electron. **30**(10), 1497–1503 (1982).

[65] B. Christensen, J. Mark, G. Jacobsen, E. Bødtker, Simple dispersion measurement technique with high resolution, Electron. Lett. **29**(1), 132–134 (1993).

[66] L. Cohen, Comparison of single-mode fiber dispersion measurement techniques, J. Lightwave Technol. **3**(5), 958–966 (1985).

[67] M. Tateda, N. Shibata, S. Seikai, Interferometric method for chro-

matic dispersion measurement in a singlemode optical fiber, IEEE J. Quantum Electron. **17**(3), 404–407 (1981).

[68] H.-T. Shang, Chromatic dispersion measurement by white-light interferometry on metre-length single-mode optical fibres, Electron. Lett. **17**, 603–605 (1981).

[69] P. L. Francois, M. Monerie, C. Vassallo, Y. Durteste, F. R. Alard, Three ways to implement interferencial techniques: application to measurements of chromatic dispersion, birefringence, and nonlinear susceptibilities, J. Lightwave Technol. **7**(3), 500–513 (1989).

[70] S. Diddams, J.-C. Diels, Dispersion measurements with white-light interferometry, J. Opt. Soc. Am. B **13**(6), 1120 (1996).

[71] M. J. Saunders, W. B. Gardner, Interferometric determination of dispersion variations in single-mode fibers, J. Lightwave Technol. **5**(12), 1701–1705 (1987).

[72] G. Genty, H. Ludvigsen, M. Kaivola, K. Hansen, Measurement of anomalous dispersion in microstructured fibers using spectral modulation, Opt. Express **12**(5), 929–934 (2004).

[73] T. M. Kardaś, C. Radzewicz, Broadband near-infrared fibers dispersion measurement using white-light spectral interferometry, Opt. Commun. **282**(22), 4361–4365 (2009).

[74] J. C. Knight, J. Broeng, T. A. Birks, P. S. J. Russell, Photonic band gap guidance in optical fibers, Science **282**, 1476–1478 (1998).

[75] A. Baz, G. Bouwmans, L. Bigot, Y. Quiqumpois, Pixelated high-index ring Bragg fibers, Opt. Express **20**(17), 18795–18802 (2012).

[76] J. J. D. Joannopoulos, S. Johnson, J. N. J. Winn, R. R. D. Meade, *Photonic crystals: molding the flow of light* (Princeton University press, 2008).

[77] J. C. Knight, R. P. S. J. Birks, T. A., J. P. de Sandro, Properties of photonic crystal fiber and the effective index model, J. Opt. Soc. Am. A **15**(3), 748–752 (1998).

[78] M. Koshiba, K. Saitoh, Applicability of classical optical fiber theories to holey fibers, Opt. Lett. **29**(15), 1739–1741 (2004).

[79] N. A. Mortensen, J. R. Folkenberg, M. D. Nielsen, K. P. Hansen, Modal cutoff and the V parameter in photonic crystal fibers, Opt. Lett **28**(20), 1879–1881 (2003).

[80] J. Broeng, T. Søndergaard, S. E. Barkou, Waveguidance by the photonic bandgap effect in optical fibres, J. Opt. A: Pure Appl. Opt. **1**, 477–482 (1999).

[81] J. Broeng, S. E. Barkou, T. Søndergaard, A. Bjarklev, Analysis of air-guiding photonic bandgap fibers, Opt. Lett **25**(2), 96–98 (2000).

[82] F. Benabid, P. J. Roberts, Guidance mechanisms in hollow-core photonic crystal fiber, Proc. SPIE **6901**, 69010U–1–10 (2008).

[83] F. Benabid, J. C. Knight, C. Antonopoulos, P. S. J. Russell, Stimulated Raman scattering in photonic crystal fiber, Science (80-.). **298**, 399–403 (2002).

[84] F. H. Stillinger, D. R. Herrick, Bound states in the continuum, Phys. Rev. A **11**(2), 446–454 (1975).

[85] F. Couny, F. Benabid, P. J. Roberts, P. S. Light, M. G. Raymer, Generation and photonic guidance of multi-octave optical-frequency combs, Science **318**, 1118–1122 (2007).

[86] J. C. Travers, W. Chang, J. Nold, N. Y. Joly, P. S. J. Russell, Ultrafast nonlinear optics in gas-filled hollow-core photonic crystal fibers [Invited], J. Opt. Soc. Am. B **28**(12), 11–26 (2011).

[87] P. S. J. Russell, P. Hölzer, W. Chang, A. Abdolvand, J. C. Travers, Hollow-core photonic crystal fibres for gas-based nonlinear optics, Nat. Photonics **8**(4), 278–286 (2014).

[88] N. Y. Joly, J. Nold, W. Chang, P. Hölzer, A. Nazarkin, G. K. Wong, F. Biancalana, P. S. J. Russell, Bright spatially coherent wavelength-tunable deep-UV laser source using an Ar-filled photonic crystal fiber, Phys. Rev. Lett. **106**, 1–4 (2011).

[89] K. F. Mak, J. C. Travers, P. Hölzer, N. Y. Joly, P. S. J. Russell, Tunable vacuum-UV to visible ultrafast pulse source based on gas-filled Kagome-PCF, Opt. Express **21**(9), 10942–10953 (2013).

[90] A. Ermolov, K. F. Mak, M. H. Frosz, J. C. Travers, P. S. J. Rus-

sell, Supercontinuum generation in the vacuum ultraviolet through dispersive-wave and soliton-plasma interaction in a noble-gas-filled hollow-core photonic crystal fiber, Phys. Rev. A **92**, 033821–1–7 (2015).

[91] C. Martelli, J. Canning, K. Lyytikainen, N. Groothoff, Water-core Fresnel fiber, Opt. Express **13**(10), 3890–3895 (2006).

[92] G. S. Wiederhecker, C. M. B. Cordeiro, F. Couny, F. Benabid, S. A. Maier, J. C. Knight, C. H. B. Cruz, H. L. Fragnito, Field enhancement within an optical fibre with a subwavelength air core, Nat. Photonics **1**, 115–118 (2007).

[93] Y. Fink, J. N. Winn, S. Fan, C. Chen, J. Michel, J. D. Joannopoulos, E. L. Thomas, A Dielectric Omnidirectional Reflector, Science **282**, 1679–1683 (1998).

[94] S. G. Johnson, M. Ibanescu, M. Skorobogatiy, O. Weisberg, T. D. Engeness, M. SoljaЁĞ, S. A. Jacobs, J. D. Joannopoulos, Y. Fink, Low-loss asymptotically single-mode propagation in large-core OmniGuide fibers, Opt. Express **9**(13), 748–779 (2001).

[95] S. G. Johnson, M. Ibanescu, M. Skorobogatiy, O. Weisberg, T. D. Engeness, S. A. Jacobs, J. D. Joannopoulos, Y. Fink, Breaking the glass ceiling : hollow OmniGuide fibers, Proc. SPIE **4655**, 1–15 (2002).

[96] J. Canning, Diffraction-free mode generation and propagation in optical waveguides, Opt. Commun. **207**, 35–39 (2002).

[97] J. Canning, E. Buckley, K. Lyytikainen, Propagation in air by field superposition of scattered light within a Fresnel fiber, Opt. Lett **28**(4), 230–232 (2003).

[98] J. Canning, E. Buckley, K. Lyttikainen, T. Ryan, Wavelength dependent leakage in a Fresnel-based air-silica structured optical fibre, Opt. Commun. **205**, 95–99 (2002).

[99] R. Beravat, G. K. L. Wong, M. H. Frosz, X. M. Xi, P. S. J. Russell, Twist-induced guidance in coreless photonic crystal fiber: A helical channel for light, Sci. Adv. **2**, 1–5 (2016).

[100] G. K. L. Wong, R. Beravat, X. M. Xi, M. H. Frosz, P. S. J. Russell, Twist-induced waveguiding in coreless photonic crystal fiber: a new guidance mechanism, in *Optical Fiber Communication Conference 2016* (Anaheim, 2016), 1–3.

[101] P. S. J. Russell, R. Beravat, G. K. L. Wong, Helically twisted photonic crystal fibres, Philos. Trans. R. Soc. A **375**, 1–18 (2017).

[102] K. Saitoh, M. Koshiba, Empirical relations for simple design of photonic crystal fibers, Opt. Express **13**(1), 267–274 (2005).

[103] S. Johnson, J. Joannopoulos, Block-iterative frequency-domain methods for Maxwell's equations in a planewave basis, Opt. Express **8**(3), 173–190 (2001).

[104] T. P. White, B. T. Kuhlmey, R. C. McPhedran, D. Maystre, G. Renversez, C. M. de Sterke, L. C. Botten, Multipole method for microstructured optical fibers. I. Formulation, J. Opt. Soc. Am. B **19**(10), 2322–2330 (2002).

[105] K. Saitoh, M. Koshiba, Full-vectorial imaginary-distance beam propagation method based on a finite element scheme: application to photonic crystal fibers, EEE J. Quantum Electron. **38**(7), 927–933 (2002).

[106] B. J. Ainslie, C. R. Day, A review of single-mode fibers with modified dispersion characteristics, J. Light. Technol. **4**(8), 967–979 (1986).

[107] J. C. Knight, J. Arriaga, T. A. Birks, W. J. Wadsworth, P. S. J. Russell, Anomalous dispersion in photonic crystal fiber, IEEE Photonics Technol. Lett. **12**(7), 807–809 (2000).

[108] W. H. Reeves, D. V. Skryabin, F. Biancalana, J. C. Knight, P. S. J. Russell, F. G. Omenetto, A. Efimov, A. J. Taylor, Transformation and control of ultra-short pulses in dispersion- engineered photonic crystal fibres, Nature **424**, 511–515 (2003).

[109] D. Mogilevtsev, T. A. Birks, P. S. J. Russell, Group-velocity dispersion in photonic crystal fibers, Opt. Lett. **23**(21), 1662–1664 (1998).

[110] J. K. Ranka, R. S. Windeler, A. J. Stentz, Optical properties of high-delta air silica microstructure optical fibers, Opt. Lett. **25**(11), 796–

798 (2000).

[111] W. Reeves, J. Knight, P. S. J. Russell, P. Roberts, Demonstration of ultra-flattened dispersion in photonic crystal fibers, Opt. Express **10**(14), 609–613 (2002).

[112] A. Ferrando, E. Silvestre, P. Andres, J. Miret, M. Andres, Designing the properties of dispersion-flattened photonic crystal fibers, Opt. Express **9**(13), 687–697 (2001).

[113] K. Hansen, Dispersion flattened hybrid-core nonlinear photonic crystal fiber, Opt. Express **11**(13), 1503–1509 (2003).

[114] J. Hansryd, P. A. Andrekson, Broad-band continuous-wave-pumped fiber optical parametric amplifier with 49-dB gain and wavelength-conversion efficiency, IEEE Photonics Technol. Lett. **13**(3), 194–196 (2001).

[115] K. Saitoh, M. Koshiba, Highly nonlinear dispersion-flattened photonic crystal fibers for supercontinuum generation in a telecommunication window, Opt. Express **12**(10), 2027–2032 (2004).

[116] T. A. Birks, J. C. Knight, P. S. J. Russell, Endlessly single-mode photonic crystal fiber, Opt. Lett. **22**(13), 961–963 (1997).

[117] P. S. J. Russell, Photonic crystal fibers, Science (80-.). **299**, 358–362 (2003).

[118] J. C. Knight, T. a. Birks, R. F. Cregan, P. S. J. Russell, J. de Sandro, Large mode area photonic crystal fibre, Electron. Lett. **34**(13), 1347–1348 (1998).

[119] J. C. Baggett, T. M. Monro, K. Furusawa, D. J. Richardson, Comparative study of large-mode holey and conventional fibers, Opt. Lett. **26**(14), 1045–1047 (2001).

[120] N. Mortensen, M. D. Nielsen, J. R. Folkenberg, A. Petersson, H. R. Simonsen, Improved large-mode-area endlessly single-mode photonic crystal fibers, Opt. Lett. **28**(6), 393–395 (2003).

[121] J. Limpert, T. Schreiber, S. Nolte, H. Zellmer, A. Tünnermann, R. Iliev, F. Lederer, J. Broeng, G. Vienne, A. Petersson, C. Jakobsen, High-power air-clad large-mode-area photonic crystal fiber laser, Opt.

Express **11**(7), 818–823 (2003).

[122] P. L. Kelley, I. P. Kaminow, G. G. P. Agrawal, *Nonlinear fiber optics* (Academic Press, 2001).

[123] F. Luan, J. Knight, P. S. J. Russell, S. Campbell, D. Xiao, D. Reid, B. Mangan, D. Williams, P. Roberts, Femtosecond soliton pulse delivery at 800nm wavelength in hollow-core photonic bandgap fibers, Opt. Express **12**(5), 835–840 (2004).

[124] D. G. Ouzounov, F. R. Ahmad, D. Muller, N. Venkataraman, M. T. Gallagher, M. G. Thomas, J. Silcox, K. W. Koch, A. L. Gaeta, Generation of megawatt optical solitons in hollow-core photonic band-gap fibers, Science **301**, 1702–1704 (2003).

[125] M. Onishi, T. Okuno, T. Kashiwada, S. Ishikawa, N. Akasaka, M. Nishimura, Highly nonlinear dispersion-shifted fibers and their application to broadband wavelength converter, Opt. Fiber Technol. **4**(2), 204–214 (1998).

[126] A. V. Husakou, J. Herrmann, Supercontinuum generation, four-wave mixing, and fission pf higher-order solitons in photonic-crystal fibers, J. Opt. Soc. Am. B **19**(9), 2171–2182 (2002).

[127] K. T. V. Grattan, A. Agrawal, N. Kejalakshmy, B. M. A. Rahman, Soft glass equiangular spiral photonic crystal fiber for supercontinuum generation, IEEE Photonics Technol. Lett. **21**(22), 1722–1724 (2009).

[128] H. Ebendorff-Heidepriem, P. Petropoulos, S. Asimakis, V. Finazzi, R. Moore, K. Frampton, F. Koizumi, D. Richardson, T. Monro, Bismuth glass holey fibers with high nonlinearity, Opt. Express **12**(21), 5082–5087 (2004).

[129] D. Méchin, L. Brilland, J. Troles, T. Chartier, P. Besnard, Recent advances in very highly nonlinear Chalcogenide Photonic Crystal Fibers and their applications, Proc. SPIE **8257**, 8257–1–7 (2012).

[130] R. Guan, F. Zhu, Z. Gan, D. Huang, S. Liu, Stress birefringence analysis of polarization maintaining optical fibers, Opt. Fiber Technol. **11**(3), 240–254 (2005).

[131] V. Ramaswamy, R. H. Stolen, M. D. Divino, W. Pleibel, Birefringence

in elliptically clad borosilicate single-mode fibers, Appl. Opt. **18**(24), 4080–4084 (1979).

[132] A. Ortigosa-Blanch, J. C. Knight, W. J. Wadsworth, J. Arriaga, B. J. Mangan, T. A. Birks, P. S. J. Russell, Highly birefringent photonic crystal fibers, Opt. Lett. **25**(18), 1325–1327 (2000).

[133] T. Hansen, J. Broeng, S. Libori, E. Knudsen, A. Bjarklev, J. Jensen, H. Simonsen, Highly birefringent index-guiding photonic crystal fibers, IEEE Photonics Technol. Lett. **13**(6), 588–590 (2001).

[134] K. Suzuki, H. Kubota, S. Kawanishi, M. Tanaka, M. Fujita, Optical properties of a low-loss polarization-maintaining photonic crystal fiber, Opt. Express **9**(13), 676–680 (2001).

[135] K. Saitoh, M. Koshiba, Photonic bandgap fibers with high birefringence, IEEE Photonics Technol. Lett. **14**(9), 1291–1293 (2002).

[136] A. Michie, J. Canning, K. Lyytikäinen, M. Aslund, J. Digweed, Temperature independent highly birefringent photonic crystal fibre, Opt. Express **12**(21), 5160–5165 (2004).

[137] A. M. R. Pinto, M. Lopez-Amo, Photonic crystal fibers for sensing applications, J. of Sensors **2012**, 1–21 (2012).

[138] K. Mori, K. Sato, H. Takara, T. Ohara, Supercontinuum lightwave source generating 50 GHz spaced optical ITU grid seamlessly over S-, C- and L-bands, Electron. Lett. **39**(6), 544—-546 (2003).

[139] K. Bizheva, B. Považay, B. Hermann, H. Sattmann, W. Drexler, M. Mei, R. Holzwarth, T. Hoelzenbein, V. Wacheck, H. Pehamberger, Compact, broad-bandwidth fiber laser for sub-2-μm axial resolution optical coherence tomography in the 1300-nm wavelength region, Opt. Lett **28**(9), 707–709 (2003).

[140] T. R. Schibli, K. Minoshima, F. L. Hong, H. Inaba, A. Onae, H. Matsumoto, I. Hartl, M. E. Fermann, Frequency metrology with a turn-key all-fiber system, Opt. Lett **29**(21), 2467–2469 (2004).

[141] V. Nagarajan, E. Johnson, P. Schellenberg, W. Parson, R. Windeler, A compact versatile femtosecond spectrometer, Rev. Sci. Instrum. **73**(12), 4145–4149 (2002).

[142] B. Saleh, M. Teich, *Fundamentals of photonics* (John Wiley & Sons, 2007).

[143] I. H. Malitson, Interspecimen comparison of the refractive index of fused silica, J. Opt. Soc. Am. **55**(10), 1205–1209 (1965).

[144] C. A. De Francisco, B. V. Borges, M. A. Romero, A semivectorial method for the modeling of photonic crystal fibers, Microw. Opt. Technol. Lett. **38**(5), 418–421 (2003).

[145] M. H. Frosz, T. Sørensen, O. Bang, Nanoengineering of photonic crystal fibers for supercontinuum generation, Proc. SPIE **5950**, 59500–1–8 (2005).

[146] M. H. Frosz, P. Falk, O. Bang, The role of the second zero-dispersion wavelength in generation of supercontinua and bright-bright soliton-pairs across the zero-dispersion wavelength, Opt. Express **13**(16), 6181–6195 (2005).

[147] P. Falk, M. H. Frosz, O. Bang, Supercontinuum generation in a photonic crystal fiber with two zero-dispersion wavelengths tapered to normal dispersion at all wavelengths, Opt. Express **13**(19), 7535–7540 (2005).

[148] M. H. Frosz, O. Bang, A. Bjarklev, Soliton collision and Raman gain regimes in continuous-wave pumped supercontinuum generation, Opt. Express **14**(20), 9391–9407 (2006).

[149] P. Falk, M. H. Frosz, O. Bang, P. Andersen, A. Bjarklev, Supercontinuum generation in a photonic crystal fiber tapered to normal dispersion for all wavelengths, Proc. SPIE **5855**, 5855–1–5 (2005).

[150] M. Frosz, P. Falk, L. Pedersen, O. Bang, A. Bjarklev, Supercontinuum generation in untapered and tapered photonic crystal fibers with two zero dispersion wavelengths, Proc. SPIE **5733**, 5733–1–9 (2005).

[151] T. M. Monro, D. J. Richardson, N. G. Broderick, P. J. Bennett, Modeling large air fraction holey optical fibers, J. Lightwave Technol. **18**(1), 50–56 (2000).

[152] T. M. Monro, D. J. Richardson, N. G. Broderick, P. J. Bennett, Holey optical fibers: an efficient modal model, J. Lightwave Technol. **17**(6),

1093–1102 (1999).

[153] P. Hlubina, D. Ciprian, R. Chlebus, Spectral-domain interferometric technique used to measure group index dispersion of holey fibers, Opt. Commun. **281**, 4008–4013 (2008).

[154] Q. Ye, C. Xu, X. Liu, W. H. Knox, M. F. Yan, R. S. Windeler, B. Eggleton, Dispersion measurement of tapered air-silica microstructure fiber by white-light interferometry, Appl. Opt. **41**(22), 4467–4470 (2002).

[155] L. Labonté, P. Roy, D. Pagnoux, F. Louradour, C. Restoin, G. Mélin, E. Burov, Experimental and numerical analysis of the chromatic dispersion dependence upon the actual profile of small core microstructured fibres, J. Opt. A: Pure Appl. Opt. **8**, 933–938 (2006).

[156] P. Hlubina, M. Szpulak, D. Ciprian, T. Martynkien, W. Urbanczyk, Measurement of the group dispersion of the fundamental mode of holey fiber by white-light spectral interferometry, Opt. Express **15**(18), 11073–11081 (2007).

[157] P. Hlubina, D. Ciprian, M. H. Frosz, K. Nielsen, Measurement of chromatic dispersion of microstructured polymer fibers by white-light spectral interferometry, Proc. SPIE **7389**, 73890J–1–9 (2009).

[158] P. Peterka, J. KaÅĹka, P. Honzátko, D. Káčik, Measurement of chromatic dispersion of microstructure optical fibers using interferometric method, Opt. Appl. **38**(2), 295–303 (2008).

[159] H. Choi, C. Kee, K. Hong, J. Sung, S. Kim, D. Ko, J. Lee, J. Kim, H. Y. Park, Dispersion and birefringence of irregularly microstructured fiber with an elliptic core, Appl. Opt. **46**(35), 8493–8498 (2007).

[160] G. Stępniewski, J. Pniewski, M. Klimczak, T. Martynkien, D. Pysz, R. Stępień, I. Kujawa, K. Borzycki, R. Buczyński, Broadband dispersion measurement of photonic crystal fibers with nanostructured core, Opt. Quant. Electron. **47**(3), 807–814 (2015).

[161] J. Satsuma, N. Yajima, Initial value problems of one-dimensional self-modulation of nonlinear waves in dispersive media, Progr. Theor. Phys. Suppl. **55**, 284–306 (1974).

[162] M. W. Chbat, P. R. Prucnal, M. N. Islam, C. E. Soccolich, J. P. Gordon, Long-range interference effects of soliton reshaping in optical fibers, J. Opt. Soc. Am. B **10**(8), 1386–1395 (1993).

[163] C. Lin, L. G. Cohen, W. G. French, H. M. Presby, Measuring dispersion in single-mode fibers in the 1.1–1.3 µm spectral region – a pulse synchronization technique, IEEE J. Quantum Electron. **16**(1), 33–36 (1980).

[164] D. Ouzounov, D. Homoelle, W. Zipfel, W. W. Webb, A. L. Gaeta, J. West, J. Fajardo, K. Koch, Dispersion measurements of microstructured fibers using femtosecond laser pulses, Opt. Commun. **192**, 219–223 (2001).

[165] T. H. Maiman, Stimulated optical radiation in ruby, Nature **187**, 493–494 (1960).

[166] W. J. Jones, B. P. Stoicheff, Inverse Raman spectra: induced absorption at optical frequencies, Phys. Rev. Lett. **13**(22), 657–659 (1964).

[167] R. Brewer, Frequency shifts in self-focused ligth, Phys. Rev. Lett. **19**(1), 8–10 (1967).

[168] Y. Ueda, K. Shimoda, Observation of stimulated Raman emission and stimulated Rayleigh-wing scattering from self-trapped filaments of a laser beam, Jpn. J .Appl .Phys. **6**(5), 628–633 (1967).

[169] F. Shimizu, Frequency broadening in liquids by a short light pulse, Phys. Rev. Lett. **19**(19), 1097–1100 (1967).

[170] N. Bondarenko, I. Eremina, V. Talanov, Broadening of spectrum in self-focusing of light in crystals, JETP Lett. **12**(3), 85–87 (1970).

[171] R. L. Fork, C. V. Shank, C. Hirlimann, R. Yen, W. J. Tomlinson, Femtosecond white-light continuum pulses, Opt. Lett. **8**(1), 1–3 (1983).

[172] J. Manassah, P. Ho, A. Katz, R. R. Alfano, Ultrafast supercontinuum laser source, Photonics Spectra **18**, 53–59 (1984).

[173] J. T. Manassah, R. R. Alfano, M. Mustafa, Spectral distribution of an ultrafast supercontinuum laser source, Phys. Lett. **107**(7), 305–309 (1985).

[174] Alfano, R. R., *The supercontinuum laser source* (Springer, 2006).

[175] A. Dubietis, G. Tamošauskas, R. Šuminas, V. Jukna, A. Couairon, Ultrafast supercontinuum generation in bulk condensed media (Invited review), Lith. J. Phys. **57**(3), 113–157 (2017).

[176] R. H. Stolen, E. P. Ippen, A. R. Tynes, Raman oscillation in glass optical waveguide, Appl. Phys. Lett. **20**(2), 62–64 (1972).

[177] E. P. Ippen, R. H. Stolen, Stimulated Brillouin scattering in optical fibers, Appl. Phys. Lett. **21**(11), 539–541 (1972).

[178] R. H. Stolen, A. Ashkin, Optical Kerr effect in glass waveguide, Appl. Phys. Lett. **22**(6), 294–296 (1973).

[179] R. H. Stolen, C. Lin, Self-phase-modulation in silica optical fibers, Phys. Rev. A **17**(4), 1448–1453 (1978).

[180] R. H. Stolen, Phase-matched-stimulated four-photon mixing in silica-fiber waveguides, IEEE J. Quantum Electron. **11**(3), 100–103 (1975).

[181] C. Lin, R. H. Stolen, New nanosecond continuum for excited-state spectroscopy, Appl. Phys. Lett. **28**(4), 216–218 (1976).

[182] a. S. Gouveia-Neto, M. E. Faldon, J. R. Taylor, Solitons in the region of the minimum group-velocity dispersion of single-mode optical fibers, Opt. Lett. **13**(9), 770–772 (1988).

[183] P. Beaud, W. Hodel, B. Zysset, H. P. Weber, Ultrashort pulse propagation, pulse breakup, and fundamental soliton formation in a single-mode optical fiber, IEEE J. Quantum Electron. **23**(11), 1938–1946 (1987).

[184] J. Schütz, W. Hodel, H. P. Weber, Nonlinear pulse distortion at the zero dispersion wavelength of an optical fibre, Opt. Commun. **95**, 357–365 (1993).

[185] M. N. Islam, G. Sucha, I. Bar-Joseph, M. Wegener, J. P. Gordon, D. S. Chemla, Femtosecond distributed soliton spectrum in fibers, J. Opt. Soc. Am. B **6**(6), 1149–1158 (1989).

[186] Y. Kodama, A. Hasegawa, Nonlinear pulse propagation in a monomode dielectric guide, IEEE J. Quantum Electron. **23**(5), 510–

524 (1987).

[187] M. N. Islam, G. Sucha, I. Bar-Joseph, M. Wegener, J. P. Gordon, D. S. Chemla, Broad bandwidths from frequency-shifting solitons in fibers, Opt. Lett. **14**(7), 370–372 (1989).

[188] T. Morioka, K. Mori, M. Saruwatari, More than 100-wavelength-channel picosecond optical pulse generation from single laser source using supercontinuum in optical fibres, Electron. Lett. **29**(10), 862–864 (1993).

[189] H. Takara, S. Kawanishi, T. Morioka, K. Mori, M. Saruwatari, 100 Gbit/s optical waveform measurement with 0.6ps resolution optical sampling using subpicosecond supercontinuum pulses, Electron. Lett. **30**(14), 1152–1153 (1994).

[190] T. Morioka, S. Kawanishi, K. Mori, M. Saruwatari, Transform-limited, femtosecond WDM pulse generation by spectral filtering of gigahertz supercontinuum, Electron. Lett. **30**(14), 1166–1168 (1994).

[191] T. Morioka, S. Kawanishi, K. Mori, M. Saruwatari, Nearly penalty-free, <4 ps supercontinuum Gbit/s pulse generation over 1535-1560 nm, Electron. Lett. **30**(10), 790–791 (1994).

[192] Kawanishi S., Takara H., Morioka T., Kamatani O., Saruwatari M., 200 Gbit/s and 100 km time-division-multiplexed optical-transmission using supercontinuum pulses with prescaled PLL timing extraction and all-optical demultiplexing, Electron. Lett. **31**(10), 816–817 (1995).

[193] B. Mikulla, L. Leng, S. Sears, B. C. Collings, M. Arend, K. Bergman, Broad-band high-repetition-rate source for spectrally sliced WDM, IEEE Photonics Technol. Lett. **11**(4), 418–420 (1999).

[194] T. Okuno, M. Onishi, M. Nishimura, Generation of ultra-broad-band supercontinuum by dispersion-flattened and decreasing fiber, IEEE Photonics Technol. Lett. **10**(1), 72–74 (1998).

[195] K. Mori, H. Takara, S. Kawanishi, Analysis and design of supercontinuum pulse generation in a single-mode optical fiber, J. Opt. Soc. Am. B **18**(12), 1780–1792 (2001).

[196] W. Wadsworth, J. Knight, A. Ortigosa-Blanch, J. Arriaga, E. Silvestre, P. S. J. Russell, Soliton effects in photonic crystal fibres at 850 nm, Electron. Lett. **36**(1), 53 (2000).

[197] A. V. Husakou, J. Herrmann, Supercontinuum generation of higher-order solitons by fission in photonic crystal fibers, Phys. Rev. Lett. **87**(20), 203901–1–4 (2001).

[198] A. Ortigosa-Blanch, J. C. Knight, P. S. J. Russell, Pulse breaking and supercontinuum generation with 200-fs pump pulses in photonic crystal fibers, J. Opt. Soc. Am. B **19**(11), 2567 – 2572 (2002).

[199] A. V. Gorbach, D. V. Skryabin, J. M. Stone, J. C. Knight, Four-wave mixing of solitons with radiation and quasi-nondispersive wave packets at the short-wavelength edge of a supercontinuum, Opt. Express **14**(21), 9854–9863 (2006).

[200] J. Herrmann, U. Griebner, N. Zhavoronkov, A. Husakou, D. Nickel, J. C. Knight, W. J. Wadsworth, P. S. J. Russell, G. Korn, Experimental evidence for supercontinuum generation by fission of higher-order solitons in photonic fibers, Phys. Rev. Lett. **88**(17), 173901–1–4 (2002).

[201] M. Lehtonen, G. Genty, H. Ludvigsen, M. Kaivola, Supercontinuum generation in a highly birefringent microstructured fiber, Appl. Phys. Lett. **82**(14), 2197–2199 (2003).

[202] S. Coen, A. H. L. Chau, R. Leonhardt, J. D. Harvey, J. C. Knight, W. J. Wadsworth, P. S. J. Russell, White-light supercontinuum generation with 60-ps pump pulses in a photonic crystal fiber, Opt. Lett. **26**(17), 1356–1358 (2001).

[203] T. Schreiber, J. Limpert, H. Zellmer, A. Tünnermann, K. P. Hansen, High average power supercontinuum generation in photonic crystal fibers, Opt. Commun. **228**, 71–78 (2003).

[204] J. Price, W. Belardi, T. Monro, A. Malinowski, A. Piper, D. Richardson, Soliton transmission and supercontinuum generation in holey fiber, using a diode pumped Ytterbium fiber source, Opt. Express **10**(8), 382–387 (2002).

[205] L. Provino, J. Dudley, H. Maillotte, N. Grossard, R. S. Windeler,

B. Eggleton, Compact broadband continuum source based on microchip laser pumped microstructured fibre, Electron. Lett. **37**(9), 982–984 (2001).

[206] P. Champert, S. Popov, J. Taylor, Multi-watt average power continuum generation in holey fibers pumped by compact fiber-based source, in *Conference on Lasers and Electo-Optics (CLEO) 2001* (Baltimore, 2001), 4–5.

[207] A. V. Avdokhin, S. V. Popov, J. R. Taylor, Continuous-wave, high-power, Raman continuum generation in holey fibers, Opt. Lett. **28**(15), 1353–1355 (2003).

[208] F. Vanholsbeeck, S. Martin-Lopez, M. González-Herráez, S. Coen, The role of pump laser incoherence in continuous-wave supercontinuum generation, Opt. Express **13**(17), 6615–6625 (2005).

[209] A. Demircan, U. Bandelow, Supercontinuum generation by the modulation instability, Opt. Commun. **244**, 181–185 (2005).

[210] X. Jiang, N. Y. Joly, M. A. Finger, F. Babic, G. K. L. Wong, J. C. Travers, P. S. J. Russell, Deep-ultraviolet to mid-infrared supercontinuum generated in solid-core ZBLAN photonic crystal fibre, Nat. Photonics **9**, 133–139 (2015).

[211] P. Domachuk, N. A. Wolchover, M. Cronin-Golomb, A. Wang, A. K. George, C. M. B. Cordeiro, J. C. Knight, F. G. Omenetto, Over 4000 nm bandwidth of mid-IR supercontinuum generation in sub-centimeter segments of highly nonlinear tellurite PCFs, Opt. Express **16**(10), 7161–7168 (2008).

[212] J. H. Price, X. Feng, A. M. Heidt, G. Brambilla, P. Horak, F. Poletti, G. Ponzo, P. Petropoulos, M. Petrovich, J. Shi, M. Ibsen, W. H. Loh, H. N. Rutt, D. J. Richardson, Supercontinuum generation in non-silica fibers, Opt. Fiber Technol. **18**, 327–344 (2012).

[213] K. M. Hilligsøe, T. V. Andersen, H. N. Paulsen, C. K. Nielsen, K. Mølmer, S. Keiding, R. Kristiansen, K. P. Hansen, J. J. Larsen, Supercontinuum generation in a photonic crystal fiber with two zero dispersion wavelengths, Opt. Express **12**(6), 1045–1054 (2004).

[214] G. Genty, M. Lehtonen, H. Ludvigsen, M. Kaivola, Enhanced bandwidth of supercontinuum generated in microstructured fibers, Opt. Express **12**(15), 3471–3480 (2004).

[215] A. Kudlinski, B. Cumberland, J. Travers, G. Bouwmans, Y. Quiquempois, A. Mussot, CW supercontinuum generation in photonic crystal fibres with two zero-dispersion wavelengths, AIP Conf. Proc. **1055**, 15–18 (2008).

[216] I. Bugar, I. V. Fedotov, A. B. Fedotov, M. Koys, R. Buczynski, D. Pysz, J. Chlpik, F. Uherek, A. M. Zheltikov, Polarization-controlled dispersive wave redirection in dual-core photonic crystal fiber, Laser Phys. **18**(12), 1420–1428 (2008).

[217] R. Buczynski, D. Pysz, T. Martynkien, D. Lorenc, I. Kujawa, T. Nasilowski, F. Berghmans, H. Thienpont, R. Stepien, Ultra flat supercontinuum generation in silicate dual core microstructured fiber, Laser Phys. Lett. **6**(8), 575–581 (2009).

[218] X. Qi, S. Chen, T. Liu, J. Hou, Enhanced visible supercontinuum generation in seven-core photonic crystal fiber, Proc. SPIE **10016**, 100160C–1–6 (2016).

[219] M. Klimczak, K. Komolibus, T. Piwoński, B. Siwicki, D. Pysz, R. Stepień, T. Ochalski, R. Buczyński, Impact of steepness of pump temporal pulse profile on spectral flatness and correlation of supercontinuum in all-solid photonic crystal fibers with flattened normal dispersion, J. Opt. **16**, 1–9 (2014).

[220] A. M. Heidt, Pulse preserving flat-top supercontinuum generation in all-normal dispersion photonic crystal fibers, J. Opt. Soc. Am. B **27**(3), 550–559 (2010).

[221] B. Siwicki, M. Klimczak, G. Sobon, J. Sotor, D. Pysz, R. Stepien, K. Abramski, R. Buczynski, Numerical simulations of spectral broadening in all-normal dispersion photonic crystal fiber at various pump pulse conditions, Opt. Eng. **54**(1), 016102–1–8 (2015).

[222] R. Buczynski, D. Pysz, R. Stepien, A. J. Waddie, I. Kujawa, R. Kasztelanic, M. Franczyk, M. R. Taghizadeh, Supercontinuum

generation in photonic crystal fibers with nanoporous core made of soft glass, Laser Phys. Lett. **8**(6), 443–448 (2011).

[223] J. Pniewski, T. Stefaniuk, G. Stepniewski, D. Pysz, T. Martynkien, R. Stepien, R. Buczynski, Limits in development of photonic crystal fibers with a subwavelength inclusion in the core, Opt. Mater. Express **5**(10), 2366–2376 (2015).

[224] K. Blow, D. Wood, Theoretical description of transient stimulated Raman scattering in optical fibers, IEEE J. Quantum Electron. **25**(12), 2665–2673 (1989).

[225] R. H. Stolen, J. P. Gordon, W. J. Tomlinson, H. A. Haus, Raman response function of silica-core fibers, J. Opt. Soc. Am. B **6**(6), 1159–1166 (1989).

[226] J. Hult, A fourth-order Runge-Kutta in the interaction picture method for simulating supercontinuum generation in optical fibers, J. Lightwave Technol. **25**(12), 3770–3775 (2007).

[227] Francois, P. L., Nonlinear propagation of ultrashort pulses in optical fibres - Total field formulation in the frequency-domain, J. Opt. Soc. Am. B **8**(2), 276–293 (1991).

[228] M. N. Islam, L. F. Mollenauer, R. H. Stolen, J. R. Simpson, H.-T. Shang, Cross-phase modulation in optical fibers, Opt. Lett. **12**(8), 625–627 (1987).

[229] P. Champert, S. V. Popov, J. R. Taylor, Generation of multiwatt, broadband continua in holey fibers, Opt. Lett. **27**(2), 122–124 (2002).

[230] D. Grischkowsky, A. C. Balant, Optical pulse compression based on enhanced frequency chirping, Appl. Phys. Lett. **41**(1), 1–3 (1982).

[231] J. S. Russell, Report on waves, in *14th meeting of the British association for the advancement of science* (York, 1845).

[232] T. Dauxois, M. Peyrard, *Physics of solitons* (Cambridge University press, 2006).

[233] J. R. Taylor (ed), *Optical solitons - theory and experiment* (Cambridge University press, 1992).

[234] L. F. Mollenauer, R. H. Stolen, J. P. Gordon, Experimental observa-

tion of picosecond pulse narrowing and solitons in optical fibers, Phys. Rev. Lett. **45**(13), 1095–1098 (1980).

[235] K. Tai, A. Hasegawa, N. Bekki, Fission of optical solitons induced by stimulated Raman effect, Opt. Lett. **13**(5), 392–394 (1988).

[236] C. Chen, P. L. Kelley, Nonlinear pulse compression in optical fibers: scaling laws and numerical analysis, J. Opt. Soc. Am. B **19**(9), 1961–1967 (2002).

[237] I. Cristiani, R. Tediosi, L. Tartara, V. Degiorgio, Dispersive wave generation by solitons in microstructured optical fibers, Opt. Express **12**(1), 124–135 (2004).

[238] N. Akhmediev, M. Karlsson, Cherenkov radiation emitted by solitons in optical fibers, Phys. Rev. A **51**(3), 2602–2607 (1995).

[239] P. Wai, C. Menyuk, Y. Lee, H. Chen, Nonlinear pulse propagation in the neighborhood of the zero-dispersion wavelength of monomode optical fibers 464–466 (1986).

[240] P. K. Wai, H. H. Chen, Y. C. Lee, Radiations by solitons at the zero group-dispersion wavelength of single-mode optical fibers, Phys. Rev. A **41**(1), 426–439 (1990).

[241] G. Agrawal, Nonlinear fiber optics: its history and recent progress, J. Opt. Soc. Am. B **28**(12), 1–10 (2011).

[242] J. P. Gordon, Theory of the soliton self-frequency shift, Opt. Lett. **11**(10), 662–664 (1986).

[243] A. A. Voronin, A. M. Zheltikov, Soliton self-frequency shift decelerated by self-steepening, Opt. Lett. **33**(15), 1723–1725 (2008).

[244] D. V. Skryabin, F. Luan, J. C. Knight, P. S. J. Russell, Soliton self-frequency shift cancellation in photonic crystal fibers, Science **301**, 1705–1708 (2003).

[245] N. Nishizawa, T. Goto, Characteristics of pulse trapping by ultrashort soliton pulse in optical fibers across zero-dispersion wavelength, Opt. Express **10**(21), 1151–1160 (2002).

[246] G. Genty, M. Lehtonen, H. Ludvigsen, Effect of cross-phase modulation on supercontinuum generated in microstructured fibers with

sub-30 fs pulses, Opt. Express **12**(19), 4614–4624 (2004).

[247] A. V. Gorbach, D. V. Skryabin, Light trapping in gravity-like potentials and expansion of supercontinuum spectra in photonic-crystal fibres, Nat. Photonics **1**(11), 653–657 (2007).

[248] D. V. Skryabin, A. V. Yulin, Theory of generation of new frequencies by mixing of solitons and dispersive waves in optical fibers, Phys. Rev. E **72**, 016619–1–10 (2005).

[249] A. Efimov, A. Taylor, F. Omenetto, A. Yulin, N. Joly, F. Biancalana, D. Skryabin, J. Knight, P. S. J. Russell, Time-spectrally-resolved ultrafast nonlinear dynamics in small-core photonic crystal fibers: experiment and modelling, Opt. Express **12**(26), 6498–6507 (2004).

[250] A. Mussot, E. Lantz, H. Maillotte, T. Sylvestre, C. Finot, S. Pitois, Spectral broadening of a partially coherent CW laser beam in single-mode optical fibers, Opt. Express **12**(13), 2838–2843 (2001).

[251] S. Kobtsev, S. Smirnov, Modelling of high-power supercontinuum generation in highly nonlinear, dispersion shifted fibers at CW pump, Opt. Express **13**(18), 6912–6918 (2005).

[252] R. H. Stolen, C. Lee, R. K. Jain, Development of the stimulated Raman spectrum in single-mode silica fibers, J. Opt. Soc. Am. B **1**(4), 652–657 (1984).

[253] M. N. Islam, G. Sucha, I. Bar-Joseph, M. Wegener, J. P. Gordon, D. S. Chemla, Femtosecond distributed soliton spectrum in fibers, J. Opt. Soc. Am. B **6**(6), 1149–1158 (1989).

[254] N. A. Mortensen, C. F. A. S, D. Birkerød, Effective area of photonic crystal fibers, Opt. Express **10**(7), 341–348 (2002).

[255] K. Saitoh, M. Koshiba, N. A. Mortensen, Nonlinear photonic crystal fibres: pushing the zero-dispersion towards the visible, New J. Phys. **8**, 1–9 (2006).

[256] A. W. Snyder, A. W. Snyder, Coupling of modes on a tapered dielectric cylinder, IEEE Trans. Microw. Theory Tech. **18**(7), 383–392 (1970).

[257] T. A. Birks, W. J. Wadsworth, P. S. J. Russell, Supercontinuum generation in tapered fibers, Opt. Lett. **25**(19), 1415–1417 (2000).

[258] W. J. Wadsworth, A. Ortigosa-Blanch, J. C. Knight, T. A. Birks, T.-P. M. Man, P. S. J. Russell, Supercontinuum generation in photonic crystal fibers and optical fiber tapers: a novel light source, J. Opt. Soc. Am. B **19**(9), 2148–2155 (2002).

[259] J. Teipel, D. Türke, H. Giessen, A. Zintl, B. Braun, Compact multi-Watt picosecond coherent white light sources using multiple-taper fibers, Opt. Express **13**(5), 1734–1742 (2005).

[260] D. Kane, R. Trebino, 1991 Optical Society of America annual meeting: summaries of papers presented at the annual meeting of the Optical Society of America (Optical Society of America, 1991).

[261] D. J. Kane, R. Trebino, Characterization of arbitrary femtosecond pulses using frequency-resolved optical gating, IEEE J. Quantum Electron. **29**(2), 571–579 (1993).

[262] R. Trebino, D. J. Kane, Using phase retrieval to measure the intensity and phase of ultrashort pulses: frequency-resolved optical gating, J. Opt. Soc. Am. A **10**(5), 1101–1111 (1993).

[263] D. J. Kane, R. Trebino, Single-shot measurement of the intensity and phase of an arbitrary ultrashort pulse by using frequency-resolved optical gating, Opt. Lett. **18**(10), 823–825 (1993).

[264] R. Trebino, *Frequency-resolved optical gating: the measurement of ultrashort laser pulses* (Kluwer, 2002).

[265] R. Trebino, K. W. Delong, D. N. Fittinghoff, J. N. Sweetser, M. A. Krumbugel, B. A. Richman, D. J. Kane, Measuring ultrashort laser pulses in the time-frequency domain using frequency-resolved optical gating, Rev. Sci. Instrum. **68**(9), 3277–3295 (1997).

[266] K. W. Delong, R. Trebino, Improve ultrashort pulse-retrieval algorithm for frequency-resolved optical gating, J. Opt. Soc. Am. A **11**(9), 2429–2437 (1994).

[267] J. Paye, M. Ramaswamy, J. G. Fujimoto, E. P. Ippen, Measurement of the amplitude and phase of ultrashort light pulses from spectrally resolved autocorrelation, Opt. Lett. **18**(22), 1946–1948 (1993).

[268] K. W. Delong, D. N. Fittinghoff, R. Trebino, B. Kohler, K. Wilson,

Pulse retrieval in frequency-resolved optical gating based on the method of generalized projections, Opt. Lett. **19**(24), 2152–2154 (1994).

[269] D. J. Kane, G. Rodriguez, A. Taylor, T. S. Clement, Simultaneous measurement of two ultrashort laser pulses from a single spectrogram in a single shot, J. Opt. Soc. Am. B **14**(4), 935–943 (1997).

[270] K. W. DeLong, R. Trebino, J. Hunter, W. E. White, Frequency-resolved optical gating with the use of second-harmonic generation, J. Opt. Soc. Am. B **11**(11), 2206–2215 (1994).

[271] K. W. DeLong, R. Trebino, D. J. Kane, Comparison of ultrashort-pulse frequency-resolved-optical-gating traces for three common beam geometries, J. Opt. Soc. Am. B **11**(9), 1595–1608 (1994).

[272] B. Kohler, V. V. Yakovlev, K. R. Wilson, J. Squier, K. W. Delong, R. Trebino, Phase and intensity characterization of femtosecond pulses from a chirped-pulse amplifier by frequency-resolved optical gating, Opt. Lett. **20**(5), 483–485 (1995).

[273] D. J. Kane, R. Trebino, Characterization of arbitrary femtosecond pulses using frequency-resolved optical gating, IEEE J. Quantum Electron. **29**(2), 571–579 (1993).

[274] T. S. Clement, A. J. Taylor, D. J. Kane, Single-shot measurement of the amplitude and phase of ultrashort laser pulses in the violet, Opt. Lett. **20**(1), 70–72 (1995).

[275] J. N. Sweetser, D. N. Fittinghoff, R. Trebino, Transient-grating frequency-resolved optical gating, Opt. Lett. **22**(8), 519–521 (1997).

[276] T. Tsang, M. a. Krumbügel, K. W. Delong, D. N. Fittinghoff, R. Trebino, Frequency-resolved optical-gating measurements of ultrashort pulses using surface third-harmonic generation, Opt. Lett. **21**(17), 1381–1383 (1996).

[277] S. Yang, A. M. Weiner, K. R. Parameswaran, M. M. Fejer, Ultrasensitive second-harmonic generation frequency-resolved optical gating by aperiodically poled LiNbO$_3$ waveguides at 1.5 micron, Opt. Lett. **30**(16), 2164–2166 (2005).

[278] G. Stibenz, G. Steinmeyer, Interferometric frequency-resolved optical gating, Opt. Lett. **32**(7), 2617–2626 (2007).

[279] S. Linden, H. Giessen, J. Kuhl, XFROG - a new method for amplitude and phase characterization of weak ultrashort pulses, Phys. Stat. Sol. B **206**, 119–124 (1998).

[280] P. O'Shea, M. Kimmel, X. Gu, R. Trebino, Highly simplified device for ultrashort-pulse measurement, Opt. Lett. **26**(12), 932–934 (2001).

[281] L. Xu, E. Zeek, R. Trebino, Simulations of frequency-resolved optical gating for measuring very complex pulses, J. Opt. Soc. Am. B **25**(6), 70–80 (2008).

[282] R. Trebino, Measuring the seemingly immeasurable, Nat. Photonics **5**, 189–192 (2011).

[283] S. Linden, J. Kuhl, H. Giessen, Amplitude and phase characterization of weak blue ultrashort pulses by downconversion, Opt. Lett. **24**(8), 569–571 (1999).

[284] J. Ratner, R. Trebino, XFROG retrieval of extremely complex pulses, in *Frontiers in Optics 2011* (San Jose, 2011), 1–2.

[285] J. Zhang, A. Shreenath, M. Kimmel, E. Zeek, R. Trebino, S. Link, Measurement of the intensity and phase of attojoule femtosecond light pulses using optical-parametric-amplification cross-correlation frequency-resolved optical gating, Opt. Express **11**(6), 601–609 (2003).

[286] L. Xu, X. Gu, M. Kimmel, P. O'Shea, R. Trebino, A. Galvanauskas, Ultra-broadband IR continuum generation and its phase measurement using cross-correlation FROG, in *Conference on Lasers and Electro-Optics (CLEO) 2001* (Baltimore, 2001), volume CTuN1, 198–200.

[287] P. O. Shea, M. Kimmel, X. Gu, R. Trebino, Increased-bandwidth in ultrashort-pulse measurement using an angle-dithered nonlinear-optical crystal, Opt. Express **7**(10), 342–349 (2000).

[288] J. Dudley, X. Gu, L. Xu, M. Kimmel, E. Zeek, P. O'Shea, R. Trebino, S. Coen, R. Windeler, Cross-correlation frequency resolved optical

gating analysis of broadband continuum generation in photonic crystal fiber: simulations and experiments, Opt. Express **10**(21), 1215–1221 (2002).

[289] X. Gu, L. Xu, M. Kimmel, E. Zeek, P. O'Shea, A. P. Shreenath, R. Trebino, R. S. Windeler, Frequency-resolved optical gating and single-shot spectral measurements reveal fine structure in microstructure-fiber continuum, Opt. Lett. **27**(13), 1174–1176 (2002).

[290] Q. Cao, X. Gu, E. Zeek, M. Kimmel, R. Trebino, J. Dudley, R. Windeler, Measurement of the intensity and phase of supercontinuum from an 8-mm-long microstructure fiber, Appl. Phys. B **77**, 239–244 (2003).

[291] A. Efimov, A. Taylor, F. Omenetto, A. Yulin, N. Joly, F. Biancalana, D. Skryabin, J. Knight, P. S. J. Russell, Time-spectrally-resolved ultrafast nonlinear dynamics in small-core photonic crystal fibers: experiment and modelling, Opt. Express **12**(26), 6498–6507 (2004).

[292] B. Tsermaa, B. K. Yang, M. W. Kim, J. S. Kim, Characterization of supercontinuum and ultraviolet pulses by using XFROG, J. Opt. Soc. Korea **13**(1), 158–165 (2009).

[293] J. Teipel, K. Franke, D. Türke, F. Warken, D. Meiser, M. Leuschner, H. Giessen, Characteristics of supercontinuum generation in tapered fibers using femtosecond laser pulses, Appl. Phys. B **77**, 245–251 (2003).

[294] S. N. Bagaev, V. I. Denisov, V. F. Zakharyash, V. M. Klementyev, S. M. Kobtsev, I. I. Korel', S. A. Kuznetsov, S. V. Kukarin, V. S. Pivtsov, S. V. Smirnov, N. V. Fateev, Spectral and temporal characteristics of a supercontinuum in tapered optical fibres, Quantum. Electron. **34**(12), 1107–1115 (2004).

[295] T. C. Wong, M. Rhodes, R. Trebino, Single-shot measurement of the complete temporal intensity and phase of supercontinuum, Optica **1**(2), 119–124 (2016).

[296] G. Genty, S. Coen, J. M. Dudley, Fiber supercontinuum sources, J. Opt. Soc. Am. B **24**(8), 1771–1785 (2007).

[297] R. R. Cordero, P. Roth, On two methods to evaluate the uncertainty of derivatives calculated from polynomials fitted to experimental data, Metrologia **42**, 39–44 (2005).

[298] R. L. Fork, O. E. Martinez, J. P. Gordon, Negative dispersion using pairs of prisms, Opt. Lett. **9**(5), 150–152 (1984).

[299] J. Santhanam, G. P. Agrawal, Raman-induced spectral shifts in optical fibers: general theory based on the moment method, Opt. Commun. **222**, 413–420 (2003).

[300] J. R. D. Oliveira, M. a. D. Moura, J. M. Hickmann, a. S. L. Gomes, Self-steepening of optical pulses in dispersive media, J. Opt. Soc. Am. B **9**(11), 2025 (1992).

[301] S. Coen, D. A. Wardle, J. D. Harvey, Observation of non-phase-matched parametric amplification in resonant nonlinear optics, Phys. Rev. Lett. **89**(27), 1–4 (2002).

[302] F. Vanholsbeeck, P. Emplit, S. Coen, Complete experimental characterization of the influence of parametric four-wave mixing on stimulated Raman gain, Opt. Lett. **28**(20), 1960–1962 (2003).

[303] F. Mitschke, *Fiber optics. Physics and technology* (Springer, 2010).

Curriculum Vitae

Personal information

Name, surname:	Julius Vengelis
Date of birth:	12 August 1989
Place of birth:	Vilnius, Lithuania
E-mail:	julius.vengelis@gmail.com

Education

2014 - 2018	Vilnius University, Faculty of Physics, Laser Research Center. *Physics PhD studies*
2012 - 2014	Vilnius University, Faculty of Physics. *Laser physics and optical technologies Master degree studies*
2008 - 2012	Vilnius University, Faculty of Physics. *Applied physics Bachelor degree studies*
2008	Vilnius Karoliniškės gymnasium. *Secondary education*
2006 - 2008	Vilnius University, Faculty of Mathematics and Informatics. *Lithuanian school of young mathematicians*

Work experience

2011 - present	Laboratory assistant, Engineer, Research assistant at Vilnius University, Faculty of Physics, Laser Research Center.

Honors and awards

2017	SPIE student travel grant
2016	EUCALL young researcher travel grant
2014	Magna Cum Laude Honors. Graduated Master's studies with Magna Cum Laude diploma